Semiconductors, Vol. 36, No. 1, 2002, pp. 1–20. Translated from Fizika i Tekhnika Poluprovodnikov, Vol. 36, No. 1, 2002, pp. 3–23.
Original Russian Text Copyright © 2002 by Ravich, Nemov.

REVIEW

Hopping Conduction via Strongly Localized Impurity States of Indium in PbTe and Its Solid Solutions

Yu. I. Ravich and S. A. Nemov
St. Petersburg State Technical University, St. Petersburg, 195251 Russia

Submitted May 24, 2001; accepted for publication May 30, 2001

Abstract—Experimental investigations of the transport phenomena (electric conduction; Seebeck, Hall, and Nernst–Ettingshausen effects) in PbTe and $Pb_{1-x}Sn_xTe$ solid solutions with high content of In impurity (up to 20 at. %) at temperatures of up to 400 K are reviewed. Many properties of these substances are similar to those of noncrystalline materials. The experimental data are analyzed in terms of hopping conduction via strongly localized impurity states related to In atoms. Temperature dependences of transport coefficients, which are uncommon to IV–VI compounds; inversion of thermoelectric power with negative Hall coefficient; and a positive Nernst–Ettingshausen coefficient are accounted for. The activation energy of hopping conduction, which characterizes the effective energy spread of impurity levels; the effective radius of the wave function; and the energy dependence of the density of localized states are found from experimental data. The discussion of the experimental data on hopping conduction is preceded by a brief description of resonance and deep localized electron states related to indium impurities in IV–VI compounds. Particular attention is given to the specific features of impurity states in samples with high In content, in which the hopping conduction is observed. *© 2002 MAIK "Nauka/Interperiodica".*

INTRODUCTION

Group III impurities impart specific properties to IV–VI semiconductors, which are mainly associated with the formation of deep and resonance electron states. The general effect is the pinning of the chemical potential at the impurity levels. However, the electronic properties of semiconductors doped with different Group III elements are quite diverse. Moreover, the doping of different compounds of the above type with one and the same Group III impurity produces dissimilar results. The differences in properties arise depending on the part of the electronic spectrum in which the impurity levels lie. For example, indium in PbTe and other lead chalcogenides gives rise to various states in the conduction band, near its edge; the chemical potential is pinned in this part of the energy spectrum, and, therefore, In acts as a donor. Thallium in lead chalcogenides and indium in SnTe form resonance states inside the valence band and appear as acceptors.

Finally, on adding Sn to PbTe, the level of In impurity states is shifted to the conduction band bottom and crosses it, so that localized states are formed in the band gap of $Pb_{1-x}Sn_xTe$ solid solutions in a certain range of x values. This effect also occurs in PbTe at high In content (ca. 15–20 at. %). The pinning of the chemical potential in the band gap leads to low free carrier densities, and localized states play a significant role in transport phenomena; i.e., charge transport mainly occurs via hopping conduction.

At relatively low In content in PbTe (up to approximately 2 at. %), the position of impurity levels relative to the conduction band bottom is the same over the whole sample, and the Fermi level pinning leads to an exceptional spatial uniformity of the electron density, despite the significant amount of uncontrolled, electrically active impurities and intrinsic defects distributed nonuniformly in space. By contrast, at high In content, or in $Pb_{1-x}Sn_xTe$ solid solutions, electron density fluctuations, energy spread of impurity states, and random potential relief appear owing to the dependence of the energy of impurity states on the content of In and Sn. Consequently, retaining their crystal structure, samples with high In content acquire many properties of disordered systems and, in particular, Fermi-glasses.

This review presents the results of experimental studies and theoretical analysis of transport phenomena in PbTe and $Pb_{0.78}S_{0.22}Te$ solid solutions with high In content, in which hopping conduction is predominant. Indium impurity states are strongly localized, and, therefore, the hopping conduction is observed at much higher impurity densities and temperatures, compared with the conventional semiconductors with shallow impurity states (Ge, GaAs, etc.). Analysis of the experimental data on hopping conduction yields such important characteristics as the radii of impurity wave functions, the spread of energy levels, and the density of localized states.

The discussion of the hopping conduction is preceded by a brief review of basic properties of In impurity in PbTe and $Pb_{1-x}Sn_xTe$ solid solutions, with particular attention given to the case of high In content.

References to original papers are given in the course of presentation, but here, in the Introduction, we mention reviews concerned with the properties of IV–VI

1063-7826/02/3601-0001$22.00 © 2002 MAIK "Nauka/Interperiodica"

semiconductors [1–4], the role of Group III impurities in these compounds [3–9], and hopping conduction in semiconductors [10–14].

1. INDIUM IMPURITY STATES IN PbTe AND ITS SOLID SOLUTIONS

1.1. Resonance States in PbTe

Lead telluride, along with other lead chalcogenides, crystallizes in an NaCl-type cubic lattice [1–3]. PbTe is characterized by a very high static dielectric constant (on the order of 10^2–10^3 and higher), and a substantial (an order of magnitude and even higher) difference between the static and high-frequency dielectric constants. Like any of the IV–VI semiconductors, PbTe grows with strong deviations from stoichiometry, and its intrinsic defects, including vacancies, are electrically active: vacancies in the lead sublattice are acceptors, and those in the tellurium sublattice, donors. Typical electron and hole densities arising because of the stoichiometry violations are on the order of 10^{18}–10^{19} cm^{-3}.

The band gap of PbTe is relatively narrow: 0.19 eV at low temperatures; with increasing temperature, the gap becomes wider, reaching ca. 0.32 eV at 300 K [1]. The absolute extrema of the electron and hole bands lie at the same point of k space, at the edge of the Brillouin zone in the $\langle 111 \rangle$ direction (L point). The constant-energy surfaces near the extrema are four ellipsoids of revolution, elongated along the $\langle 111 \rangle$ axes. The effective masses near the band edges are small; e.g., the transverse effective mass of electrons near the conduction band bottom is $0.024m_0$, and the longitudinal effective mass is 10 times heavier. The principal mechanisms of carrier scattering in lead chalcogenides at not-too-low temperatures are polar and non-polar scattering by optical phonons and scattering by acoustic oscillations [15, 16].

Group VII atoms (halogens), which substitute Te in the PbTe lattice, produce a profound donor effect: alkali metal impurities substituting Pb are acceptors. However, direct observation of the donor and acceptor impurity states is impossible for these impurity centers since, owing to the high dielectric constant and small effective mass of carriers, the wave functions of shallow Coulomb centers overlap, and the impurity levels merge with the allowed band already at impurity concentrations as low as 10^{13}–10^{14} cm^{-3} [1, 5]. The concentrations of electrically active defects in the purest samples substantially exceed these values. High carrier densities hinder observation and investigation of deep levels.

The mechanism of doping of PbTe and its analogs with Group III elements is much more complex [5, 9]. At first glance, it seems that these impurities must behave as acceptors when they substitute Group IV atoms, and Tl is, indeed, an acceptor in lead chalcogenides, but Ga and In are donors. Indium shows limited donor activity in PbTe and, in the presence of halogens, compensates their donor action, thus exhibiting acceptor properties. Indium is an acceptor in SnTe, which is an analog of PbTe. Investigations of resonance and localized states of indium in IV–VI compounds gave insight into the nature of the complex donor–acceptor action of this impurity [5].

An essential specific feature of the In impurity in PbTe is its pinning effect on the chemical potential, discovered by Kaidanov *et al*. [5, 17, 18]. The pinning of the chemical potential was first revealed and studied when investigating the dependence of the Hall coefficient on temperature, pressure, and content of In impurity, additional I and Na impurities, and excess Pb and Te. Despite the unusually high solubility of indium in PbTe (up to 24 at. % [19]), the electron density found from the Hall coefficient does not exceed several units multiplied by 10^{18} cm^{-3}. The Hall electron density measured at 4.2 K is the same, $(7.0 \pm 0.1) \times 10^{18}$ cm^{-3}, for samples with In content y varying between 0.3 and 2.5 at. %, which corresponds to a Fermi level position of 0.073 eV. A strong nonmonotonic temperature dependence of the Hall coefficient was revealed, together with its pronounced dependence on pressure.

All these features were accounted for in terms of partially filled quasilocal (resonance) impurity states of indium in PbTe, with energy $\varepsilon_i = 0.07$ eV above the conduction band bottom at low temperature. With increasing In content, the Fermi energy and the free electron density grow until the Fermi level reaches the impurity state level, after which there is no further increase in the electron density in the conduction band, and the Fermi energy is pinned at ε_i. With increasing temperature, the impurity levels sink into the band gap, whereas under hydrostatic pressure they go upwards, in both cases dragging along the Fermi level and correspondingly changing the Hall electron density.

An analysis of the Hall coefficient as a function of temperature gave a temperature dependence of the chemical potential, which coincides with the impurity level, shown for several PbTe:In samples in Fig. 1. The dependence $\mu(T)$ is mostly linear, with a temperature coefficient $\partial\varepsilon_i/\partial T = -(3 \pm 1) \times 10^{-4}$ eV/K. It seems that the dependence $\varepsilon_i(T)$ becomes weaker and is even reversed at elevated temperatures and high In content. The correctness of experimental data processing in these cases will be discussed below in Section 2.

A striking example of the chemical potential pinning is presented by data on supplementary doping of PbTe:In with conventional donor or acceptor impurities, which create no localized or resonance states, but alter the number of electrons on In atoms or in the allowed bands. The effect of additional doping with an I (donor) or Na (acceptor) is negligible until the content of I or Na becomes equal to the In content (see Fig. 2), after which the Hall density changes in accordance with the doping action of the additional impurity.

The simplest explanation of these properties was offered by Kaidanov's model [5], which is based on the assumption that, ignoring the electrons that passed from In atoms into the conduction band, the impurity band is half-filled, and the capacity of the impurity band is two electrons per In atom. This concept neglects electron–electron interaction at a single impurity center (Hubbard energy *U*). Despite the evidently approximate character of this model, it satisfactorily accounts for the overwhelming majority of experimental data, especially those concerning transport phenomena.

Measurements performed for additionally doped samples at T = 4.2 K allowed estimation of some parameters of the impurity states. The position of the impurity levels is nearly independent of the In content, which indicates that, even at In content of up to 2 at. %, the overlapping of the wave functions of impurity states is weak. This means that the wave function radius does not exceed 10–15 Å; i.e., the impurity states are strongly localized. Data on hopping conduction, described below (Section 3.1), confirmed and refined this conclusion.

In the case of supplementary doping in the pinning range, the chemical potential shifts by no more than 3%. Hence, it follows that the broadening of the resonance level does not exceed $\Gamma \approx 0.005$ eV when In content y = 1 at. %. As shown below (Section 1.3), the situation changes drastically and the band of impurity states broadens sharply at an In content above 2 at. %.

The narrow width of the density-of-states peak of quasilocal states ensures a very strict pinning of the chemical potential relative to the conduction band edge, despite the inevitably nonuniform distribution of impurities and electrically active defects throughout the sample. The pinning of the chemical potential results in high spatial uniformity of the carrier density. In general, micro-nonuniformities in the density of electrically active impurities, including statistically equilibrium fluctuations, give rise to fluctuations of the free carrier density in semiconductors and, consequently, lead to an increase in the magnetoresistance with growing magnetic induction in the range of classically strong magnetic fields. The magnetoresistance leveling-off, predicted by the theory for homogeneous semiconductors, was first observed in PbTe:In samples [5, 18].

Another prominent manifestation of the exceptionally high uniformity of carrier density in PbTe:In samples is the unique pattern of Shubnikov–de Haas (SdH) oscillations. Normally, 2–3 peaks are observed in magnetic field dependences of PbTe resistivity [20], and the oscillations associated with higher Landau levels are broadened owing to the nonuniform carrier density. By contrast, up to 28 peaks of SdH oscillations have been observed in PbTe doped with 1 at. % In [21].

The chemical potential pinning indicates that the density of electronic states at the Fermi level is high, and, thus, one would expect some manifestations of electron spin paramagnetism. Meanwhile, a search for paramagnetic effects in indium-doped PbTe and its solid solutions gave a definitely negative result [22–24].

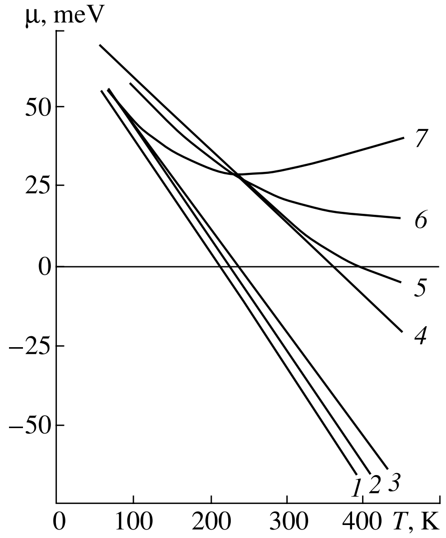

Fig. 1. Temperature dependence of the chemical potential determined from the Hall coefficient [17]. Indium content: (*1*) 0.6, (*2*, *3*) 0.5, (*4*) 0.1, (*5*) 1, (*6*) 3, and (*7*) 6 at. %.

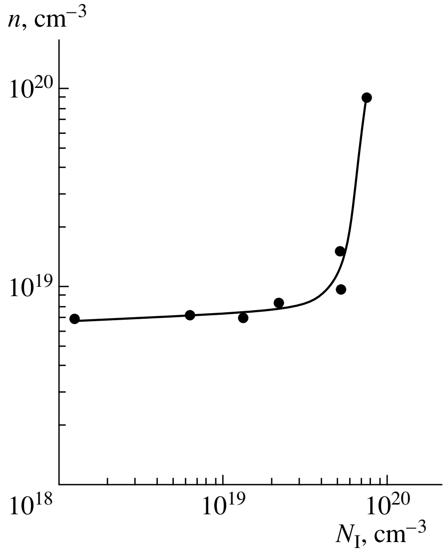

Fig.2. Hall density of electrons vs. the content of supplementary I impurity in PbTe:In [18] (theoretical curve and experimental points). T = 77 K, $N_{\mathrm{In}} = 0.9 \times 10^{20}$ cm^{-3}.

The situation in indium-doped IV–VI compounds appeared to be similar to amorphous semiconductors [12, 25], and the contradiction between the chemical potential pinning and the absence of paramagnetism was eliminated by invoking one and the same model of centers with negative Hubbard energy *U*. It was assumed by Moĭzhes *et al.* [22, 26, 27], in order to account for the properties of PbTe:In, and by Anderson [25], for amorphous semiconductors, that effective attraction between two localized electrons may arise owing to deformation of the atomic subsystem by electrons. In this case, the energy of two single-electron states is higher than that of one two-electron state, and the localized states are either empty or they are filled with two electrons with opposite spins. The proposed model not only accounts for the absence of paramagnetic effects and explains the results obtained in studying X-ray photoelectron spectra [24], but it also gives deeper insight into current–voltage characteristics of PbTe:In tunneling MOS structures [28, 29].

The superconductivity of some IV–VI compounds doped with Group III atoms is one more manifestation of the negative correlation energy of electrons in quasilocal states (Moĭzhes, [30–33]). Originally, Chernik and Lykov [34, 35] discovered bulk superconductivity in PbTe:Tl with a critical temperature of 1.4 K (up to 2.2 K upon supplementary doping with Na [36, 37]), which is unusually high for semiconductors. Later, superconductivity with an even higher critical temperature (up to 4 K) was observed in SnTe:In [38], where In impurity levels lie inside the valence band, as in PbTe:Tl. Also, a correlation was revealed between the superconductivity and the resonance scattering in IV–VI semiconductors doped with Group III atoms: these two effects occur simultaneously when resonance states are created against the background of the valence band; the dependence of the intensity of resonance scattering on the content of additional impurity, which modifies the Fermi level position, correlates with the corresponding dependences of the critical temperature of superconductivity and other parameters characterizing the phase transition [5, 6, 9].

However, no manifestations of the negative correlation energy have been noticed in transport phenomena involving impurity states (resonance scattering and hopping conduction). When resonance scattering is observed, the impurity levels are strongly broadened owing to the hybridization of impurity and band states [6, 9]. As shown below, hopping conduction is observed at high In content, when the energy spread of localized impurity states is wide. Presumably, the broadening of the band of localized or resonance states masks in both cases the possible manifestations of the effective attraction of localized electrons.

As mentioned above, the reason for effective attraction between localized electrons is the polarization of the atomic environment of an impurity center: when a center is occupied by a pair of electrons, the local deformation of the crystal lattice is enhanced, and the total energy of the system decreases. Another effect due to the interaction of localized electrons with the lattice is long-term relaxation of the nonequilibrium electron density: at temperatures below 20 K the redistribution of electrons between the impurity and band states in PbTe:In and $Pb_{1-x}Sn_xTe$:In solid solutions is characterized by times reaching several hours [5, 7, 39–43]. In experiments, the equilibrium was disturbed by radiation, which induced photoconductivity, by quantizing magnetic field, or by high electric field.

The theoretical explanation of the long-term relaxation consists in that any electronic transition is accompanied by a change in the charge state of an impurity center, which requires a rearrangement of the surrounding atomic subsystem [44, 45]; therefore, the relaxation process is thermally activated, and, on lowering the temperature to below 20 K, the relaxation time increases by several orders of magnitude.

The long-term relaxation gives rise to an abnormally high photoconductivity [7, 39, 42] responsible for the absence of resonance scattering in PbTe:In at low temperatures [6, 18]. The metastable nature of the impurity states accounts for the lack of features related to the density-of-states peak of indium in tunneling characteristics of MOS structures, with hysteresis of the current–voltage characteristic observed instead on reversing the direction of the voltage sweep [28, 29].

Further, we discuss the hopping conduction mainly at temperatures of 100 K and higher, and, therefore, lattice reconstruction associated with electron hopping will not be considered.

1.2. Impurity States in $Pb_{1-x}Sn_xTe$ Solid Solutions

In PbTe-based solid solutions doped with In, the chemical potential is pinned at a level which strongly depends on the solid solution composition. Replacing Te with other chalcogens, Se and S, shifts the pinning level, which coincides with the impurity level, toward the conduction band. Replacing Pb with lighter elements, Sn and Ge, shifts the impurity level toward the band gap. Of particular interest is the dependence of the impurity state energy ε_i in $Pb_{1-x}Sn_xTe$ on the content of tin, x.

With x gradually increasing, inversion of the electron and hole bands occurs in this semiconductor: the energy gap E_g first decreases and then a zero-gap state is attained, upon which the states of L_6^+ and L_6^- symmetry change places, and the gap starts to grow with x increasing up to the value corresponding to SnTe [1–4]. At low temperatures, the inversion occurs at $x = 0.35$, this parameter grows with increasing temperature. Figure 3 shows, as a function of x, the position of the In impurity level in such an inverted band structure [5]. At $x < 0.22$, the level approaches the conduction band bottom at a rate $\partial\varepsilon_i/\partial x = -(0.3–0.4)$ eV to enter the energy gap at $x \approx 0.22$, which is about 0.07 eV wide at this Sn content. Thus, a resonance impurity state becomes localized at $x \gtrsim 0.22$, and the chemical potential is pinned inside the energy gap, which leads to extremely low free carrier densities unachievable without Fermi level pinning with any IV–VI compound growth technology.

Investigations of galvanomagnetic effects at low temperatures, including SdH oscillations, have shown [47–49] that In levels lie in the energy gap near the conduction band bottom at $x = 0.22$ and reach the middle of the gap at $x = 0.26$; further, the samples become

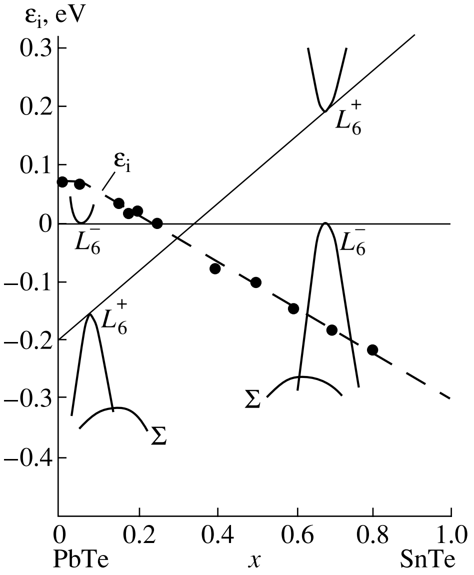

Fig. 3. Band diagram of $Pb_{1-x}Sn_xTe$ solid solutions and the position of the In impurity level vs. x at $T = 0$ K [5].

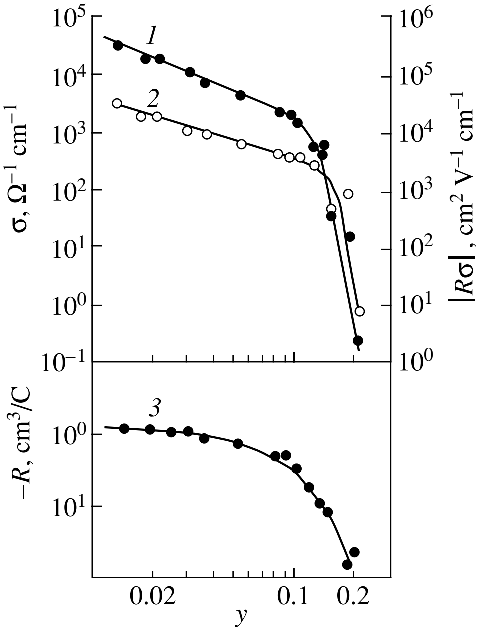

Fig. 4. (*1*) Conductivity, (*2*) Hall mobility, and (*3*) Hall coefficient vs. In content y in $Pb_{1-y}Sn_yTe$ solid solution at $T = 4.2$ K [52].

p-type, and the levels enter the valence band at $x = 0.29$. At higher x values approaching $x = 1$ (SnTe), the impurity states lie deep in the valence band, and resonance scattering and superconductivity are observed [38, 50].

Since the position of In impurity levels depends on the Sn content, it would be expected that the impurity band is broadened noticeably, compared with the In impurity levels in PbTe, as a result of spatial fluctuations of x in $Pb_{1-x}Sn_xTe$ solid solutions. Although this phenomenon has not been studied experimentally in $Pb_{1-x}Sn_xTe$:In, a similar broadening has been observed in several studies for the impurity band of Tl resonance states in $PbSe_{1-x}S_x$:Tl solid solutions [51].

1.3. Specific Features of Impurity States at High In Content

At In content y below 2.5 at. %, the energy of impurity states depends on y only slightly. At higher y, a significant dependence $\varepsilon_i(y)$ appears, which is accompanied by quite a few modifications of the PbTe:In properties. The specific action of the In impurity at its content up to 20 at. % was studied in [52, 53]. Indium was introduced, as the impurity substituting Pb atoms, into samples grown by the Bridgeman technique; in other words, $Pb_{1-y}In_yTe$ solid solutions were studied. The position of the impurity level as a function of y was determined at $T = 4.2$ K.

Figure 4 presents the electrical conductivity σ, Hall coefficient R, and Hall mobility $|R\sigma|$ as functions of y. The Hall coefficient, which is extremely stable below $y < 0.025$, steadily grows in absolute value by nearly two orders of magnitude, with y increasing further in the range under study. This increase indicates that the In impurity level is shifted, together with the chemical potential pinned to it, toward the conduction band bottom. Figure 5 shows the impurity state energy ε_i (determined from the Hall density) as a function of the In content y. The decrease in ε_i is linear in approximately the y range of 0.05–015, with a derivative $\partial\varepsilon_i/\partial x \approx -0.55$ eV; with the linear run of $\varepsilon_i(y)$ retained beyond this range, the impurity level would leave the conduction band at $y = 0.18$. It seems, however, that the decrease in ε_i becomes slower when the impurity level approaches the energy gap, and the level remains inside

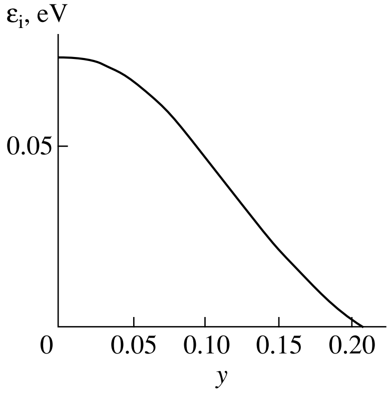

Fig. 5. Position of the In impurity level in PbTe vs. In content y at low temperatures [52].

the conduction band up to $y = 0.20$. This feature of the $\varepsilon_i(y)$ curve will be discussed again below.

As seen from the curve for σ, the decrease in the conductivity $|R\sigma|$ with increasing y is due to a decrease in both the density (because of the chemical potential shift) and mobility of electrons. At an In content of $y \lesssim 0.12$, the decrease in mobility is relatively gradual and is accounted for by the increasing number of scattering In atoms. The scattering cross-section is on the order of 10^{-16} cm^2, which is a value typical of scattering by short-range potential and is even smaller than that for halogen atoms. This means that there is no resonance scattering, similarly to the case of small y.

At $y > 0.12$, the decrease in conductivity and mobility becomes steeper, which was attributed in [54] to the appearance of a random potential relief [54]. The abrupt decrease in conductivity occurs when the chemical potential enters the energy range in which the conduction band edge fluctuates, which not only leads to electron scattering but also distorts the current lines. An estimate of the characteristic potential relief amplitude $\delta V \approx 0.03$ eV was found from the chemical potential at $y = 0.12$.

The origination of the relief is directly connected with the dependence of the position of impurity levels pinning the chemical potential on the content of In atoms. At small y, impurity content fluctuations do not make the electron concentration nonuniform, owing to the chemical potential pinning. By contrast, at high y, the ε_i value and the energy spacing between the chemical potential and the conduction band edge fluctuate in parallel with the In content. Therefore, the decrease in mobility with increasing y results both from the increase in the potential relief amplitude and from the depression of the Fermi level. The appearance of the concentration nonuniformity, intimately associated with the potential relief, is confirmed by independent experimental data: the unusually clear pattern of the SdH oscillations, described above, and the leveling-off of the magnetoresistance in strong nonquantizing magnetic fields are only observed at $y < 0.02$ and disappear abruptly when y exceeds this value.

Other origins of the potential relief are possible at high In content, e.g., mechanical stresses produced by random spatial nonuniformity of the lattice constant at y fluctuations. One more possible source of the potential relief is spinodal decomposition of the $Pb_{1-y}In_yTe$ solid solution into phases with different y values. As shown in [54], electrons in indium impurity states make a negative contribution to the second derivative of the free energy density with respect to y, which favors spinodal decomposition. Finally, in PbTe-based solid solutions such as $(Pb_{1-x}Sn_x)_{1-y}In_yTe$, fluctuations of the Sn content are also accompanied by ε_i nonuniformity and enhancement of the potential relief.

When, with increasing y, the Fermi level passes into the energy gap, a metal–dielectric transition [11] occurs in an inhomogeneous conductor. The nonuniformity of the electron density, associated with a random potential relief, affects the energy ε_i obtained experimentally at $T = 4.2$ K in the In content range $y \approx 0.15$–0.20, in which the center of the impurity band lies near the conduction band edge. In this case, the local conductivity in a major part of a sample, in which the chemical potential lies below the conduction band bottom, is very low, and this part of the sample is similar to dielectric inclusions. Current flows through a metal cluster while it extends across the whole sample, i.e., as long as the Fermi level lies above the percolation threshold for a random potential. As known from the percolation theory [11], for effective metallic conduction to occur, it suffices that the low-resistivity cluster occupies only about 16% of the total volume; in other words, the percolation threshold lies below the mean level of the potential relief.

If a level $\varepsilon_i(\bar{y})$ lying below the conduction band bottom corresponds to the mean value $y = \bar{y}$, but $\bar{y}$ is still smaller than the threshold value y_c corresponding to the breakdown of a metal cluster, then we determine ε_i for a continuous low-resistance cluster, in which $y < \bar{y}$; i.e., we find a ε_i value higher than $\varepsilon_i(\bar{y})$. Therefore, the nonlinearity of the $\varepsilon_i(y)$ curve at high y in Fig. 5 is spurious; in fact, the impurity level passes into the energy gap already at $y \approx 0.18$–0.19.

The potential relief also affects the temperature dependence of conductivity in samples with high In content $y = 0.15$–0.20 [53]. With the carrier scattering considered to be elastic, the conductivity can be represented as an integral over energy

$$\sigma = \int\left(-\frac{\partial f_0}{\partial \varepsilon}\right)\sigma(\varepsilon)\,d\varepsilon, \qquad (1)$$

where f_0 is the Fermi–Dirac distribution function, and the quantity $\sigma(\varepsilon)$ characterizes the contribution of electrons with energy ε to the conduction. A random potential must give rise to a strong dependence on energy $\sigma(\varepsilon)$ in the energy range δV near the conduction band edge.

With the temperature raised from 4.2 to about 30 K, thermal excitation of electrons results in that the number of electrons with relatively high energy, whose mobility is suppressed by the relief to a lesser extent, grows, which leads to higher σ. At temperatures above 30 K, account should be taken of the temperature shift of the impurity levels and the chemical potential toward the energy gap and the resulting decrease in the electron density in the conduction band and in the conductivity σ with increasing temperature. The $\sigma(T)$ dependence exhibits a maximum near 30 K in the y range under study.

At temperatures of 100 K and higher, the $\sigma(T)$ behavior changes again; new features appear that will be considered in the following chapter. To conclude this section, we note that the concept of indium in PbTe as

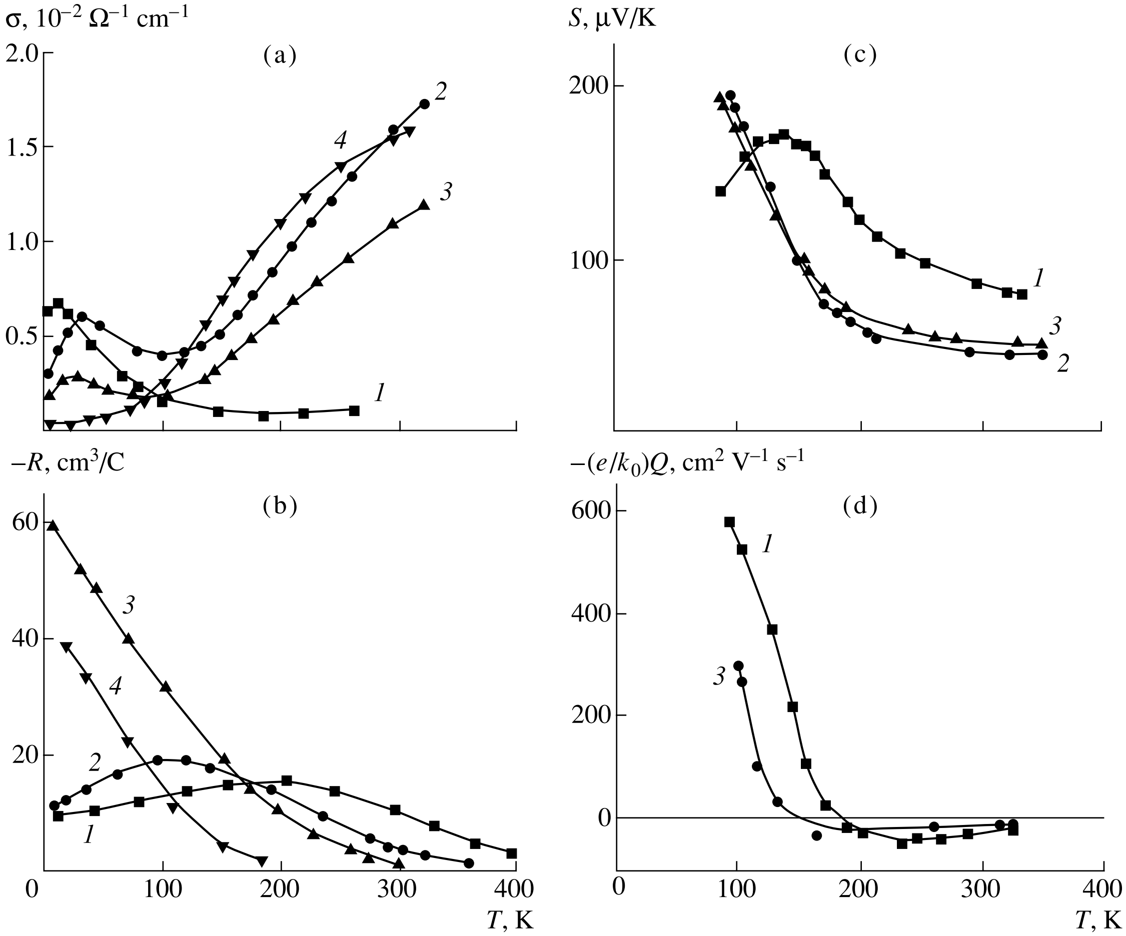

Fig. 6. Temperature dependences of (a) conductivity, and (b) Hall, (c) Seebeck, and (d) Nernst–Ettingshausen coefficients in $Pb_{1-y}Sn_yTe$ with high In content [53]. y = (*1*) 0.145, (*2*) 0.16, (*3*) 0.20, and (*4*) 0.22.

an impurity giving rise to localized or quasi-local states could, surprisingly, be employed for the qualitative description of properties of rather concentrated $Pb_{1-y}In_yTe$ solid solutions, with y as large as about 0.2.

2. HOPPING CONDUCTION IN PbTe

Temperature dependences of kinetic coefficients were studied in $Pb_{1-y}In_yTe$ solid solutions in a wide range of y variation, including high values $y \approx 0.15$–0.20 [53]. Measurements were done with the same Bridgeman-grown samples that were used to study low-temperature properties described in the preceding Section 1.3. Figure 6 presents the results of measurements of conductivity σ and Hall R, Seebeck S, and Nernst-Ettingshausen Q coefficients in samples with the largest y.

The temperature dependence of conductivity $\sigma(T)$ at $T < 100$ K was discussed above (Section 1.3). A noteworthy feature at $T > 100$ K is a steep increase in conductivity at $y = 0.16$–0.22. At low temperatures, the conductivity decreases with increasing y; by contrast, at relatively high temperatures, the conductivity grows with In content at the mentioned y values.

At relatively high temperatures, where the conductivity increases with temperature, the Hall coefficient R decreases rapidly as temperature is raised. The decrease in the Hall coefficient becomes faster at higher y. At about room temperature, the Hall density $(e|R|)^{-1}$ approaches the In concentration in order of magnitude. The fast fall of the Hall coefficient also leads to a decrease in the Hall mobility $|R\sigma|$.

The thermoelectric power S also decreases with increasing temperature, although slower than R does. In samples with relatively low In content, up to $y = 0.02$, the kinetic coefficients virtually coincide in samples doped with indium and halogens at equal Hall densities; by contrast, at high y, the thermoelectric power is higher in absolute value in indium-doped samples, and its temperature dependence is the opposite.

The temperature dependence of the Nernst–Ettingshausen coefficient Q also differs from that in halogen-doped samples. In particular, the sign of Q changes from negative, which is typical of lead chalcogenides, to positive in going to high temperatures. After the change of sign, the Nernst–Ettingshausen coefficient is an order of magnitude smaller than that at $T \leq 100$ K, which correlates with the drop of the Hall mobility.

The observed dependences are rather smooth and neatly change from one to another, which confirms the absence of phase transitions.

Passing to a discussion of the possible theoretical models of the transport phenomena in the high-temperature part of the interval under study, we note that the transition to intrinsic conduction is commonly characterized by an increase in conductivity, a decrease in the Seebeck and Hall coefficients, and a positive sign of the Nernst–Ettingshausen coefficient. However, very high Hall densities (up to 10^{20}–10^{21} cm^{-3}) give no way of assuming that intrinsic conduction is improbable at any plausible band-structure parameters. Moreover, the electron gas must be strongly degenerate at such high concentrations over the entire temperature range under study, and the fast activation-type rise in electron density is incompatible with strong degeneration.

Based on these considerations, the authors of [53] interpreted the observed dependences as evidence of hopping conduction via localized impurity states. Even very strongly localized wave functions must overlap at high In impurity content, thus enabling the hopping conduction. Transition to a metal-type conduction over the impurity band does not occur because of the strong fluctuations of the impurity level energies. Electron transitions between the impurity centers are necessarily phonon-assisted, and, therefore, the temperature dependence of hopping conduction σ_h is activation-type (ε_3-conduction):

$$\sigma_h = \sigma_3 \exp\left(-\frac{\varepsilon_3}{kT}\right). \tag{2}$$

Experimental $\ln\sigma_h(1/T)$ dependences were used to evaluate the activation energy $\varepsilon_3 \approx 0.03$ eV characterizing the spread of energy levels. Hence, it was concluded that the energy level position strongly fluctuates. This result is not surprising, because, at high y, In atoms frequently lie close to one another, even occupying neighboring sites of the metal sublattice, and their environment may differ in the absence of ordering, which leads to different impurity level energies.

In the order of magnitude, the activation energy ε_3 is in agreement with the potential relief amplitude (see Section 1.3). Thus, the random potential in PbTe:In is largely associated with the fluctuations of the In impurity level position.

The possibility of observing high-temperature hopping conduction in PbTe:In is made more likely by the fact that the impurity levels, together with the chemical potential pinned to them, move into the energy gap at a high temperature. As a result, the electron density in the conduction band decreases with increasing temperature, and the growing hopping conduction becomes the principal mechanism of conduction.

Although the Hall, Seebeck, and Nernst–Ettingshausen coefficients in the hopping conduction range were not discussed in detail in [53], it was mentioned that the experimentally observed specific temperature dependences of these effects are in qualitative agreement with the hopping conduction model. In particular, the Hall coefficient is small in the case of hopping conduction and does not reflect the true electron density; i.e., identifying the electron density with the Hall density leads to an overestimated carrier density and chemical potential.

In this connection, the question arises as to whether the hopping conduction takes place along with the band conduction in samples with relatively low ($y < 0.1$) In content at high temperatures ($T > 300$ K). As seen in Fig. 1, the temperature dependence of the chemical potential found from the Hall-effect data, which coincides with the temperature dependence of the impurity level, is nonlinear at $y \geq 0.01$ and even nonmonotonic at $y = 0.06$ [17]. It was shown in [53] that calculation of the chemical potential by the method used in [17] yields at $y \geq 0.10$ an incredibly steep rise in the chemical potential at high temperatures, where the hopping conduction, disregarded in [17], is significant. Since the curves for different y transform smoothly from one into another, it seems natural to conclude that the nonlinearity of the $\mu(T)$ dependence in the samples with $y \approx 0.01$–0.03 is spurious and stems from disregarding the hopping conduction, which is important at high temperatures even at relatively small In content.

3. HOPPING TRANSPORT IN $Pb_{0.78}Sn_{0.22}Te$ SOLID SOLUTIONS

As shown in the preceding section, observation of the hopping conduction in PbTe is enabled by the fact that the In impurity level moves into the energy gap at high temperatures, and the impurity state becomes localized. Hence, it follows that better conditions for studying the hopping conduction are provided by $Pb_{1-x}Sn_xTe$ solid solutions, where In impurity levels lie within the band gap already at $T = 0$ and $x \geq 0.22$, and, with increasing temperature and In content, these move even deeper into the energy gap.

Indeed, studies of transport phenomena in $(Pb_{0.78}Sn_{0.22})_{1-y}In_yTe$ at y between 2 and 20 at. % furnished a clear and detailed pattern of the hopping transport; its analysis yielded reliable evidence in favor of the hopping nature of conduction, as well as several important parameters of In impurity states. The results concerning the hopping transport in these solid solutions were reported in [55–62].

The samples were fabricated by the cermet technology, commonly used for IV–VI semiconductors, with subsequent homogenizing annealing at 650°C for 100 h. The characteristic grain size was about 0.1 mm. The conductivity σ, thermoelectric power S, and Hall R and

Nernst–Ettingshausen Q coefficients were measured in the temperature range 4.2–400 K.

3.1. Electrical Conductivity

As seen in Fig. 7, the measured conductivity falls with decreasing temperature, with σ varying within several orders of magnitude in the temperature range under study. Such a dramatic variation indicates the exponential temperature dependence of the conductivity. In contrast to PbTe, in which the conductivity rise occurs only at $y \geq 0.15$, in $(Pb_{0.78}Sn_{0.22})_{1-y}In_yTe$ solid solutions it starts at $y = 0.03$ and continues until $y = 0.15$, with transition to metallic conduction (Mott transition) at $y = 0.2$.

If we assume that the conduction in samples with high In content is due to electrons in extended states, then the electron density can be evaluated from the Hall coefficient (see Section 3.4) to be very high (up to $\approx 10^{22}$ cm^{-3}). At such densities, the Fermi level must lie deep in the conduction band, as in the case of metals. Meanwhile, at $0.03 \geq y \geq 0.15$, σ is smaller than 350 Ω^{-1} cm^{-1}, which, according to Mott [12], is the minimum metallic conductivity for the case when the chemical potential lies near the middle of the allowed band. Hence, it follows that the transport is effected by localized electrons.

In the temperature range 100–400 K, the dependences $\ln\sigma(1/T)$ are represented by straight lines (Fig. 8). This circumstance was attributed in [55, 56] to hopping conduction with nearest-neighbor hopping (ε_3-conduction), which is described by relation (2).[1] Table 1 presents the hopping conduction parameters, ε_3 and σ_3, determined from the straight line slope and the intercept on the ordinate axis.

The activation energy of hopping conduction, ε_3, is on the same order of magnitude (several tens of meV) as that in PbTe:In. At $y > 5$ at. %, it decreases substantially with increasing In content, i.e., with decreasing distance between the neighboring In atoms. This points to correlation between the energies of impurity states of closely spaced In atoms, which is due to large-scale random chemical potential. In this case, the higher the concentration, the smaller the hopping range and the narrower the energy scatter of transitions between nearest neighbors.

The activation energy ε_3 was also determined in samples containing 3 and 5 at. % In with the introduction of up to 2.5 at. % supplementary donors or acceptors, Cl and Tl, which produce no impurity levels near the chemical potential. Within the scatter of the obtained experimental values (±5 eV), the activation energy is independent of the content of a supplementary dopant and is close to the value presented in Table 1. Since the activation energy characterizes the energy spread of the localized levels, this means that the introduction of the mentioned amount of additional impurities has no significant effect on the energy spectrum of levels created by In atoms.

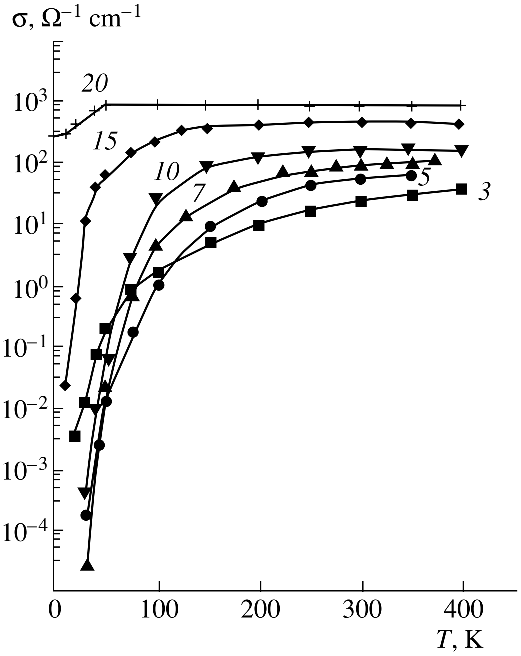

Fig. 7. Conductivity vs.temperature for $(Pb_{0.78}Sn_{0.22})_{1-y}In_yTe$ with high In content [55]. Curve numbers correspond to y, at. %; the same for Fig. 8.

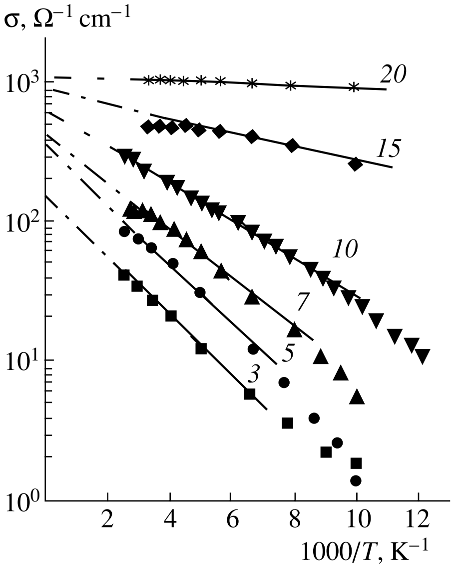

Fig. 8. Conductivity in logarithmic scale vs.1/T [56].

---

[1] In the first of the cited reports [55], a part of the obtained data on conductivity and thermoelectric power was accounted for by the conduction due to thermal excitation of electrons into the conduction band above the mobility threshold (ε_1-conduction). Refinement of the experimental data and detailed analysis of the whole of their set led the authors to conclude that ε_3-conduction is observed at T = 100–400 K at any indium content in the range y = 3–15 at. %).

Table 1. Parameters of hopping conduction in $(Pb_{0.78}Sn_{0.22})_{1-y}In_yTe$ [56]

y	$N_{In}^{-1/3}$, Å	σ_3, Ω^{-1} cm^{-1}	ε_3, meV
0.03	13	160	44
0.05	11	360	43
0.07	10	420	34
0.10	8.8	620	26
0.15	7.6	890	11

Analysis of the limiting conductivity, σ_3, as a function of the In impurity concentration, N_{In}, is the most direct and precise of all the methods for evaluating the radius a of a localized wave function, employed in studying impurity states of Group III elements in IV–VI compounds. The following formula was obtained for this dependence in terms of the percolation theory [11]:

$$\sigma_3 = \sigma_{30}\exp(-1.73/aN_{In}^{1/3}). \quad (3)$$

The slope of the straight line, which represents the $\ln\sigma_3(N_{In}^{-1/3})$ dependence according to (3), is defined by the parameter a. As seen from Fig. 9, the dependence is nearly linear and the slope of the straight line $a \approx 6$ Å. Thus, the obtained result confirms the concept of strong localization of In impurity states and is in agreement with the estimate obtained from the onset of a strong $\varepsilon_i(y)$ dependence (see Subsection 1.1).

Some qualitative conclusions concerning the wave function radius can also be obtained from the transition to metallic conduction at $y = 0.2$. The value of 0.2 is the percolation threshold for the problem of sites in a face-centered cubic crystal lattice [11]. Thus, metallization occurs provided that an infinite cluster is formed from In atoms separated by the minimum possible distance between the sites of the metallic face-centered sublattice in which In impurity atoms reside. Hence, it also follows that the wave function radius a is on the same order of magnitude as the inter-site distance in the sublattice, i.e., several Angströms.

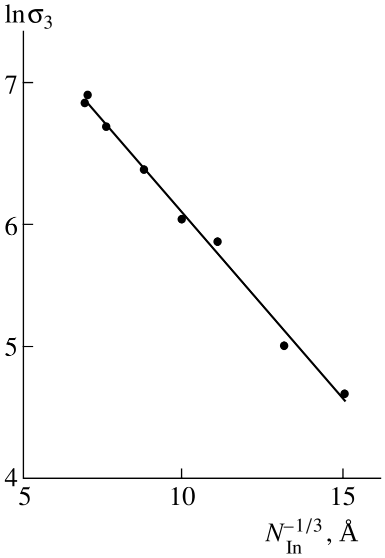

Fig. 9. Logarithm of the limiting hopping conductivity σ_3 vs. $N_{In}^{-1/3}$ [56]. The slope of the straight line corresponds to $a = 5.8$ Å.

Let us now discuss the applicability conditions for relations (2) and (3), which were obtained in terms of the theory of hopping conduction via nearest neighbors. For the hopping to occur mainly between nearest neighbors, it is necessary that the following inequality be satisfied:

$$2/aN_{In}^{1/3} > \varepsilon_3/kT. \quad (4)$$

An exponential temperature dependence is observed when

$$\varepsilon_3/kT > 1. \quad (5)$$

Substituting the obtained parameters a and ε_3 into (4) and (5), we see that both inequalities are satisfied, being, however, not too strong in the most part of the temperature and concentration ranges under study. For example, the left- and right-hand sides of (4) are, respectively, 4.3 and 2.1 at $y = 0.03$ and $T = 200$ K. Similar estimates are also obtained for $y = 0.07$ [56]. Thus, at temperatures above 100 K, the transport occurs via nearest-neighbor hopping; i.e., the average hopping distance is temperature-independent. At temperatures below 100 K, inequality (4) is reversed, and variable-range-hopping conduction must appear [11], with the weaker temperature dependence described by the Mott law:

$$\sigma_h = \sigma_0\exp[-(T_0/T)^{1/4}]. \quad (6)$$

However, conductivity measurements [55, 59] revealed that at $T < 100$ K there is only a slight tendency toward the weakening of the conductivity dependence on temperature, with experimental data differing widely between different samples. No regular trends with smooth transition from one relationship to another were found, presumably, as a result of the influence of inter-grain boundaries. We will return to the discussion of the possibility of variable-range-hopping conduction further, when considering thermoelectric power (Section 3.2).

3.2. Thermoelectric Power

Figures 10a and 10b show temperature dependences of the thermoelectric power in the temperature range 100–400 K for samples with varied In content.

The first remarkable fact is that the Seebeck coefficient S is negative over the entire temperature range under study in the samples with $y = 0.02$–0.03, whereas for $y \geq 0.05$ its sign changes to positive when the temperature is lowered below 200 K, with the Hall coefficient remaining negative. This sign reversal for the thermoelectric power, with the Hall coefficient sign unchanged, is common to noncrystalline solids [12] and is accounted for by the negative derivative of the energy dependence of the density of states, $dg/d\varepsilon < 0$ (or derivative $d\sigma(\varepsilon)/d\varepsilon < 0$), near the chemical potential level.

The positive thermoelectric power was accounted for in [55] as follows. With increasing In content, the impurity band broadens, partially overlapping with the conduction band which lies close, with a zero gap between the impurity and band states and a dip possibly appearing instead in the dependence of the density of states g on energy (pseudo-gap). From the existence of a minimum in the $g(\varepsilon)$ function, it follows that a maximum necessarily exists below and that there is an energy range in which the density of states decreases with increasing energy (Fig. 11). If the chemical potential μ lies within this range, the thermoelectric power may have a sign opposite to that of the charge carriers. Since the number of states in the impurity band is twice the total number of electrons supplied by In atoms (see Section 1.1), this position of the chemical potential is possible if the impurity band is not quite symmetric, which is not surprising in the case of overlapping between the impurity and band states. We will revert to the discussion of the nature of the $g(\varepsilon)$ function in the next section.

In the proposed model, the chemical potential lies within the range of localized states created by the In impurity, whereas the delocalized (extended) states lie above it. In view of the fact that the system under study is strongly disordered owing to the chaotic distribution of In, Sn, and Pb atoms in the cation sublattice, some part of the extended electronic states may also be localized. The boundary between the localized and delocalized states (mobility threshold ε_c) lies above the chemical potential. The conventional band conduction is effected by electrons with energies $\varepsilon > \varepsilon_c$, and, therefore, the mobility threshold plays the role of the conduction band edge in the materials under study, and the band conduction is to be activated across the energy gap $\varepsilon_c - \mu$.

Let us now discuss the temperature dependence of thermoelectric power. In the temperature range ≈100–200 K, the absolute value of the Seebeck coefficient $|S|$ grows with decreasing temperature, in qualitative agreement with the dependence $|S| \propto T^{-1}$ obtained by means of the percolation theory for nearest-neighbor hopping [13, 14]. At temperatures above 200 K, the thermoelectric power is proportional to T, as in metals and heavily doped semiconductors, whereas the percolation theory predicts its leveling-off with increasing temperature [12–14]. It may be stated that the experimental temperature dependence of the Seebeck coefficient is described by the relation $S = AT + BT^{-1}$. It is this dependence that was obtained theoretically in terms of the effective medium model to describe the experimental data for Fermi glasses [13, 63]:

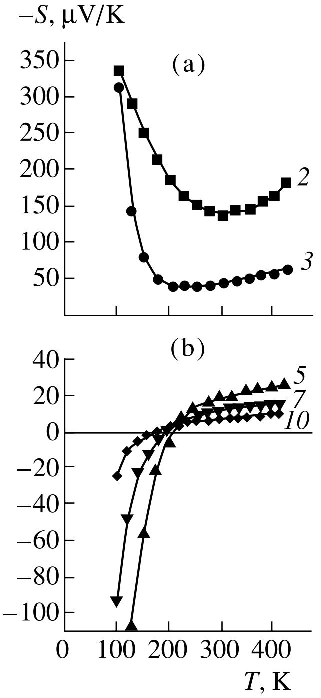

Fig. 10. Thermoelectric power vs. temperature for $(\mathrm{Pb}_{0.78}\mathrm{Sn}_{0.22})_{1-y}\mathrm{In}_y\mathrm{Te}$ solid solutions [57]. Curve numbers correspond to In content y, at. %.

$$S = -\frac{5k}{6e}\left(\frac{\varepsilon_3^2}{2kT} + \frac{2}{3}\pi^2 kT\right)\left(\frac{d\ln g}{d\varepsilon}\right)_{\varepsilon = \mu}, \tag{7}$$

where ε_3 is the activation energy of hopping conduction.

If the density of states and its derivative change only slightly with temperature, the transition from $S \propto T^{-1}$ to

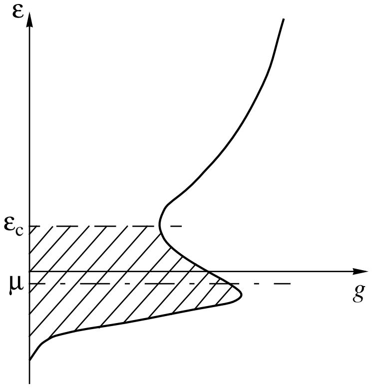

Fig. 11. Energy spectrum of $(\mathrm{Pb}_{0.78}\mathrm{Sn}_{0.22})_{1-y}\mathrm{In}_y\mathrm{Te}$ solid solution at $y \geq 0.05$, proposed to account for the experimental data on thermoelectric power [55]. The range of localized states is hatched.

$S \propto T$ dependence gives rise to a minimum in $|S|$ at a temperature

$$T_{\min} = \sqrt{3}\varepsilon_3/2\pi k. \tag{8}$$

This shape is characteristic of the $|S|(T)$ curve at $y = 0.02$–0.03 (Fig. 10a). The activation energy can be evaluated from the experimental value of $T_{\min}$ to be $\varepsilon_3 = 62$ meV at $y = 0.03$, having the same order of magnitude as the activation energy $\varepsilon_3 = 44$ meV determined from conductivity. However, the very fact of the thermoelectric power sign reversal indicates that the logarithmic derivative of the density of states at the chemical potential level $(d\ln g/d\varepsilon)_{\varepsilon=\mu}$ changes substantially, and, therefore, the method determining the activation energy from the minimum of the $|S(T)|$ function can only be used for evaluation. In the above-cited papers [56–62], the activation energy ε_3 was mainly determined from the temperature dependence of conductivity, and, using relation (7), it was then used to find $(d\ln g/d\varepsilon)_{\varepsilon=\mu}$ at a given temperature from the thermoelectric power.

As mentioned above, at $y \geq 0.05$ and $T < 200$ K, the chemical potential lies in the range of negative $dg/d\varepsilon$ derivatives, and the thermoelectric power is positive. At the same time, at relatively high temperatures, $T = 200$–400 K, the thermoelectric power is negative at any In content y. Hence, it follows that, first, the energy spectrum (density of localized states $g(\varepsilon)$) changes fundamentally with y, and, second, the chemical potential shifts with temperature relative to features in the $g(\varepsilon)$) function. Hence, for experiments in which the chemical potential is varied in a controlled manner at fixed In, content and temperature are of special interest. Experiments of this kind, performed with samples doped with supplementary, electrically active impurities, are discussed in the next section.

To complete the review of thermoelectric power in the samples without supplementary doping, let us briefly discuss the temperature dependence of the Seebeck coefficient at $T < 100$ K. As follows from estimates based on the inequality (4), a transition to variable-range-hopping conduction must occur on lowering the temperature to below 100 K, but the large scatter of the experimental data on conductivity gave no way of observing this effect. It would be expected that intergrain boundaries produce a weaker effect on the zero-current Seebeck effect, compared with that on the conductivity, and, therefore, thermoelectric power measurements could reveal features characteristic of the variable-range-hopping conduction at $T < 100$ K. In the case of the nearest-neighbor hopping, the $|S|$ value decreases with increasing temperature at relatively low temperatures, 100–200 K. At the same time, according to the theory [12, 64], passing to the case of variable-range-hopping radically changes the temperature dependence of the thermoelectric power: the Seebeck coefficient decreases when the average hopping distance grows with decreasing temperature.

Indeed, thermoelectric power measurements in $(Pb_{0.78}Sn_{0.22})_{0.97}In_{0.03}Te$ solid solutions (with and without supplementary doping with Cl) in the temperature interval including the $T < 100$ K range demonstrated that $|S|$ exhibits a maximum at $T \approx 50$ K, and, at $T < 50$ K, the thermoelectric power decreases as the temperature is lowered, which is characteristic of variable-range-hopping conduction. The temperature of sign reversal of the derivative $d|S|/dT$ agrees in order of magnitude with the theoretical estimate presented above. A power-law dependence of the thermoelectric power is observed at $20\text{ K} < T < 50$ K, which is somewhat weaker than that predicted by the theory [12, 64]. However, $|S|$ sharply decreases with temperature at $T < 20$ K, much faster than the theory predicts. Possibly, this circumstance is associated with the transition to temperatures at which long-term relaxation of the density of localized electrons occurs as a result of reconstruction of the atomic subsystem in electronic transitions (Section 1.1). This effect must hinder hopping, and, therefore, the hopping conduction may become less effective and be replaced by band conduction, for which the low-temperature thermoelectric power is small. An increase in the relative contribution of the band conduction can also be favored by the approach of the impurity levels to the conduction band at low temperatures.

3.3. Thermoelectric Power in the Case of Supplementary Doping

The chemical potential μ can be shifted by supplementary doping with donors or acceptors that produce no localized states near the chemical potential level, which allows scanning of the spectrum of localized states of electrons on In impurity atoms. The thermoelectric power and some other kinetic coefficients were measured in $Pb_{0.78}Sn_{0.22}Te$ solid solutions containing 3 and 5 at. % of In, with supplementary doping with Cl donors (0–2.5 at. %) or Tl acceptors (0–2 at. %) [58–62]. Chlorine and Tl, as well as In, were introduced as substitutional impurities into the anion or cation sublattices, respectively. Although Tl gives rise to resonant states in PbTe and its solid solutions [5, 9], the corresponding energy levels lie deep inside the valence band, far from the chemical potential level in the samples with a high content of In donors. Filling of Tl acceptor states with electrons exerts a compensating acceptor effect, with each Tl atom receiving one electron and Cl atoms being singly charged donors.

Figure 12 presents the thermoelectric power as a function of temperature in the samples with $y = 0.05$ and additionally doped with Cl or Tl. The most striking experimental result is the reversal of the thermoelectric power sign to negative upon doping, in sufficient amounts, with either donors or acceptors at relatively low temperatures (150 K and below), where the thermoelectric power is positive in samples not subjected to supplementary doping. The obtained dependence of the thermoelectric power on the content of electrically active impurities is absolutely unusual for semiconductors with broad allowed bands, to which IV–VI compounds belong. Indeed, the conventional negative thermoelectric power is obtained in the samples doped with In donors up to 3 at. %, whereas raising the In content to 5 at. % and more leads to anomalous positive thermoelectric power at relatively low ($T < 200$ K) temperatures. The thermoelectric power sign is reversed to negative upon addition of the Tl acceptor. Raising the content of donors in the samples with 5 at. % In by adding up to 2 at. % Cl makes the positive thermoelectric power higher, but, when the Cl content reaches 2.5 at. %, the thermoelectric power also reverses its sign and its absolute value increases sharply. Such effects of doping are, however, completely accounted for in terms of the hopping conduction model with a complex spectrum of localized states, including a density-of-states peak and a dip at higher energies. When the chemical potential is shifted, the derivative $dg/d\varepsilon$ twice changes its sign near $\varepsilon = \mu$, which leads, in accordance with (7), to the corresponding changes in the sign of S.

In samples with 3 at. % In, in which the thermoelectric power S is negative at any temperature, it also remains negative upon supplementary doping with Cl or Tl [58, 59]. However, at y = 3 at. % as well, the behavior of the thermoelectric power under supplementary doping is not quite usual: raising the content of both donors and acceptors leads to higher $|S|$ values, which is due to the nonmonotonic energy dependence of the derivative $dg/d\varepsilon$.

Analysis of how the thermoelectric power depends on the content of supplementary impurities yields the density of localized states as a function of energy. Once the experimental value of S is known, and the activation energy of hopping conductivity ε_3 is found from the temperature dependence of conductivity σ, for any given composition and temperature, relation (7) yields the quantity

$$f = \left(\frac{d\ln g}{d\varepsilon}\right)_{\varepsilon=\mu}, \tag{9}$$

which is obtained as a function of the electron density in localized states n.

The prevalence of the hopping conduction mechanism indicates that only a negligible part of the total amount of electrons are in the extended states, and the density n is equal to the difference between the donor and acceptor concentrations:

$$n = N_{\mathrm{In}} + N_{\mathrm{Cl}} - N_{\mathrm{Tl}}. \tag{10}$$

Varying the content of Cl and Tl, we obtain the function $f(n)$ at fixed In content keeping the nature of the density-of-states function $g(\varepsilon)$ unchanged. When varying the chemical potential μ, we have

$$f = \frac{1}{g}\frac{dg}{d\mu} = \frac{1}{g}\frac{dg}{dn}\frac{dn}{d\mu} = \frac{dg}{dn}, \tag{11}$$

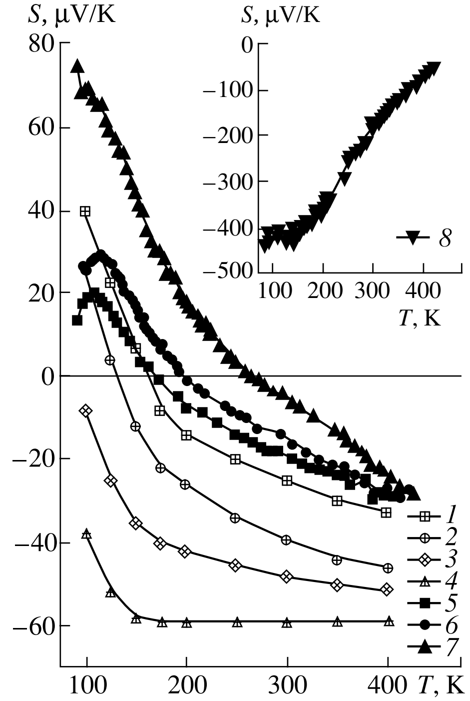

Fig. 12. Thermoelectric power vs. temperature for $(Pb_{0.78}Sn_{0.22})_{0.95}In_{0.05}Te$ additionally doped with Cl or Tl [62]. N_{Tl} = (*1*) 0, (*2*) 1, (*3*) 1.5, and (*4*) 2 at. %; N_{Cl}: (*5*) 0, (*6*) 1, (*7*) 2, and (*8*) 2.5 at. %.

since

$$\frac{dn}{d\mu} = g. \tag{12}$$

Taking into account that the absolute values of n and g approach zero when the chemical potential μ is lowered to the impurity band edge, we integrate (11):

$$g(n) = \int_0^n f(n')dn'. \tag{13}$$

The function $\mu(n)$ is found by integrating (12):

$$\mu - \mu_0 = \int_{n_0}^{n} \frac{dn'}{g(n')}, \tag{14}$$

where n_0 and μ_0 are the minimum values of n and μ in the samples under study, which are attained in the sample with the highest content of acceptor (Tl). Numerical integration of (13) and (14) yields the function $g(\mu)$ in the parametric form: $g(n)$ and $\mu(n)$. The unavoidable extrapolation of the experimental function $f(n)$ to $n = 0$ brings some arbitrariness into the calculation, thus impairing its accuracy, but the result of calculation by means of (13) is independent of the extrapolation method.

Figures 13 and 14 show the results of the above-described calculations for $y = 0.05$ and $y = 0.03$, respec-

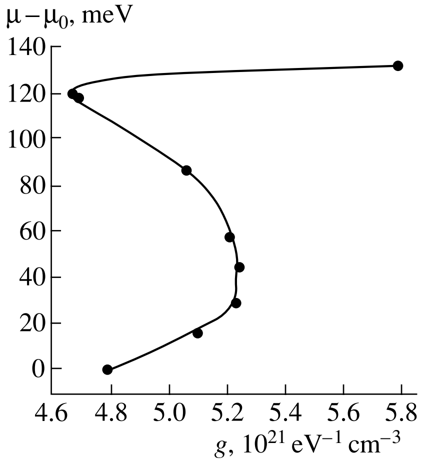

Fig. 13. Density of localized electronic states in $(Pb_{0.78}Sn_{0.22})_{0.95}In_{0.05}Te$ solid solution at $T = 150$ K [62].

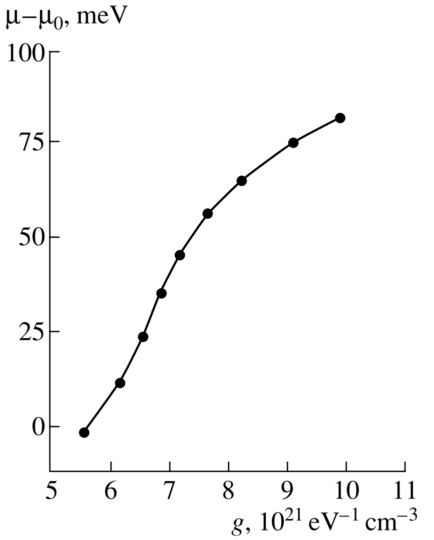

Fig. 14. Density of localized electronic states in $(Pb_{0.78}Sn_{0.22})_{0.97}In_{0.03}Te$ solid solution at $T = 300$ K [61].

tively. The curve obtained at $T = 150$ K for the higher In content, $y = 0.05$, exhibits a peak and a minimum, which lies approximately 80 meV above the peak. This result confirms the proposed model of the nonmonotonic dependence of the density of localized states on energy.

The minimum in the function $g(\varepsilon)$ is not deep: the density of states varies by about 10% between the minimum and the peak. Presumably, the true $g(\varepsilon)$ dependence is somewhat sharper, but the function is smoothed by thermal broadening of the edge of the energy distribution of electrons. If the transport is effected by the electrons in the vicinity of the chemical potential, it can be shown that the major contribution to the thermoelectric power comes from energy regions about $4kT$ wide (the width of two energy regions, above and below the chemical potential, is doubled owing to the factor $\varepsilon - \mu$ under the integral over energy). At $T = 150$ K, $4kT = 52$ meV, which is only slightly less than the distance between the peak and the minimum in $g(\varepsilon)$, so the smoothing of the function may be significant. With temperature raised to 300 K, the averaging of the density of states over the energy interval may eliminate the nonmonotonic details of $g(\varepsilon)$. This may be the second reason (along with the lowering of the chemical potential) for the negative thermoelectric power at relatively high temperatures of 200–400 K at any y values.

As can be seen from Fig. 14, the calculated dependence $g(\varepsilon)$ is monotonic at $y = 0.03$ and $T = 300$ K; however, a trace of the peak of impurity states remains in the form of an inflection in the curve. In this case, the curve is smoothed to an even greater extent, compared with $y = 0.05$ and $T = 150$ K (calculation for low temperatures at $y = 0.03$ was impossible because of the strong scatter of the experimental points).

The curves presented in Figs. 13 and 14 show that the band of localized states extends into the energy gap to a depth of at least 100 meV. This value is much larger than the activation energy of hopping conduction ($\varepsilon_3 \approx 40$ meV), which is determined by the average energy distance between the electron levels at the neighboring impurity centers; at the same time, the overall width of the band of localized states may be enhanced by a large-scale potential relief. This furnishes one more piece of evidence in favor of the existence of a large-scale potential relief, repeatedly mentioned above in Sections 1.3, 2, and 3.1.

3.4. Hall Effect

Experimental data on the Hall effect in $Pb_{0.78}Sn_{0.22}Te$ solid solutions with high content of In have played an important role in establishing the mechanism of conduction in these compounds. The sign of the Hall coefficient R is invariably negative, even at positive thermoelectric power S, which is typical of Fermi glasses. At high temperatures, Hall densities $n_H = (e|R|)^{-1}$ grow with increasing In content (see Fig. 15) and attain the values of 10^{21}–10^{22} cm^{-3}, i.e., exceed the In concentration at the highest content of indium. The assumption that all these electrons are in the conduction band leads to the conclusion that the electron gas is strongly degenerate. At the same time, as follows from a steep decrease in $|R|$ with increasing temperature (Fig. 16), the temperature dependence of the Hall density is activated, which contradicts the assumption of strong degeneration.

As is known from the theory of hopping conduction, the Hall coefficient, which is proportional to the off-diagonal component of the conductivity tensor in a transverse magnetic field, σ_{xy}, is negligible in the case of hopping conduction [11, 13]. The reason for this is that the probability of hopping between two sites is independent of the magnetic field in weak fields, and hopping between three or more sites is to be considered in calculating the hopping contribution to σ_{xy}. The smallness of $|R_h|$ in the purely hopping mechanism requires that the contribution of delocalized conduction band electrons be taken into account in calculating the total Hall coefficient R, even in the case when the conductivity σ_{xx} is dominated by hopping, $\sigma_{xx} \approx \sigma_h$. The model used in this situation is similar to the double-band model for semiconductors [11] and yields the relation

$$R = \frac{R_b\sigma_b^2 + R_h\sigma_h^2}{(\sigma_b + \sigma_h)^2}, \qquad (15)$$

where the subscript b indicates the contribution of conduction band electrons with energies above the mobility threshold. Neglecting, in accordance with the aforesaid, the partial Hall coefficient R_h and the band contribution to the conductivity σ_b, we obtain

$$R \approx R_b\left(\frac{\sigma_b}{\sigma_h}\right)^2. \qquad (16)$$

Assuming that the electron density in the delocalized states depends on temperature as $\exp(-\varepsilon_1/kT)$, we obtain the temperature dependence of the Hall coefficient in the following form [11]:

$$R \propto \exp\left(\frac{2\varepsilon_3 - \varepsilon_1}{kT}\right). \qquad (17)$$

In general, $\varepsilon_3 \ll \varepsilon_1$ in weakly doped compensated semiconductors with hydrogen-like impurity centers, and the Hall coefficient $|R|$ grows exponentially with temperature in the range of hopping conduction [11, 65]. By contrast, in materials with strongly localized impurity states, which are the object of the present review, R steeply decreases with increasing temperature, which indicates an exponential rise in the Hall density n_H with a positive activation energy

$$\varepsilon_R = 2\varepsilon_3 - \varepsilon_1. \qquad (18)$$

From $\varepsilon_R > 0$, it follows that $\varepsilon_1 < 2\varepsilon_3$. Moreover, the experimental data indicate that ε_R is nearly twice the activation energy of conductivity ε_3. For example, at $y = 0.03$, the activation energies $\varepsilon_R \approx 80$ meV and $\varepsilon_3 = 44$ meV [55]; at $y = 0.07$, the respective parameters are $\varepsilon_R \approx 72$ meV and $\varepsilon_3 = 34$ meV. Although the accuracy of the evaluation of ε_R and ε_3 is insufficient for determining the activation energy of band conductivity (ε_1-conductivity), we may conclude that either ε_1 is small, as compared with ε_3, or the band conduction is not activated at all. Therefore, the hopping conductivity grows faster than the band conductivity with increasing temperature, and the Hall coefficient decreases.

Thus, the hopping conduction in the samples with high In content at temperatures 100–400 K can be considered high-temperature as compared with that in the conventional weakly doped semiconductors.

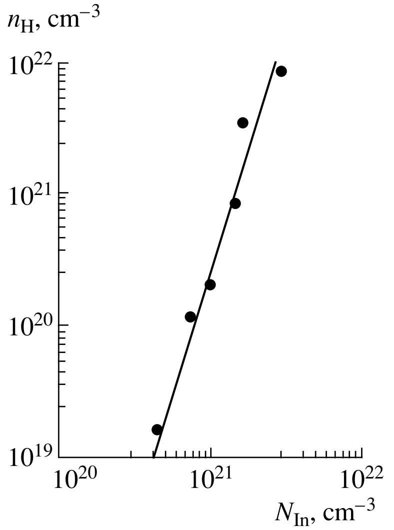

Fig. 15. Hall density of electrons n_H vs. In content N_{In} in $Pb_{0.78}Sn_{0.22}Te$:In at room temperature [55].

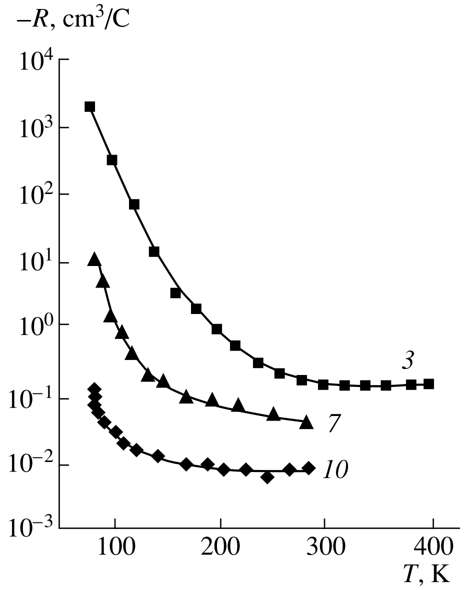

Fig. 16. Temperature dependence of the Hall coefficient in $Pb_{0.78}Sn_{0.22}Te$:In [55, 59]. Curve numbers correspond to the In impurity content, at. %.

At first glance, it seems strange that the activation energy of ε_1-conductivity is small, whereas the chemical potential μ increases significantly upon supplementary doping with chlorine but does not reach the mobility threshold ε_c and remains within the band of impurity states; i.e., the quantity $\varepsilon_c - \mu$ is on the same order of magnitude as ε_3 in the temperature range 100–400 K under study (Figs. 11, 13, and 14). This contradiction is resolved if account is taken of the pronounced temperature dependence of the position of the impurity band center relative to the conduction band edge, which is observed at relatively small In content in PbTe [5, 17]

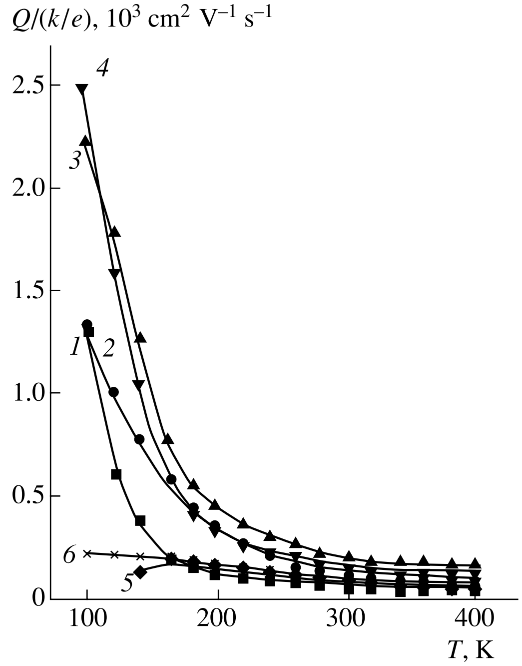

Fig. 17. Temperature dependence of the Nernst–Ettingshausen coefficient in $(Pb_{0.78}Sn_{0.22})_{0.97}In_{0.03}Te$ [59]. Samples: (*1*) without supplementary doping; supplementary doping with chlorine: (*2*) 1, (*3*) 2, and (4) 3 at. %; and thallium: (*5*) 1, and (*6*) 1.5 at. %.

(Section 1.1). Assuming that $\varepsilon_c - \mu$ decreases with increasing temperature in the same way as ε_i does at small *y*, we obtain for the energy gap $\varepsilon_c - \mu$

$$\varepsilon_c - \mu = \text{const} + ckT, \qquad (19)$$

where the temperature-independent dimensionless parameter *c* is equal to about 3 ± 1. The activation-type temperature dependence of the density of delocalized electrons is described by the first constant in relation (10), which, therefore, should be identified with the parameter ε_1. Since, at low temperatures $T \longrightarrow 0$ K, the indium impurity level in $Pb_{0.78}Sn_{0.22}Te$ lies near the conduction band edge (Section 1.2), the parameter ε_1 may be small, in agreement with the experimental data on the Hall effect (and also on the Nernst–Ettingshausen effect, see below, Section 3.5). The quite probable decrease in the mobility of delocalized electrons with increasing temperature also reduces ε_1 and can even make it negative, which corresponds to a decrease in the band conductivity σ_b with increasing temperature. At the same time, the energy gap $\varepsilon_c - \mu$ is large enough at high temperatures, owing to the second term in (19), e.g., $\varepsilon_c - \mu \approx 80$ meV at $T = 300$ K.

The fast decrease in the Hall coefficient with increasing temperature [in accordance with (16)] also makes the Hall mobility lower:

$$|R\sigma| = |R_b\sigma_b|\frac{\sigma_b}{\sigma} \propto \exp\left(\frac{\varepsilon_3 - \varepsilon_1}{kT}\right). \qquad (20)$$

Since $\sigma_b \ll \sigma$, the Hall mobility $|R\sigma|$ is much lower than the corresponding value for the band conductivity $|R_b\sigma_b|$, and, at room temperature, experiment gives values of about 1 $cm^2 V^{-1} s^{-1}$ (and less) at high In content $y \geq 10$ at. %. The rise in the reciprocal value $|R\sigma|^{-1}$ is characterized by an activation energy approximately equal to ε_3, in agreement with the experiment. As shown below, the temperature dependence of the Hall mobility can also be obtained by measuring the Nernst–Ettingshausen effect.

3.5. Nernst–Ettingshausen Effect

The transverse Nernst–Ettingshausen effect (TNEE) was studied in $Pb_{0.78}Sn_{0.22}Te$ solid solutions with In content $y = 0.03$ in the temperature range of 100–400 K [59, 61]. Figure 17 presents the experimental temperature dependences of the TNEE coefficient *Q*.

In the investigated solid solutions with high indium content, the room-temperature *Q* is an order of magnitude lower, and the ratio of *Q* to the Hall mobility is an order of magnitude higher than the respective values in halogen-doped PbTe samples [66–68]. An even greater difference between the indium- and halogen-doped samples consists in the sign of the Nernst–Ettingshausen coefficient. In conventional charge transport by delocalized electrons, the TNEE coefficient in the extrinsic conduction range is proportional to the scattering parameter *r*, which describes the dependence of the relaxation time τ on energy ε:

$$r = \frac{\partial \ln \tau}{\partial \ln \varepsilon}. \qquad (21)$$

In lead chalcogenides and their solid solutions, the parameter *r* is negative owing to phonon scattering and strong nonparabolicity of the electron dispersion; therefore, a negative TNEE coefficient is commonly observed upon doping with halogens [66], whereas in the samples under study with high In content, the TNEE is positive.

Finally, the TNEE coefficient steeply decreases with increasing temperature by 3–4 orders of magnitude in the range $T = 100$–400 K in all samples of $Pb_{0.78}Sn_{0.22}Te$.

The above temperature dependence and the very small value of *Q* for hopping conduction have the same physical origin as the similar properties of the Hall coefficient. Indeed, the phenomenological relation for the TNEE coefficient contains two terms, one proportional, similarly to the Hall coefficient, to the quantity

$$\sigma_{xy} = \int\left(-\frac{\partial f_0}{\partial \varepsilon}\right)\sigma_{xy}(\varepsilon)d\varepsilon, \qquad (22)$$

Table 2. Measured kinetic coefficients in $(Pb_{0.78}Sn_{0.22})_{0.97}In_{0.03}Te$ without supplementary doping [59] and theoretical estimates of summands in (25) [61] made upon calculating Q_2 (see text)

Experimental data						Theoretical estimates			
T, K	σ, Ω^{-1} cm^{-1}	S, μV/K	R, cm^3/C	$\lvert R\sigma\rvert$ cm^2 V^{-1} s^{-1}	$Q(k/e)$ cm^2 V^{-1} s^{-1}	$Q_1(k/e)$ cm^2 V^{-1} s^{-1}	$Q_2(k/e)$ cm^2 V^{-1} s^{-1}	$Q_3(k/e)$ cm^2 V^{-1} s^{-1}	$Q_1 + Q_2 + Q_3/(k/e)$ cm^2 V^{-1} s^{-1}
150	5	–80	–17	85	300	50	475	–80	445
200	12	–41	–2.7	25	150	15	140	–12	143
300	28	–45	–0.35	10	80	6	54	–5	55

and the other, to the off-diagonal component of the tensor defining the thermoelectric and thermomagnetic effects:

$$b_{xy} = \frac{1}{eT}\int\left(-\frac{\partial f_0}{\partial \varepsilon}\right)(\varepsilon-\mu)\sigma_{xy}(\varepsilon)d\varepsilon. \tag{23}$$

In a transverse magnetic field, the quantity b_{xy} defines the component of current along the x-axis at a temperature gradient along the y axis. The smallness of the function $\sigma_{xy}(\varepsilon)$, which determines the smallness of the Hall coefficient R, also leads to negligible values of both summands in the expression for the TNEE coefficient in the case of the hopping conduction mechanism. Hence, it follows that two types of conduction are to be taken into account simultaneously in calculating Q, similarly to the case of R. The “double-band” model yields the following expression for the TNEE coefficient:

$$Q = Q_b\frac{\sigma_b}{\sigma} + Q_h\frac{\sigma_h}{\sigma} + \frac{\sigma_b\sigma_h}{\sigma^2}(S_b - S_h)(R_b\sigma_b - R_h\sigma_h), \tag{24}$$

where the designations used for partial quantities are the same as in the preceding section. Neglecting Q_h and R_h and taking into account that $\sigma \approx \sigma_h$ and $S = S_h$, we obtain an expression for Q, comprising three summands [59]:

$$Q \approx Q_1 + Q_2 + Q_3 = Q_b\frac{\sigma_b}{\sigma} + S_bR\sigma - SR\sigma. \tag{25}$$

In calculating Q_3, there is no need to use microscopic theory, because the third term in (25) contains only independently measured coefficients, σ, S, and R. The term Q_3 is negative at $y = 0.03$ since $S < 0$ and $R < 0$. Its absolute value is significantly lower than the measured total TNEE coefficient Q (Table 2).

Calculation of the positive term Q_2 requires that the partial band-related thermoelectric power S_b be calculated using the formula

$$S_b = -\frac{1}{eT}\frac{\int\limits_{\varepsilon_c}^{\infty}\left(-\frac{\partial f_0}{\partial \varepsilon}\right)(\varepsilon-\mu)\sigma_b(\varepsilon)d\varepsilon}{\int\limits_{\varepsilon_c}^{\infty}\left(-\frac{\partial f_0}{\partial \varepsilon}\right)\sigma_b(\varepsilon)d\varepsilon}. \tag{26}$$

When using (26), we must take into account the existence of the potential relief, which is responsible for the increase in $\sigma_b(\varepsilon)$ with energy at $\varepsilon > \varepsilon_c$. In calculating S_b, it was assumed [61] that, above the mobility threshold, the current flows through percolation channels, and the function $\sigma_b(\varepsilon)$ is proportional to $(\varepsilon - \varepsilon_c)^t$, where t is the critical conductivity index $t = 1.6$ [11]. At relatively high temperatures, $T \geq 100$ K, it was assumed that $\mu < \varepsilon_c$, and the Boltzmann distribution function was used for f_0. A calculation requiring no further assumptions gave the following formula [61]:

$$S_b = -\frac{k}{e}\left(t + 1 + \frac{\varepsilon_c - \mu}{kT}\right). \tag{27}$$

Further numerical estimation of S_b and Q_2 in [61] was based on the assumption that the energy gap $\varepsilon_c - \mu$ is equal to the activation energy of band conductivity ε_1 [61]. It was found that the positive second summand in (25) is larger than the two others, and approaches, in order of magnitude, the experimental value of the TNEE coefficient, which made it possible to account for the obtained sign and value of Q. To refine the estimations made in [61], let us consider the temperature dependence of $\varepsilon_c - \mu$ (19), replacing the first constant with ε_1, which is negligible as follows from the temperature dependences of the Hall (Section 3.4) and Nernst–Ettingshausen (this section, below) coefficients. Then, (27) takes the following form:

$$S_b = -\frac{k}{e}(t + 1 + c). \tag{28}$$

At $t = 1.6$ and $c \approx 3$, we obtain the following expression for Q_2:

$$Q_2 \approx 5.6\frac{k}{e}|R\sigma|. \tag{29}$$

The results of Q calculation using (29) are also presented in Table 2. Taking into account the temperature dependence of $\varepsilon_c - \mu$ improved the numerical agreement between the theoretical estimates and the experiment.

In evaluating the quantity Q_b appearing in the first summand of (25), we must keep in mind that, within a kT-vicinity of the mobility threshold, the density of states can be considered a weak function of energy rather than being proportional to $\varepsilon^{1/2}$, as it is near the conduction band bottom. Therefore, we have the quantity $\varepsilon - \varepsilon_c$ (instead of the conventional $\varepsilon^{3/2}$) under the integrals over energy, which define the kinetic coefficients. In spite of this circumstance, the conventional equation was obtained for Q_b [59, 61]:

$$Q_b = -\frac{k}{e} r R_b \sigma_b, \tag{30}$$

where the effective scattering parameter r defines the relative contribution of electrons with different energies to the integrand Q_b. All the integrals appearing in the expression for Q_b contain the quantity

$$\sigma(\varepsilon) = (\varepsilon - \varepsilon_c)\tau(\varepsilon) \propto (\varepsilon - \varepsilon_c)^{1+r}. \tag{31}$$

Hence, it follows that $1 + r = t$ and $r = 0.6$. Substituting this value into (30) and using formulas (20) and (25), we obtain [61]

$$Q_1 \approx 0.6\frac{k}{e}|R\sigma|. \tag{32}$$

The positive term Q_1 is an order of magnitude smaller than Q_2; its numerical estimates and the calculated overall quantity $Q_1 + Q_2 + Q_3$ are given in Table 2 together with its experimental value Q. Among the estimates of the three summands in (25), that of Q_1 is the least reliable, because it includes an assumption concerning the value of the effective parameter r. It would be expected, however, that, since Q_1 is relatively small, the roughness of its estimation may introduce only a minor error into the overall Q coefficient, which is mainly determined by Q_2.

Similar to the case of the standard theory of the Nernst–Ettingshausen effect in semiconductors, Q is proportional to the Hall mobility $|R\sigma|$, which, for the materials under study, accounts for the small values of the measured Q. At the same time, the calculated coefficient is positive at $|R\sigma|$, and its absolute value is an order of magnitude higher than that in the conventional theory for the case of scattering by acoustical phonons ($r = -0.5$), which ensures agreement between theory and the experiment in the sign of Q and in the order of magnitude of $Q/|R\sigma|$.

The proportionality of all the three summands in Q to the Hall mobility $|R\sigma|$ accounts for the observed fast decrease in the TNEE coefficient with increasing temperature. According to (20), this decrease is exponential, with the activation energy of Q^- given by $\varepsilon_Q = \varepsilon_3 - \varepsilon_1$. Determining the ε_Q value from the experimental data, we obtain $\varepsilon_Q = 37$ meV, which is close to ε_3 and indicates that ε_1 is small, as do the results of ε_R determination.

Thus, the positive sign, magnitude, and temperature dependence of the Nernst–Ettingshausen coefficient are accounted for, along with other transport phenomena discussed above, in terms of the dominant hopping conduction and involvement of delocalized electrons with energies above the mobility threshold in kinetic effects in transverse magnetic field.

CONCLUSION

In summary, we present the complete body of evidence in favor of the hopping conduction observed in $(Pb_{0.78}Sn_{0.22})_{1-y}In_yTe$ solid solutions.

1. The exponential increase in conductivity as a function of temperature, with the activation energy ε_3.

2. The increase in conductivity as a function of indium content.

3. The conductivity is significantly lower than the minimum metallic conductivity at “metallic” Hall densities of carriers.

4. A high Hall density (up to 10^{21}–10^{22} cm^{-3}) is observed at room temperature along with its activation-type temperature dependence.

5. Low Hall mobilities (to tenths of cm^2 V^{-1} s^{-1} at room temperature) point to transport over localized states.

6. The observed coexistence of a positive thermoelectric power with a negative Hall coefficient is typical of disordered systems.

7. The temperature dependence of the thermoelectric power S is typical of Fermi glasses: at low temperatures, ≈20–50 K, $|S|$ grows with temperature, as in the case of variable-range-hopping conduction; upon transition to nearest-neighbor hopping, $|S|$ decreases with increasing temperature, approximately as $1/T$; with further increase in temperature, $|S|$ starts to grow again (as T). The boundary of the variable-range-hopping conduction range is in agreement with theoretical estimates.

8. Unusual behavior of the thermoelectric power upon doping with supplementary electrically active impurities that produce no localized states. In particular, in some cases, acceptor doping leads to thermoelectric power sign reversal from positive to negative.

9. The Nernst–Ettingshausen coefficient Q is abnormally small, owing to the small Hall mobility $|R\sigma|$; at the same time, the $Q/|R\sigma|$ ratio is an order of magnitude higher than that in conventional semiconductors with extrinsic conduction. The values of both Q and $Q/|R\sigma|$ are in agreement with the theoretical estimates in terms of hopping conduction combined with conduction by electrons in delocalized states above the mobility threshold.

10. The transverse Nernst–Ettingshausen coefficient is positive, in contrast to that usually observed in lead chalcogenides in the extrinsic conduction range.

11. Activation-type temperature dependences of the quantities reciprocal to the Hall and Nernst–Ettingshausen coefficients. The first of these is characterized by an activation energy close to $2\varepsilon_3$, and the second, by an activation energy close to ε_3. This is due to the combination of two factors: the rise in the hopping conduc-

tion with temperature, and the absence of fast increase in the conduction by delocalized electrons because of the growing energy distance between the mobility threshold and the chemical potential.

Thus, the entire vast body of experimental data indicates, with account taken of the existence of interrelated parameters describing various transport phenomena, that hopping conduction via strongly localized indium impurity states occurs in $(\mathrm{Pb}_{0.78}\mathrm{Sn}_{0.22})_{1-y}\mathrm{In}_y\mathrm{Te}$ solid solutions.

REFERENCES

1. Yu. I. Ravich, B. A. Efimova, and I. A. Smirnov, *Semiconducting Lead Chalcogenides* (Plenum, New York, 1970); *Methods for Studying the Semiconductors in Applications to PbTe, PbSe, PbS Lead Chalcogenides* (Nauka, Moscow, 1968).
2. R. Dalven, in *Solid State Physics*, Ed. by H. Ehrenreich, F. Seitz, and D. Turnbull (Academic, New York, 1973), Vol. 28, p. 179.
3. R. Darnhaus, G. Nimtz, and B. Schlicht, *Narrow Gap Semiconductors* (Springer-Verlag, Berlin, 1983), Springer Tracts in Mod. Phys. **98**.
4. *Lead Chalcogenides: Physics and Applications*, Ed. by D. Khokhlov (Gordon and Breach, New York, 2000).
5. V. I. Kaĭdanov and Yu. I. Ravich, Usp. Fiz. Nauk **145**, 51 (1985) [Sov. Phys. Usp. **28**, 31 (1985)].
6. V. I. Kaĭdanov, S. A. Nemov, and Yu. I. Ravich, Fiz. Tekh. Poluprovodn. (St. Petersburg) **26**, 201 (1992) [Sov. Phys. Semicond. **26**, 113 (1992)].
7. B. A. Akimov, A. D. Dmitriev, D. R. Khokhlov, and L. I. Ryabova, Phys. Status Solidi A **137**, 9 (1993).
8. Yu. I. Ravich, in *CRC Handbook of Thermoelectrics*, Ed. by D. M. Rowe (CRC Press, Boca Raton, 1995), p. 67.
9. S. A. Nemov and Yu. I. Ravich, Usp. Fiz. Nauk **168**, 817 (1998) [Phys. Usp. **41**, 735 (1998)].
10. N. F. Mott and W. D. Twose, Adv. Phys. **10** (38), 107 (1961); Usp. Fiz. Nauk **79**, 691 (1963).
11. B. I. Shklovskiĭ and A. L. Efros, *Electronic Properties of Doped Semiconductors* (Nauka, Moscow, 1979; Springer-Verlag, New York, 1984).
12. N. F. Mott and E. A. Davis, *Electronic Processes in Non-Crystalline Materials* (Clarendon, Oxford, 1979; Mir, Moscow, 1982), Vol. 1.
13. H. Böttger and V. V. Bryksin, *Hopping Conduction in Solids* (VCH, Weinheim, 1985).
14. *Hopping Transport in Solids*, Ed. by B. Shklovskii and M. Pollak (North-Holland, Amsterdam, 1991).
15. Yu. I. Ravich, B. A. Efimova, and V. I. Tamarchenko, Phys. Status Solidi B **43**, 11 (1971); **43**, 453 (1971).
16. D. M. Zayachuk, Fiz. Tekh. Poluprovodn. (St. Petersburg) **31**, 217 (1997) [Semiconductors **31**, 173 (1997)].
17. A. A. Averkin, V. I. Kaĭdanov, and R. B. Mel'nik, Fiz. Tekh. Poluprovodn. (Leningrad) **5**, 91 (1971) [Sov. Phys. Semicond. **5**, 75 (1971)].
18. V. I. Kaĭdanov, R. B. Mel'nik, and I. A. Chernik, Fiz. Tekh. Poluprovodn. (Leningrad) **7**, 759 (1973) [Sov. Phys. Semicond. **7**, 522 (1973)].
19. A. I. Rosenberg, R. Grierson, I. C. Wooley, and C. Nicolic, Trans. AIME **230**, 342 (1964).
20. K. F. Cuff, M. R. Ellett, and C. D. Kuglin, J. Appl. Phys. **32**, 2179 (1961).
21. S. N. Lykov and I. A. Chernik, Fiz. Tekh. Poluprovodn. (Leningrad) **14**, 47 (1980) [Sov. Phys. Semicond. **14**, 25 (1980)].
22. Yu. V. Andreev, K. I. Geĭman, I. A. Drabkin, *et al.*, Fiz. Tekh. Poluprovodn. (Leningrad) **9**, 1879 (1975) [Sov. Phys. Semicond. **9**, 1235 (1975)].
23. S. N. Lykov and I. A. Chernik, Fiz. Tekh. Poluprovodn. (Leningrad) **14**, 1861 (1980) [Sov. Phys. Semicond. **14**, 1112 (1980)].
24. I. A. Drabkin, M. A. Kvantov, V. V. Kompaniets, and Yu. P. Kostikov, Fiz. Tekh. Poluprovodn. (Leningrad) **16**, 1276 (1982) [Sov. Phys. Semicond. **16**, 815 (1982)].
25. P. W. Anderson, Phys. Rev. Lett. **34**, 953 (1975).
26. B. Ya. Moĭzhes and I. A. Drabkin, in *Problems in Modern Physics* (Nauka, Leningrad, 1980), p. 128.
27. I. A. Drabkin and B. Ya. Moĭzhes, Fiz. Tekh. Poluprovodn. (Leningrad) **15**, 625 (1981) [Sov. Phys. Semicond. **15**, 357 (1981)].
28. V. I. Kaĭdanov, S. A. Rykov, and M. A. Rykova, Fiz. Tverd. Tela (Leningrad) **31** (8), 68 (1989) [Sov. Phys. Solid State **31**, 1316 (1989)].
29. V. I. Kaĭdanov, S. A. Rykov, M. A. Rykova, and O. V. Syuris, Fiz. Tekh. Poluprovodn. (Leningrad) **24**, 144 (1990) [Sov. Phys. Semicond. **24**, 87 (1990)].
30. B. Ya. Moĭzhes, Pis'ma Zh. Tekh. Fiz. **7**, 570 (1981) [Sov. Tech. Phys. Lett. **7**, 244 (1981)].
31. B. Ya. Moĭzhes and S. G. Suprun, Fiz. Tverd. Tela (Leningrad) **27**, 1395 (1985) [Sov. Phys. Solid State **27**, 842 (1985)].
32. B. Ya. Moĭzhes and S. G. Suprun, Fiz. Tverd. Tela (Leningrad) **29**, 441 (1987) [Sov. Phys. Solid State **29**, 252 (1987)].
33. T. H. Geballe, B. Ya. Moyzhes, and P. H. Dickinson, in *Proceedings of Spring Meeting of the Materials Research Society, San Francisco, 1999*.
34. I. A. Chernik and S. N. Lykov, Pis'ma Zh. Tekh. Fiz. **7**, 94 (1981) [Sov. Tech. Phys. Lett. **7**, 40 (1981)].
35. I. A. Chernik and S. N. Lykov, Fiz. Tverd. Tela (Leningrad) **23**, 1400 (1981) [Sov. Phys. Solid State **23**, 817 (1981)]; Fiz. Tverd. Tela (Leningrad) **23**, 2956 (1981) [Sov. Phys. Solid State **23**, 1724 (1981)]; Fiz. Tverd. Tela (Leningrad) **23**, 3548 (1981) [Sov. Phys. Solid State **23**, 2062 (1981)].
36. V. I. Kaĭdanov, S. A. Nemov, R. V. Parfen'ev, and D. V. Shamshur, Pis'ma Zh. Éksp. Teor. Fiz. **35**, 517 (1982) [JETP Lett. **35**, 639 (1982)].
37. I. A. Chernik, S. N. Lykov, and N. I. Grechko, Fiz. Tverd. Tela (Leningrad) **24**, 2931 (1982) [Sov. Phys. Solid State **24**, 1661 (1982)].
38. G. S. Bushmarina, I. A. Drabkina, V. V. Kompaniets, *et al.*, Fiz. Tverd. Tela (Leningrad) **28**, 1094 (1986) [Sov. Phys. Solid State **28**, 612 (1986)].
39. B. M. Vul, I. D. Voronova, G. A. Kalyuzhnaya, *et al.*, Pis'ma Zh. Éksp. Teor. Fiz. **29**, 21 (1979) [JETP Lett. **29**, 18 (1979)].

40. B. M. Vul, S. P. Grishechkina, and T. Sh. Ragimova, Fiz. Tekh. Poluprovodn. (Leningrad) **16**, 1452 (1982) [Sov. Phys. Semicond. **16**, 928 (1982)].
41. B. A. Akimov, N. B. Brandt, S. A. Bogoslovskiĭ, *et al.*, Pis'ma Zh. Éksp. Teor. Fiz. **29**, 11 (1979) [JETP Lett. **29**, 9 (1979)].
42. B. A. Akimov, N. B. Brandt, L. I. Ryabova, and D. R. Khokhlov, Pis'ma Zh. Tekh. Fiz. **6**, 1269 (1980) [Sov. Tech. Phys. Lett. **6**, 544 (1980)].
43. S. N. Lykov and I. A. Chernik, Fiz. Tekh. Poluprovodn. (Leningrad) **14**, 47 (1980) [Sov. Phys. Semicond. **14**, 25 (1980)]; Fiz. Tekh. Poluprovodn. (Leningrad) **14**, 1232 (1980) [Sov. Phys. Semicond. **14**, 730 (1980)].
44. B. A. Volkov, V. V. Osipov, and O. A. Pankratov, Fiz. Tekh. Poluprovodn. (Leningrad) **14**, 1387 (1980) [Sov. Phys. Semicond. **14**, 820 (1980)].
45. B. A. Volkov and O. A. Pankratov, Dokl. Akad. Nauk SSSR **255**, 93 (1980) [Sov. Phys. Dokl. **25**, 922 (1980)].
46. Yu. Kagan and K. A. Kikoin, Pis'ma Zh. Éksp. Teor. Fiz. **31**, 367 (1980) [JETP Lett. **31**, 335 (1980)].
47. B. A. Akimov, R. S. Vadkhva, V. P. Zlomanov, *et al.*, Fiz. Tekh. Poluprovodn. (Leningrad) **11**, 1077 (1977) [Sov. Phys. Semicond. **11**, 637 (1977)].
48. B. A. Akimov, L. I. Ryabova, O. V. Yatsenko, and S. M. Chudinov, Fiz. Tekh. Poluprovodn. (Leningrad) **13**, 752 (1979) [Sov. Phys. Semicond. **13**, 441 (1979)].
49. B. A. Akimov, V. P. Zlomanov, L. I. Ryayabova, *et al.*, Fiz. Tekh. Poluprovodn. (Leningrad) **13**, 1293 (1979) [Sov. Phys. Semicond. **13**, 759 (1979)].
50. G. S. Bushmarina, B. F. Gruzinov, I. A. Drabkina, *et al.*, Fiz. Tekh. Poluprovodn. (Leningrad) **18**, 2203 (1984) [Sov. Phys. Semicond. **18**, 1374 (1984)].
51. A. N. Veĭs, V. I. Kaĭdanov, and S. A. Nemov, Fiz. Tekh. Poluprovodn. (Leningrad) **14**, 1054 (1980) [Sov. Phys. Semicond. **14**, 628 (1980)].
52. V. V. Golubev, N. I. Grechko, S. N. Lykov, *et al.*, Fiz. Tekh. Poluprovodn. (Leningrad) **11**, 1704 (1977) [Sov. Phys. Semicond. **11**, 1001 (1977)].
53. S. N. Lykov, Yu. I. Ravich, and I. A. Chernik, Fiz. Tekh. Poluprovodn. (Leningrad) **11**, 1731 (1977) [Sov. Phys. Semicond. **11**, 1016 (1977)].
54. L. I. Bytenskiĭ, P. P. Konstantinov, and Yu. I. Ravich, Fiz. Tekh. Poluprovodn. (Leningrad) **14**, 1027 (1980) [Sov. Phys. Semicond. **14**, 613 (1980)].
55. S. A. Nemov, Yu. I. Ravich, A. V. Berezin, *et al.*, Fiz. Tekh. Poluprovodn. (St. Petersburg) **27**, 299 (1993) [Semiconductors **27**, 165 (1993)].
56. Yu. I. Ravich, S. A. Nemov, and V. I. Proshin, Fiz. Tekh. Poluprovodn. (St. Petersburg) **29**, 1448 (1995) [Semiconductors **29**, 754 (1995)].
57. S. A. Nemov, V. I. Proshin, and Yu. I. Ravich, Fiz. Tekh. Poluprovodn. (St. Petersburg) **30**, 2164 (1996) [Semiconductors **30**, 1128 (1996)].
58. T. G. Abaĭdulina, S. A. Nemov, V. I. Proshin, and Yu. I. Ravich, Fiz. Tekh. Poluprovodn. (St. Petersburg) **30**, 2173 (1996) [Semiconductors **30**, 1133 (1996)].
59. S. A. Nemov, Yu. I. Ravich, V. I. Proshin, and T. G. Abaĭdulina, Fiz. Tekh. Poluprovodn. (St. Petersburg) **32**, 311 (1998) [Semiconductors **32**, 280 (1998)].
60. S. A. Nemov, V. É. Gasumyants, V. I. Proshin, *et al.*, Fiz. Tekh. Poluprovodn. (St. Petersburg) **34**, 926 (2000) [Semiconductors **34**, 889 (2000)].
61. Yu. I. Ravich and S. A. Nemov, Fiz. Tekh. Poluprovodn. (St. Petersburg) **35**, 164 (2001) [Semiconductors **35**, 158 (2001)].
62. S. A. Nemov, D. A. Potapova, Yu. I. Ravich, and S. D. Khanin, Fiz. Tekh. Poluprovodn. (St. Petersburg) **35**, 1197 (2001) [Semiconductors **35**, 1144 (2001)].
63. N. T. E. Whall, J. Phys. C **14**, L887 (1981).
64. *Hopping Transport in Solids*, Ed. by B. Shklovskii and M. Pollak (North-Holland, Amsterdam, 1991), p. 143; I. P. Zvyagin, *Kinetic Phenomena in Unordered Semiconductors* (Mosk. Gos. Univ., Moscow, 1984).
65. H. Fritzsche and M. Cuevas, Phys. Rev. **96**, 1226 (1954).
66. M. K. Zhitinskaya, V. I. Kaĭdanov, and I. A. Chernik, Fiz. Tverd. Tela (Leningrad) **8**, 295 (1966) [Sov. Phys. Solid State **8**, 246 (1966)].
67. I. A. Chernik, V. I. Kaĭdanov, and E. P. Ishutinov, Fiz. Tekh. Poluprovodn. (Leningrad) **2**, 995 (1968) [Sov. Phys. Semicond. **2**, 825 (1969)].
68. Yu. I. Ravich, E. A. Gurieva, I. N. Dubrovskaya, *et al.*, Fiz. Tverd. Tela (Leningrad) **12**, 917 (1970) [Sov. Phys. Solid State **12**, 711 (1970)].

Translated by D. Mashovets

Semiconductors, Vol. 36, No. 1, 2002, pp. 102–109. Translated from Fizika i Tekhnika Poluprovodnikov, Vol. 36, No. 1, 2002, pp. 109–116.

Formation of Silicon Nanocrystals with Preferred (100) Orientation in Amorphous Si:H Films Grown on Glass Substrates and Exposed to Nanosecond Pulses of Ultraviolet Radiation

M. D. Efremov*, V. V. Bolotov, V. A. Volodin*, S. A. Kochubeĭ*, and A. V. Kretinin*****

** Institute of Semiconductor Physics, Siberian Division, Russian Academy of Sciences,*
pr. Akademika Lavrent'eva 13, Novosibirsk, 630090 Russia
e-mail: efremov@isp.nsc.ru
*** Institute of Sensor Electronics, Siberian Division, Russian Academy of Sciences,*
pr. Mira 55, Omsk, 644077 Russia
**** Novosibirsk State University, ul. Pirogova 2, Novosibirsk, 630090 Russia*

Submitted March 26, 2001; accepted for publication May 11, 2001

Abstract—Using Raman scattering, it was ascertained that silicon nanocrystals with sizes exceeding 2 nm are formed in amorphous silicon films exposed to nanosecond ultraviolet laser radiation with energy densities ranging from 75 to 150 mJ/cm^2; it is shown that these nanocrystals have sizes no smaller than 2 nm and have preferred (100) orientation along the normal to the film surface. In a system of mutually oriented Si nanocrystals, anisotropic behavior of the Raman scattering intensity was experimentally detected in various polarization configurations, which made it possible to determine the volume fraction of oriented nanocrystals. The orientational effect is presumably caused by both the macroscopic fields of elastic stresses in the film and the local fields of elastic stresses around the nanocrystals. *© 2002 MAIK "Nauka/Interperiodica".*

1. INTRODUCTION

The formation of nanocrystals in amorphous silicon (*a*-Si) films and the study of their properties is a topical problem. Detection of the effects caused by localization of electrons and phonons in nanocrystals is of particular interest. Since the band gap of crystalline Si (1.1 eV) is smaller than the mobility gap in hydrogenated *a*-Si (*a*-Si:H), which can be as large as 1.9 eV [1], we may expect that quantum-mechanical size effects for charge carriers in nanocrystals affect the optical and electrical properties of the obtained films. The possibility of the controlled formation of crystalline-phase nuclei with the aim of obtaining polycrystalline Si films with specified parameters is of interest from the standpoint of applications. Since the formation of arrays of thin-film transistors on inexpensive (nonrefractory) glass substrates is required for the production of liquid-crystal displays, amorphous films should be crystallized under conditions that exclude the heating of the substrates to a temperature higher than the glass-softening point. In this context, it is expedient to use pulsed exposures to ultraviolet radiation [2]. In this case, radiation is absorbed in the film and does not heat the substrate, so the substrate has no time to be heated to a temperature above the softening point during the pulse. The main disadvantage of polysilicon films formed by liquid-phase epitaxy is the fact that the films are nonplanar [3], which is related to the necessity of scanning treatments for obtaining large-area films. In this context, one of the promising methods for crystallization of the *a*-Si films is the formation of crystalline-phase nuclei (nanocrystals) using pulsed laser treatments with the subsequent growth of these nuclei under the conditions of solid-phase crystallization [4–7]. In the context of growing the textured polysilicon films with improved electrical characteristics and with high uniformity of the parameters, the possibility of forming a system of nanocrystals that are aligned in the same direction, owing to the self-organization effects under the nonequilibrium conditions of nanosecond laser treatments, is of particular interest [8]. In this study, we attempted to elucidate the mechanisms for the origination of the preferred orientation of Si nanocrystals and to gain insight into the polarization-related features of the Raman scattering in a system of oriented nanocrystals.

2. EXPERIMENTAL

The samples to be studied were 100-nm-thick *a*-Si films formed on a Corning 7059 glass substrate using plasma-chemical deposition at a temperature of 230°C. For laser treatments of the films, we used an XeCl excimer laser with a radiation wavelength of 308 nm. The pulse duration was 5 ns. For the above wavelength, the absorption coefficient for *a*-Si is 1.5×10^6 cm^{-1}; as a result, the laser-radiation energy is completely absorbed within the *a*-Si film. The substrate temperature measured at the rear surface remained close to ~300 K under the employed conditions of the laser treatment. In our experiments, the densities of the laser-radiation energy in a pulse were either higher or lower than the threshold density that is required for the origination of macroscopic molten regions in the *a*-Si film. The melting threshold determined from an experiment with optical reflection with nanosecond-scale time resolution amounted to 120–150 mJ/cm^2 [9]. Our samples were irradiated either with a single laser pulse or with a series of up to thousand pulses with low energy density in order to form a high concentration of Si nanocrystals. The pulse repetition rate was 2 Hz, which excluded the possibility of heating the substrate. The laser-beam aperture was rectangular, with an aspect ratio of 3 : 1. The pulse energy was stable in time to within 3%. The laser radiation was unpolarized.

The Raman spectra were measured at room temperature in the configuration of quasi-backscattering. We used a system automated in the CAMAC standard and based on a DFS-52 monochromator (LOMO, St. Petersburg). We used the 488-nm line of an Ar laser as the pump for the Raman process. In order to implement the various polarization configurations for the Raman scattering, we employed a half-wave plate to rotate the plane of the light polarization, a Glan prism, and a depolarizing wedge.

3. RESULTS AND DISCUSSION

3.1. Formation of Nanocrystals in the a-Si Films Exposed to Pulsed Ultraviolet Radiation

As a result of the absence of translational symmetry, optical transitions in *a*-Si are not restricted by the law of conservation of momentum; therefore, the Raman spectrum of *a*-Si in the optical range is characterized by the effective density of vibrational states and is represented by a broad band peaked in the vicinity of 480 cm^{-1} [10]. The vibrational eigenmodes of nanocrystals are spatially localized; as a result, the Raman spectrum of nanocrystals is characterized by a peak, the position of which depends heavily on the size of nanocrystals and, as they become larger than 50 nm, does not differ much from that of the Raman spectrum peak in single-crystal Si (520 cm^{-1}) [11, 12]. The peak width is controlled by a spread in nanocrystal sizes and also by the phonon lifetime. The peak intensity is proportional to the nanocrystalline-phase fraction. In Fig. 1, we show the Raman spectra of both the starting *a*-Si film and the films subjected to various treatments with excimer-laser radiation. As can be deduced from the Raman spectrum of the starting film (curve *1*), there are no nanocrystalline inclusions in this film. This is also corroborated by the results of studying the starting films using electron microscopy.

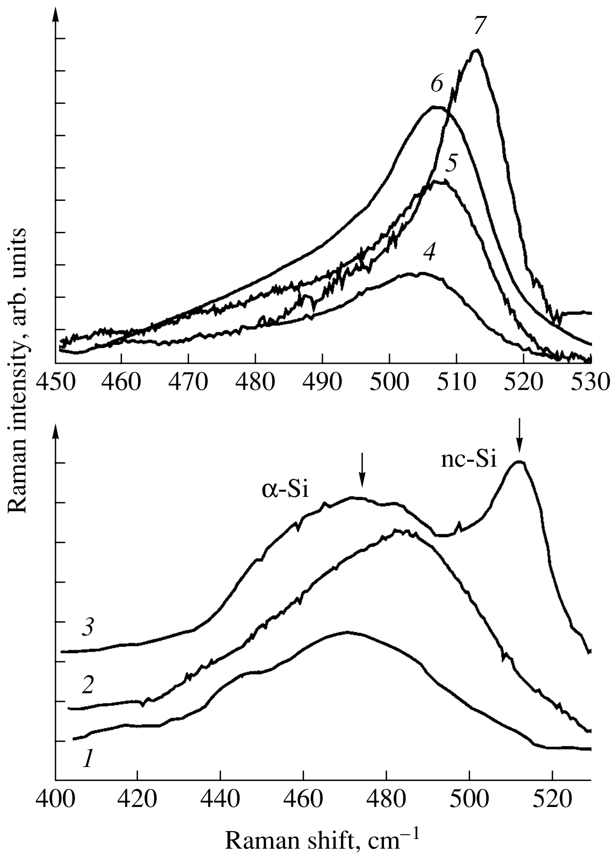

Fig. 1. The Raman spectra of the *a*-Si:H films formed by plasma-chemical deposition (curve *1* corresponds to the starting film) after laser-radiation treatments under the following conditions (the energy density in a pulse and the number of pulses are given): (*2*) 80 mJ/cm^2, 1 pulse; (*3*) 110 mJ/cm^2, 1 pulse; (*4*) 75 mJ/cm^2, 1000 pulses; (*5*) 80 mJ/cm^2, 1000 pulses; (*6*) 90 mJ/cm^2, 500 pulses; and (*7*) 100 mJ/cm^2, 500 pulses.

In Fig. 1 (curves *2*–*7*), we also show the Raman spectra of the *a*-Si films subjected to pulsed treatments by the excimer-laser radiation with energy densities of 75–110 mJ/cm^2 and with the number of pulses ranging from 1 to 1000. We studied the concentration of Si nanocrystals as a function of the conditions of the laser irradiation. It can be seen that a single laser pulse with an energy density of 80 mJ/cm^2 is insufficient for the formation of a significant number of nanocrystals in the film (curve *2*). Only a certain modification of the "amorphous" Raman peak is observed: its intensity increased, and the peak shifted to higher frequencies. A band caused by scattering at optical phonons localized in silicon nanocrystals (nc-Si) is observed in the Raman spectrum of the sample subjected to the excimer-laser irradiation with an energy density of 110 mJ/cm^2 (curve *3*). This "nanocrystalline" band is peaked at 512 cm^{-1}, which corresponds to the average crystallite size of 4–5 nm [12]. The fraction α of the nanocrystalline phase can be determined from the ratio between the integrated intensities of the "amorphous" and "nanoc-

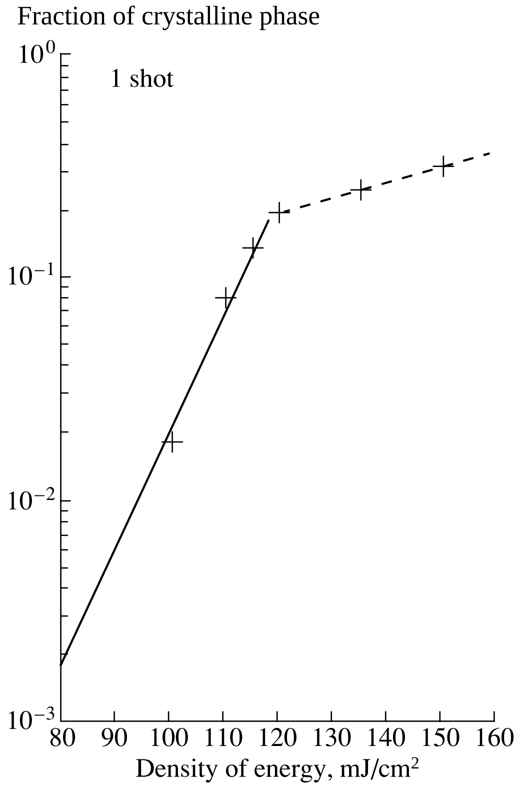

Fig. 2. Fraction of crystalline phase in silicon films after exposure to a single pulse of the excimer-laser radiation as a function of the energy density in a pulse.

rystalline” peaks (I_a and I_{nc}, respectively) using the following expression:

$$\alpha = I_{\mathrm{nc}}/(\sigma I_a + I_{\mathrm{nc}}). \qquad (1)$$

Here, σ is the ratio between the integrated cross sections for scattering by nc-Si and *a*-Si ($\Sigma_{\mathrm{nc}}/\Sigma_a$); this ratio is equal to 0.88 [13]. According to calculations, the fraction of crystalline phase in this sample is 0.08. In order to form a significant number of nanocrystals in the case of laser-pulse treatments with lower energy densities, we have to use a treatment with a series of pulses. The Raman spectra of the samples subjected to a series of pulses are also shown in Fig. 1 (curves *4*–*7*); the parameters of the treatments are given in the caption to Fig. 1. In all of these samples, the fraction of nanocrystalline phase was larger than one-half. As can be seen, as the energy density of laser irradiation varies, the “nanocrystalline” peak shifts; as is well known, the position of this peak is governed by the average size of nanocrystals. The mean size of nanocrystals can be determined using the convolution of effective density of vibrational states [14, 15]. According to calculations, the mean size of nanocrystals was 1.8 nm for sample *4*, 2.0 nm for samples *5* and *6*, and 3.0 nm for sample *7* (the sample numbers correspond to the numbers at the curves in Fig. 1). The general tendency is the following: an increase in the energy density in a pulse leads to an increase in the mean size of the forming nuclei of the crystalline phase (nanocrystals). The data obtained using high-resolution electron microscopy (HREM) corroborated the data of Raman spectroscopy [7, 8]. The electron microscopy data also indicate that nucleation during pulsed exposures to ultraviolet radiation occurs homogeneously. The technology for preparing the samples for HREM includes the removal of silicon films from the glass substrates by chemical etching. As a result, the film thickness decreases from 1000 to 200–300 Å, both from the surface side and from the heterointerface side. Since the nanocrystals are surrounded by an amorphous matrix, they are formed in the depth of the film itself, rather than as a result of heterogeneous nucleation at the surface or heterointerface [7, 8].

Dependence of the nanocrystalline-phase fraction on the energy density in a pulse was studied for the samples exposed to a single pulse. The results are generalized in Fig. 2. If we approximate the obtained experimental data by straight lines, we can see that a kink is observed in the lines in the vicinity of the power density of 120 mJ/cm^2. Apparently, if the energy density exceeds this value, a transition to the liquid-phase crystallization occurs, which is consistent with the published data [9]. Thus, we may assume that laser treatments with an energy density no higher than 120 mJ/cm^2 do not give rise to macroscopic molten regions.

3.2. Raman Scattering in a System of Oriented Nanocrystals

It is well known that the light scattered inelastically by the crystal-lattice vibrations is polarized; its polarization is governed by the Raman scattering tensor and the polarization of the incident radiation. Under the conditions far from those for the resonance Raman scattering (scattering by the mechanisms of either the deformation potential or the Vol’kenshtein additive polarizability of the bonds [16, 17]), the tensors of quasi-backscattering Raman process in the principal crystallographic axes X = [001], Y = [010], and Z = [100] can be represented as

$$R'(X) = \begin{pmatrix} 0 & a & 0 \\ a & 0 & 0 \\ 0 & 0 & 0 \end{pmatrix}, \quad R'(Y) = \begin{pmatrix} 0 & 0 & a \\ 0 & 0 & 0 \\ a & 0 & 0 \end{pmatrix},$$

$$R'(Z) = \begin{pmatrix} 0 & 0 & 0 \\ 0 & 0 & a \\ 0 & a & 0 \end{pmatrix},$$

where the axes X, Y, and Z correspond to the directions of deformation-related displacements induced by phonons [16]. For the quasi-backscattering by the (110) surface and for the choice of the axes as X = [001], Y =

$[1\bar{1}0]$, and $Z = [110]$, the Raman scattering tensors are transformed to the following form:

$$R(X) = \begin{pmatrix} 0 & a & 0 \\ a & 0 & 0 \\ 0 & 0 & 0 \end{pmatrix}, \quad R(Y) = \frac{1}{\sqrt{2}}\begin{pmatrix} 0 & 0 & -a \\ 0 & 0 & 0 \\ -a & 0 & 0 \end{pmatrix},$$

$$R(Z) = \frac{1}{\sqrt{2}}\begin{pmatrix} 0 & 0 & a \\ 0 & 0 & a \\ a & a & 0 \end{pmatrix}.$$

According to the symmetry selection rules for the Raman process, the scattering intensity I_{CS} is proportional to $(\mathbf{E}_i R\mathbf{E}_s)^2$, where $\mathbf{E}_i$ and $\mathbf{E}_s$ are the polarization vectors of the incident and scattered light, respectively. For the quasi-backscattering, the vectors $\mathbf{E}_i$ and $\mathbf{E}_s$ lie in the plane that is perpendicular to the direction of the incident light; in the case under consideration, this direction is designated as $Z = [110]$, and the configuration is designated as $Z(\mathbf{E}_i\mathbf{E}_s)\bar{Z}$. In this configuration, scattering by longitudinal phonons is forbidden for any polarizations $\mathbf{E}_i$ and $\mathbf{E}_s$, the transverse phonon TO_X (atoms are displaced in the X direction) is active in the $Z(YY)\bar{Z}$ configuration, and the transverse phonon TO_Y (atoms are displaced in the Y direction) is active in the $Z(XY)\bar{Z}$ configuration [16]. If the sample is rotated by an angle φ, the basis vectors of the laboratory frame are represented by the following formulas in the system of coordinates linked to the principal axes of the sample:

$$X' = (\sin\varphi/\sqrt{2}, -\sin\varphi/\sqrt{2}, \cos\varphi),$$

$$Y' = (\cos\varphi/\sqrt{2}, -\cos\varphi/\sqrt{2}, -\sin\varphi).$$

The Raman scattering intensity for the TO_X phonon in the $X'X'$, $Y'Y'$, and $X'Y'$ configurations is then proportional to

$$\sin^4\varphi, \quad \cos^4\varphi, \quad \text{and} \quad \sin^2\varphi\cos^2\varphi.$$

For the TO_Y phonon and for the same scattering configurations, this intensity is proportional to

$$4\sin^2\varphi\cos^2\varphi, \quad 4\sin^2\varphi\cos^2\varphi, \quad \text{and}$$
$$(\cos^2\varphi - \sin^2\varphi)^2.$$

In relation to the angle of rotation about the Z-axis, the total Raman scattering intensity for transverse phonons ($\mathrm{TO}_X + \mathrm{TO}_Y$) is proportional to

$$I_{X'X'} = \sin^4\varphi + 4\sin^2\varphi\cos^2\varphi,$$

in the $X'X'$ configuration;

$$I_{Y'Y'} = \cos^4\varphi + 4\sin^2\varphi\cos^2\varphi,$$

in the $Y'Y'$ configuration; and

$$I_{X'Y'} = \sin^2\varphi\cos^2\varphi + (\cos^2\varphi - \sin^2\varphi)^2$$

in the $X'Y'$ configuration.

Thus, if the crystallographic axis [110] of all silicon nanocrystals were oriented along the normal to the film surface and if, in addition, all the nanocrystals were mutually aligned in the planar direction, then, by rotating either the sample or the polarization plane of incident light and the analyzer for scattered light, we could observe the modulation of the Raman scattering intensity in various configurations; as a result, the intensity may vary from zero to the largest value.

We now assume that the [110] axis of a fraction of nanocrystals γ is oriented along the normal to the film surface, whereas the remaining nanocrystals are oriented randomly. A fraction of [110]-oriented nanocrystals are mutually oriented in the planar direction, whereas the remaining nanocrystals are oriented randomly in the planar direction. Designating the fraction of mutually oriented crystalline nuclei by ρ, we now average the intensity of Raman scattering due to nanocrystals that remain misoriented in the planar direction; as a result, we obtain the following polarization dependences for the Raman scattering intensity:

$$\begin{aligned} I_{X'X'} &\propto \gamma[\rho(\sin^4\varphi + 4\sin^2\varphi\cos^2\varphi) \\ &\quad + (7/8)(1-\rho)] + (1-\gamma), \\ I_{Y'Y'} &\propto \gamma[\rho(\cos^4\varphi + 4\sin^2\varphi\cos^2\varphi) \\ &\quad + (7/8)(1-\rho)] + (1-\gamma), \\ I_{X'Y'} &\propto \gamma\{\rho(\sin^2\varphi\cos^2\varphi + [\cos^2\varphi - \sin^2\varphi]^2) \\ &\quad + (5/8)(1-\rho)\} + (3/4)(1-\gamma). \end{aligned} \tag{2}$$

Here, $0 \le \rho \le 1$ and $0 \le \gamma \le 1$. It is noteworthy that, for completely random orientation, the ratio between the Raman scattering intensities in the transverse and longitudinal configurations is equal to 3/4 [18]. The contribution of misoriented silicon nanocrystals is accounted for by the isotropic second terms in expressions (2), whereas the mutually oriented nanocrystals yield the anisotropic (dependent on the angle φ) component of the Raman scattering intensity.

In Fig. 3, we show the Raman spectra obtained when the sample was rotated in reference to the polarization vector of the incident light. Depending on the angle of rotation about the Z-axis, we observed a variation in the ratio between the Raman scattering intensities in the $X'X'$, $Y'Y'$, and $X'Y'$ configurations. When the ratio between the Raman scattering intensities in the $X'Y'$ and $X'X'$ configurations ($I_{X'Y'}/I_{X'X'}$) attains its maximum, then, according to formulas (2), this corresponds to the condition $\varphi = 0°$; i.e., the X'-axis is parallel to the crystallographic direction of the [001]-oriented nanocrystals. The smallest ratio between the intensities $I_{X'Y'}/I_{X'X'}$ was observed for the rotation angle $\varphi = 45°$ (Fig. 3). Analyzing the spectra shown in Fig. 3, we may note that a different Raman scattering intensity is observed for dissimilar polarization configurations; furthermore, rota-

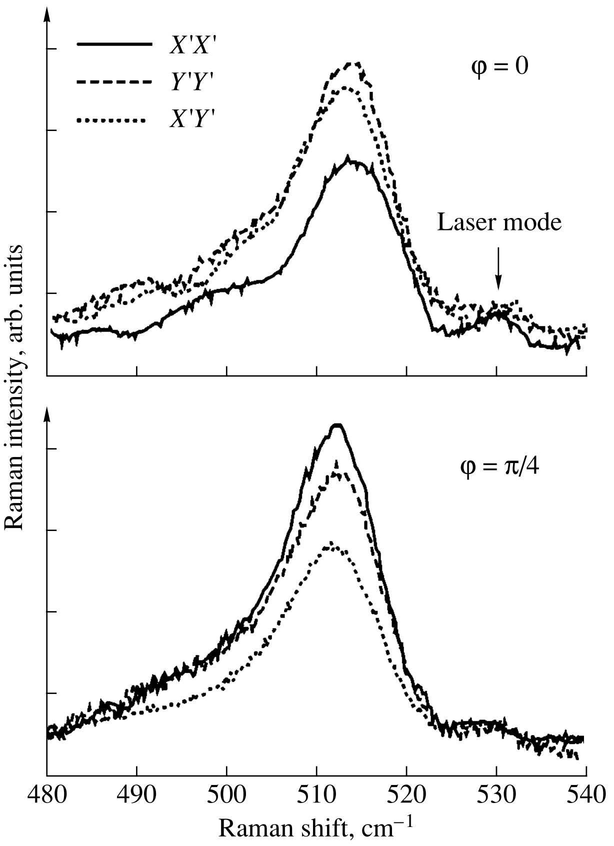

Fig. 3. The Raman spectra recorded in different polarization configurations for two orientations of the sample with respect to the polarization directions of the incident light (the rotation angle of the sample φ is indicated). The sample is an *a*-Si/nc-Si film subjected to 500 pulses of laser radiation with energy density of 100 mJ/cm^2 in a pulse.

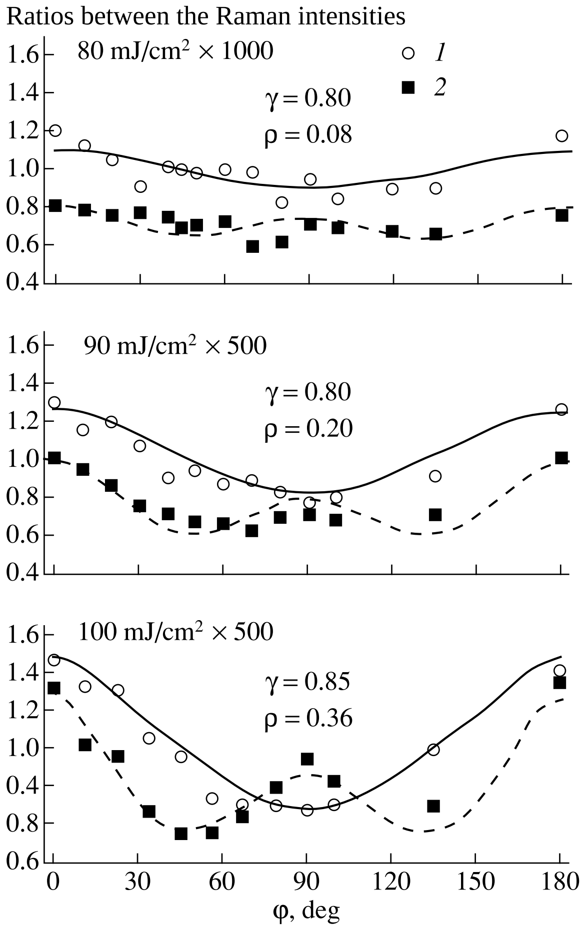

Fig. 4. Experimentally measured ratios between the Raman scattering intensities in different configurations (*1*) $I_{Y'Y'}/I_{X'X'}$ and (*2*) $I_{X'Y'}/I_{X'X'}$ to be compared with the values calculated using formula (2). The quantity φ is an angle between the crystallographic direction [001] of mutually oriented nanocrystals and the direction of polarization of the incident light *X*'. The solid lines represent the results of calculations of the ratio $I_{Y'Y'}/I_{X'X'}$, whereas the dashed lines correspond to calculations of $I_{X'Y'}/I_{X'X'}$. The conditions of laser irradiations (the energy density in a pulse and the number of pulses) and also the values of the parameters γ and ρ used in the calculations are indicated.

tion of the sample appreciably affects the ratio between the intensities, which indicates that the Raman scattering cross section is anisotropic. Thus, the anisotropic behavior of the Raman scattering intensity can be attributed to the emergence of preferred orientation in a system of nanocrystals and to correlation in their orientation in the planar direction [19]. The sample under consideration was subjected to pulsed excimer-laser radiation (500 pulses with an energy density of 100 mJ/cm^2 in a pulse). Based on the position of the Raman scattering peak (512 cm^{-1}), which corresponds to the scattering by optical modes localized in the silicon nanocrystals, we may conclude that the size of the nanocrystals is about 3 nm [12]; the fact that the peaks are fairly narrow (14 cm^{-1}), compared to the published data [11, 20], indicates that the spread in the nanocrystal sizes is small. A certain asymmetry of the peak and a low-energy wing of the peaks in the region of 490–500 cm^{-1} may be related to the contribution of misoriented Si located in the space between the oriented Si nanocrystals or to scattering by longitudinal modes localized in the nanocrystals. The special features observed at 530 cm^{-1} are related to the plasma mode of laser radiation at this wave number; this mode is not completely suppressed by the interference filter. As was mentioned above, an analysis of the ratio between the intensities of Raman scattering in nanocrystals and in amorphous phase [formula (1)] suggests that the content of crystalline phase is higher than 50%.

The Raman spectra of different samples containing silicon nanocrystals were measured in relation to the angle φ. All peaks corresponding to scattering by localized optical phonons in nanocrystals were approximated with Lorentzian curves using computer-based fitting based on the least-squares method. For all spectra, we calculated the integrated Raman scattering intensity; all intensities were then normalized to the intensity in the *X*'*X*' configuration. In Fig. 4, we show the calculated curves compared with experimental polarization dependences of the Raman scattering intensities on the angle φ for three different samples. By comparing the results of calculations based on formula (2) with experimental data, we determined the fraction of the [110]-oriented nanocrystals γ and the fraction of the nanocrystals oriented mutually in the planar direction ρ. We observe a quantitative agreement of the results of theoretical calculations with experimental angular dependences of the ratios between the Raman scattering intensities in various polarization configurations. For the sake of comparison, we studied the polarization dependences of the intensity of the Raman scattering in different configurations of polycrystalline silicon film, in which the crystalline grains were oriented randomly according to the data obtained using electron microscopy. In this case, the Raman scattering intensity was independent of the angle φ, and the Raman scattering intensities in the $X'X'$, $Y'Y'$, and $X'Y'$ configurations coincided within experimental error.

3.3. Possible Mechanisms for the Origination of Preferred Nanocrystal Orientation

The effect of the emergence of the preferred orientation of crystalline grains in a film deposited on vitreous substrates has been observed previously in polycrystalline films formed using plasma-chemical deposition. In this case, most of the crystallites are oriented in such a way that their crystallographic planes, (110), (100), and (311), are parallel to the growth plane [21], with the (110) orientation encountered most often. Presumably, the emergence of the preferred orientations is caused by the fact that certain surfaces are energetically more favorable for growth; it is these surfaces that “survive” during the film deposition. This is related to a difference in the free surface energies for dissimilarly oriented surfaces [21]. Origination of a preferred crystallyte orientation with respect not only to the structure normal but also to a certain planar direction, which resulted in the formation of textured polysilicon layers, was related to the existence of the preferred direction in the system, which coincides with the direction of the gaseous-mixture flow [22]. However, the mechanisms suggested so far based on the assumption that the crystallization rates are different for dissimilar crystallographic directions can be used to account for the film texture only in the course of deposition and in the processes of liquid-phase crystallization [3, 23], rather than in the course of solid-phase crystallization.

In our experiments, using both the electron-microscopy and Raman scattering spectroscopy data, we observed no other preferred orientations of nanocrystals with respect to the film-surface normal (except for the [110] orientation). The emergence of preferred [110] orientation along the normal to the film can be attributed to the effect of stresses both existing in the (amorphous film)–substrate system and emerging around the forming nanocrystal, owing to the difference in the densities of amorphous and crystalline phases. Consideration of stresses in the film–substrate system yields an addition of 0.27 meV/kbar per atom to the difference between the chemical potentials in the crystalline and amorphous phases [6, 7]. Consideration of stresses in nanocrystal–(amorphous medium) systems yields an even larger contribution to the chemical-potential difference. This addition amounts to 11.4 meV per atom [6, 7] if the spherical nanocrystal is considered as the dilatation center in an amorphous medium; this may affect appreciably the nucleation dynamics. Apparently, if the nucleus concentration is sufficiently high, it is necessary to take into account an additional contribution to the free energy; this contribution arises due to the interaction of nuclei via the stress fields. Since the formation of a crystalline nucleus in the amorphous phase gives rise to additional symmetry in the planar direction, it may be expected that the formation of interacting nanocrystals is accompanied with the emergence of preferred orientation in the planar direction. It is also well known that, for cubic crystals with a high degree of symmetry (silicon represents such a crystal), an elastic contribution to the Gibbs free energy depends on the crystal orientation in the fields of both uniaxial and biaxial stresses [24]. Therefore, one of the possible explanations of the correlation between the orientations of nanocrystals is based on their orientation in the fields of thermoelastic stresses that arise during the pulsed laser heating.

The dependence of the fraction of oriented nanonocrystals on the energy density in a laser pulse is also important (Fig. 4). A decrease in the energy density and, as a result, a decrease in the average size of nanocrystals resulted in a reduction in the correlation between their mutual orientations. This fact also confirms the hypothesis that the mutual orientation occurs owing to the effect of stresses, because, for smaller nanocrystals, the stresses around the nanocrystal as a dilatation center are lower, and the contribution of the elastic component to the Gibbs free energy for the critical nucleus is smaller.

3.4. Formation of Textured Polysilicon Films on Nonoriented Substrates. Optical Properties of Amorphous Films Containing Nanocrystals

As was mentioned above, the application-related interest in the processes of self-organization and mutual orientation of nanocrystals is caused by the possibility of forming polysilicon films with improved structural and electrical characteristics and also by the new optical properties of an nc-Si/*a*-Si:H system. Solid-phase crystallization during an in-furnace annealing (at 550°C) of the films that contained the silicon nanocrystals nucleated by previous laser treatment resulted in the formation of the [110]-oriented polysilicon texture on the nonoriented glass substrates. Under optimal conditions of preliminary treatment of *a*-Si films with the excimer-laser pulses with low energy density and subsequent thermal annealing, the relative area occupied by textured regions was as large as 80%, and the lateral sizes of textured regions were no smaller than 20–30 μm [6]. In this situation, a close correspondence (with the deviation in the orientation of neighboring crystallites no larger than 6°) between the orientations of grains is observed. This correspondence was observed not only in the direction along the normal to the structure surface but also in the planar direction, which gave rise to a system of point reflections in electron diffraction patterns that were similar to the pattern of reflections characteristic of single-crystal, [110]-oriented silicon [6]. The lower estimation of the charge-carrier mobility in such structures, which was obtained from experiments with steady-state photoconductivity and from the decay time of transient photoconductivity, yielded the value of 70 $cm^2 V^{-1} s^{-1}$; in contrast to this, the mobility in the films that were not preliminarily subjected to laser radiation was several times lower. In the photoconductivity spectra of *a*-Si films containing nanocrystals, which had an average size of about 2 nm and were formed in the course of pulsed laser treatment, a peak at 1.15 eV was observed. In these films, the content of nanocrystalline phase was lower than 1%; as the volume occupied by nanocrystalline phase increased (as a result of using laser pulses with higher energy densities), the magnitude of photoresponse decreased, which can be caused by the partial dehydrogenation of the films. Photoluminescence in the visible region of the spectrum has been observed at room temperature in the *a*-Si:H films with Si nanocrystals [25]. The nanocrystals were formed either directly during plasma-chemical treatment or as a result of exposure to high-power laser radiation; the latter could give rise to partial evaporation of the Si film accompanied with formation of nanoislands [25]. In the films under consideration, we observed a peak at about 1.5 μm in the photoluminescence spectrum excited by a solid-state laser with wavelength of 1.06 μm. Nanocrystals in these films were also formed using pulsed laser treatments; the average size of the nanocrystals was 4 nm, and the fraction of nanocrystalline phase was 70%. Photoluminescence in the above spectral region was not observed in the starting *a*-Si films, which suggests that the observed effect was related to the formation of nanocrystals.

4. CONCLUSION

The treatments of *a*-Si:H films with pulses of ultraviolet-laser radiation, with energy densities below the melting threshold for the films result in the formation of nanocrystals in these films; nanocrystal sizes are no smaller than 2 nm and depend on the energy density in a pulse. It was found that silicon nanocrystals have a preferred [110] orientation along the normal to the structure surface. Anisotropic behavior of the cross section for the Raman scattering is observed in a system of oriented nanocrystals. An analysis of the angular dependences of the Raman scattering intensities in different polarization configurations in the context of the suggested model makes it possible to determine the fraction of mutually oriented nanocrystals. The emergence of the preferred mutual orientation of nanocrystals in the planar direction in the initially isotropic amorphous silicon film grown on the glass substrate may be caused by their orientation in the fields of elastic stresses and also by the phenomenon of self-organization as a result of interaction between nanocrystals via the deformation-related mechanism.

ACKNOWLEDGMENTS

This study was supported by the Russian Foundation for Basic Research, project no. 00-02-17946.

REFERENCES

1. H. Fritzsche, in *Advances in Disordered Semiconductors*, Vol. 1: *Amorphous Silicon and Related Materials*, Ed. by H. Fritzsche (World Scientific, Singapore, 1989; Mir, Moscow, 1991).
2. J. E. Fair, Solid State Technol. **8**, 47 (1992).
3. A. B. Limanov, V. A. Chubarenko, V. M. Borisov, *et al.*, Mikroélektronika **28**, 30 (1999).
4. V. V. Bolotov, M. D. Efremov, L. I. Fedina, *et al.*, in *Abstracts of Spring Meeting of Material Research Society, San Francisco, 1993*, p. A9.54.
5. M. D. Efremov, V. V. Bolotov, V. A. Volodin, *et al.*, in *Proceedings of the 15th International Conference on Coherent and Nonlinear Optics, St. Petersburg, Russia, 1995.*
6. M. D. Efremov, V. V. Bolotov, V. A. Volodin, *et al.*, J. Phys.: Condens. Matter **8**, 273 (1996).
7. M. D. Efremov, V. V. Bolotov, V. A. Volodin, *et al.*, Solid State Phenom. **57–58**, 507 (1997).
8. M. D. Efremov, V. A. Volodin, V. V. Bolotov, *et al.*, Solid State Phenom. **69–70**, 557 (1999).
9. T. Sameshima and S. Usui, J. Appl. Phys. **70**, 1281 (1991).
10. J. E. Smith, Jr., M. H. Brodsky, B. L. Crowder, and M. I. Nathan, Phys. Rev. Lett. **26**, 642 (1971).
11. Z. Iqbal, S. Veptek, A. P. Webb, and P. Capezzuto, Solid State Commun. **37**, 993 (1981).
12. Jian Zi, H. Büscher, C. Falter, *et al.*, Appl. Phys. Lett. **69**, 200 (1996).
13. R. Tsu, J. Gonzalez-Hernandez, S. S. Chao, *et al.*, Appl. Phys. Lett. **40**, 534 (1982).
14. H. Richter, Z. P. Wang, and L. Ley, Solid State Commun. **39**, 625 (1981).
15. V. Paillard and P. Puech, J. Appl. Phys. **86**, 1921 (1999).

16. G. Bauer and W. Richter, in *Optical Characterization of Epitaxial Semiconductor Layers* (Springer-Verlag, Berlin, 1996), p. 138.
17. M. V. Vol'kenshteĭn, Dokl. Akad. Nauk SSSR **32**, 185 (1941).
18. D. Bermejo and M. Cardona, J. Non-Cryst. Solids **32**, 405 (1978).
19. M. D. Efremov, V. V. Bolotov, V. A. Volodin, and S. A. Kochubei, Solid State Commun. **108**, 645 (1998).
20. E. Bustarret, M. A. Hachicha, and M. Brunel, Appl. Phys. Lett. **52**, 1675 (1988).
21. Yong Sun, T. Miyasato, and J. K. Wigmore, Appl. Phys. Lett. **70**, 508 (1997).
22. G. Q. Di, H. Lin, N. Uchida, *et al.*, Appl. Phys. Lett. **68**, 69 (1996).
23. N. M. Igonina, Author's Abstracts of Candidate's Dissertation (Novosibirsk, 1985).
24. D. R. McKenzie and M. M. M. Bilek, J. Appl. Phys. **86**, 230 (1999).
25. K. M. A. El-Kader, J. Oswald, J. Kocha, and V. Chab, Appl. Phys. Lett. **64**, 2555 (1994).

Translated by A. Spitsyn

Semiconductors, Vol. 36, No. 1, 2002, pp. 110–115. Translated from Fizika i Tekhnika Poluprovodnikov, Vol. 36, No. 1, 2002, pp. 117–123.
Original Russian Text Copyright © 2002 by Ivanov-Omskiĭ, Tagliaferro, Fanchini, Yastrebov.

AMORPHOUS, VITREOUS, AND POROUS SEMICONDUCTORS

Density of States in Amorphous Carbon and Its Modification by Annealing

V. I. Ivanov-Omskiĭ*, A. Tagliaferro, G. Fanchini**, and S. G. Yastrebov***
** Ioffe Physicotechnical Institute, Russian Academy of Sciences, St. Petersburg, 194021 Russia*
*** Politecnico di Torino, Torino, 10129 Italy*
e-mail: Yastrebov@pop.ioffe.rssi.ru

Submitted May 28, 2001; accepted for publication May 30, 2001

Abstract—The effect of annealing on the electron density of states in amorphous carbon *a*-C and amorphous hydrogenated carbon *a*-C:H has been studied. *a*-C and *a*-C:H layers were grown by magnetron sputtering of a graphite target in, respectively, argon and argon–hydrogen plasmas. Optical transmission spectra were studied experimentally in the range 1.5–5.6 eV, and ellipsometric parameters were measured at the He–Ne laser wavelength. The spectral dependence of the imaginary part of the dielectric function was reconstructed. A model describing the optical response of amorphous carbon was developed on the basis of the hypothesis that there are fluctuations of the sp^2 fragment sizes in the allotropic composition of amorphous carbon. The optical gap E_g in both types of material is accounted for by the presence of fragments of critical size. Experimental data were used to reconstruct, with the use of model parameters, the energy dependence of the density of states in the ground and excited bands, and the plasma frequencies for electrons involved in optical transitions are found. It is shown that the bands of both the ground and excited states are inhomogeneously broadened sets of levels, which are symmetrical about the Fermi level. The behavior of the model parameters E_g and E_G (energy corresponding to the peak of the Gaussian distribution) and the plasma frequency with annealing temperature shows, for materials of both types, a substantial rise in the size and number of critical fluctuations with increasing temperature. © *2002 MAIK “Nauka/Interperiodica”.*

1. INTRODUCTION

The problem of the energy spectrum of amorphous semiconductors cannot be formulated in a unified way because of the wide diversity of their structural types. This is manifested in the fact that the quantitative description of the fundamental absorption edge in a sufficiently wide spectral range is complicated. As is known, the most general approach to this problem, allowing comparison with experiment, was developed by Tauc [1], who relied upon the assumption that the energy spectrum of electrons is quadratic in momentum. This assumption is insufficiently justified for narrow bands, which, presumably, is the case for amorphous carbon. It seems that the inconsistency of approaches taken by different researchers to the analysis of the shape of the fundamental absorption edge in amorphous carbon [2, 3] is due to this circumstance.

In the present study, we develop a model of the energy spectrum of amorphous carbon, which represents the structure of *a*-C as a homonanocomposite containing nanosize fragments of sp^2-bound carbon. It is well known that there is no gap in the energy spectrum of π electrons in bulk graphite. The small size of graphite-like fragments in sp^2-bound carbon [2, 3] leads to quantum-confinement effects and gives rise to a gap. Averaging of the contributions of optical transitions in these fragments causes inhomogeneous broadening of quantum-well levels into bands, which imparts a Gaussian shape to the density-of-states function. Similar concepts were developed in the preceding works of the authors of [2], but only in the present study was the density-of-states function obtained in an analytical form that is applicable to the quantitative description of the experimental fundamental absorption edge.

The proposed model of the electronic structure of amorphous carbon is used to describe the dependence of the absorption edge in *a*-C and *a*-C:H on the thermal annealing temperature; this model ensures good agreement with the experiment. The employed model is based on a self-similarity hypothesis according to which a certain macroscopic fragment of size L is regarded as a structural unit of amorphous carbon, with the volume L^3 containing a set of molecular structures of size a, and fluctuations of this parameter govern the optical properties of the material.

In section 2, the experimental procedure and experimental results are briefly considered. A structural model of amorphous carbon is presented and its quantitative description is given in Section 3. The calculation is compared with experiment in Section 4, and the effect of annealing on the density of states in amorphous carbon is analyzed quantitatively in Section 5.

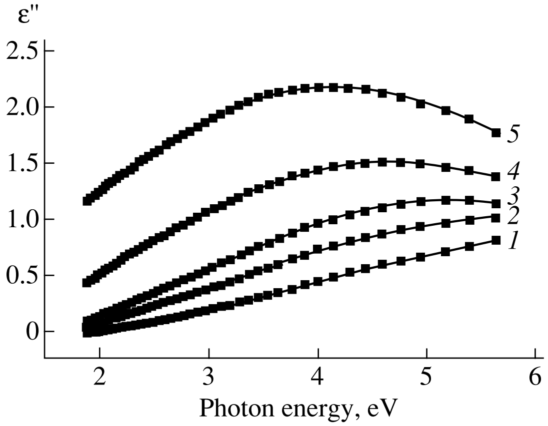

Fig. 1. Spectral dependences of the imaginary part of the dielectric constant of (*1*) an unannealed *a*-C:H film and films annealed at (*2*) 310, (*3*) 360, (*4*) 415, and (*5*) 475°C. Points, experimental data; curves, fitting with expression (5).

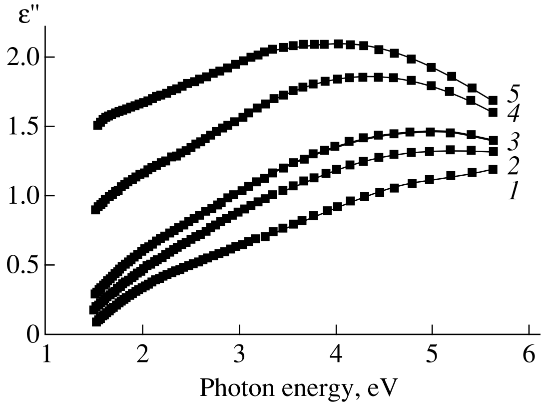

Fig. 2. Spectral dependences of the imaginary part of the dielectric constant of (*1*) unannealed *a*-C film and films annealed at (*2*) 310, (*3*) 360, (*4*) 415, and (*5*) 475°C. Points, experimental data; curves, fitting with expression (5).

2. EXPERIMENTAL

Amorphous carbon layers were deposited by dc magnetron sputtering of a graphite target onto fused silica substrates. A 1 : 4 mixture of hydrogen and argon was used as the working gas to obtain *a*-C:H films, and pure argon, in the case of *a*-C. The substrate temperature during growth was 200°C, the gas pressure in the working chamber constituted 8–9 mTorr, and the magnetron power was maintained at 0.36 kW. The time of *a*-C and *a*-C:H film growth was chosen to be 40 and 30 min, respectively, which gave the layer thicknesses of 770 and 740 Å.

The transmission of the films deposited onto fused silica in the visible spectral range (200–850 nm) was measured on a Hitachi U-3410 double-beam spectrophotometer. The light spot on a sample was 0.5×0.5 cm^2 in size. Ellipsometric measurements were carried out with an LEF-3M ellipsometer at a photon energy of 1.96 eV in reflection arrangement. The grown films were subjected to successive isochronous annealings in a vacuum (at residual pressure of 1 mtorr) in the temperature range 260–475°C. The spectral and ellipsometric measurements were done in air immediately after every annealing. According to ellipsometric data, the parameters of annealed films remained unchanged during a month of exposure to air.

The obtained ellipsometric data (film thicknesses, refractive index of the material, and its extinction coefficient at He–Ne laser wavelength) were used to reconstruct the spectral dependence of the extinction coefficient.

The dependence of the extinction coefficient on wavelength was obtained using the Kramers–Kronig relation. From the spectral dependences of the refractive index and extinction coefficient, the spectral dependence of the imaginary part of the dielectric constant shown in Figs. 1 and 2 was determined. It can be seen from Fig. 1 that the imaginary part of the dielectric constant of an *a*-C:H film is a monotonic function of energy at low annealing temperatures, but, at a certain temperature, a spectral feature appears, which becomes more pronounced and shifts to lower energies with increasing annealing temperature. A similar type of behavior is observed for the dependence for *a*-C (Fig. 2).

3. DIELECTRIC FUNCTION OF AMORPHOUS CARBON

3.1. Structural Model of Amorphous Carbon

In considering the structural model of amorphous carbon, let us adopt, to a first approximation, the fluctuation hypothesis, according to which spatial fluctuations of the density of π electrons are present in the material. It is assumed in the present study that the fundamental optical absorption edge of amorphous carbon is formed by averaged contributions from optical transitions in separate fragments of the sp^2 phase with Gaussian distribution. In view of the existence of certain kinetic limitations imposed on the growth of structures with a large number of π electrons, their size distribution function is limited by the largest possible, i.e., critical, fluctuation, and the number of fragments exceeding the critical fluctuation in size is small.

A characteristic feature of the electronic spectrum within a fragment is that the minimum energy of the quantum absorbable by the system is the energy of the first allowed optical transition between the highest occupied (HOMO) and lowest unoccupied (LUMO) states. Hence, it follows that the critical fluctuation is responsible, in the formation of the fundamental optical absorption edge, for the minimum energy E_g of the absorbed quantum (Fig. 3).

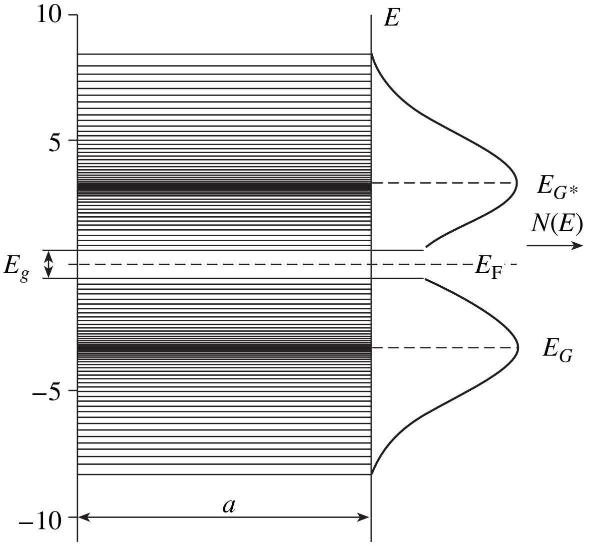

Fig. 3. Scheme of energy levels responsible for the optical properties of amorphous carbon. The Fermi level lies between the lowest unoccupied and highest occupied states.

3.2. Calculation of the Dielectric Function

Let us now obtain basic relations that will enable an interpretation of experimental data. For this purpose, let us consider an optical transition between the energy levels $E_0^{(l)}$ and $E_u^{(n)}$ in the region of fluctuation of the amorphous carbon film composition, which can be represented as a potential well of certain effective width a. To describe the optical response of such a system to the action of an electromagnetic wave, we consider a single-electron model of the resulting optical electron transition. Let an electron pass from an occupied state o in l-th fragment with energy $E_0^{(l)}$ and wave vector $\mathbf{k}_0$ into a n-th unoccupied state u ($n = l$) with energy $E_u^{(n)}$ and wave vector $\mathbf{k}_u$. Taking into account the fact that the fragment is spatially limited, as well as the uncertainty relation between the electron momentum and the coordinate, we neglect the momentum conservation law and write an expression for the dielectric constant of a two-level system, *lo–nu*, in the form

$$\varepsilon''_{(ln)}(\hbar\omega) = \frac{K}{(\hbar\omega^2)a_{ln}^3}\left|P_{ou}^{(ln)}\right|^2\delta(E_u^{(n)} + E_0^{(l)} - \hbar\omega)$$

$$= \frac{K}{(\hbar\omega^2)a_{ln}^3}\left|P_{ou}^{(ln)}\right|^2\delta(E - E_u^{(n)})\delta(E + E_0^{(l)} - \hbar\omega), \qquad (1)$$

$$\left|P_{ou}^{(ln)}\right|^2 = \left|\langle u^{(n)}|\nabla|o^{(l)}\rangle\right|^2,$$

$$K = \left(\frac{2\pi e\hbar^2}{m}\right)^2.$$

Let us introduce the density-of-states functions

$$N_u^{(n)}(E) = \frac{N_0}{V}\delta(E - E_u^{(n)}),$$
$$N_o^{(l)}(E) = \frac{N_0}{V}\delta(E + E_o^{(l)}), \qquad (1a)$$

where N_0 is the number of pairs of levels in a sample of volume V. This gives

$$\varepsilon''_{(ln)}(\hbar\omega) = \frac{K}{(\hbar\omega^2)a_{ln}^3}\left|P_{ou}^{(ln)}\right|^2\delta(E_u^{(n)} + E_0^{(l)} - \hbar\omega)$$
$$= \frac{KV^2}{(\hbar\omega^2)N_0^2a_{ln}^3}\left|P_{ou}^{(ln)}\right|^2 N_u^{(n)}(E)N_o^{(l)}(E - \hbar\omega). \qquad (2)$$

When making a_{ln}^3 approach $V = L^3$, it is assumed that $\overline{\left|P_{ou}^{(ln)}\right|^2} = |P_{ou}|^2$; i.e., the matrix element tends towards its mean value, and E_o, to $E_g/2$. Here, the value E_g corresponds to the energy of a HOMO–LUMO transition in a critical fluctuation. In this case, expression (2) tends to

$$\varepsilon''_{(ln)}(\hbar\omega) = \frac{KV}{(\hbar\omega^2)N_0^2}|P_{ou}|^2$$
$$\times \int_{-\frac{E_g}{2}}^{\hbar\omega - \frac{E_g}{2}} N_u^{(n)}(E)N_o^{(l)}(E - \hbar\omega)dE. \qquad (3)$$

Expression (3) is an equation with unknown integrand. To solve this equation, we use, as a first approximation, a Gaussian density-of-states function [2]:

$$N_u(E) = 0, \quad E \le \frac{E_g}{2};$$
$$N_u(E) = \frac{N_0}{V}\frac{D^{1/2}}{\sqrt{2\pi}s_u}\exp\left[-\frac{1}{2}\left(\frac{E - E_u}{s_u}\right)^2\right], \quad E > \frac{E_g}{2}; \qquad (4)$$
$$N_o(E) = 0, \quad E \ge -\frac{E_g}{2};$$

$$N_o(E) = \frac{N_0}{V}\frac{D^{1/2}}{\sqrt{2\pi}s_u}\exp\left[-\frac{1}{2}\left(\frac{E + |E_o|}{s_o}\right)^2\right], \quad E < \frac{E_g}{2}.$$

Here, parameter D is defined by normalization conditions requiring that the integral of the density-of-states function over energy in the interval from $E_g/2$ to infinity be equal to N_0/V; $s_u = s_o = s$ is the dispersion; $E_u = E_{G*}$, $|E_o| = E_G$; and $E_G = E_{G*}$ are the energies corresponding to the peak in the Gaussian distribution. It is noteworthy that a correction to the solution of Eq. (3) can be found by refining the coefficients of the further expansion of (4) in Gaussians. However, as shown below, the first approximation is suitable in the case in

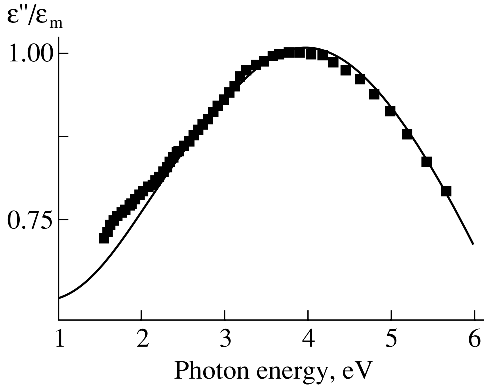

Fig. 4. Normalized dielectric function of *a*-C film subjected to 1-h annealing at 475°C. Points, experiment; solid line, calculation at $s = 1.495$ eV, $E_G = 2.947$ eV. $\varepsilon_m = \varepsilon''(\hbar\omega_m)$.

question for fitting the results of calculation to experimental data with sufficient accuracy. Integrating (3), we finally have

$$\varepsilon''(\hbar\omega) = \frac{A}{(\hbar\omega)^2}\exp\left[-\frac{(2E_G-\hbar\omega)^2}{4s^2}\right]\operatorname{erf}\left(\frac{\hbar\omega-E_g}{2s}\right), \quad (5)$$

$$A = \frac{C_2D}{2s\sqrt{\pi}}, \quad C = \frac{KV^2}{N_0^2}|P_{ou}|^2.$$

Assuming that $E_g = 0$, we have the case considered in [2]. It can be readily seen from (5) that ε" vanishes at $\hbar\omega = E_g$, being the largest at $\hbar\omega \approx 2E_G$.

4. COMPARISON OF THE MODEL WITH EXPERIMENT

Let us analyze the experimental frequency dependence of the imaginary part of the dielectric constant. For this purpose, we use expression (5) containing four fitting parameters. In this connection, particular attention was given in the present study to the uniqueness of the obtained solutions, and, therefore, the problem of finding the parameters was solved in stages. In the initial stage, expression (5) was used for the value $E_g = 0$, and three fitting parameters had to be determined: A, E_G, and s. Expression (5) was normalized to the maximum value of the dielectric function $\varepsilon''(\hbar\omega_m)$ for each curve processed. Coefficient A was thereby eliminated from Eq. (5), the number of unknowns was reduced to 2, and the equation was transformed into

$$\frac{\varepsilon''(\hbar\omega)}{\varepsilon''(\hbar\omega_m)} = \frac{(\hbar\omega_m)^2}{(\hbar\omega)^2} \times \frac{\exp\left(-\frac{(\hbar\omega-\hbar\omega_m)(\hbar\omega+\hbar\omega_m-4E_G)}{4s^2}\right)\operatorname{erf}\left(\frac{\hbar\omega}{2s}\right)}{\operatorname{erf}\left(\frac{\hbar\omega_m}{2s}\right)}. \quad (6)$$

Figure 4 presents a normalized frequency dependence of the imaginary part of the dielectric function.

It can be shown that a system of two equations formed with the use of (6) at two ω values has a unique solution for the pair E_G and s (see APPENDIX). Figure 4 shows, by a solid line, the values calculated by means of (6) for the solutions obtained for E_G and s. Further, the least-squares method was applied, with the thus-found approximate solution used as a starting approximation. A search for the minimum of the functional composed of the difference of squared expression (5) and experimental data was done using the Newton method to give the results listed in Tables 1 and 2.

In a similar way, Eq. (5) was solved at finite E_g values, but with an additional fitting parameter introduced

Table 1. Parameters of the first stage of fitting and plasma frequencies for *a*-C

T, °C	A, eV^2	E_G, eV	s, eV	$(\hbar\omega_p)^2$, eV^2	χ^2, 10^{-5}
200	38.25 ± 2.23	3.13 ± 0.06	1.21 ± 0.03	18	205
310	38.78 ± 1.01	2.93 ± 0.04	1.15 ± 0.02	18	239
360	42.34 ± 1.12	2.92 ± 0.03	1.74 ± 0.02	20	177
415	51.24 ± 0.42	2.96 ± 0.02	1.39 ± 0.01	29	26
475	54.75 ± 0.37	3.01 ± 0.01	1.56 ± 0.01	34	23

Table 2. Parameters of the first stage of fitting and plasma frequencies for *a*-C : H

T, °C	A, eV^2	E_G, eV	s, eV	$(\hbar\omega_p)^2$, eV^2	χ^2, 10^{-5}
200	27.83 ± 0.95	3.19 ± 0.04	1.02 ± 0.02	11	32
310	30.43 ± 1.03	2.96 ± 0.04	0.98 ± 0.02	12	112
360	34.37 ± 0.86	2.89 ± 0.03	1.02 ± 0.02	14	131
415	42.34 ± 0.68	2.84 ± 0.02	1.13 ± 0.03	20	114
475	54.03 ± 0.58	2.82 ± 0.02	1.28 ± 0.01	30	100

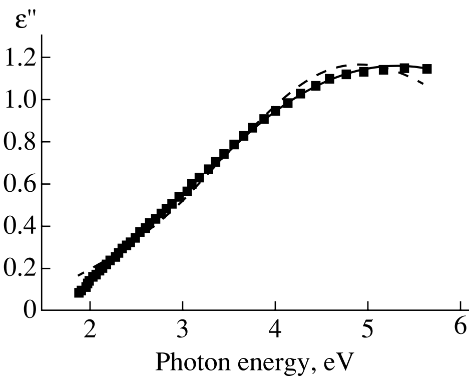

Fig. 5. Final result of a calculation optimization procedure. Points, experiment; solid line, calculation by expression (5) at $E_g \neq 0$; dashed line, calculation at $E_g = 0$.

in this stage. To eliminate this parameter, the experimental data were supplemented using a polynomial extrapolation into the low-energy part of the spectrum. As a first approximation to E_g, the value obtained from the intersection of the curve representing the supplemented dielectric constant with the energy axis was used. A further approximation in solving Eq. (5) was done by successively applying the Newton method to the starting E_G, s, and K values set using Tables 1 and 2. The results of fitting for different groups of materials are presented in Tables 3 and 4. Let us introduce for two stages ($E_g = 0$, $E_g \neq 0$) a fitting criterion χ^2 in the form of a sum of average squared discrepancies between the calculated and experimental data. Let us compare the fitting criteria for $E_g = 0$ and $E_g \neq 0$. As follows from Tables 1–4, the condition $E_g \neq 0$ (Tables 3 and 4) better describes the experimental data. It should be noted, however, that at relatively high annealing temperatures the difference between the solutions obtained in the first and second stages vanishes, which reflects the decrease in the E_g value upon annealing.

Figure 5 presents, as an example, the final result achieved in optimizing the calculation procedure for curve *3* in Fig. 1. It can be seen that the case when the parameter E_g is nonzero gives the best fit to the experimental data.

Thus, the problem of determining a set of unknowns can be solved at the minimum number of fitting parameters with the use of symmetric Gaussians.

5. EFFECT OF THERMAL ANNEALING

Let us apply the developed procedure to study the effect of thermal annealing on the fundamental absorption edge in *a*-C and *a*-C:H.

We characterize the effect of annealing by the values of E_g and E_G and the concentration of electrons involved in optical transitions (an increase in this concentration corresponds to graphitization of the material in annealing). For this purpose, we use the expression for the frequency of plasma oscillations of electrons, ω_p, related to the imaginary part of the dielectric function of the material by

$$(\hbar\omega_p)^2 = \frac{2}{\pi}\int_0^\infty \hbar\omega\varepsilon''(\omega)d\hbar\omega. \qquad (7)$$

The values calculated using (7) are also presented in the tables. It follows from Tables 3 and 4 that, in the case of *a*-C, the plasma frequency depends on the annealing temperature nonmonotonically, in agreement with the data of [3]. It was shown in [3] that for *a*-C films the temperature dependence of the film thickness has the form of a curve peaked at around $T = 360°C$, whereas

Table 3. Parameters of the second stage of fitting and plasma frequencies for *a*-C

T, °C	A, eV^2	E_g, eV	E_G, eV	s, eV	$(\hbar\omega_p)^2$, eV^2	N, 10^{22} cm^{-3}	χ^2, 10^{-5}
200	80.36 ± 5.88	1.35 ± 0.01	4.52 ± 0.13	2.35 ± 0.08	45.2	3.15	18
310	54.69 ± 1.41	1.26 ± 0.01	3.57 ± 0.04	1.89 ± 0.04	30.3	2.1	17
360	52.60 ± 1.06	1.12 ± 0.02	3.36 ± 0.03	1.74 ± 0.03	29.1	2.1	21
415	52.84 ± 0.64	0.27 ± 0.07	3.06 ± 0.02	1.49 ± 0.03	30.5	2.1	23
475	54.75 ± 0.37	0	3.01 ± 0.01	1.56 ± 0.01	34.2	2.4	23

Table 4. Parameters of the second stage of fitting and plasma frequencies for *a*-C : H

T, °C	A, eV^2	E_g, eV	E_G, eV	s, eV	$(\hbar\omega_p)^2$, eV^2	N, 10^{22} cm^{-3}	χ^2, 10^{-5}
200	47.13 ± 2.05	1.77 ± 0.02	3.99 ± 0.06	1.65 ± 0.04	21.8	1.53	3
310	46.08 ± 1.16	1.79 ± 0.01	3.67 ± 0.04	1.73 ± 0.03	22.8	1.6	4
360	42.67 ± 0.60	1.63 ± 0.01	3.28 ± 0.02	1.52 ± 0.02	20.8	1.5	5
415	47.48 ± 0.52	1.26 ± 0.02	3.10 ± 0.02	1.60 ± 0.02	25.4	1.78	9
475	59.43 ± 0.55	0.95 ± 0.03	2.95 ± 0.01	1.65 ± 0.03	34.4	2.41	13

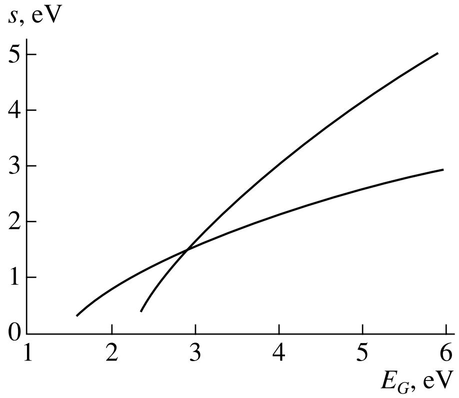

Fig. 6. Set of roots for equations formed with expression (6). The intersection point corresponds to solution s = 1.495 eV, E_G = 2.947 eV.

the thickness of *a*-C:H films steadily decreases with temperature. This nonmonotonic behavior was attributed to relaxation of elastic strains in thermal treatment of *a*-C films. Presumably, the nonmonotonic variation of the film thickness in the course of annealing leads to nonmonotonic changes in its density and, consequently, in plasma frequency. With the temperature increasing further (T > 360°C), the plasma frequency grows steadily with temperature. At the same time, in the case of *a*-C:H films, the plasma frequency remains virtually constant in the temperature range 200–360°C and then grows steadily, also in agreement with [3]. In both cases the energy gap E_g of *a*-C and *a*-C:H decreases steadily. Changes in the parameter E_g reflect the behavior of the critical fluctuation of the sp^2 phase in annealing, and, therefore, a conclusion can be made that the size of the critical fluctuation grows with temperature. The simultaneous increase in the plasma frequency indicates an increase in the total number of fluctuations per unit volume at temperatures exceeding 360°C. It also follows from the presented data that, in the optimal-size fluctuations, the distance between the centers of bands of energy levels is within the range 6–8 eV for samples of both types. The comparatively high transition energies suggest that the energy terms of optimal fragments, formed in part by σ electron states, contribute to the absorption. In the course of annealing, the distance between the centers of the bands composed of levels decreases somewhat.

It should also be noted that, since all structural changes in a film in the course of its annealing are accompanied by loss of hydrogen, the role of the latter in limiting the size of the critical fluctuation both in the formation of the material and in its thermal degradation during annealing should not be underestimated.

6. CONCLUSION

Thus, a model that can account for the experimental dependences of the optical characteristics on the annealing temperature was developed. The fundamental absorption edge is presented analytically in the form of the Tauc model generalized to the case of amorphous carbon and related materials. The spectral dependence of the imaginary part of the dielectric function reflects the existence of a sp^2 phase fragment of critical size, which depends on the hydrogen concentration in a film.

The developed model was used to reconstruct the energy spectrum of electrons. It is shown that the energy spectrum is formed by symmetrically lying bands of levels, which are broadened according to the Gaussian law. This broadening is associated with the inhomogeneous broadening of energy levels, whose number grows with annealing temperature.

APPENDIX

If we substitute in the left-hand side of Eq. (6) two experimental values of the normalized dielectric function, we obtain a system of two equations with two unknowns that has a unique solution. For this purpose, let us choose two points in the normalized dependence $\varepsilon''(\hbar\omega)/\varepsilon(\hbar\omega_m)$ (Fig. 4), one at low (2.59 eV) and the other at high energies (5.64 eV). Using the enumerative technique, we find all roots s, E_G of Eq. (6) for both experimental values.

Figure 6 presents a set of roots for equations formed with the use of expression (6) for an *a*-C film. The solution of the problem corresponds to the intersection of the sets of roots. Thus, it can be seen from Fig. 6 that, in the case in question, a unique solution exists in the energy range 1–6 eV. Apparently, at known $\varepsilon''(\hbar\omega)$, E_G, and s, the A value can be found using (5), which, in the case under consideration, is $A \approx 80$ eV^2.

ACKNOWLEDGMENT

This study was supported by the Russian Foundation for Basic Research (project no. 00-02-17004).

REFERENCES

1. J. Tauc, R. Grigorovici, and A. Vancu, Phys. Status Solidi **15**, 627 (1966).
2. D. Dasgupta, F. Demichelis, C. F. Pirri, and A. Tagliaferro, Phys. Rev. B **43** (3), 2131 (1991).
3. V. I. Ivanov-Omskiĭ, A. V. Tolmachev, and S. G. Yastrebov, Fiz. Tekh. Poluprovodn. (St. Petersburg) **35** (2), 227 (2001) [Semiconductors **35**, 220 (2001)].

Translated by M. Tagirdzhanov

Semiconductors, Vol. 36, No. 1, 2002, pp. 116–120. Translated from Fizika i Tekhnika Poluprovodnikov, Vol. 36, No. 1, 2002, pp. 124–128.

PHYSICS OF SEMICONDUCTOR DEVICES

A Graded-Gap Detector of Ionizing Radiation

J. Požela*, K. Požela, A. Šilėnas, V. Jasutis, L. Dapkus,
A. Kinduris, and V. Jucienė

Institute of Semiconductor Physics, Vilnius, 2600 Lithuania

**e-mail: pozela@uj.pfi.lt*

Submitted May 8, 2001; accepted for publication May 31, 2001

Abstract—The current response of $Al_xGa_{1-x}As$ graded-gap layers to optical and X-ray radiation was studied. A graded-gap electric field in the 15-μm-thick $Al_xGa_{1-x}As$ layers, with x varying from 0 to 0.4, ensures the complete collection of charges generated by ionizing radiation and makes it possible to attain the value of 0.25 A/W for the current–power sensitivity of $Al_xGa_{1-x}As$. In the layers with a lowered doping level of the narrow-gap region of the graded-gap $Al_xGa_{1-x}As$ layer, the voltage–power sensitivity to X-ray radiation with energy lower than 15 keV is as high as 1.6×10^3 V/W in the photovoltaic mode. © *2002 MAIK "Nauka/Interperiodica".*

1. INTRODUCTION

Semiconductor layers whose band gap varies with thickness (the so-called graded-gap structures) can be used as ionizing-radiation detectors with either optical [1, 2] or current [3, 4] responses. In the first case, the detector sensitivity is controlled by the quantum yield of the ionizing-radiation conversion to optical radiation and by the efficiency of extracting the latter radiation through a wide-gap window of the graded-gap crystal in the direction of an external photodetector. Although an optical-response detector has a clear advantage in that it makes it possible to observe the luminescence pattern of ionizing radiation incident on the crystal with high spatial resolution, the external quantum yield of such a detector is low [2].

In the second case, the graded-gap field is used to collect the charge generated by ionizing radiation in the bulk of the graded-gap layer. The difference between the built-in fields for holes and electrons and also between their mobilities makes it possible to separate the charges and observe the graded-gap photovoltage [3, 4]. A fairly high graded-gap field can ensure the highly efficient collection of generated charges in the crystal.

In this paper, we report the results of studying the current response of graded-gap $Al_xGa_{1-x}As$ layers to optical and X-ray radiation. We determined the conditions for the complete collection of nonequilibrium charge carriers generated by ionizing generation using only the graded-gap field, without applying any external voltage. We considered the means for a drastic increase in the voltage–power sensitivity of graded-gap detectors in the case of the $Al_xGa_{1-x}As$-layer doping which is nonuniform over the thickness.

2. THE GRADED-GAP PHOTOVOLTAGE AND CURRENT RESPONSE IN A GRADED-GAP LAYER

When a graded-gap semiconductor is illuminated, photovoltage arises owing to the band-gap gradient; this photovoltage has been experimentally observed [3, 4]. Let us determine the photocurrent and photovoltage in the graded-gap structure represented in Fig. 1a when nonequilibrium electrons Δn and holes Δp are generated by external ionizing radiation. The electron j_n and hole j_p currents in such a structure are given by

$$j_n = \sigma_n\left(\frac{1}{e}\frac{dE_C}{dz} + F_V + F_0\right), \qquad (1)$$

$$j_p = \sigma_p\left(\frac{1}{e}\frac{dE_V}{dz} + F_V + F_0\right), \qquad (2)$$

$$\sigma_n = e\mu_n(n_0 + \Delta n), \quad \sigma_p = e\mu_p(p_0 + \Delta p), \qquad (3)$$

where e is the elementary charge; n_0 and μ_n, and p_0 and μ_p are the equilibrium concentrations and mobilities of electrons and holes; F_V is the electric field caused by the graded-gap photovoltage; F_0 is the field caused by external voltage sources; and E_C and E_V are the energies corresponding to the conduction-band bottom and the valence-band top. The fields of the graded-gap structure for holes $\frac{1}{e}\frac{dE_V}{dz}$ and electrons $\frac{1}{e}\frac{dE_C}{dz}$ are related to the gradient of the band gap E_g by the formula

$$\frac{dE_g}{dz} = \frac{dE_C}{dz} - \frac{dE_V}{dz}. \qquad (4)$$

According to (1), (2), and (4), the current flowing through the graded-gap structure is equal to

$$j = j_n + j_p = \sigma_n \frac{1}{e}\frac{dE_g}{dz} + (\sigma_n + \sigma_p)\frac{1}{e}\frac{dE_V}{dz} + (\sigma_n + \sigma_p)(F_V + F_0). \tag{5}$$

The current response to the generation of nonequilibrium electrons and holes $\Delta n = \Delta p$ is given by

$$j_{\Delta n} = \sigma_{\Delta n}\frac{1}{e}\frac{dE_g}{dz} + (\sigma_{\Delta n} + \sigma_{\Delta p})\left(\frac{1}{e}\frac{dE_V}{dz} + F_0\right) + (\sigma_n + \sigma_p)F_V, \tag{6}$$

where

$$\sigma_{\Delta n} = e\mu_n \Delta n, \quad \sigma_{\Delta p} = e\mu_p \Delta p. \tag{7}$$

In formula (6), it is implied that $\frac{dE_V}{dz}$ is unaffected by the nonequilibrium-carrier generation if the latter is uniform across the layer.

We use the condition $F_0 + F_V = 0$ to determine the short-circuit current as

$$j_{\mathrm{sc}} = \sigma_{\Delta n}\frac{1}{e}\frac{dE_g}{dz} + (\sigma_{\Delta n} + \sigma_{\Delta p})\frac{1}{e}\frac{dE_V}{dz}. \tag{8}$$

For $F_0 = 0$, we use the condition $j_{\Delta n} = 0$ to obtain the following formula for the graded-gap field:

$$F_V = j_{\mathrm{sc}}(\sigma_n + \sigma_p)^{-1}. \tag{9}$$

The graded-gap photovoltage is given by

$$U_V = \int_0^L F_V dz. \tag{10}$$

For a doped p-type semiconductor, we have $\frac{dE_V}{dz} \approx 0$, so that the short-circuit current can be represented as

$$j_{\mathrm{sc}}(p_0) \approx \frac{dE_g}{dz}\mu_n \Delta n. \tag{11}$$

For the graded-gap photovoltage in a p-type semiconductor layer with thickness L in the case of uniform doping over the coordinate z and the photogeneration $\Delta n = \Delta p$, we obtain

$$U_V = \int_0^L F_V dz = \frac{b\Delta n}{(b+1)\Delta n + p_0}\frac{1}{e}\Delta E_g, \tag{12}$$

where $b = \mu_n/\mu_p$ and

$$\Delta E_g = E_g(L) - E(0). \tag{13}$$

The current sensitivity of a graded-gap crystal is identical to that of a conventional homogap photoresistor to which the voltage inducing the field $F_0 = \frac{1}{e}\frac{dE_g}{dz}$ is applied. However, the fact that it is unnecessary to apply an external voltage ensures a drastic decrease in the current-noise level in a graded-gap photoconductor compared to a homogap photoconductor. The high valence-band electrical conductivity of a graded-gap crystal ensures a low level of thermal noise, which offers many points in favor of a graded-gap detector compared to a photodetector based on the *p–i–n* junction.

The current sensitivity of a graded-gap p-$\mathrm{Al}_x\mathrm{Ga}_{1-x}\mathrm{As}$ structure is controlled by the drift velocity of electrons in the graded-gap field of the conduction band. If there is no drift of electrons, the steady-state number of charge-carrier pairs involved in recombination is equal to

$$\Delta n = \frac{d\Delta N}{dt}\tau, \tag{14}$$

where $d\Delta N/dt$ is the number of pairs generated by ionizing radiation per unit time in unit volume, and τ is the recombination time. In the doped $\mathrm{Al}_x\mathrm{Ga}_{1-x}\mathrm{As}$ semiconductor, the recombination time is $\tau \approx 10^{-9}$ s.

If there is drift, a fraction of electrons leaves the layer with thickness L without having a chance to recombine, and this fraction is involved in the photocurrent

$$j = e\Delta n v_{\mathrm{dr}} = e\frac{d\Delta N}{dt}L\frac{\tau}{t_{\mathrm{dr}}}, \tag{15}$$

where t_{dr} is the time it takes for an electron to pass the L-thick layer with the drift velocity v_{dr}. The photoelectric gain

$$K = \tau/t_{\mathrm{dr}} \tag{16}$$

represents what fraction of electron–hole pairs, generated in the layer L, is involved in the photocurrent. For $K = 1$, we have a complete collection of the charge carriers generated in the crystal.

In a uniformly doped graded-gap crystal, the time of transit through the layer L is given by

$$t_{\mathrm{dr}} = \frac{L^2}{\mu\left\{\frac{1}{e}[E_g(L) - E_g(0)] + U_V + U_0\right\}}. \tag{17}$$

For $\mathrm{Al}_x\mathrm{Ga}_{1-x}\mathrm{As}$ with x varying in the range of 0–0.4, the transit time $t_{\mathrm{dr}} \approx L^2/2.2 \times 10^3$ s. For $L = 15$ μm, t_{dr} becomes almost equal to the lifetime $\tau_r = 10^{-9}$ s, so that $K \approx 1$. We can decrease or increase the transit time t_{dr} by applying an external voltage U_0 to the layer.

The number of electron–hole pairs generated in unit time as a result of the absorption of ionizing radi-

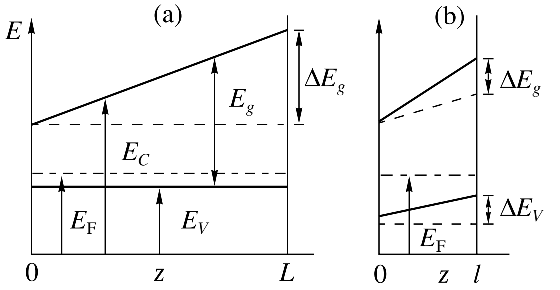

Fig. 1. Schematic representation of variations in the energies of the conduction- (E_C) and valence-band (E_V) edges with depth z in the graded-gap p-$Al_xGa_{1-x}As$ layers for (a) a uniformly doped layer with a thickness L and (b) a nonuniformly doped layer with a thickness l. E_F stands for the Fermi level, and E_g denotes the band gap.

ation with power $W_X(L)$ in a layer with thickness L is equal to

$$\frac{d\Delta NL}{dt} = W_X(L)/E_T, \tag{18}$$

where E_T is the average energy required for the generation of a pair. Substituting (18) into (15), we obtain the following expression for the current–power sensitivity:

$$\beta_j = \frac{j}{W_X(L)} = \frac{eK}{E_T}. \tag{19}$$

For $Al_xGa_{1-x}As$, we obtain $E_T \approx 4$ eV and $\beta_j = 0.25$ A/W if the charge carriers generated within the layer are completely collected ($K = 1$). In the case of $\Delta n = \Delta p \ll p_0$, the voltage–power sensitivity is given by

$$\beta_v = \frac{U_v}{W_X(L)} = \beta_j \frac{L}{\sigma_p}. \tag{20}$$

For $p_0 = 10^{16}$ cm^{-3}, $\mu_p = 400$ cm^2 V^{-1} s^{-1}, and $L = 10^{-3}$ cm, we obtain $\beta_v = 0.4 \times 10^{-3}$ V/W. Such voltage–power sensitivity of a graded-gap layer has been observed experimentally [3, 4].

The low voltage–power sensitivity is caused by the high electrical conductivity of the active layer in a graded-gap structure. A high electrical conductivity results in a fast dielectric relaxation of nonequilibrium charges separated by the graded-gap field. The voltage–power sensitivity can be enhanced by reducing the electrical conductivity of even a fraction of the graded-gap layer.

We now consider a p-type graded-gap layer with nonuniform doping over the layer thickness. Let the doping be such that E_V changes linearly over the layer thickness (Fig. 1b). According to (8) and (9), the graded-gap field in this layer is given by

$$F_v(z) = \left[\sigma_{\Delta n}\frac{1}{e}\frac{dE_g}{dz} + (\sigma_{\Delta n} + \sigma_{\Delta p})\frac{1}{e}\frac{dE_V}{dz}\right] \times [\sigma_n(z) + \sigma_p(z)]^{-1}. \tag{21}$$

For $\sigma_{p0} \gg \sigma_{\Delta n} > \sigma_{\Delta p} > \sigma_{n0}$, we obtain

$$F_v(z) \approx \frac{\Delta n}{p_0(z)}\left\{\frac{b}{e}\frac{dE_g}{dz} + \frac{(b+1)}{e}\frac{dE_V}{dz}\right\}. \tag{22}$$

Correspondingly, the graded-gap photovoltage is equal to

$$U_v = \frac{\Delta n}{p_0(0)}\frac{kT}{e\Delta E_V}[b\Delta E_g + (b+1)\Delta E_V] \times \left[1 - \exp\left(-\frac{\Delta E_V}{kT}\right)\right], \tag{23}$$

where it is assumed that the following relations are valid for the layer with thickness l:

$$\frac{dE_V}{dz} = \frac{\Delta E_V}{l}, \quad \frac{dE_g}{dz} = \frac{\Delta E_g}{l}$$

$$p_0(z) = p_0(0)\exp\left(\frac{\Delta E_V}{l}\frac{z}{kT}\right).$$

It is noteworthy that, in view of $\Delta E_g \neq 0$, the photovoltage across the graded-gap p–p^+ junction exceeds the photovoltage across the homogap p–p^+ junction.

Nonuniform doping gives rise to two important effects. First, the short-circuit current increases owing to the emergence of the field $\frac{1}{e}\frac{dE_g}{dz}$, which is combined with the graded-gap field $\frac{1}{e}\frac{dE_V}{dz}$ and has the same sign as the latter. Second, the graded-gap photovoltage increases drastically owing to the reduction of the majority-carrier concentration in the depletion region $p_0(0)$. For $\Delta E_V = 0.3$ eV, the graded-gap photovoltage in this sensitive layer increases by more than six orders of magnitude compared to that in the heavily doped region of the graded-gap crystal.

It is expedient to form the sensitive layer in the narrow-gap region of the graded-gap crystal. This layer then also serves as a collector for nonequilibrium charge carriers coming from the remaining part of the graded-gap structure with the thickness of $L \approx \tau v_{dr}$.

An increase in resistivity of the high-sensitivity layer is limited by the requirement for the rapid establishment of voltage across this layer. If we stipulate that the relaxation time for voltage should be no longer than the recombination time τ for charge carriers in the structure, the highest resistivity of the depletion layer ρ_m is limited by the inequality

$$\rho_m \leq \frac{\tau}{\varepsilon}, \tag{24}$$

where the dielectric constant of $Al_xGa_{1-x}As$ is equal to $\varepsilon = 9 \times 10^{-13}$ s/(Ω cm). If $\tau = 10^{-9}$ s in $Al_xGa_{1-x}As$, the resistivity is $\rho_m \leq 1.1 \times 10^3$ Ω cm, which corresponds to $p_0 \geq 1.4 \times 10^{13}$ cm^{-3} in the p-type layer.

3. EXPERIMENT

Liquid-phase epitaxy was used to grow 15–50-μm-thick Zn-doped $Al_xGa_{1-x}As$ layers on GaAs substrate. The hole concentration in the layers was about 10^{18} cm^{-3}. The aluminum fraction changed linearly across the layer depth from $x = 0.4$ at the substrate to x = 0 at the outer layer surface. A lightly doped region was formed at the upper ($x = 0$) layer surface. The grown layers were separated from the substrate, and small-area (10^{-2} cm^2) current contacts were deposited on both sides of the layers. The sample area was about 10^{-1} cm^2.

Experimental measurements of the photovoltage spectral dependences in the obtained samples verified the presence of a high-sensitivity region at the narrow-gap surface of the $Al_xGa_{1-x}As$ layer. If the layers are illuminated from the narrow-gap side ($x = 0$), high photovoltages are observed; these photovoltages increase as the carrier-generating light penetrates deeper into the layers (see Fig. 2).

If the layers are illuminated from the wide-gap side, the effects of the transit time and the coefficient K on the photovoltage are observed. For $\lambda = 0.6$ μm, the charge carriers are generated near the wide-gap surface of the layer, and the time of their transit through the entire 15-μm-thick layer is $\tau_{dr} \approx 10^{-9}$ s. As the wavelength increases, the generation region shifts to the wide-gap portion of the crystal according to the linear variation in the band gap; as a result, the transit time decreases. If the wavelength is changed to $\lambda = 0.8$ μm, the transit time decreases by several times, and the current amplification ($K > 1$) is observed. Correspondingly, the graded-gap photovoltage increases by a factor of 4. When the excitation-photon energy is decreased further to $E < E_g$, the electron–hole pairs cease to be generated and the graded-gap photovoltage is no longer observed (see Fig. 2).

In Fig. 3, we show the results of measuring the dependence of the graded-gap photovoltage in the $Al_xGa_{1-x}As$ crystals on the intensity of X-ray radiation emitted at the Cu and Cr anodes. The intensity is assumed to be proportional to the anode current in the source of X-ray radiation.

The integrated power of radiation emitted by the source with a Cu anode and measured at the location of the graded-gap detector is $W_V = 43 \times 10^{-6}$ W/cm² for $I_a = 20$ mA and $U_a = 30$ kV. About 50% of the power incident on the crystal is absorbed in the $Al_xGa_{1-x}As$ layer with a thickness of $L = 15$ μm. Hence, we find that the voltage–power sensitivity of the graded-gap detector is equal to $\beta_V \approx 1.6 \times 10^3$ V/W.

Consequently, the sensitivity of the nonuniformly doped, graded-gap $Al_xGa_{1-x}As$ layer is found to exceed the sensitivity of uniformly doped layers reported previously [3, 4] by five–six orders of magnitude.

Such a high sensitivity verifies the determining role of the depletion layer in the formation of graded-gap photovoltage. Such a high photovoltage is observed only in the structures with a lightly doped surface layer. The photovoltage was lower than 10^{-3} V in the structures that did not contain a depletion layer and incorporated the low-resistivity current contacts.

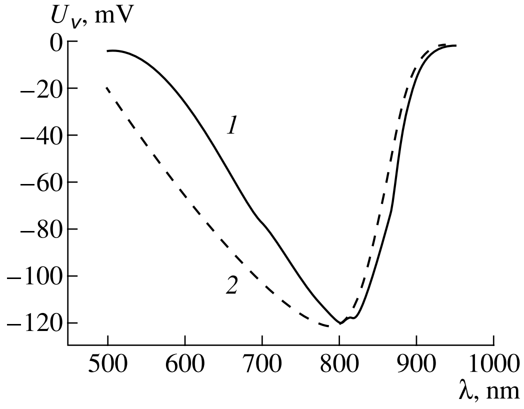

Fig. 2. Dependence of the graded-gap photovoltage U_V on the wavelength of photons in the case of illumination of the graded-gap $Al_xGa_{1-x}As$ crystal from the wide-gap side ($x = 0.4$, curve *1*) and from the narrow-gap side ($x = 0$, curve *2*).

Measurements of the dependence of the graded-gap photovoltage on the structure thickness verified the important role of transit time in the formation of photovoltage. The experimentally observed photovoltage in an $Al_xGa_{1-x}As$ structure with a thickness of $L = 15$ μm (Fig. 3, curve *1*) is higher by a factor of 6 than that in a structure with a thickness of $L = 50$ μm (curve *2*), which corresponds to a variation in the amplification coefficient K for the same $\Delta E_g \approx 0.4$ eV.

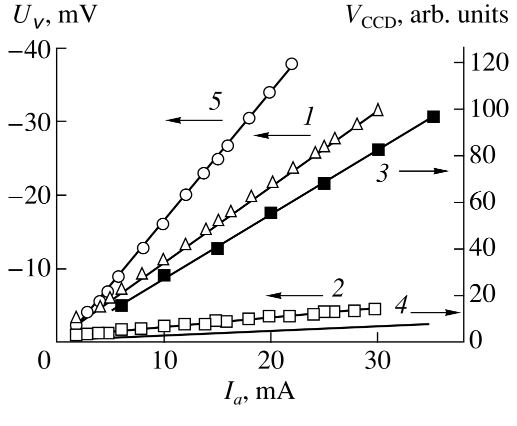

Fig. 3. Dependences of the graded-gap photovoltage U_V (curves *1*, *2*, *5*) and the X-ray-excited luminescence intensity V_{CCD} (curves *3*, *4*) on the X-ray-radiation intensity expressed in terms of the anode current I_a of the X-ray source. The source anode is made of (*1*, *2*) Cr and (*3*–*5*) Cu. The anode voltage is $U_a = 30$ kV. The quantity V_{CCD} corresponds to the output of the luminescence detector based on the charge-coupled devices (CCD) for the exposure time of 0.3 s. The thickness of the samples L was equal to (*1*, *4*, *5*) 15 and (*2*, *3*) 50 μm.

In Fig. 3, we also show the results of measuring the luminescence intensity of the same crystals as a function of the flux of X-ray radiation; a video camera incorporating the charge-coupled devices (CCD) was used in the measurements. An inverse pattern is observed: the intensity of radiative recombination in the sample with $L = 50$ μm (curve *3*) exceeds by a factor of 11 the corresponding intensity in the sample with $L = 15$ μm (curve *4*).

Thus, the experiments lend support to the view that a reduction in the current export of charge carriers in a graded-gap layer enhances the intensity of luminescence in the crystal; in contrast, an increase in the current export quenches the luminescence.

It follows from the above that the graded-gap $Al_xGa_{1-x}As$ structures with current response can be used with good results to detect ionizing radiation with the absorption coefficient $\alpha > L_K^{-1}$, where $L_K \approx 1.5 \times 10^{-3}$ cm is the layer thickness for which $K = 1$. Such a coefficient of absorption in $Al_xGa_{1-x}As$ corresponds to the X-ray photons with energies below 15 keV. In order to detect the radiation that penetrates deep into $Al_xGa_{1-x}As$, one has to use thick graded-gap layers. In these layers, we have $K < 1$, and, thus, it is appropriate to use a graded-gap radiation detector with the luminescence response.

4. CONCLUSION

(i) The graded-gap field in an $Al_xGa_{1-x}As$ layer with a gradient of $x = 0$–0.4 and a thickness of 15 μm ensures the complete collection of the charge generated by ionizing radiation in the layer. The relatively small mean energy required for the formation of an electron–hole pair in $Al_xGa_{1-x}As$ (4 eV) makes it possible to attain a high yield of the nonequilibrium-charge generation when the ionizing radiation is absorbed. Both factors are conducive to obtaining the current–power sensitivity of an $Al_xGa_{1-x}As$ detector at a level of $\beta_j = 0.25$ A/W.

(ii) The voltage–power sensitivity of the detector is directly proportional to the ohmic resistance of the $Al_xGa_{1-x}As$ layer. A layer with increased resistance from the narrow-gap side of the graded-gap structure enhances the sensitivity of the $Al_xGa_{1-x}As$ detector by several orders of magnitude. The experimental voltage–power sensitivity of the 15-μm-thick graded-gap $Al_xGa_{1-x}As$ layer with a lightly doped surface region is higher than $\beta_V \approx 1.6 \times 10^3$ V/W under X-ray irradiation using a Cu anode with $U_a = 30$ kV.

(iii) It is appropriate to use the graded-gap $Al_xGa_{1-x}As$ layers with current response to detect the ionizing radiation with a penetration depth no greater than 15 μm. The fact that there is no need for external current and voltage sources and also the low internal resistance of the layer ensure a reduction of the noise level in the graded-gap detectors compared to conventional photodetectors.

REFERENCES

1. J. Požela, K. Požela, A. Šilėnas, *et al.*, Nucl. Instrum. Methods Phys. Res. A **434**, 169 (1999).
2. J. Požela, K. Požela, A. Šilėnas, *et al.*, Lith. Phys. J. **39**, 139 (1999).
3. A. N. Imenkov, N. Nazarov, B. S. Suleĭmenov, *et al.*, Fiz. Tekh. Poluprovodn. (Leningrad) **12**, 2377 (1978) [Sov. Phys. Semicond. **12**, 1413 (1978)].
4. Zh. I. Alférov, V. M. Andreev, Yu. M. Zadiranov, *et al.*, Pis'ma Zh. Tekh. Fiz. **4**, 369 (1978) [Sov. Tech. Phys. Lett. **4**, 149 (1978)].

Translated by A. Spitsyn

Semiconductors, Vol. 36, No. 1, 2002, pp. 21–25. Translated from Fizika i Tekhnika Poluprovodnikov, Vol. 36, No. 1, 2002, pp. 24–28.
Original Russian Text Copyright © 2002 by Aleksandrov.

ATOMIC STRUCTURE AND NONELECTRONIC PROPERTIES OF SEMICONDUCTORS

Influence of the Screening Effect on Passivation of *p*-Type Silicon by Hydrogen

O. V. Aleksandrov

St. Petersburg State Electrotechnical University, ul. Professora Popova 5, St. Petersburg, 197376 Russia
e-mail: aleks_ov@mailbox.alkor.ru

Submitted January 31, 2001; accepted for publication May 11, 2001

Abstract—Passivation of *p*-Si by hydrogen through its diffusion was simulated by solving diffusion–kinetic equations with allowance made for hydrogen–acceptor-pair formation, internal electric field, and the screening effect. Screening of hydrogen and acceptor ions by free carriers leads to a decrease in the radius of interaction between the ions and to the weakening of the concentration dependence of hydrogen diffusivity in heavily doped Si. At a binding energy of the pairs of 0.70–0.79 eV, calculated and experimental concentration profiles of holes and the hydrogen–acceptor pairs are in agreement over a wide range of boron concentrations, from 4×10^{14} to 1.2×10^{20} cm^{-3}. The radius of the Coulomb interaction of hydrogen and boron ions is 35 Å in lightly doped Si and decreases as the dopant concentration increases. © *2002 MAIK “Nauka/Interperiodica”.*

1. INTRODUCTION

The treatment of single-crystal Si doped with acceptor impurities (B, Al, Ga, In, Tl) in hydrogen-containing plasma, water vapor, or aqueous solutions in the temperature range from 65 to 200°C results in an increase of surface-layer resistivity [1–3]. This effect is found to be related to the passivation of acceptors with hydrogen ions via the formation of neutral hydrogen–acceptor pairs A^-H^+ (A^- is an ionized acceptor) [1, 2] rather than to compensation by hydrogen donors as presumed by Pantelides [4]. The structure and symmetry of the A^-H^+ pairs in the Si lattice was discussed by Pearton *et al.* [2]. They suppose that a hydrogen atom is most probably located near the center of the bond between a host Si atom and an acceptor atom (bond-centered configuration), as well as at the extension of this bond beyond the impurity atom (dopant-antibonding configuration). The width of the passivated region is proportional to the square root of time and decreases as the dopant concentration increases; depth profiles of hydrogen are step-shaped, with the step height equal to the dopant concentration; and hydrogen accumulation near the surface is observed [1, 2].

A series of models is proposed for describing hydrogen diffusion in *p*-Si. These models take into account different charge states of hydrogen atoms with corresponding different diffusion coefficients [5–7], the influence of the internal electric field on diffusion of ionized hydrogen [5–9], the interaction between hydrogen and dopant atoms [6–10], the formation of H_2 molecules [6, 11], and multiple capture of H atoms by acceptors [11]. The step-like shape of the depth profiles of hydrogen is explained by its trapping at acceptors with the formation of immobile complexes [6–11], as well as by the effect of the internal electric field [8]. The accumulation of hydrogen, which is not involved in passivation, in the surface layer is related to its trapping at surface defects produced by treatment in plasma [6, 7], as well as to the repeated capture of hydrogen atoms by acceptors in heavily doped Si [11]. The effect of dopant concentration on the width of the passivated region was studied elsewhere [8, 10, 12]. This effect is explained by the increase in hydrogen diffusivity owing to the influence of the internal electric field in the region where acceptors are compensated by hydrogen donors [8]. However, hydrogen diffusion in *p*-Si was found to result in passivation rather than compensation of acceptors [1, 2]. Moreover, in this case, the plateau in the hydrogen profiles should narrow down as the dopant concentration decreases, which is inconsistent with the experimental data. Kalejs and Rajendran [10] and Herrero *et al.* [12] explained the observed narrowing of the passivated region with increasing dopant concentration by intensification of the formation of (hydrogen ion)–(ionized acceptor) complexes. The width of the passivated region, L, is estimated from the effective diffusion coefficient, $D_{ef} = L^2/t$, where t is the passivation time. According to Kalejs and Rajendran [10], D_{ef} varies inversely with the boron concentration C_B (at 150°C):

$$D_{ef} = \frac{8.5 \times 10^{14} D_H}{C_B}, \qquad (1)$$

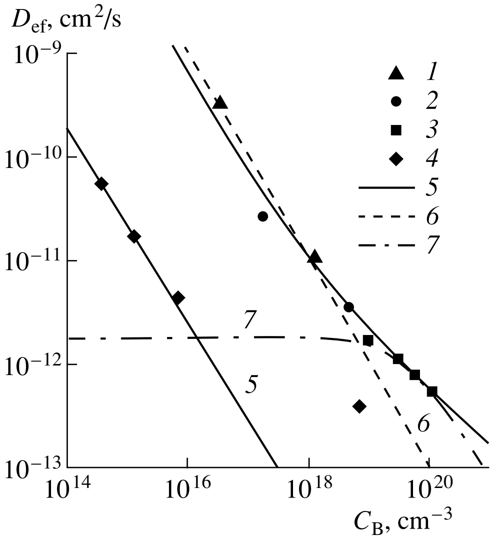

Fig. 1. Dependences of effective hydrogen diffusivity on the boron concentration in Si. Dots represent the published data (*1*) [13], (*2*) [14], (*3*) [12], and (*4*) [18] for $T = (1–3)$ 150 and (*4*) 122°C. Curves represent model calculations for (*5*) $E_B = 0.73$ eV and $T = 150°C$ and $E_B = 0.79$ eV and $T = 122°C$ and calculations by (*6*) formula (1) and (*7*) formula (2).

where D_H is the diffusivity of free hydrogen. Herrero *et al.* [12] reported the following dependence:

$$D_{ef} = \frac{D_H}{1 + rC_B \exp(E_B/kT)}, \tag{2}$$

where E_B is the binding energy of the hydrogen–boron complexes [$E_B = (0.6 \pm 0.1)$ eV], r is an empirical parameter ($r = 7 \times 10^{-5}/5 \times 10^{22}$), k is the Boltzmann constant, and T is the absolute temperature. Figure 1 presents dependences (1) and (2) along with experimental values of L^2/t (at 150°C) reported elsewhere [12–14]. As can be seen from Fig. 1, formula (1) adequately describes the experimental results only at low concentrations, and formula (2), only at high concentrations. It can also be seen that the exponent m in the experimental $D_{ef}(C_B^m)$ dependence varies from $m = -1$ to $m \cong -0.5$ as the dopant concentration increases. In my opinion, this finding points to weakening of the interaction of H^+ ions with A^- acceptors in the heavily doped material, which is attributable to the effect of screening of the ions by free carriers.

This study is devoted to simulation of the passivation of *p*-Si by hydrogen with allowance made for the screening effect.

2. EQUATIONS OF THE MODEL

We presume that hydrogen in *p*-Si can exist in a two charge state: neutral H^0 and positive H^+, which are related to each other by the charge-exchange reaction

$$H^0 + h^+ \underset{k_2}{\overset{k_1}{\rightleftarrows}} H^+, \tag{3}$$

where h^+ denotes a hole. A positively charged hydrogen ion H^+ interacts with a negatively charged acceptor ion A^- to form an immobile donor–acceptor pair H^+A^-:

$$H^+ + A^- \underset{k_4}{\overset{k_3}{\rightleftarrows}} H^+A^-. \tag{4}$$

Diffusion of the neutral and positively charged hydrogen species with the formation of the immobile hydrogen–acceptor pairs is described by the following system of diffusion–kinetic equations:

$$\frac{\partial H^0}{\partial t} + D_H^0 \frac{\partial^2 H^0}{\partial x^2} - k_1 H^0 p + k_2 H^+. \tag{5}$$

$$\begin{aligned} \frac{\partial H^+}{\partial t} &= D_H^+ \frac{\partial^2 H^+}{\partial x^2} + k_1 H^0 p - k_2 H^+ - k_3 H^+ A^- \\ &\quad + k_4 W - D_H^+ \frac{\partial}{\partial x}\left(\frac{H^+}{p}\frac{\partial p}{\partial x}\right), \end{aligned} \tag{6}$$

$$\frac{\partial W}{\partial t} = -\frac{\partial A^-}{\partial t} = k_3 H^+ A^- - k_4 W. \tag{7}$$

Here, D_H^0 and D_H^+ are the diffusivities of free hydrogen in the neutral and ionized states, respectively; k_1 and k_2 are the rate constants of direct and reverse reactions (3), respectively; k_3 and k_4 are the rate constants of direct and reverse reactions (4), respectively; W is the concentration of the pairs; and p is the hole concentration

$$p = \frac{1}{2}[A^- - H^+ + \sqrt{(A^- - H^+)^2 + 4n_i^2}], \tag{8}$$

where n_i is the intrinsic carrier concentration. The last term of Eq. (6) accounts for the effect of the internal electric field on the diffusion of H^+ ions. Combining Eqs. (5)–(7), we obtain

$$\frac{\partial H}{\partial t} = D_H^0 \frac{\partial^2 H^0}{\partial x^2} + \frac{\partial}{\partial x}\left(D_H^+ h_E \frac{\partial H^+}{\partial x}\right), \tag{9}$$

where $H = H^0 + H^+ + W$ is the total hydrogen concentration, and h_E accounts for the effect of the internal electric field on the diffusion of H^+ ions:

$$h_E = 1 - \frac{H^+}{p}\frac{\partial p/\partial x}{\partial H^+/\partial x}. \tag{10}$$

The conditions for local equilibrium in reactions (3) and (4) are

$$H^+ = k_{12} H^0 p, \tag{11}$$

$$W = k_{34} H^+ A^-, \tag{12}$$

respectively. Here, $k_{12} = k_1/k_2$ is the rate constant of reaction (3), and $k_{34} = k_3/k_4$ is the rate constant of reaction (4). If these conditions are satisfied, we can transform Eq. (9) into a diffusion equation with the diffusion coefficient dependent on the component concentrations:

$$\frac{\partial \mathrm{H}}{\partial t} = \frac{\partial}{\partial x}\left(D_{\mathrm{H}}\frac{\partial \mathrm{H}}{\partial x}\right), \tag{13}$$

where

$$D_{\mathrm{H}} = \frac{D_{\mathrm{H}}^0\mathrm{H}^0 + D_{\mathrm{H}}^+ h_E \mathrm{H}^+}{\mathrm{H}} = \frac{D_{\mathrm{H}}^0 + D_{\mathrm{H}}^+ h_E k_{12} p}{1 + k_{12}p + k_{12}k_{34}p\mathrm{A}^-}. \tag{14}$$

The boundary condition for the diffusion problem is the requirement for a constant concentration of neutral hydrogen at the surface (at $x = 0$): $\mathrm{H}^0(0, t) = \mathrm{H}_{\mathrm{s}}^0 = \mathrm{const}$. Then, for the total hydrogen concentration at the surface, we obtain the boundary condition

$$\mathrm{H}_{\mathrm{s}} = \mathrm{H}_{\mathrm{s}}^0[1 + k_{12}p_{\mathrm{s}}(1 + k_{34}\mathrm{A}_{\mathrm{s}}^-)], \tag{15}$$

where p_{s} and $\mathrm{A}_{\mathrm{s}}^-$ are the surface concentrations of holes and free acceptor ions, respectively.

3. PARAMETERS OF THE MODEL

Parameters of the model are D_{H}^0, D_{H}^+, k_{12}, k_{34}, and $\mathrm{H}_{\mathrm{s}}^0$. Since a large body of data show that the diffusivity of hydrogen in intrinsic, i.e., containing no traps, Si [1–3] is high, we use the experimental value of D_{H}^0, which provides the maximum diffusivity obtained by extrapolation to the passivation temperature: $D_{\mathrm{H}}^0 = 9.4 \times 10^{-3}\exp(-0.48/kT)$ [15]. Seager and Anderson [9] demonstrated that, at temperatures of ~300 K, D_{H}^+ was close to the value obtained by the extrapolation [15]. Therefore, we set $D_{\mathrm{H}}^+ = D_{\mathrm{H}}^0$.

The rate constant of charge-exchange reaction (3) is determined by the level produced by H^+ in the band gap: $(k_{12})^{-1} = p_{\mathrm{H}} = N_{\mathrm{v}}\exp[(E_{\mathrm{H}}^+ - E_{\mathrm{V}})/kT]$, where N_{v} is the effective density of states in the valence band, $(E_{\mathrm{H}}^+ - E_{\mathrm{V}})$ is the energy position of the H^+ level in the Si band gap relative to the valence-band top ($E_{\mathrm{H}}^+ = E_{\mathrm{V}} + 0.60$ eV [6, 7]), and p_{H} is the hole concentration when the Fermi level coincides with the E_{H}^+ level. The rate constant of reaction of the hydrogen–acceptor-pair formation (4) $k_{34} = k_3/k_4$, where $k_3 = 4\pi R D_{\mathrm{H}}^+$, $k_4 = \nu\exp[-(E_{\mathrm{B}} + E_{\mathrm{M}})/kT]$, R is the radius of interaction between the H^+ and A^- ions, ν is the frequency of vibrations of the ions within the pair, E_{B} is the binding energy of the ions within the pair, and E_{M} is the activation energy for migration of the H^+ ions. Zundel and Weber [16] determined the vibration frequencies and the activation energy for annealing of the hydrogen–acceptor pairs in Si, $E_{\mathrm{A}} = E_{\mathrm{B}} + E_{\mathrm{M}}$. For example, for the B–H pairs, $\nu = 2.8 \times 10^{14}$ s^{-1}, and $E_{\mathrm{A}} = (1.28 \pm 0.03)$ eV [16], whence it follows that $E_{\mathrm{B}} \cong 0.8$ eV at $E_{\mathrm{M}} = 0.48$ eV.

Choosing the surface concentration of neutral hydrogen $\mathrm{H}_{\mathrm{s}}^0$, we started from the assumption that the passivation of *p*-Si resulted from the formation of the $\mathrm{H}^+\mathrm{A}^-$ pairs rather than from the compensation by hydrogen donors. More precisely, the concentration $\mathrm{H}_{\mathrm{s}}^+$ cannot exceed the acceptor concentration in Si, C_{A}. The condition $\mathrm{H}_{\mathrm{s}}^+ < C_{\mathrm{A}}$ is satisfied at $\mathrm{H}_{\mathrm{s}}^0 < p_{\mathrm{H}}$, where $p_{\mathrm{H}} \cong 3 \times 10^{11}$–$1 \times 10^{12}$ cm^{-3} for $E_{\mathrm{H}}^+ = E_{\mathrm{V}} + 0.60$ eV and at the passivation temperature $T = 122$–150°C.

There is a wide scatter in values of R predicted by different models: from 0.5 Å [10] to 50–100 Å [9]. We can estimate the interaction radius based on the condition that the energy of the interaction between the ions is equal to the thermal energy kT. For the Coulomb interaction between the H^+ and A^- ions in the Si lattice, we obtain $R \cong 35$ Å at $T = 122$–150°C. For high doping levels, the interaction radius apparently cannot be greater than the Debye length. In this context, we assume that, with allowance made for the screening effect, the effective radius of the interaction between the H^+ and A^- ions is described by the relation

$$R_L = \frac{RL_{\mathrm{D}}}{R + L_{\mathrm{D}}}, \tag{16}$$

where $L_{\mathrm{D}} = \sqrt{\frac{\varepsilon\varepsilon_0 kT}{q^2 C_{\mathrm{A}}}}$ is the Debye length, ε is the relative permittivity of Si, ε_0 is the permittivity of free space, and q is the elementary charge. At low acceptor concentrations ($C_{\mathrm{A}} < 2 \times 10^{16}$ cm^{-3}), we have $L_{\mathrm{D}} > 10R$, and $R_L \cong R$. At high acceptor concentrations ($C_{\mathrm{A}} > 2 \times 10^{20}$ cm^{-3}), $L_{\mathrm{D}} < 0.1R$ and $R_L \cong R_{\mathrm{D}}$.

For the used values of the parameters, characteristic lifetimes of the H^+ ions in the free and bound states ($1/(k_3\mathrm{A}^-)$ and $1/k_4$, respectively), as well as the times of the charge exchange in reaction (3), are much shorter than the used passivation times. In this case, because of a fast exchange of particles between the states [17], conditions for local equilibrium (11) and (12) are actually met, the surface concentration H_{s} is independent of time, and the diffusion coefficient D_{H} is a function of the total hydrogen concentration.

4. RESULTS OF CALCULATIONS AND DISCUSSION

Diffusion Eq. (13) with diffusion coefficient (14) and the boundary condition at the surface (15) was

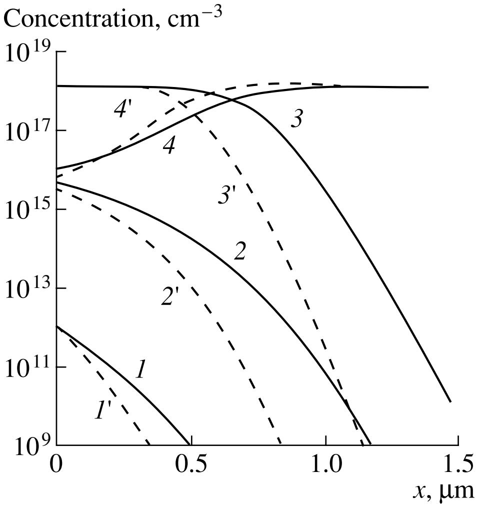

Fig. 2. Depth profiles of the components in boron-doped silicon ($C_B = 1.3 \times 10^{18}$ cm^{-3}): (*1*, *1*') H^0, (*2*, *2*') H^+, (*3*, *3*') *W*, and (*4*, *4*') B^-. The profiles were calculated (*1*–*4*) with and (*1*'–*4*') without regarding the screening effect for $H^0_s = 1 \times 10^{12}$ cm^{-3} and $E_B = 0.73$ eV ($T = 150$°C, $t = 10$ min).

solved numerically by the finite-difference method using the implicit difference scheme. The concentrations of the diffusion components were determined from the total hydrogen concentration by the iteration method, using the conditions for local equilibrium (11) and (12) and the condition for constant local concentration of the acceptor impurity.

Figure 2 shows depth dependences of the component concentrations H^0, H^+, *W*, and A^- in silicon containing uniformly distributed boron with a concentration of $C_B = 1.3 \times 10^{18}$ cm^{-3}. At the obtained values of the parameters, $W > H^+ > H^0$ at all depths. Near the surface, the concentration of the complexes is close to the acceptor concentration, $W \cong C_A$, which results in a corresponding decrease in the concentrations of free acceptor ions and holes and, consequently, in passivation of the surface layer of silicon. The width of the passivated region is larger if the screening effect is taken into account (compare curves *1*–*4* and *1*'–4'). Figure 3 presents calculated profiles of the hydrogen-acceptor pairs in silicon heavily doped with boron (1×10^{19}–1.2×10^{20} cm^{-3}) and corresponding experimental profiles obtained by Herrero *et al.* [12] from infrared-reflectance spectra for a passivation temperature of 150°C. As can be seen from Fig. 3, the calculated profiles are in reasonable agreement with the experimental data at $H^0_s = 1 \times 10^{12}$ cm^{-3} and $E_B = 0.73$ eV. Figure 4 shows calculated profiles of holes in silicon doped to lower boron concentrations (from 4×10^{14}–7.5×10^{18} cm^{-3}) and corresponding experimental profiles obtained by Pankove [18] by the spreading-resistance method for a passivation temperature of 122°C. The experimental profiles fit the calculated ones reasonably well at $H^0_s = 1 \times 10^9$ to 2×10^{10} cm^{-3} and $E_B \cong 0.79$ and 0.70 eV for low (4×10^{14} to 7.4×10^{15} cm^{-3}) and high (5×10^{18} cm^{-3}) concentrations, respectively. Calculated dependences of $D_{ef} = L^2/t$ on the dopant concentration for $T = 150$ and

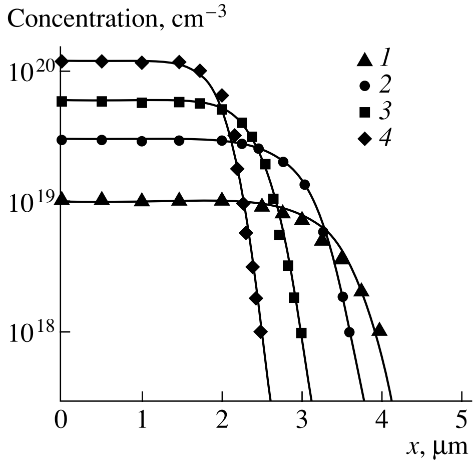

Fig. 3. Depth profiles of the pairs in passivated Si doped with boron to concentration C_B = (*1*) 10^{19}, (*2*) 3×10^{19}, (*3*) 6×10^{19}, and (*4*) 1.2×10^{20} cm^{-3}. Dots correspond to experimental data [12]. The solid lines represent model calculations for $H^0_s = 1 \times 10^{12}$ cm^{-3} and $E_B \cong 0.74$ eV ($T = 150$°C, $t = 20$ h).

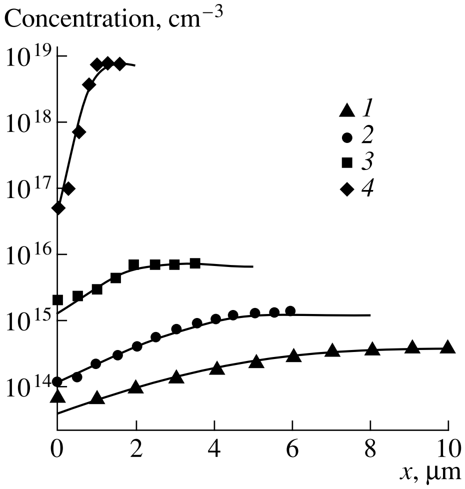

Fig. 4. Depth profiles of holes in passivated Si doped with boron to concentration C_B = (*1*) 4×10^{14}, (*2*) 1.3×10^{15}, (*3*) 7.4×10^{15}, and (*4*) 5×10^{18} cm^{-3}. Dots correspond to experimental data [18]. The solid lines represent the model calculations for H^0_s = (*1*, *4*) 2×10^{10}, (*2*) 1.3×10^{10}, and (*3*) 10^9 cm^{-3}; E_B = (*1*–*3*) 0.79 and (*4*) 0.70 eV; $T = 122$°C; and t = (*1*–*3*) 1 and (*4*) 4 h.

122°C are shown in Fig. 1 (solid curves). The depth at which the concentration of the pairs or holes is half the dopant concentration is taken as the width of the passivated region L. As can be seen from Fig. 1, the dependences calculated in the context of the model with allowance made for the screening effect allow us to adequately describe the dependence of D_{ef} on the dopant concentration both at low and high acceptor concentrations. With the used values of the parameters appearing in formula (14), $k_{12}p \gg 1$ and $k_{34}A \gg 1$ in the entire range of the dopant concentration; therefore, $D_H \cong \frac{D_H^0 h_E}{k_{34}A^-}$. At low acceptor concentrations ($C_A < 2 \times 10^{16}$ cm^{-3}), k_{34} is independent of the concentration, and $D_H \sim 1/C_A$ at $A^- \cong C_A$ at the diffusion front. At high acceptor concentrations ($C_A > 2 \times 10^{20}$ cm^{-3}), $k_{34} \sim 1/\sqrt{C_A}$, and we have $D_H \sim \sqrt{C_A}$ at $A^- \cong C_A$ at the diffusion front.

The binding energy obtained for lightly doped Si, $E_B \cong 0.79$ eV, agrees with the experimental data [16], whereas the value obtained for heavily doped Si, $E_B =$ 0.70–0.73 eV, is slightly lower. This result is attributable to the influence of the screening not only on the interaction radius but also on the binding energy. It should be noted that the theoretical value of the binding (dissociation) energy of the B^-H^+ pair in the bond-centered configuration is 0.70 eV [19], which is fairly close to the value obtained in this study. The surface concentration of neutral hydrogen ($H_s^0 < p_H$) is apparently determined by the particular experimental conditions for hydrogenation. The value $R = 35$ Å corresponds to the interaction radius in the case of a pure Coulomb interaction between the H^+ and A^- ions in the Si lattice. This value lies between 0.5 Å [10] and 50–100 Å [9] and approaches the values of 30 and 40 Å, determined by Mathiot [6] and Zundel and Weber [16], respectively.

It should be noted that the above-listed models [2, 9–11] ignore the decomposition of the hydrogen–acceptor pairs, whereas the present model implies that the formation of the pairs is a reversible process because of their short lifetime ($1/k_4 < 100$ s) at passivation temperatures. The decrease in the effective interaction radius owing to the screening effect [see (16)] allows us to describe the passivation of *p*-Si over a wide range of dopant concentrations without considering the formation of H_2 molecules and the multiple capture of H atoms by acceptors [6, 11].

5. CONCLUSION

Hydrogen passivation of *p*-Si with various dopant concentrations was simulated by solving the diffusion–kinetic equations for free hydrogen in the neutral and positive charge states. The formation of the hydrogen–acceptor pairs, the internal electric field, and the screening effect were taken into account. Quantitative agreement between the calculated and experimental profiles over a wide rage of boron concentrations (from 4×10^{14} to 1.2×10^{20} cm^{-3}) was obtained using the data on hydrogen diffusivity in intrinsic silicon [15], the donor level $E_H^+ = E_V + 0.60$ eV [6, 7], the surface concentration of neutral hydrogen $H_s^0 < p_H$, and the binding energy of the pairs $E_B = 0.70$–0.79 eV that was close to the data reported by Zundel and Weber [16]. The radius of the interaction between hydrogen and acceptor ions in the Si lattice is governed by the Coulomb interaction ($R = 35$ Å for lightly doped Si). As the dopant concentration increases, the interaction radius decreases according to formula (16), owing to the screening of the ions by free carriers.

REFERENCES

1. N. M. Johnson, C. Doland, F. Ponce, *et al.*, Physica B (Amsterdam) **170**, 3 (1991).
2. S. J. Pearton, J. W. Corbett, and M. Stavola, *Hydrogen in Crystalline Semiconductors* (Springer-Verlag, Berlin, 1992), Chaps. 2, 4, 9.
3. Y. Ohmura, K. Abe, M. Ohtaka, *et al.*, Mater. Sci. Forum **258-263**, 185 (1997).
4. S. T. Pantelides, Appl. Phys. Lett. **50**, 995 (1987).
5. M. Capizzi and A. Mittiga, Appl. Phys. Lett. **50**, 918 (1987).
6. D. Mathiot, Phys. Rev. B **40**, 5867 (1989).
7. R. Rizk, P. de Mierry, D. Ballutaud, *et al.*, Phys. Rev. B **44**, 6141 (1991).
8. E. D. Gornushkina and R. Sh. Malkovich, Élektron. Tekh., Ser. 6, No. 7, 73 (1991).
9. C. H. Seager and R. A. Anderson, Appl. Phys. Lett. **53**, 1181 (1988).
10. J. P. Kalejs and S. Rajendran, Appl. Phys. Lett. **55**, 2763 (1989).
11. J. T. Borenstein, J. W. Corbett, and S. J. Pearton, J. Appl. Phys. **73**, 2751 (1993).
12. C. P. Herrero, M. Stutzmann, A. Breitschwerdt, and P. V. Santos, Phys. Rev. B **41**, 1054 (1990).
13. B. Y. Tong, X. W. Wu, C. R. Yang, and S. K. Wong, Can. J. Phys. **67**, 379 (1989).
14. N. M. Johnson and M. D. Moyer, Appl. Phys. Lett. **46**, 787 (1985).
15. A. van Wieringen and N. Warmoltz, Physica (Amsterdam) **22**, 849 (1956).
16. T. Zundel and J. Weber, Phys. Rev. B **39**, 13549 (1989).
17. R. Sh. Malkovich, in *Mathematical Foundations of Diffusion in Semiconductors* (Nauka, St. Petersburg, 1999), Chap. 4, p. 154.
18. J. I. Pankove, R. O. Wance, and J. E. Berkeyheiser, Appl. Phys. Lett. **45**, 1100 (1984).
19. C. G. Van de Walle, Phys. Rev. B **49**, 4579 (1994).

Translated by N. Izyumskaya

Semiconductors, Vol. 36, No. 1, 2002, pp. 26–33. Translated from Fizika i Tekhnika Poluprovodnikov, Vol. 36, No. 1, 2002, pp. 29–36.
Original Russian Text Copyright © 2002 by Bogoboyashchiĭ.

ELECTRONIC AND OPTICAL PROPERTIES OF SEMICONDUCTORS

Special Features of Hopping Conduction in p-$Hg_{0.78}Cd_{0.22}Te$ Crystals under Conditions of Dual Doping

V. V. Bogoboyashchiĭ
Kremenchug State Polytechnical University, Kremenchug, 39614 Ukraine

Submitted February 20, 2001; accepted for publication April 3, 2001

Abstract—At T = 4.2–125 K, the electrical conductivity and Hall effect were studied in p-$Hg_{0.78}Cd_{0.22}Te$ crystals that contained 3×10^{16} cm^{-3} Cu atoms and 1.83×10^{16} cm^{-3} of Hg vacancies (either simultaneously or independently of each other). In such crystals, the ε_1 conductivity over the valence band is dominant at temperatures above 10–12 K, whereas the hopping conduction is prevalent at temperatures below 8–10 K. In the samples containing copper atoms and mercury vacancies simultaneously, conductivity with variable-range hopping is observed. It is found that the ε_1 conductivity of the copper-doped crystals is independent of the presence of mercury vacancies, whereas the hopping conductivity increases appreciably if these vacancies are introduced into the undoped crystal. This phenomenon is attributed to attachment of holes to the neutral mercury vacancies. The energy of this attachment is calculated, and it is found that this energy is equal to 3.7 meV for the ground state. The fluctuation-related broadening of the impurity band in the solid solutions gives rise to the overlap of the impurity bands formed by the copper acceptor levels and by the levels of holes attached to vacancies. *© 2002 MAIK “Nauka/Interperiodica”.*

1. INTRODUCTION

An impurity band in a semiconductor crystal is typically considered as the band of allowed levels in the band gap which correspond to the lowest energy for detachment of electrons (holes) that are trapped by the impurity-atom electrostatic field and neutralize the impurity-atom charge. The position of this band, the structure of the corresponding density of states, and the parameters of the states have been adequately studied, both experimentally and theoretically (see, for example, [1]).

Less commonly, another impurity-level band, i.e., an analogue of the upper Hubbard band in ordered systems [2], is included in the impurity band. This additional band emerges if a semiconductor incorporates neutral donors or acceptors (i.e., at fairly low temperatures and under conditions of slight or partial compensation) due to their ability to accept an additional charge carrier. A donor accepts an excess electron and becomes negatively charged (the D^- state), whereas an acceptor acquires an excess hole and becomes positively charged (the A^+ state).

Specificity of filling the upper Hubbard impurity band consists in the fact that only the D^- levels located below the Fermi level F or the A^+ levels lying above the Fermi level can be occupied at $T = 0$. On the other hand, being located (theoretically) within the band gap, these impurity levels are almost adjacent to the corresponding intrinsic band of allowed energies. In particular, for an isolated hydrogen-like donor (acceptor), the attachment energy amounts merely to ~10% of the corresponding ionization energy [3, 4]. Accordingly, the relative positions of the Fermi level and the D^- or A^+ levels is typically quite reversed. Because of this, the upper Hubbard impurity band rarely manifests itself in physical phenomena observed in lightly doped crystals [1]; correspondingly, there are scarcely any direct experimental data on the parameters of the states in this band.

Experimentally, the existence of the D^- band (or the A^+ band) can be indirectly verified by studying the properties of heavily doped semiconductors. In particular, the metal–insulator transition in doped, lightly compensated semiconductor crystals (the Mott transition) is typically related to overlap of the upper and lower Hubbard impurity bands [2]. In addition, the origin of the ε_2 conduction observed in the above crystals in the vicinity of the Mott transition is generally attributed to activation of the charge carriers from the lower Hubbard band to the corresponding upper band [1, 2]. However, the validity of this hypothesis has been questioned [1].

In this context, the issue concerning the localization of states in the D^- and A^+ bands is of interest. As a rule, it is assumed that these states have a fairly large radius, because the attachment energy is low, and that, as a result of their overlap, a wide band is bound to be formed even in the case of moderate-level doping [1, 2]. In contrast, it has been assumed recently [4, 5] that the charge carriers bound by an isolated donor or acceptor are identical; therefore, the binding energy is assumed to be distributed uniformly between these charge carriers. In this situation, the radius of a state in the upper Hubbard band must exceed only slightly the neutral-center radius, whereas the attached charge carriers must be localized if the doping level is moderate.

Experimentally, the D^- (or A^+) states can be detected and identified at low dopant concentrations owing to specificity of occupation of these states at $T = 0$. In this context, it seems pertinent to study narrow-gap p-$Hg_{1-x}Cd_xTe$ crystals [4]. On the one hand, conduction over the impurity band of this semiconductor is comparatively easy to observe, because this conduction dominates over the ε_1 conduction in the valence band at comparatively high temperatures [6]. On the other hand, in this case there are two types of shallow-level acceptors with appreciably different ionization energies. The simple impurity acceptors (for example, copper atoms at the cationic lattice site Cu_{Hg}) have a low binding energy (about 7.5 meV [7]), whereas the energy of detachment of a hole from a neutral mercury vacancy V_{Hg} (the doubly charged acceptor) exceeds 15 meV [8]. The defects of both types can be easily introduced into $Hg_{1-x}Cd_xTe$ crystals using annealing and diffusion-induced doping [4]. By varying the concentrations of Cu_{Hg} and V_{Hg}, one can change the relative position of the Fermi level and the A^+ V_{Hg}-type levels, which may be conducive to detection of these levels in the electron-transport phenomena at low temperatures. In what follows, we report the results of such an experiment.

2. EXPERIMENTAL

In our studies, we used homogeneous and structurally perfect single-crystal undoped $Hg_{1-x}Cd_xTe$ (x = 0.218–0.222) wafers, 0.12-cm thick. The wafers were cut from ingots grown by vertical planar crystallization with a solid-phase feeding and were annealed in saturated Hg vapors in order to eliminate the Hg vacancies. After this annealing, the extrinsic electron concentration in the crystals was about 3×10^{14} cm^{-3}, with the mobility being higher than 2×10^5 cm^2 V^{-1} s^{-1} and the lifetime longer than 2×10^{-6} s at 77 K. The dislocation density in the annealed wafers was no higher than 3×10^5 cm^{-2}. There were no inclusions or dislocation rosettes.

The reference samples were cut from the wafers; a thin Cu layer (~3×10^{15} at/cm^3) was deposited in vacuum onto the remaining part of the wafers. Copper was fired in the crystals for 3 days at 200°C in an atmosphere of saturated mercury vapors until its complete dissolution. According to the previous data [9], the above heat treatment ensured a fairly uniform distribution of copper across the wafer section.

After introduction of copper, the wafers were cut into samples about 1.2×0.3 cm^2 in area and 0.1 cm thick. The samples were polished in a Br_2 solution in HBr in order to remove the damaged layer, and the Hall coefficient (R_H) of each of the samples was measured at 77 K in a magnetic field of $B = 2$ T, in which case Cu atoms were completely ionized and R_H was almost independent of B [10]. We used the value of R_H to determine the concentration of free holes p_{77}, which we identified with the electrically active copper concentration.

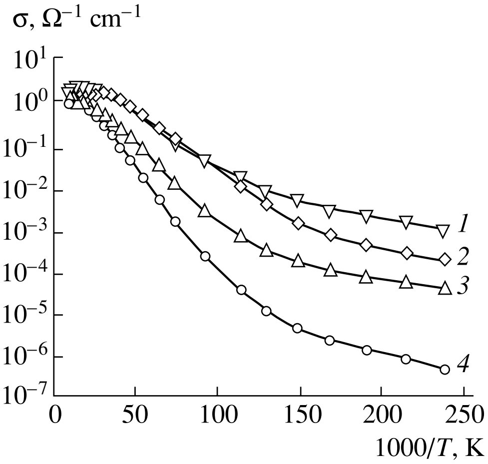

Fig. 1. Temperature dependences of electrical conductivity in the p-$Hg_{0.78}Cd_{0.22}Te$ crystals. (*1, 2*) The crystals doped with Cu and annealed in Hg vapors at T = (*1*) 420 and (*2*) 280°C; $[Cu_{Hg}] = 3.1 \times 10^{16}$ cm^{-3}; and concentration of vacancies $[V_{Hg}]$ = (*1*) 1.8×10^{16} and (*2*) $< 10^{14}$ cm^{-3}. (*3*) Undoped crystals annealed in Hg vapors at 420°C ($[Cu_{Hg}] \ll 10^{15}$ cm^{-3} and $[V_{Hg}] = 1.8 \times 10^{16}$ cm^{-3}). (*4*) Undoped crystals annealed in Te vapors at 240°C ($[Cu_{Hg}] \ll 10^{15}$ cm^{-3} and $[V_{Hg}] = 1.8 \times 10^{16}$ cm^{-3}).

The doped samples were divided into two groups. The samples of the first group were brought into the two-phase equilibrium state by annealing either in mercury vapors at 420°C or in tellurium vapors at 240°C in order to generate a certain number of V_{Hg} vacancies in the bulk of the samples. The duration of annealing was chosen according to the requirement that the entire sample bulk would be in complete equilibrium with the vapor phase by the end of annealing [11]. The reference (undoped) $Hg_{0.78}Cd_{0.22}Te$ samples cut from the same starting wafers were annealed together with the doped samples.

The concentration of the active Hg vacancies in undoped reference samples was determined after the above heat treatment from the value of p_{77} measured using the Hall effect method. The concentration of the V_{Hg} vacancies in the doped samples was identified with that in undoped reference samples. According to the measurements, all the crystals contained about 1.8×10^{16} cm^{-3} of active Hg vacancies.

The samples of the second group were not subjected to additional annealing; thus, they were nearly stoichiometric and did not contain the V_{Hg} vacancies.

We then measured the temperature dependences of the Hall coefficient (in a field of $B = 0.03$ T) and the electrical conductivity of the samples in the temperature range of 4.2–125 K. The results of measuring the dependences of electrical conductivity σ on $1/T$ in the

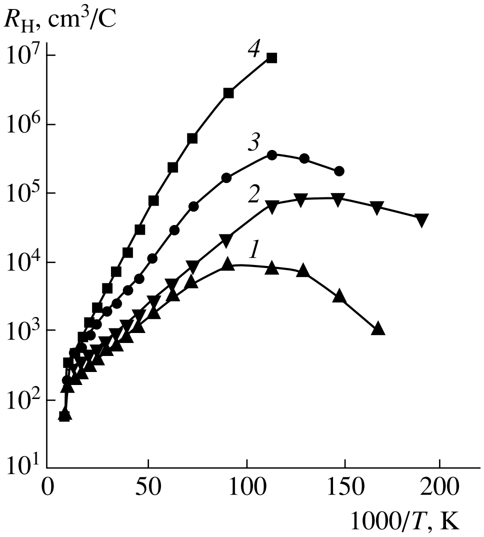

Fig. 2. Temperature dependences of the Hall coefficient for p-$Hg_{0.78}Cd_{0.22}Te$ crystals in a weak magnetic field (the numbers at the curves correspond to those in Fig. 1).

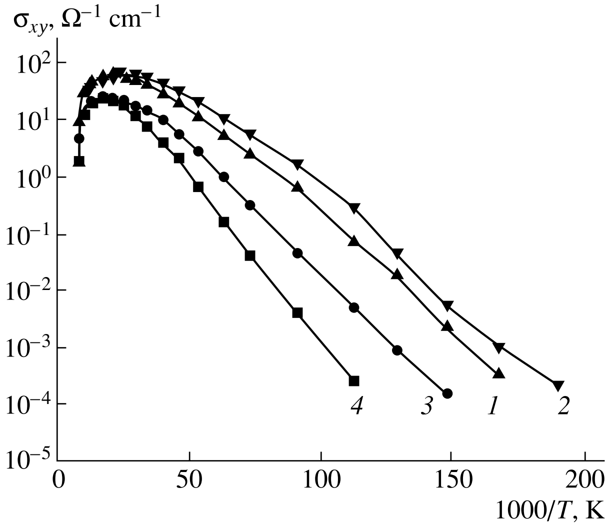

Fig. 3. Temperature dependences of the component σ_{xy} of the electrical-conductivity tensor for p-$Hg_{0.78}Cd_{0.22}Te$ crystals in a magnetic field of $B = 0.03$ T (the numbers at the curves correspond to those in Fig. 1).

region of freezing out of extrinsic conductivity are shown in Fig. 1 for a number of the samples under investigation. The results obtained for the remaining crystals are similar.

The ε_1 conductivity caused by free holes in the valence band is dominant in all crystals at temperatures higher than 10–15 K. The ε_1 conductivity competes with hopping conductivity at intermediate temperatures (in the ranges of 5.5–8.5 K for Cu-doped stoichiometric samples and 7–12 K for the samples containing Hg vacancies). The hopping mechanism of the charge transport with low activation energy is prevalent at the lowest temperatures.

In doped crystals, the value of the ε_1 conductivity in the freezing-out region is nearly independent of the presence of Hg vacancies and of the conditions of their introduction into the crystal. At the same time, this conductivity far exceeds the conductivity of undoped crystals with the same concentration of V_{Hg} vacancies. In contrast to this, in the region of hopping charge transport, the conductivity of the samples that are doped with copper and simultaneously contain Hg vacancies far exceeds the conductivity of the samples containing only one type of these two acceptors.

In the temperature range where ε_1 conductivity is prevalent, the Hall coefficient R_H is positive and increases as the temperature T is lowered (Fig. 2). In the region of transition to hopping conductivity, R_H remains positive but decreases with decreasing T. The maximum of R_H corresponds to the temperature at which the contributions of the hopping and valence-band mechanisms are almost identical. At the lowest temperatures, in which case ε_1 conductivity is frozen out completely, the Hall effect voltage cannot be measured, which indicates that the mobility of the charge carriers in the acceptor band is extremely low.

Evidently, such behavior of the Hall effect is caused by the change in the prevalent charge-transport mechanism as the temperature is lowered [1]. Under these conditions (i.e., when several types of the charge carriers are present), it is more convenient to use the nondiagonal components σ_{xy} of the conductivity tensor, rather than the coefficient R_H, in the analysis of experimental data. As is well known, in contrast to R_H, the tensor σ_{ik} is an additive quantity and is formed as a result of summing the contributions made by the charge carriers of all types.

It is sufficient to take into account only the light and heavy holes in the valence band and the charge carriers in the impurity band in the σ_{ik} tensor of the p-$Hg_{0.78}Cd_{0.22}Te$ crystals at low temperatures. Since the field was weak ($B = 0.03$ T) in our experiments, a strong inequality $(\mu B)^2 \ll 1$ was valid for all the above charge carriers. Therefore, we calculated the components of the tensor σ_{ik} using the formulas

$$\sigma_{xx} = \sigma, \quad \sigma_{xy} = R_H\sigma^2 B, \qquad (1)$$

where σ is the electrical conductivity of the sample for $B = 0$.

The results of calculating the quantity σ_{xy} are shown in Fig. 3. It can be seen that the portion of the dependence $\sigma_{xy}(T)$ with low activation energy, which corresponds to hopping conductivity, is not observed in all cases. In other words, the hopping mechanism in p-$Hg_{0.78}Cd_{0.22}Te$ hardly gives rise to the Hall voltage, which is quite consistent with theoretical predictions [2]. This makes it possible to calculate the contribution σ_1 of the valence-band conductivity in the region of the mixed charge-transport mechanism using the equality $\sigma_{xy}/\sigma = \mu_H B$, which is valid under the condition $(\mu_H B)^2 \ll 1$, where $\mu_H = R_H\sigma$. When calculating the quantity ε_1, we took into account that $\mu_H \propto T^{3/2}$ at temperatures below 12 K, because, in this case, free holes are scattered predominantly by impurity ions, whereas the ε_1 conductivity is almost completely frozen out; therefore, the number of scattering centers is temperature-independent [7].

Subtracting the value of σ_1 (calculated for a given temperature using the above-described method) from the electrical conductivity σ, we obtain the contribution σ_h of the hopping conductivity. In Fig. 4, we show the thus obtained curves that represent the dependences $\sigma_h(T)$ for the samples containing both Cu_{Hg} and V_{Hg} defects. It can be seen that, in this case, the hopping-conductivity variation with temperature obeys the Mott law [12] at $T < 10$ K; i.e., we have $\sigma_h = \sigma_0\exp[-(T_0/T)^{1/4}]$. The parameter T_0 varies from sample to sample in a very narrow range: $T_0 = (1.1 \pm 0.2) \times 10^5$ K.

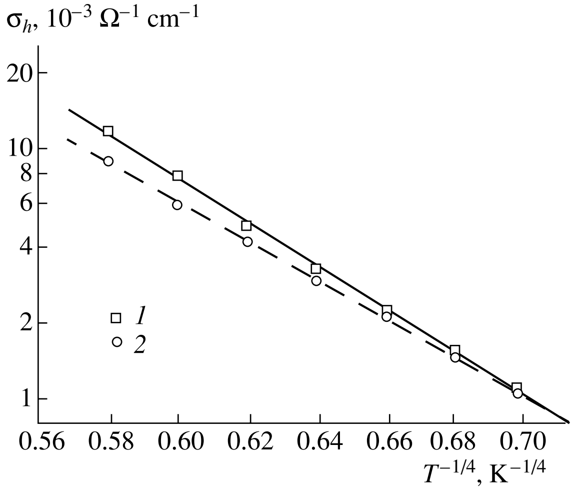

Fig. 4. Temperature dependences of hopping conductivity σ_h in p-$Hg_{0.78}Cd_{0.22}Te$ crystals (*1*) doped with Cu and annealed in Hg vapors at 420°C ($[Cu_{Hg}] = 3.1 \times 10^{16}$ cm^{-3} and $[V_{Hg}] = 1.8 \times 10^{16}$ cm^{-3}) and (*2*) doped with Cu and annealed in Te vapors at 240°C ($[Cu_{Hg}] = 3.1 \times 10^{16}$ cm^{-3} and $[V_{Hg}] = 1.8 \times 10^{16}$ cm^{-3}).

3. MODEL

According to [1, 2], the behavior of conductivity via the acceptor band of a p-type semiconductor is controlled to a great extent by the structure of the density of states in this band. If there are only simple shallow-level acceptors in the crystal, the impurity band consists of two narrow peaks (the lower and upper Hubbard bands) under the conditions of light doping. At $T = 0$, the lower Hubbard band is separated from the valence band by the neutral-acceptor ionization energy, whereas the A^+ band is spaced from this band by the attachment energy of an excess hole.

The ionization energy E_{A1} of a simple shallow-level acceptor in a diamond-like semiconductor has been calculated [13] by numerical simulation performed in terms of the effective-mass method. In the limit of $m_{lh}/m_{hh} \longrightarrow 0$, where m_{lh} and m_{hh} are the masses of the light and heavy holes, we obtain

$$E_{A1} = \frac{4}{9}\frac{m_{hh}e^4}{2\varepsilon_0^2\hbar^2}. \tag{2}$$

According to [14], the same relation is yielded by the variational method under the condition of $m_{lh}/m_{hh} \longrightarrow 0$. In particular, we obtained $E_{A1} \approx 7.9$ meV for the Cu acceptor in $Hg_{0.78}Cd_{0.22}Te$, in which case $m_{lh}/m_{hh} \approx 10^{-2}$, $m_{hh} \approx 0.4m_0$ [10], and $\varepsilon_0 = 17.4$ [15]; this value of E_{A1} is in good agreement with experimental data [7].

The energy of attachment of a hole to a simple shallow-level acceptor in $Hg_{0.78}Cd_{0.22}Te$ (E_{A1}^+) has been estimated using the variational method at $E_{A1}^+ \approx 0.07E_{A1}$ [4]; this energy governs the energy position of the A^+ band.

For slight compensation with donors, a fraction of the acceptor levels on the order of N_D, where N_D is the number of donors, is split off and is shifted to the valence band [1]. As a result, an additional peak emerges in the acceptor band; the position of this peak is shifted from that of the main peak by [1]

$$\varepsilon_A = \frac{e^2}{\varepsilon_0}\left(\frac{4\pi}{\varepsilon}N_A\right)^{1/3}. \tag{3}$$

In this case, the Fermi level F is located below the isolated-acceptor level by $0.61\varepsilon_A$ at $T = 0$ [1].

Assuming that $N_A = 3 \times 10^{16}$ cm^{-2} and $\varepsilon_0 = 17.4$ [14] in (3), we obtain $\varepsilon_A \approx 4.2$ meV. Consequently, at $T = 0$, the maximum of the split-off peak of the impurity acceptor band and the Fermi level are located at about 3.7 meV and at 5.3 meV, respectively, above the valence-band top in the $Hg_{0.78}Cd_{0.22}Te$ crystals under investigation that contain 3×10^{16} cm^{-3} of Cu atoms and no vacancies.

If Hg vacancies are introduced into the Cu-doped $Hg_{1-x}Cd_xTe$ narrow-gap crystal, the second (vacancy) acceptor band composed of two peaks and also the vacancy-related A^+ band emerge in the band gap; as a result, the acceptor band acquires a more complicated structure.

The ionization energy $E_{A2}^{(1)}$ of a neutral vacancy and the ionization energy $E_{A2}^{(2)}$ of a singly charged Hg vacancy have been estimated theoretically [4]. It has been found that $E_{A2}^{(2)} = 4E_{A1}$ and $E_{A2}^{(1)} \approx 2E_{A1}$. For $Hg_{0.78}Cd_{0.22}Te$, we obtain $E_{A2}^{(1)} \approx 16$ meV, which is also quite consistent with experimental data [8].

Parameters of multiparticle states of mercury vacancy

M_1	M_2	$\beta_{M_1M_2}$	Z_2^*	$\left\|\frac{W_2}{E_{A1}}\right\|$	$\frac{E_{A2}^{(2)}}{E_{A1}}$	$\frac{E_{A2}^{(1)}}{E_{A1}}$	M_3	Z_3^*	$\left\|\frac{W_3}{E_{A1}}\right\|$	$\frac{E_{A2}^{+}}{E_{A1}}$
–3/2	–1/2	1.078	1.73	5.99	4	1.99	+1/2	1.468	6.46	0.47
							+3/2	1.455	6.35	0.36
	+1/2	1.078	1.73	5.99	4	1.99	–1/2	1.468	6.46	0.47
							+3/2	1.455	6.35	0.36
	+3.2	1.116	1.72	5.925	4	1.925	–1/2	1.455	6.35	0.425
							+1/2	1.455	6.35	0.425
–1/2	+1/2	1.040	1.74	6.055	4	2.055	–3/2	1.468	6.46	0.405
							+3/2	1.468	6.46	0.405
	+3/2	1.078	1.73	5.99	4	1.99	–3/2	1.455	6.35	0.36
							+1/2	1.468	6.46	0.47
+1/2	+3/2	1.078	1.73	5.99	4	1.99	–3/2	1.455	6.35	0.36
							–1/2	1.468	6.46	0.47

The energy E_{A2}^{+} of attachment of a hole to the Hg vacancy was estimated here as the difference $W_2 - W_3$ of the energies of the two- and three-particle states of a doubly charged acceptor ($Z = 2$). The calculation was performed in terms of the effective-mass approximation using the Rietz variational method. According to this method, we considered a system that consisted of either two or three holes bound by an acceptor with the core charge of $-Ze$, and we calculated the mean value of the Hamiltonian of this system in the ground state. The trial wave functions of the ground state were represented as the product of the corresponding number of single-particle wave functions of holes bound by an acceptor with the effective core charge of $-Z^*e$. For these functions, we took the wave functions $F_{jM}(\mathbf{r})$ of the acceptors in a diamond-like semiconductor with the Luttinger Hamiltonian derived previously [13]. Here, $j = 3/2$ is the eigenvalue of the total-momentum operator in the ground state and M is the corresponding component along the quantization axis [13]. For the radial part of $F_{jM}(\mathbf{r})$, we used the trial wave function reported previously [14].

The potential energy $\bar{U}$ of a hole bound by a Z^*-charged acceptor in the one-particle state was calculated using the virial theorem, according to which $\bar{U} = -2E_{AZ^*}$, where E_{AZ^*} is the absolute value of the binding energy in this state.

The repulsion energy $U_{M_1M_2}$ for two bound holes in the many-particle state depends on the components M_1 and M_2 of the total momentum for the first and second holes, respectively. Calculation of $U_{M_1M_2}$ yields the following expression:

$$U_{M_1M_2} = \beta_{M_1M_2} Z^* E_{A1}. \tag{4}$$

The values of the coefficients $\beta_{M_1M_2}$ for various allowed combinations of the total-momentum components were calculated using the trial wave functions [13, 14] and are listed in the table.

By minimizing the mean value of the Hamiltonian with respect to the parameter Z^*, we obtain the following expressions for the two-particle state of a Z-charged acceptor:

$$\begin{gathered} Z_2^* = Z - \beta_{M_1M_2}/4, \\ W_2 = -2(Z_2^*)^2 E_{A1}, \quad a_2^* = a_h/Z_2^*. \end{gathered} \tag{5}$$

Here, $W_2(Z)$ is the energy of the two-particle state, a_2^* is the radius of this state, and $a_h = 3\varepsilon_0\hbar^2/(2m_{hh}e^2)$. Similar expressions for the three-particle state of a Z-charged acceptor are written as

$$\begin{gathered} Z_3^* = Z - \frac{\beta_{M_1M_2} + \beta_{M_1M_3} + \beta_{M_2M_3}}{6}, \\ W_3 = -2(Z_3^*)^2 E_{A1}, \quad a_3^* = a_h/Z_3^*. \end{gathered} \tag{6}$$

The results of calculations performed for $Z = 2$ are listed in the table. It can be seen that the energy of numerous states of an isolated mercury vacancy depends on the combinations of components M of the total momentum of bound holes along the quantization axis. In particular, the energy W_2 of a neutral vacancy can have three different values, whereas the energy W_3 of a vacancy in the A^+ state can have two values. As a result, a neutral Hg vacancy in $Hg_{0.78}Cd_{0.22}Te$ gives rise to three acceptor levels with the energies $E_{A2}^{(1)}$ equal to 15.2, 15.7, and 16.2 meV and to four A^+ levels with the energies E_{A2}^{+} equal to 2.8, 3.2, 3.4, and 3.7 meV, if we assume that E_{A1} = 7.9 meV. It is clear that the higher lying levels correspond to the ground state of the vacancy.

Thus, the calculation shows that the level of the A^+ state of an isolated Hg vacancy is located in the region of the peak in the impurity acceptor band and is found to be below the Fermi level; the above peak is split off owing to interaction with positively charged donors. Consequently, in this model, the vacancies cannot affect the low-temperature conductivity, and this contradicts the experimental data.

Therefore, an additional broadening of the acceptor band in the crystals of semiconductor solid solutions was taken into account; this broadening is caused by the effect of microscopic fluctuations in the composition [14]. As a result, under the conditions of light doping, the density of states in each of the peaks of this band is described by the split Gaussian distribution with the following root-mean-square (rms) deviation:

$$\langle E_A\rangle \approx 0.22\left|\frac{\partial E_A}{\partial x}\right|\sqrt{\frac{x}{\pi N a^2}}. \qquad (7)$$

Here, N is the concentration of lattice sites in the metal sublattice and a is the radius of the state.

We assume that, for $Hg_{0.78}Cd_{0.22}Te$, ε_0 = 17.4 [15], $|\partial E_V/\partial x|$ = 0.35 eV [16], $m_{hh} \approx 0.4m_0$ [10], and $N = 1.5 \times 10^{22}$ cm^{-3}; we also take into account that $a = a_h/Z^*$. We then obtain the following rms deviations for various peaks in the density of impurity states of the semiconductor: $\langle E_{A1}\rangle \approx 0.8$ meV, $\langle E^+_{A1}\rangle \approx 0.5$ meV, $\langle E^{(1)}_{A2}\rangle \approx 1.8$ meV, and $\langle E^+_{A2}\rangle \approx 1.4$ meV. As a result, the calculated density of states $g_A(E)$ in the impurity band of Cu-doped, lightly compensated p-$Hg_{0.78}Cd_{0.22}Te$ crystal containing Hg vacancies acquires the form shown in Fig. 5. The peak corresponding to the energy of detachment of a hole from a singly charged vacancy is not shown, because this peak emerges only if there are such vacancies, and there are none of these in the case under consideration. The values of $g_A(E)$ were calculated using the data reported in [1, 14] on the assumption that the degree of compensation of the crystals is equal to 0.05, which corresponds to the average donor concentration of $N_D = 1.5 \times 10^{15}$ cm^{-3} in the material under consideration [17].

It can be seen that the tails of the lower Hubbard impurity band and the vacancy A^+ band overlap. In this situation, at $T = 0$, some of the holes will be transferred from the impurity acceptor levels to the higher lying A^+ levels of Hg vacancies, so that the Fermi level will be found pinned in the region of overlap of the peaks (see Fig. 5).

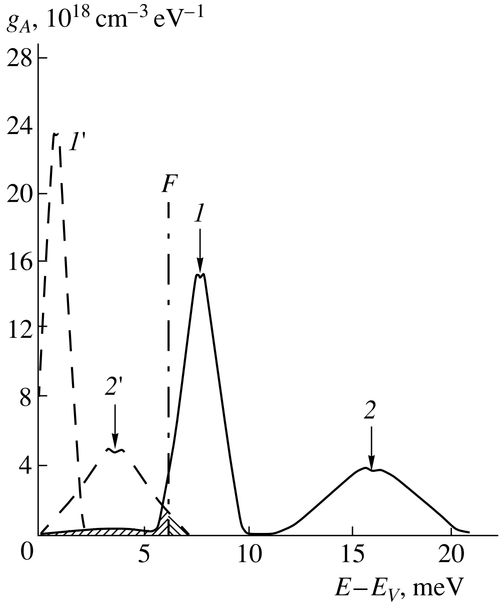

Fig. 5. The calculated density of states in the acceptor band of p-$Hg_{0.78}Cd_{0.22}Te$ crystals at T = 0 K. The following parameters were used in the calculation: $[Cu_{Hg}] = 3.1 \times 10^{16}$ cm^{-3}, $[V_{Hg}] = 1.8 \times 10^{16}$ cm^{-3}, and $N_D = 1.5 \times 10^{15}$ cm^{-3}. The solid lines correspond to the lower Hubbard band, and dashed lines correspond to the upper Hubbard band (curves *1* and *1*' outline the impurity bands, and curves *2* and *2*' outline the vacancy bands). The hatched areas correspond to the Cu levels free of holes and the occupied A^+ levels of the Hg vacancies. The Fermi level position is denoted by *F*.

4. DISCUSSION

The suggested model makes it possible to account for almost all qualitative special features of hopping conductivity in the crystals under consideration.

In fact, the calculations show that the Hg vacancies in $Hg_{0.78}Cd_{0.22}Te$ have deeper acceptor levels compared to the Cu_{Hg} defects. Therefore, the vacancies can appreciably enhance the number of free holes in the crystal, either under the condition of complete compensation of Cu_{Hg} acceptors by donors or at sufficiently high temperatures in which case the conductivity caused by the impurity acceptors is exhausted. This pattern is clearly illustrated in Fig. 1. In the region of freeze-out, the ε_1 conductivity in undoped crystals containing only V_{Hg} vacancies is much lower than the conductivity of the doped samples. However, in the crystals containing both V_{Hg} vacancies and Cu atoms, the conductivity is higher than that in the doped (but stoichiometric) crystals only at temperatures above 50–70 K, i.e., in the region of exhaustion of the extrinsic ε_1 conductivity. Thus, the acceptor levels of vacancies are indeed located above the Cu-induced levels. The A^+ levels of vacancies accept holes. Therefore, occupation of these levels can cause only an insignificant decrease in the occupancy of the valence band; thus, these vacancies most likely act as donors.

The hopping conductivity of p-$Hg_{0.78}Cd_{0.22}Te$ crystals containing both Cu_{Hg} and V_{Hg} defects far exceeds the hopping conductivity of the samples that contain only a single type of acceptor (Fig. 1). Consequently, after introduction of vacancies, the density of states g_A in the vicinity of the Fermi level at $T = 0$ changes. It is clear that this effect cannot be related to the emergence of new acceptor levels (for example, the levels belonging to the Cu_{Hg}–V_{Hg} complexes), because an addition of V_{Hg} defects to the doped samples has no affect on the resistivity of these samples in the region of the ε_1 conductivity. Therefore, the observed phenomenon can best be explained on the basis of the notion about the A^+ band formed by the Hg vacancies.

It can be seen from Fig. 5 that the Hubbard vacancy band overlaps with the split-off peak of the acceptor impurity band. In this situation, the density of states at the Fermi level $g_A(F) \neq 0$; therefore, we should observe here either the hopping conductivity that features a decreasing activation energy and obeys the Mott law $\sigma_h = \sigma_0\exp[-(T_0/T)^{1/4}]$ if the states in both overlapping bands are localized or metallic conductivity if the states in the A^+ band are delocalized. This conclusion, based on the model, is supported by experimental data, with the first of the above possibilities being realized (see Fig. 4).

The actual density of acceptor states that are located in the vicinity of the Fermi level and control the hopping conductivity in the crystals under investigation can be estimated on the basis of the theory [1, 2] according to which

$$g_A(F) = \frac{21.2}{k_B T_0 a^3}. \tag{8}$$

The characteristic size of the localized hole state should evidently be used here for the quantity a; this size controls the asymptotic behavior of the wave function of the corresponding state at large distances (see [1]), because the hopping range is appreciable in the conditions under consideration.

Assuming that, in the situation under consideration, the hops via the impurity atoms, the sizes of which exceed by 50% those of the V_{Hg} vacancies in the A^+ state, are prevalent, we obtain $a = a_l = \hbar/\sqrt{2m_{lh}E_{A1}}$ [1]. For the $Hg_{0.78}Cd_{0.22}Te$ crystals, $a_l = 25$ nm [1]; therefore, for $T_0 \approx 10^5$ K (see Fig. 4), we use relation (8) to obtain $g_A(F) \approx 1.5 \times 10^{17}$ cm^{-3} eV^{-1}, which is much less than predicted by calculation (see Fig. 5). Moreover, the aforementioned value is smaller than the density of states in the middle part of the split-off peak in the acceptor impurity band where $g_A \approx N_D/\varepsilon_A$ (see [1]): $N_D/\varepsilon_A \approx 3 \times 10^{17}$ cm^{-3} eV^{-1} for $N_D = 1.5 \times 10^{15}$ cm^{-3} and for the copper concentration $[Cu_{Hg}] = 3.1 \times 10^{16}$ cm^{-3}.

We may assume that this discrepancy is caused, for example, by overestimating the contribution of the composition fluctuations to broadening of the impurity peaks in calculations of $g_A(E)$ or by underestimating the actual density of states at the Fermi level owing to the emergence of the Coulomb gap [1]. However, it is more plausible to assume that the hops occur predominantly over the A^+ states of vacancies. In this situation, $a = a_l/Z_3^*$; as a result, the value of $g_A(E)$ calculated using the experimental data increases and becomes as large as 5×10^{17} cm^{-3} eV^{-1}. This value is fairly close to the results of calculations (see Fig. 5).

Comparing the magnitude of the hopping conductivity σ_h for the first and second cases using the theory [1] and taking into account the value of the factor σ_0 in the Mott law convinces us that the above assumption is realistic. The point is that, at 4–10 K, the ratio $(T_0/T)^{1/4} \approx 10$; i.e., it is not too large. In this situation, the value of σ_h is controlled to a great extent by the value of σ_0 that depends heavily on the localization radius (see [1]). According to estimations, the value of σ_0 is larger by 1.5 orders of magnitude for conductivity over the A^+ vacancy band than for hopping conductivity via the Cu_{Hg} impurity centers. In addition [8], the level of V_{Hg} in the $Hg_{0.78}Cd_{0.22}Te$ samples saturated with tellurium is located 15–20% higher than that in similar samples saturated with mercury (for equal concentration of V_{Hg}). Correspondingly, in the Te-saturated and Cu-doped crystals, the value of T_0 must be somewhat larger, whereas, on the contrary, the value of σ_0 is bound to be smaller. This is consistent with experimental data (see Fig. 4).

5. CONCLUSION

(i) Narrow-gap p-$Hg_{1-x}Cd_xTe$ crystals are good model material for studying the special features of hopping conductivity and the acceptor-band structure in semiconductors. On the one hand, hopping conductivity is observed at relatively high temperature (as high as 10 K) in these crystals, and, on the other hand, it is easy to control the acceptor concentration in this material.

(ii) The magnitude and behavior of hopping conductivity over the acceptor band depend not only on the presence of compensating donors, but also on the presence of other types of acceptors. In particular, the pronounced hopping conductivity obeying the Mott law $\sigma_h = \sigma_0\exp[-(T_0/T)^{1/4}]$ is observed at $T < 10$ K in the p-$Hg_{0.78}Cd_{0.22}Te$ samples that contain both Hg vacancies and Cu atoms. The mobility in the range of hopping conductivity is so low that the Hall voltage cannot be measured.

(iii) The properties of the p-$Hg_{0.78}Cd_{0.22}Te$ crystals containing Cu atoms and Hg vacancies simultaneously can be satisfactorily accounted for if both the existence of the upper Hubbard band, formed by vacancies due to their ability to accept excess holes, and the broadening of the acceptor band, due to the effect of composition fluctuations, are taken into account. According to the results of variational calculation, the hole-attachment energy for an Hg vacancy in $Hg_{0.78}Cd_{0.22}Te$ is equal to 3.7 meV.

The states in the upper Hubbard band are localized if the acceptor concentration is not too high, and hopping conductivity can occur via these states. It is this mechanism that most likely governs the low-temperature conductivity in the p-$Hg_{0.78}Cd_{0.22}Te$ crystals which simultaneously contain Cu atoms and Hg vacancies.

REFERENCES

1. B. I. Shklovskiĭ and A. L. Éfros, *Electronic Properties of Doped Semiconductors* (Nauka, Moscow, 1979; Springer-Verlag, New York, 1984).
2. N. F. Mott and E. A. Davis, *Electronic Processes in Non-Crystalline Materials* (Clarendon, Oxford, 1979; Mir, Moscow, 1982), Vol. 1.
3. E. M. Gershenzon, G. N. Gol'tsman, and A. P. Mel'nikov, Pis'ma Zh. Éksp. Teor. Fiz. **14**, 281 (1971) [JETP Lett. **14**, 185 (1971)].
4. V. V. Bogoboyashchiĭ, S. G. Gasan-zade, and G. A. Shepel'skiĭ, Fiz. Tekh. Poluprovodn. (St. Petersburg) **34** (4), 411 (2000) [Semiconductors **34**, 398 (2000)].
5. V. V. Bogoboyashchiĭ, Fiz. Tekh. Poluprovodn. (St. Petersburg) **35** (1), 34 (2001) [Semiconductors **35**, 33 (2001)].
6. A. I. Elizarov and V. I. Ivanov-Omskiĭ, Fiz. Tekh. Poluprovodn. (Leningrad) **15** (5), 927 (1981) [Sov. Phys. Semicond. **15**, 531 (1981)].
7. V. V. Bogoboyashchiĭ, Fiz. Tekh. Poluprovodn. (St. Petersburg) **34** (8), 955 (2000) [Semiconductors **34**, 916 (2000)].
8. V. V. Bogoboyashchiy, Semicond. Phys. Quantum Electron. Optoelectron. **2** (1), 62 (1999).
9. V. V. Bogoboyashchiĭ, A. I. Elizarov, V. A. Petryakov, *et al.*, Fiz. Tekh. Poluprovodn. (Leningrad) **21** (8), 1469 (1987) [Sov. Phys. Semicond. **21**, 893 (1987)].
10. V. V. Bogoboyashchiy, Proc. SPIE **3486**, 325 (1997).
11. V. V. Bogoboyashchiĭ, Kondens. Sredy Mezhfaznye Granitsy **2** (2), 132 (2000).
12. N. F. Mott, J. Non-Cryst. Solids **1**, 1 (1968).
13. B. L. Gel'mont and M. S. D'yakonov, Fiz. Tekh. Poluprovodn. (Leningrad) **5** (11), 2191 (1971) [Sov. Phys. Semicond. **5**, 1549 (1974)].
14. B. L. Gel'mont, A. R. Gadzhiev, B. L. Shklovskiĭ, *et al.*, Fiz. Tekh. Poluprovodn. (Leningrad) **8**, 2377 (1974) [Sov. Phys. Semicond. **8**, 1549 (1974)].
15. A. V. Lyubchenko, E. A. Sal'kov, and F. F. Sizov, in *Physical Foundations of Semiconductor Quantum Photoelectronics* (Naukova Dumka, Kiev, 1984), p. 126.
16. C. K. Shin and W. E. Spicer, J. Vac. Sci. Technol. B **5**, 1231 (1987).
17. K. R. Kurbanov and V. V. Bogoboyashchiĭ, Kondens. Sredy Mezhfaznye Granitsy **1** (3), 245 (1999).

Translated by A. Spitsyn

Semiconductors, Vol. 36, No. 1, 2002, pp. 34–37. Translated from Fizika i Tekhnika Poluprovodnikov, Vol. 36, No. 1, 2002, pp. 37–40.
Original Russian Text Copyright © 2002 by Skipetrov, Zvereva, Skipetrova, Volkova, Slyn'ko.

ELECTRONIC AND OPTICAL PROPERTIES OF SEMICONDUCTORS

On Stabilization of the Fermi Level in Ga-Doped PbTe-Based Alloys

**E. P. Skipetrov*, E. A. Zvereva*, L. A. Skipetrova*,
O. S. Volkova*, and E. I. Slyn'ko****
** Faculty of Physics, Moscow State University, Vorob'evy gory, Moscow, 119899 Russia*
e-mail: skip@mig.phys.msu.su
*** Institute of Material Science (Chernovtsy Branch), National Academy of Science of Ukraine,
ul. Zhovtneva 5, Chernovtsy, 274001 Ukraine*

Submitted March 19, 2001; accepted for publication April 19, 2001

Abstract—The influence of Ga doping and irradiation with high-energy electrons on the galvanomagnetic effects in n-$Pb_{1-x}Ge_xTe$:Ga ($0.04 \lesssim x \lesssim 0.06$) was investigated. Transitions to the metal-type conduction were found to occur both with an increase in the impurity content and as a result of irradiation. It is concluded that the impurity level does not pin the Fermi level. It is demonstrated that gallium doping and electron irradiation are the most effective complementary methods for controlling the electrical properties of alloys. *© 2002 MAIK "Nauka/Interperiodica".*

At the present time, the pinning of the Fermi level by a deep impurity level is considered as one of the most important properties of IV–VI semiconductors doped with impurities with a variable valence [1–3]. This effect is most pronounced for In-doped $Pb_{1-x}Sn_xTe$ alloys. For these alloys, the introduction of other impurities, intrinsic defects, or radiation defects does not affect the position of the Fermi level and electrical properties as long as the impurity or defect content is no higher than the In content [1, 2, 4].

It is possible that the Ga impurity is an exception from the general rule.

First, it was found that the charge-carrier density in PbTe:Ga depends anomalously on the impurity content [5–8]. Initially, with the introduction of Ga, a decrease in the hole density is observed. Subsequently, the charge-carrier density is close to the intrinsic one over a rather narrow range of the Ga content. In this case, the Fermi level turns out to be pinned by the deep impurity level $E_{Ga\,1}$, which is located in the band gap [2]. However, with a further increase in the Ga content, the p–n conversion occurs and the electron density increases and apparently tends toward a constant value.

Second, the electron irradiation of the $Pb_{1-x}Sn_xTe$:Ga alloys ($x = 0, 0.19, 0.23$) with the integrated flux Φ leads to the p–n conversion and a steady increase in the electron density n with an anomalously high rate ($dn/d\Phi \approx 4$ cm^{-1}) [9, 10]. This value is approximately an order of magnitude larger compared to those characteristic of undoped IV–VI semiconductors [11].

The anomalies mentioned are probably associated with the existence of the second deep level E_{Ga}, which is induced by the Ga impurity and is located in the conduction band of PbTe [12]. As the Ge content increases, this level in the $Pb_{1-x}Ge_xTe$ alloys approaches the bottom of the conduction band, and, at $x \gtrsim 0.03$, it enters the band gap. For this reason, we may expect that an increase in the Ga content and electron irradiation will only slightly affect the electrical parameters of crystals due to the pinning of the Fermi level by the deep level E_{Ga}. In order to verify this assumption, we investigated galvanomagnetic effects in the $Pb_{1-x}Ge_xTe$:Ga alloys ($x = 0.04, 0.06$), for which deep levels of Ga are located in the band gap, with the variation of the Ga content and electron integrated flux.

The single-crystal samples of n-$Pb_{1-x}Ge_xTe$:Ga with the Ga content $C_{Ga} \approx 1.5$–3 mol %, which were investigated in this study, were synthesized by vapor phase sublimation. The Ge content in the samples was monitored using the X-ray diffraction technique, whereas the impurity content was determined from the Ga content in the charge with allowance made for the impurity distribution along the ingot length. A portion of the samples was irradiated at room temperature using an ÉLU-6 linear electron accelerator with the electron energy $E = 6$ MeV, $d\Phi/dt \approx 10^{12}$ cm^{-2} s^{-1}, and $\Phi \lesssim 2.4 \times 10^{16}$ cm^{-2}. For each sample, temperature dependences of resistivity and the Hall coefficient were investigated prior to irradiation and for several integrated fluxes. The magnetic field was $B \lesssim 0.1$ T, and the temperature range was $4.2\ \text{K} \le T \lesssim 300$ K. Major parameters of the samples at 4.2 K are listed in the table.

The investigation of galvanomagnetic effects demonstrated that the electrical properties of alloys depend heavily on both the Ga content and the electron integrated flux. The samples with a low dopant content were found to have fairly high resistivity. The tempera-

Parameters of investigated n-$Pb_{1-x}Ge_xTe$:Ga samples at T = 4.2 K prior to and subsequent to irradiation with fast electrons

Sample	x	Impurity content C_{Ga}, mol %	Integrated flux Φ, 10^{16} cm^{-2}	Resistivity ρ, Ω cm	Electron density n, cm^{-3}	Mobility μ_H, cm^2 V^{-1} s^{-1}
Ge-4-7	0.04	1.5	0	9.1×10^2	$<3 \times 10^{14}$	<1
			1.2	4.8×10^{-1}	2.1×10^{16}	6.2×10^2
			2.4	1.5×10^{-2}	9.3×10^{16}	4.5×10^3
Ge-4-7'	0.04	1.5	0	2.5	1.4×10^{15}	$<2 \times 10^3$
Ge-4-9	0.04	2	0	9.9×10^{-1}	1.6×10^{16}	4.0×10^2
			1.2	3.7×10^{-3}	1.2×10^{17}	1.4×10^5
Ge-4-3	0.04	3	0	2.1×10^{-2}	6.8×10^{17}	4.4×10^2
			1.2	9.7×10^{-3}	1.0×10^{18}	6.5×10^2
Ge-6-2	0.06	1.5	0	4.8	$<10^{13}$	$<4 \times 10^3$
Ge-6-4	0.06	1.5	0	3.4×10	$<4 \times 10^{11}$	$<3 \times 10^3$
			1.2	4.6	$<2 \times 10^{15}$	$<5 \times 10$

ture dependences of resistivity ρ and the Hall coefficient R_H have a semiconductor character (Figs. 1 and 2, curves *1*) with a pronounced activation portion of extrinsic conductivity. This is indicative of the existence of deep level E_{Ga} induced by Ga in the band gap of the alloys [12]. At the lowest temperatures (T < 20 K), the resistivity tends toward a constant value, the Hall mobility of charge carriers decreases rapidly, and the signal from Hall contacts becomes undetectable (Figs. 1 and 2, curves *1*). Such behavior is apparently associated with the change in the prevalent mechanism of conduction. At low temperatures, this mechanism can be the conduction via the impurity level E_{Ga} or the surface conduction.

As the Ga content in the alloys increases, ρ and the absolute value of R_H decrease by more than 3 orders of

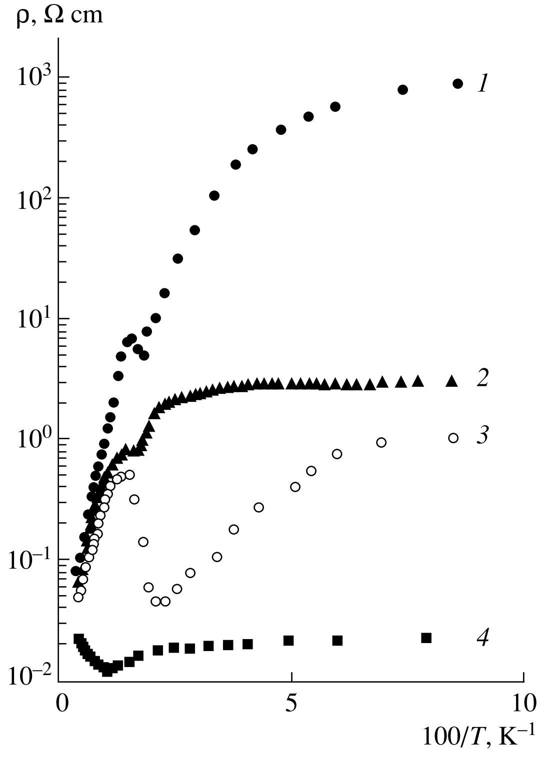

Fig. 1. Temperature dependences of resistivity for the $Pb_{0.96}Ge_{0.04}Te$:Ga alloy for the Ga content in the samples C_{Ga} = (*1*, *2*) 1.5, (*3*) 2, and (*4*) 3 mol %.

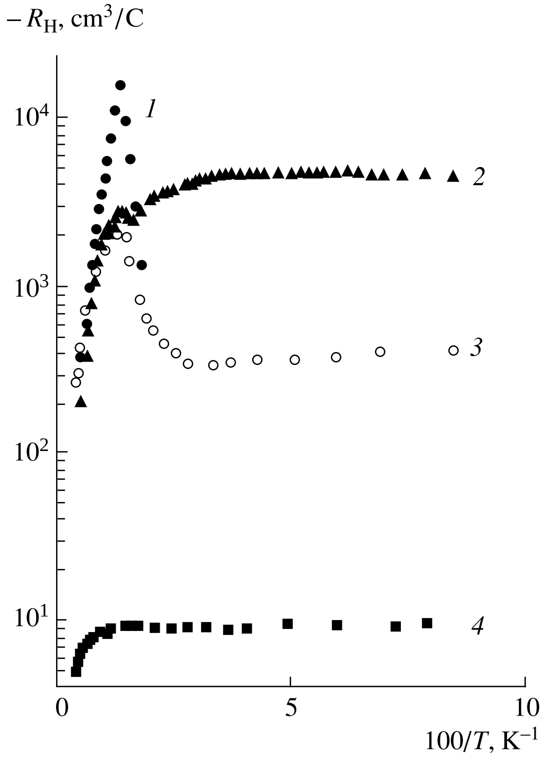

Fig. 2. Temperature dependences of the Hall coefficient for the $Pb_{0.96}Ge_{0.04}Te$:Ga alloy in relation to variation in the Ga content in the samples. Numbers at the curves denote the same as in Fig. 1.

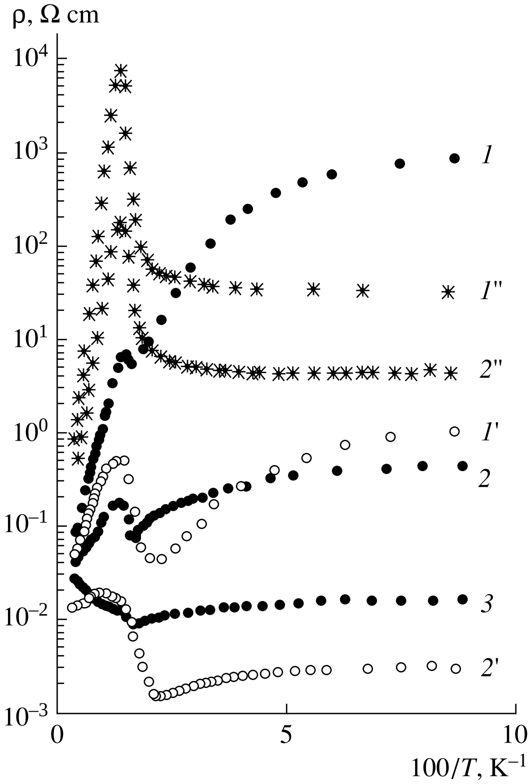

Fig. 3. Temperature dependences of resistivity in electron-irradiated $Pb_{1-x}Ge_xTe$:Ga alloys in relation to the integrated flux. (*1*–*3*) sample Ge-4-7 (C_{Ga} = 1.5 mol %), (*1*', *2*') sample Ge-4-9 (C_{Ga} = 2 mol %), and (*1*", *2*") sample Ge-6-4 (C_{Ga} = 1.5 mol %). Φ = (*1*, *1*', *1*") 0, (*2*, *2*', *2*") 1.2×10^{16}, and (*3*) 2.4×10^{16} cm^{-2}.

magnitude at low temperatures. The activation character of their temperature dependences gradually varies to the metallic one (Figs. 1 and 2, curves *2*–*4*). The free electron density calculated from the Hall coefficient increases and attains the value $n \approx 7 \times 10^{17}$ cm^{-3}. It is evident that such a character of the variation in electrical parameters is indicative of the transition of the samples from the insulating state to the metallic one. In this case, the band conduction of the electron type is the prevalent mechanism of conduction over the entire temperature range investigated.

The electron irradiation of the alloys investigated leads to variations in the character of the temperature dependences of resistivity and the Hall coefficient, which are similar to those caused by an increase in the dopant content (Fig. 3). It is clearly seen that the transition to the metallic-type conduction occurs with an increase in the integrated flux. We may assume that, similarly to the $Pb_{1-x}Sn_xTe$:Ga alloys [10], irradiation leads to the generation of predominantly donor-type radiation defects and to the appearance of corresponding resonance donor-type level E_d in the conduction band. In this case, during irradiation, the electrons from the E_d level initially occupy free states at the impurity level E_{Ga}. After that, the insulator–metal transition occurs, the Fermi level is brought into the conduction band, and the electron density may increase up to the pinning of the Fermi level by the donor level E_d.

However, it should be noted that, similarly to the $Pb_{1-x}Sn_xTe$:Ga alloys, the rate of variation in the electron density with irradiation dose turned out to be anomalously high. The estimations yield $dn/d\Phi$ = 5–6 cm^{-1}, which is difficult to explain taking into account only the emergence of the resonance radiation-defect level E_d. The increase in uniformity of the Ga distribution over the lattice and in the content of electrically active impurity atoms under the effect of irradiation may serve as the additional mechanism responsible for the high rate of defect formation [10].

The character of varying the electrical parameters of the alloys investigated suggests that no pinning of the Fermi level by the Ga level E_{Ga} is observed. An increase in the Ga content and radiation defect density leads to the transition of the Fermi level to the conduction band and to a steady increase in the electron density. Doping by Ga and electron irradiation are effective complementary methods for controlling the electrical properties of the $Pb_{1-x}Ge_xTe$ alloys. These methods make the fine adjustment of the Fermi level possible, as well as the attainment of a more uniform impurity distribution over the sample bulk.

ACKNOWLEDGMENTS

This study was supported by the Scientific Program “Universities of Russia” and the Russian Foundation for Basic Research, project nos. 00-15-96784 and 01-02-17446.

REFERENCES

1. V. I. Kaĭdanov and Yu. I. Ravich, Usp. Fiz. Nauk **145**, 51 (1985) [Sov. Phys. Usp. **28**, 31 (1985)].
2. B. A. Akimov, A. V. Dmitriev, D. R. Khokhlov, and L. I. Ryabova, Phys. Status Solidi A **137**, 9 (1993).
3. W. Dobrowolski, in *Proceedings of the 9th International Conference on Narrow Gap Semiconductors, Berlin, Germany, 2000,* Ed. by N. Puhlmann, H.-U. Muller, and M. von Ortenberg, p. 39.
4. E. P. Skipetrov, A. N. Nekrasova, and A. G. Khorosh, Fiz. Tekh. Poluprovodn. (St. Petersburg) **28**, 815 (1994) [Semiconductors **28**, 478 (1994)].
5. G. S. Bushmarina, B. F. Gruzinov, I. A. Drabkin, *et al.*, Fiz. Tekh. Poluprovodn. (Leningrad) **11**, 1874 (1977) [Sov. Phys. Semicond. **11**, 1098 (1977)].

6. G. S. Bushmarina, B. F. Gruzinov, T. T. Dedegkaev, *et al.*, Izv. Akad. Nauk SSSR, Neorg. Mater. **16**, 2136 (1980).
7. F. F. Sizov, S. V. Plyatsko, and V. M. Lakeenkov, Fiz. Tekh. Poluprovodn. (Leningrad) **19**, 592 (1985) [Sov. Phys. Semicond. **19**, 368 (1985)].
8. Z. Feit, D. Eger, and Z. Zemel, Phys. Rev. B **31**, 3903 (1985).
9. E. P. Skipetrov, A. N. Nekrasova, D. V. Pelekhov, *et al.*, Fiz. Tekh. Poluprovodn. (St. Petersburg) **28**, 1626 (1994) [Semiconductors **28**, 906 (1994)].
10. E. P. Skipetrov, Fiz. Tekh. Poluprovodn. (St. Petersburg) **29**, 1416 (1995) [Semiconductors **29**, 735 (1995)].
11. N. B. Brandt and E. P. Skipetrov, Fiz. Nizk. Temp. **22**, 870 (1996) [Low Temp. Phys. **22**, 665 (1996)].
12. E. P. Skipetrov, E. A. Zvereva, V. V. Belousov, *et al.*, Fiz. Tekh. Poluprovodn. (St. Petersburg) **34**, 932 (2000) [Semiconductors **34**, 894 (2000)].

Translated by N. Korovin

Semiconductors, Vol. 36, No. 1, 2002, pp. 38–40. Translated from Fizika i Tekhnika Poluprovodnikov, Vol. 36, No. 1, 2002, pp. 41–44.
Original Russian Text Copyright © 2002 by Kazanskiĭ, Mell, Terukov, Forsh.

ELECTRONIC AND OPTICAL PROPERTIES OF SEMICONDUCTORS

Effect of Boron Dopant on the Photoconductivity of Microcrystalline Hydrogenated Silicon Films

A. G. Kazanskiĭ*, H. Mell, E. I. Terukov***, and P. A. Forsh***
** Moscow State University, Moscow, 119899 Russia*
e-mail: Kazanski@phys.msu.su
*** Philipps-Universität Marburg, Fachbereich Physik, D-35032, Marburg, Germany*
**** Ioffe Physicotechnical Institute, Russian Academy of Sciences,*
Politekhnicheskaya ul. 26, St. Petersburg, 194021 Russia

Submitted April 12, 2001; accepted for publication April 19, 2001

Abstract—The effect of boron dopant of microcrystalline hydrogenated silicon films on the temperature dependence of photoconductivity and photoresponse time was studied. The measurements were carried out in the temperature range of 130–450 K under irradiation with 1.4-eV photons. It is established that the steady-state photoconductivity and photoresponse time increase with doping level. A model of nonequilibrium charge carrier recombination, which takes into account the mixed-phase structure of microcrystalline silicon, is suggested. The model satisfactory explains the results obtained. © *2002 MAIK "Nauka/Interperiodica".*

In spite of the wide use of microcrystalline hydrogenated silicon films (μ*c*-Si:H) in optoelectronic devices, the mechanism of generation and recombination of nonequilibrium carriers responsible for their photoconductivity remains unclear.

It is known that a correlation exists between variations in dark conductivity (σ_d) and steady-state photoconductivity ($\Delta\sigma_{ph}$) when the films are doped with donors (phosphorus) or acceptors (boron) [1–4].The value of ($\Delta\sigma_{ph}$) grows with an increase in σ_d as the films are doped. The smallest value of $\Delta\sigma_{ph}$ is observed in films that have the smallest σ_d. Such μ*c*-Si:H films have the highest photosensitivity ($\Delta\sigma_{ph}/\sigma_d$). Similar correlated changes in σ_d and $\Delta\sigma_{ph}$ with doping are observed in the films of amorphous hydrogenated silicon (*a*-Si:H) [5]. For *a*-Si:H, it is assumed that such behavior is caused by the increase in concentration of the prevalent recombination centers of nonequilibrium carriers (i.e., the neutral dangling bonds as a result of recharging [5]) due to the shift of the Fermi level to the conduction or valence bands. At present, it is also assumed that the dangling bonds play an important part in the recombination of nonequilibrium carriers in μ*c*-Si:H [6]. At the same time, the results of ESR studies in μ*c*-Si:H [7, 8] show that the concentration of neutral dangling bonds in μ*c*-Si:H does not change as a result of a considerable shift of the Fermi level (over 0.5 eV) with doping of this material. Thus, the effect of doping of μ*c*-Si:H on $\Delta\sigma_{ph}$ and on its temperature dependence calls for further studies.

In this paper, we report the results of studying the effect of doping μ*c*-Si:H films with boron on steady-state photoconductivity and its relaxation after the termination of illumination. The films of μ*c*-Si:H, 0.6–0.7 μm thick, were deposited onto a quartz substrate at a temperature of 220°C by the decomposition in glow discharge of a silane-hydrogen mixture containing 1.5% of monosilane SiH_4. The doping was performed by the introduction of diborane B_2H_6 into the reaction chamber. The volume ratio of gases ($[B_2H_6]/[SiH_4]$) was 4×10^{-6} (sample 1), 5×10^{-6} (sample 2), and 10^{-5} (sample 3). According to thermoelectric-power measurements, the films had the *p*-type of conductivity. The magnesium contacts were deposited on the film surface. The measurements were performed in a vacuum chamber with a residual pressure of 10^{-3} Pa. The films were annealed prior to the measurements for 30 minutes at a temperature of 180°C. The photoconductivity of the films was measured in the temperature range of 130–450 K under exposure to radiation from an infrared light-emitting diode with the photon energy $h\nu = 1.4$ eV and intensity 4×10^{16} cm^{-2} s^{-1}. The relaxation of the photoconductivity was recorded using a digital storage oscilloscope.

The temperature dependences of σ_d and $\Delta\sigma_{ph}$ of μ*c*-Si:H films are shown in Fig. 1. Within the temperature range used, the $\sigma_d(T)$ curves show the activation-type dependences with the activation energy E_a = 0.43 eV (sample 1), 0.27 eV (sample 2), and 0.23 eV (sample 3). The value of σ_d increases and that of E_a decreases with increasing doping level. As can be seen from Fig. 1, $\Delta\sigma_{ph}$ also increases with the doping level, and the character of its temperature variation virtually remains inchanged. In the region of $T < 220$ K, the value of $\Delta\sigma_{ph}$ in the films increases almost exponentially with the activation energy of about 0.13 eV. The further increase in temperature makes the growth of $\Delta\sigma_{ph}$ less steep, and in a high-temperature range $\Delta\sigma_{ph}$ begins to fall.

The increase in $\Delta\sigma_{ph}$ with doping can be related both to the increase in lifetime of nonequillibrium charge carriers and to the increase in their mobility. Information about the effect of doping on lifetime can be obtained from the measurements of the relaxation of photoconductivity after the termination of illumination. Figure 2 shows the influence of the doping level on the relaxation of photoconductivity at $T = 120$ K. As can be seen from Fig. 2, the relaxation of photoconductivity after the termination of illumination for all of the samples studied does not obey the exponential law and has a low-rate component. Increasing the doping level reduces the relaxation rate. This result is consistent with the data obtained in [4].

The measurements showed that the relative reduction of the relaxation rate of the photoconductivity with doping varies with temperature. The temperature variations of the photoresponse time (τ_{ph}) for the samples studied are shown in Fig. 3. A half-decay time of photoconductivity after the termination of illumination was measured as a parameter of (τ_{ph}). Note that the values of τ_{ph} were close to the instantaneous photoresponse time $\tau_{ph}(0)$ obtained from the relation $\tau_{ph}(0) = (\Delta\sigma_{ph}/(\partial(\Delta\sigma_{ph})/\partial t)^{-1})_{t=0}$. As follows from Fig. 3, the magnitude of τ_{ph} increases with doping, the relative change in τ_{ph} with doping being smaller at $T > 220$ K.

Let us analyze the results obtained. In our opinion, the increase in $\Delta\sigma_{ph}$ with doping (Fig. 1) is mainly caused by the increase in the lifetime of carriers. This increase in lifetime may be responsible for the observed increase in τ_{ph} with doping (Fig. 3). A slow relaxation of photoconductivity (Fig. 2) indicates that there is an appreciable concentration of traps of nonequilibrium carriers in μ*c*-Si:H.

It is known that the μ*c*-Si:H films have a mixed-phase structure consisting of crystalline and amorphous silicon phases, voids, and intercrystalline boundaries. According to electron microscopy data, the films studied have columnar structure normal to the substrate surface, the diameter of the columns being 30–100 nm. The columns consist of crystals from 3 to 30 nm in size [9]. The crystalline component in the Raman spectra is equal to 85% of the total area of a peak. According to data published in [10], the generation and transport of carriers in such films are controlled by the crystalline phase.

A possible energy-band diagram for the boundary of a column with amorphous and crystalline phases in μ*c*-Si:H is shown in Fig. 4. The analysis of ESR data in μ*c*-Si:H shows that most dangling-bond defects are concentrated at the boundaries of the columns [8]. The studies of the heterojunctions *a*-Si:H/*c*-Si show that the concentration of dangling bonds at the boundary of a heterojunction is as high as 10^{18} cm^{-3} [11]. The considerable density of localized states at the boundaries of columns, including the boundaries with amorphous phase, must result in the formation of barriers for the majority charge carriers (holes, in our case). The transport of carriers occurs via the parts of columns which are in contact with each other. The possible recombination transitions inside the columns (*1*) and at the boundaries (*2*) are shown by arrows. From the results of measuring $\Delta\sigma_{ph}$, one will find that the product of mobility (μ) and carrier lifetime (τ) exceeds 4×10^{-8} cm^2 V. Correspondingly, the carrier diffusion length $L = (kT\mu\tau/e)^{1/2} >$ 200 nm exceeds the sizes of columns in the temperature range studied (here, *k* and *e* are the Boltzmann constant and the elementary charge). Because of this, the trapping and recombination of carriers at the states located

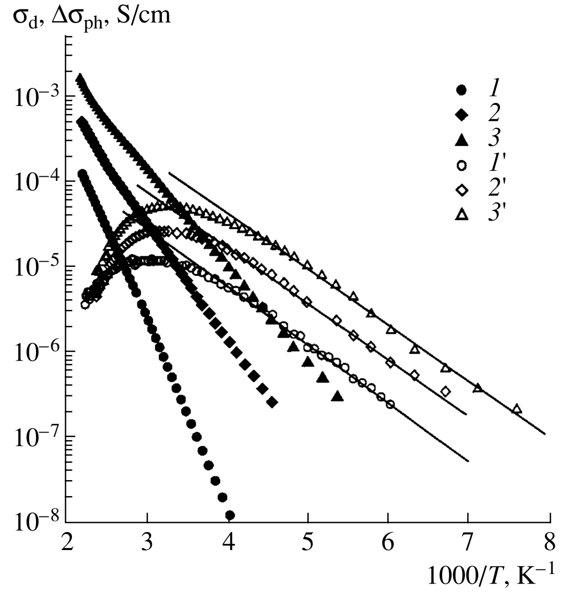

Fig. 1. Temperature dependences (*1*–*3*) of dark conductivity σ_d and (*1'*–*3'*) steady-state photoconductivity $\Delta\sigma_{ph}$ in μ*c*-Si:H films. The numbers correspond to the numeration of samples.

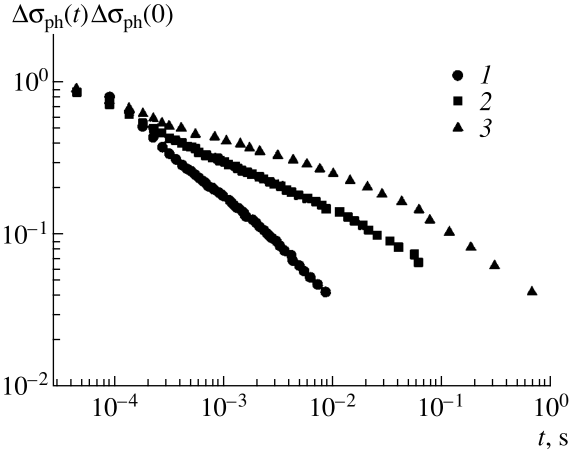

Fig. 2. Relaxation of photoconductivity in μ*c*-Si:H films at $T = 120$ K. The numbers correspond to the numeration of samples.

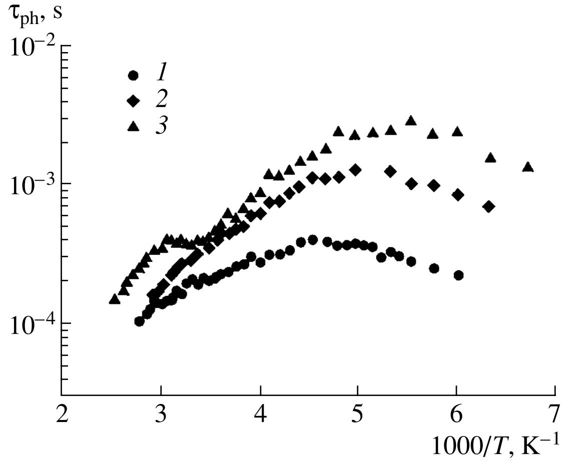

Fig. 3. Temperature dependences of photoresponse time τ_{ph} in μ*c*-Si:H films. The numbers correspond to the numeration of samples.

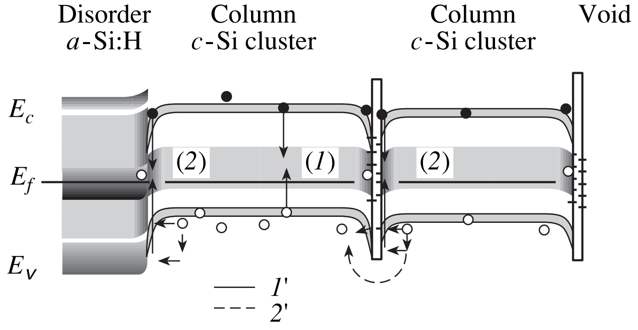

Fig. 4. Energy-band diagram of the interfaces between a microcrystalline column and crystalline and amorphous phases in boron-doped μ*c*-Si:H. *1*', possible recombination transitions of nonequilibrium carriers; *2*', transitions corresponding to carrier transport.

near the surfaces of the columns can be responsible both for the relaxation of photoconductivity and the lifetime of nonequilibrium carriers. As can be seen from Fig. 4, the occurrence of a barrier at the boundary with an amorphous phase causes the separation of majority carriers from the minority ones. In this process, the recombination via the states at the column boundaries must include the tunneling of a majority carrier with its subsequent recombination via the states of defects. Tunneling processes must be responsible for the recombination at low temperatures. This may account for the weak temperature dependence of τ_{ph} at $T < 220$ K. The increase in temperature can activate the formation of holes, which should result in the observable decrease of τ_{ph}. It should be noted that the increase in temperature initiates the activation of electrons from the potential wells near the surface of columns. Correspondingly, one should expect the enhancement of recombination flow (*1*) inside a column (if the concentration of recombination centers inside the column is sufficiently high).

A high density of states at column boundaries increases the potential-barrier height at a boundary with doping, in particular at the boundary with an amorphous phase. This must intensify the effective separation of the majority and minority carriers and reduce the probability of recombination transitions near the column surfaces. Correspondingly, the lifetime of carriers, the photoconductivity relaxation time, and the magnitude of photoconductivity must also increase. The increase in barrier height should enhance the temperature dependence of τ_{ph} in the high-temperature range, which is in fact observed in the experiment (Fig. 3).

Thus, a qualitative model of recombination of carriers in μ*c*-SI:H is suggested. This model suggests the dominant role of column boundaries with *a*-Si:H in the course of recombination of nonequilibrium carriers and provides a qualitative explanation of the effect of doping on the photoconductivity of μ*c*-SI:H.

ACKNOWLEDGMENT

This study was supported by the project INTAS-97-1910 and the program "Russian Universities".

REFERENCES

1. M. J. Williams, C. Wang, and G. Lucovsky, Mater. Res. Soc. Symp. Proc. **219**, 389 (1991).
2. R. Fluckiger, J. Meier, M. Goetz, and A. Shah, J. Appl. Phys. **77**, 712 (1995).
3. M. Bruggemann, A. Hierzenberger, R. Reining, *et al.*, J. Non-Cryst. Solids **227–230**, 982 (1998).
4. M. Bruggemann and C. Main, Phys. Rev. B **57**, R15080 (1998).
5. W. E. Spear, H. L. Steemers, P. G. LeComber, and R. A. Gibson, Philos. Mag. B **50**, L33 (1984).
6. P. Kanschat, K. Lips, and W. Fuhs, J. Non-Cryst. Solids **266–269**, 524 (2000).
7. P. Kanschat, H. Mell, K. Lips, and W. Fuhs, Mater. Res. Soc. Symp. Proc. **609**, 463 (2000).
8. F. Finger, J. Muller, C. Malten, *et al.*, J. Non-Cryst. Solids **266–269**, 511 (2000).
9. D. Ruff, H. Mell, L. Toth, *et al.*, J. Non-Cryst. Solids **227–230**, 1011 (1998).
10. A. G. Kazanskiĭ, H. Mell, E. I. Terukov, and P. A. Forsh, Fiz. Tekh. Poluprovodn. (St. Petersburg) **34**, 373 (2000) [Semiconductors **34**, 367 (2000)].
11. J. M. Essick and J. D. Cohen, Appl. Phys. Lett. **55**, 1232 (1989).

Translated by A. Zalesskiĭ

Semiconductors, Vol. 36, No. 1, 2002, pp. 41–44. Translated from Fizika i Tekhnika Poluprovodnikov, Vol. 36, No. 1, 2002, pp. 45–48.
Original Russian Text Copyright © 2002 by Davydov.

ELECTRONIC AND OPTICAL PROPERTIES OF SEMICONDUCTORS

Evaluation of Physical Parameters for the Group III Nitrates: BN, AlN, GaN, and InN

S. Yu. Davydov
St. Petersburg State Electrotechnical University, ul. Professora Popova 5, St. Petersburg, 197376 Russia

Submitted May 14, 2001; accepted for publication May 17, 2001

Abstract—Estimation of dielectric, optical, electrooptical, magnetic, elastic, photoelastic, piezoelectric, and phonon characteristics of XN (X = B, Al, Ga, In) crystals is performed by simple methods using quantum-mechanical and semiempirical approaches. The values of deformation potentials and magnetic susceptibilities are determined. The results of calculations are compared with the available experimental data and the calculations of other authors. © *2002 MAIK “Nauka/Interperiodica”.*

In spite of the fact that much attention has been paid in recent years to the experimental studies of the Group III metals (III-nitrates; see, for example, Proceedings of the Conference [1] and references therein), many characteristics, even for the most commonly used polytypes, are still not available. Consequently, theoretical investigation of III-nitrates is quite a topical problem. The *ab initio* numerical methods are usually employed for the calculation of various characteristics of these nitrates [1]. However, it is obviously of interest to use a simplified Harrison's method based on the bonding orbitals [2, 3]. This method allows one to obtain analytical expressions for a large number of physical characteristics of semiconductor crystals. We used various modifications of the bonding-orbital method in [2, 3] for the description of wide-gap semiconductors. In this study, we have applied the above method to III-nitrates, including indium nitrite, which we have not yet investigated. In contrast to [4–10], here we use the values of atomic terms taken from the tables complied by Herman and Skillman [2]. The input parameters for calculation are given in Table 1. Note that the covalence (α_c) of the compounds in the BN ⟶ InN series decreases, and the polarity (α_p) increases.

Table 2 presents the results of the calculation of high frequency (ε_∞) and static (ε_0) dielectric constants performed using the formulas given in [4]. In contrast to [2, 3], the calculation of (ε_0) was made taking into account the contribution of ion cores to screening. The bracketed values are the experimental ones taken from the reference book [11]. According to the data given in [2], $\varepsilon_\infty = 4.5$ for BN, and $\varepsilon_\infty = 4.8$ for AlH. The values of ε_∞ for BN and AlH given in [12, 13] are equal to 4.53 and 4.46, respectively. The agreement between the calculated and experimental data is quite satisfactory. It is notable that almost identical results are obtained by the *ab initio* calculations [14]. Thus, in accordance with the experiment, both high frequency and static dielectric constants obtained theoretically increase in the BN ⟶ InN series with increasing polarity of bonding α_p.

Table 2 also gives the values of electronic quadratic susceptibility χ^e_{14}, the linear electrooptical coefficient r_{41}, and photoelastic constants p_{ij} calculated for cubic

Table 1. Input parameters for the calculations: d is the nearest-neighbor distance in a crystal [2], V_2 and V_3 are the covalent and ionic energies [3], α_c and α_p are the covalence and polarity [3], and γ is the adjustable parameter in calculation of dielectric properties [2]

Quantity	BN	AlN	GaN	InN
d, Å	1.57	1.89	1.94	2.15
$-V_2$, eV	9.95	6.87	6.52	5.31
V_3, eV	3.12	4.09	3.92	4.16
α_c	0.95	0.86	0.86	0.80
α_p	0.30	0.51	0.52	0.59
γ	1.25	1.50	1.50	2.00

Note: The values of atomic terms are taken from the tables of Herman and Skillman [2].

Table 2. Results of the calculation of high-frequency (ε_∞) and static (ε_0) dielectric constants, electronic quadratic susceptibility (χ^e_{14}), linear electrooptical coefficient (r_{41}), and photoelastic constants (p_{ij}) for cubic crystals

Quantity	BN	AlN	GaN	InN
ε_∞	4.40	5.32	5.38 (5.8)	8.04(9.3)
ε_0	4.87	8.41	10.74 (12.2)	14.86
$\chi^e_{14} \times 10^{-7}$, CGSE	0.20	0.81	0.89	2.78
$r_{41} \times 10^{-7}$, CGSE	–0.05	–0.21	–0.14	–0.29
$p_{11} \times 10^2$	–29.7	–0.86	–7.3	1.1
$p_{12} \times 10^2$	–10.4	–3.0	–2.6	0.4
$p_{44} \times 10^2$	–15.2	–4.4	–3.7	0.6

Note: Experimental data [11] are shown in brackets.

1063-7826/02/3601-0041$22.00 © 2002 MAIK “Nauka/Interperiodica”

Table 3. Results of the calculation of quadratic susceptibility (χ_{ij}) and photoelastic constants (p_{ij}) for hexagonal crystals

Quantity	BN	AlN	GaN	InN
$\chi_{33} \times 10^8$, CGSE	0.92	5.4	3.7	17.4
$(\chi_{31} = \chi_{15}) \times 10^8$, CGSE	–0.46	–2.7	–1.8	–8.7
$-p_{11} \times 10^2$	34.7	10.0	8.6	–1.4
$-p_{33} \times 10^2$	37.0	10.7	9.1	–1.4
$-p_{12} \times 10^2$	9.2	2.7	2.3	–0.3
$-p_{13} \times 10^2$	6.7	1.9	1.7	–0.2
$-p_{44} \times 10^2$	11.0	3.2	2.7	–0.4
$-p_{66} \times 10^2$	12.8	3.7	3.2	–0.5

Table 4. Dimensionless Keating's force constants (α* and β*), elastic constants for cubic (C_{ij}^c) and hexagonal (C_{ij}^h) crystals, and corresponding bulk moduli (B^c and B^h) (in GPa)

Quantity	GaN	AlN	InN
α*	4.36	4.61	4.20
β*	0.92	1.12	0.80
C_{11}^c	322	325	178
C_{12}^c	156	142	92
C_{44}^c	138	147	73
B^c	211	203	121
C_{11}^h	373(390)	369(345)	204
C_{33}^h	398(398)	395(395)	217
C_{44}^h	105(105)	96(118)	50
C_{66}^h	123(123)	112	60
C_{12}^h	130(145)	145(125)	85
C_{13}^h	106(106)	120(120)	72
B^h	203	211	120

Note: The experimental data [14] are shown in brackets.

Table 5. Results of the calculation of the charge of a metallic ion (z*), the relative internal displacement (ζ), piezoelectric charge (e_p^*), and piezoelectric constant (e_{14}) for cubic crystals

Quantity	BN	AlN	GaN	InN
z*	0.20	1.04	1.06	1.76
ζ	0.62	0.72	0.72	0.77
e_p^*	–0.25	0.65	0.67	1.46
e_{14}, C/m^2	–0.19	0.54	0.53	0.95

crystals by the formulas given in [4, 5]. The values of susceptibility χ_{14}^e increase with increasing polarity α_p; the elecrtooptical coefficients, remaining negative, increase in magnitude in the BN ⟶ InN series. In contrast to the original approach [2, 3], we took into account the band effects in frames of the extended method of bonding orbitals. The photoelastic constants p_{ij}, obtained from the expressions derived previously by analogy with the elastic constants, change from large-magnitude negative values for BN to small positive values for InN. Unfortunately, the corresponding experimental data are not available to us. The same is true for the values χ_{33}, χ_{13}, and p_{ij} for hexagonal crystals. From the calculations, it follows that the magnitudes of the susceptibilities χ_{33} (>0) and χ_{13} (<0) increase in the BN ⟶ InN series; the changes in p_{ij} have the same tendency as for cubic crystals.

The results of the calculations of elastic constants for cubic, C_{ij}^c, and hexagonal, C_{ij}^h, crystals and the corresponding bulk moduli (B^c and B^h), derived by us previously in terms of the Keating–Harrison model [15, 6], are given in Table 4. In calculations, we used the experimental data on elastic properties of GaN hexagonal crystals [16] and polycrystalline AlN films [17]. It should be pointed out that the *ab initio* calculations [18] yield B^c = 195 and 195 GPa, B^h = 195 and 194 GPa, for GaN and AlN, respectively. The values of C_{ij}^h, which are close to those calculated by us, were obtained theoretically in [19].

Table 5 contains the results of the calculations of piezoelectric parameters performed by the method published in [7] for cubic crystals. The calculations show that the charge of a metallic ion z*, the relative internal displacement ζ, piezoelectric charge e_p^*, and piezoelectric constant e_{14} increase in the BN ⟶ InN series. Unfortunately, the constant e_{14} is known only from one publication [20], which gives e_{14} = 0.375 C/m^2 for cubic indium nitrate. This value is 2.5 times smaller than the value obtained by us. Generally speaking, such a discrepancy is not surprising (see, for example, [2]) because the calculation of e_{14} is a complicated problem. In this context, it is worth mentioning that there is a lack of theoretical studies in this field. We know only one publication [21] devoted to the calculation of the piezoelectric constant for hexagonal AlN and ZnO crystals.

The results of the calculation of phonon frequencies (in cm^{-1}) for cubic crystals using the formulas given in [8] are listed in Table 6. According to [22], the experimental frequencies of transverse and longitudinal optical phonons are equal to $\omega_{TO}(0)$ = 478 cm^{-1} and $\omega_{LO}(0)$ = 694 cm^{-1}, which is in excellent agreement with our results. The *ab initio* calculations [18] yield $\omega_{TO}(0)$ = 648 and 558 cm^{-1} for AlN and GaN, respectively, which is, on average, 1.5 times larger than our

Table 6. Results of the calculations of phonon frequencies (in cm^{-1}) for cubic crystals

Quantity	AlN	GaN	InN
$\omega_{TO}(0)$	454	545	474
$\omega_{LO}(0)$	606	703	640
$\omega_{TA}(2\pi/a)$	205	246	213
$\omega_{LA}(2\pi/a)$	368	442	383

Table 7. Results of the calculation of deformation potential of the conduction band (E_{dc}) and orbital diamagnetic (χ_L), paramagnetic (χ_P), core diamagnetic (χ_C), and total magnetic (χ) permittivities for cubic crystals

Quantity	BN	AlN	GaN	InN
$-E_{dc}$, eV	6.76	4.49	4.43	3.54
$\chi_L \times 10^6$	–2.43	–2.02	–1.97	–1.78
$\chi_P \times 10^6$	2.01	1.22	1.18	0.86
$\chi_C \times 10^6$	–0.01	–0.18	–0.56	–1.49
$\chi \times 10^6$	–0.43	–0.98	–1.85	–2.41

values. Similar results for the same compounds are given in [23]. The results of *ab initio* calculations [24] for GaN are also close to ours. Using the data for hexagonal GaN and AlN obtained in [25], we calculated the following frequencies at $T = 300$ K: $\omega_{TO}(0) = 532 - A_1(TO)$, $599 - E_1(TO)$, $\omega_{LO}(0) = 734 - A_1(LO)$, $741 - E_1(LO)$ for GaN; $\omega_{TO}(0) = 611 - A_1(TO)$, $670 - E_1(TO)$, $\omega_{LO}(0) = 881 - A_1(LO)$, $922 - E_1(LO)$ for AlN (henceforth, all frequencies are given in cm^{-1}). Comparison with our results obtained for cubic crystals shows that the agreement is quite satisfactory for thallium nitrate, while our values for aluminum nitrate are approximately 1.5 times smaller than the experimental ones. As for the low-frequency modes, the authors of [25] reported the following frequencies for transverse acoustic phonon $\omega_{TA}(2\pi/a)$ (E_2(low)): 144 and 245 for GaN and AlN, respectively. These values are in excellent agreement with our results for indium nitrates and smaller by a factor of 0.7 with respect to our value obtained for aluminum nitrate. The results of *ab initio* calculations of low-frequency modes of transverse acoustic phonons $\omega_{LA}(2\pi/a)(B_1(\mathrm{low}))$ in [26] differ from those obtained by us, on average, by 1.5 times. Thus, a simplified approach to the calculation of frequencies proposed in [8] yields a semiquantitative agreement with the experiment.

Table 7 contains the results of the calculation of the deformation potential (E_{dc}) of the conduction band and the orbital diamagnetic (χ_L), paramagnetic (χ_P), core diamagnetic (χ_C), and total (χ) magnetic permittivities for cubic crystals. The calculations were performed according to the method suggested in [9, 10] for cubic crystals. One can easily see the trends in the change of polarity α_p. Unfortunately, the corresponding experimental data are not available.

In conclusion, we suggest a relationship between the covalence α_c, according to Harrison, with ionicity f_i, according to Phillips (see, for example, [8]):

$$f_i = 1 - \alpha_c^3.$$

Then, in the BN → AlN → GaN → InN series, we have $f_1 = 0.13$, 0.36, 0.37, and 0.49.

To summarize, we may state that the simplified method developed by us for calculating the physical characteristics of semiconductor crystals, on the basis of a modification of Harrison's bonding-orbitals method and in combination with crystallographic analogies and some semiempirical models (like Keating's model), can provide a reasonable description of properties of III-nitrates. Such an approach allows one to estimate in a simple way a required property of both pure compounds and alloys.

REFERENCES

1. *Proceedings of the 7th International Conference on Silicon Carbide, III-Nitrides and Related Materials, Stockholm, 1997*, Ed. by G. Pensl, H. Morkoc, B. Monemar, and E. Janzen (Trans Tech Publications, Switzerland, 1998).
2. W. A. Harrison, *Electronic Structure and the Properties of Solids: The Physics of the Chemical Bond* (Freeman, San Francisco, 1980; Mir, Moscow, 1983), Vol. 1.
3. W. A. Harrison, Phys. Rev. B **27**, 3592 (1983).
4. S. Yu. Davydov and S. K. Tikhonov, Fiz. Tverd. Tela (St. Petersburg) **37**, 3044 (1995) [Phys. Solid State **37**, 1677 (1995)].
5. S. Yu. Davydov and S. K. Tikhonov, Fiz. Tekh. Poluprovodn. (St. Petersburg) **31**, 823 (1997) [Semiconductors **31**, 698 (1997)].
6. S. Yu. Davydov and A. V. Solomonov, Pis'ma Zh. Tekh. Fiz. **25** (15), 23 (1999) [Tech. Phys. Lett. **25**, 601 (1999)].
7. S. Yu. Davydov and S. K. Tikhonov, Fiz. Tekh. Poluprovodn. (St. Petersburg) **30**, 968 (1996) [Semiconductors **30**, 514 (1996)].
8. S. Yu. Davydov and S. K. Tikhonov, Fiz. Tekh. Poluprovodn. (St. Petersburg) **30**, 834 (1996) [Semiconductors **30**, 447 (1996)].
9. S. Yu. Davydov and S. K. Tikhonov, Fiz. Tekh. Poluprovodn. (St. Petersburg) **30**, 1137 (1996) [Semiconductors **30**, 602 (1996)].
10. S. Yu. Davydov and S. K. Tikhonov, Fiz. Tekh. Poluprovodn. (St. Petersburg) **30**, 695 (1996) [Semiconductors **30**, 375 (1996)].
11. *Handbook of Physical Quantities*, Ed. by I. S. Grigoriev and E. Z. Meilikhov (Énergoizdat, Moscow, 1991; CRC Press, Boca Raton, 1997).
12. *Landolt-Bornstein: Numerical Data and Functional Relationships in Science and Technology, New Series* (Springer-Verlag, Berlin, 1982), Group III, Vol. 17a.
13. J. A. Sanjurijo, E. Lopez-Cruz, P. Vogl, and M. Cardona, Phys. Rev. B **28**, 9237 (1983).

14. K. Karch, J.-M. Wagner, H. Siegle, *et al.*, in *Proceedings of the 7th International Conference on Silicon Carbide, III-Nitrides and Related Materials, Stockholm, 1997*, Ed. by G. Pensl, H. Morkoc, B. Monemar, and E. Janzen (Trans Tech Publications, Switzerland, 1998), p. 303.
15. S. Yu. Davydov and S. K. Tikhonov, Fiz. Tekh. Poluprovodn. (St. Petersburg) **30**, 1300 (1996) [Semiconductors **30**, 683 (1996)].
16. A. Polian, M. Grimsditch, and I. Grzegory, J. Appl. Phys. **79**, 3343 (1996).
17. A. V. Dobrynin, I. P. Kazakov, and G. A. Naĭda, Zarubezhn. Élektron. Tekh. **4**, 44 (1989).
18. K. Miwa and A. Fukumoto, Phys. Rev. B **48**, 7897 (1993).
19. A. F. Wright, J. Appl. Phys. **82**, 2833 (1997).
20. V. W. Chen, T. L. Tansley, and T. Osotchan, J. Appl. Phys. **75**, 7365 (1994).
21. T. Kamiya, J. Appl. Phys. **35**, 4421 (1996).
22. K. Osamura, S. Naka, and Y. Murakami, J. Appl. Phys. **46**, 3432 (1975).
23. I. Gorczyca, N. E. Christensen, E. L. Peltzer y Blanca, and C. O. Rodriguez, Phys. Rev. B **51**, 11936 (1995).
24. H. Sterner, A. Schevwiola, K. Karch, *et al.*, in *Proceedings of the 7th International Conference on Silicon Carbide, III-Nitrides and Related Materials, Stockholm, 1997*, Ed. by G. Pensl, H. Morkoc, B. Monemar, and E. Janzen (Trans Tech Publications, Switzerland, 1998), p. 264.
25. V. Yu. Davydov, Yu. E. Kitaev, I. N. Goncharuk, *et al.*, Phys. Rev. B **58**, 12899 (1998).
26. K. Karch, J.-M. Wagner, and F. Bechstedt, Phys. Rev. B **57**, 7043 (1998).

Translated by A. Zalesskiĭ

Semiconductors, Vol. 36, No. 1, 2002, pp. 45–47. Translated from Fizika i Tekhnika Poluprovodnikov, Vol. 36, No. 1, 2002, pp. 49–51.
Original Russian Text Copyright © 2002 by Nesmelova, Baryshev, Andreev.

ELECTRONIC AND OPTICAL PROPERTIES OF SEMICONDUCTORS

Optical Absorption by Transitions between Subbands of Light and Heavy Holes in *p*-$Mn_xHg_{1-x}Te$

I. M. Nesmelova*, N. S. Baryshev†, and V. A. Andreev
FNPTS NPO "State Institute of Applied Optics", Kazan', 420075 Russia
**e-mail: eugene@mi.ru*

Submitted May 8, 2001; accepted for publication May 30, 2001

Abstract—Absorption spectra of *p*-$Mn_xHg_{1-x}Te$ epitaxial films with $x = 0.12$–0.19 in the wavelength range of 2–24 μm at 300 and 80 K were measured. The absorption caused by transitions of charge carriers between subbands of light and heavy holes is calculated according to Kane's theory taking into account the effect of remote bands. The values of the effective masses of heavy and light holes are obtained as functions of solid-solution composition and temperature. The analysis of low-temperature absorption spectra was carried out; the ionization energy of the acceptor level is evaluated. *© 2002 MAIK "Nauka/Interperiodica".*

The advantage of an $Mn_xHg_{1-x}Te$ (MMT) semimagnetic semiconductor in comparison with widely used $Cd_xHg_{1-x}Te$ (MCT) solid solutions is a higher stability of electrical properties. The presence of Mn in the lattice of a ternary compound results in the hardening of the Hg–Te chemical bond, whereas, in MCT, a strong loosening of this bond takes place, which results in the instability of the material. The Mn-bond in MMT is mainly caused by the linkage of the *s*-states of the metal with the tellurium *p* states in the presence of a limited *d*–*p* hybridization.

The main physical properties of MMT (as well as MCT) solid solutions are defined by their energy structure near the Γ point (the center point of the Brillouin zone); in **kp** calculations, one should take into account at least three neighboring bands: Γ_6, Γ_7, and Γ_8. The level (narrow *d*-band) located in the valence band by ~3 eV lower than its top corresponds to the partially filled and highly localized $3d^5$ shell of Mn^{2+} ions. This level does not affect the band structure in the vicinity of the Γ point and, consequently, the electrical properties of the material. However, one can explain a number of special features observed in the transport phenomena under high magnetic field and in magnetooptical phenomena at low temperatures ($T < 40$ K) taking into account only the exchange interaction of band charge carriers with the localized *d* electrons of manganese ions [1].

The electrical properties of MCT solid solutions have been studied adequately, whereas the properties of single crystals and MMT layers are poorly understood. It is necessary to refine the values of band parameters, such as effective masses of charge carriers, scattering mechanisms of free charge carriers, and temperature dependences of a number of energy gaps.

In this paper, we report the results of studying the hole dispersion laws in the valence band of $Mn_xHg_{1-x}Te$ solid solutions; we also determined of the effective masses of heavy- (m_1) and light-hole (m_2) density of states as functions of the composition (x) and temperature (T). The analysis of low-temperature absorption spectra is carried out, and the ionization energies of the acceptor level (E_a) as a function of x are determined at $T = 80$ K.

The authors of publications [2–4] used the values $m_1 = (0.5$–$0.55)m_0$ in theoretical processing of experimental data on MMT samples with $x = 0.08$–0.30; in [5], it was assumed that $m_1 = 0.4m_0$ for the samples with $x = 0.20$–0.22. The electronic parameters of surface layers of MMT single crystals with $x = 0.00$–0.019 were studied in [6]; the values of $m_1 = (0.10$–$0.21)m_0$ were obtained.

We studied the absorption spectra of *p*-$Mn_xHg_{1-x}Te$ ($x = 0.12$–0.19) epitaxial films prepared by liquid-phase epitaxy from tellurium solutions–melts. With the aim of reducing the hole concentration, the layers were subjected to long-term annealing in mercury vapor; as a result, samples with a concentration of uncompensated acceptors $p = 10^{15}$–10^{16} cm^{-3} at 300 K were obtained. Absorption spectra were measured using an IKS-21 spectrometer in the range of 2–24 μm at $T =$ 300 and 80 K.

In the materials with *p*-type conduction and Kane's band structure, the absorption from the long-wavelength side of the fundamental band edge (at photon energies less than the band gap, $h\nu < E_g$) is caused mainly by hole transitions between subbands of the valence band. It has been shown previously [7] that this absorption plays a significant role for InAs, InSb, and CdHgTe. The theoretical processing of experimental spectra allows us to determine the dispersion law and effective masses both for heavy and light holes.

---

† Deceased.

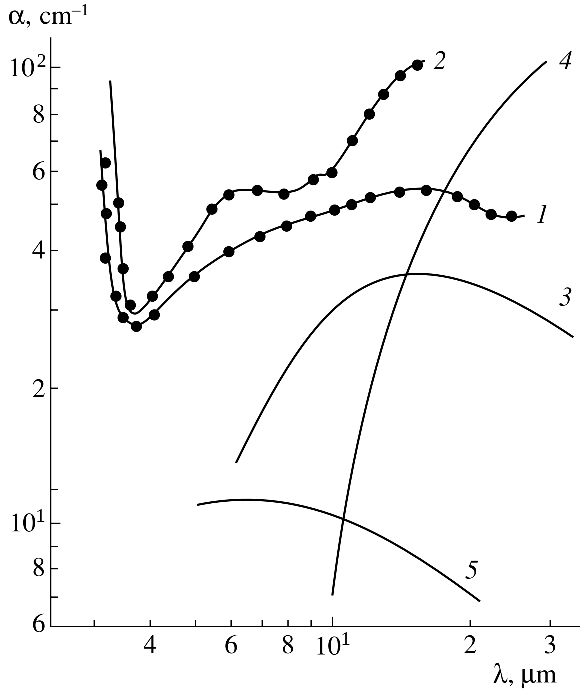

Fig. 1. Absorption spectra of a p-$Mn_xHg_{1-x}Te$ sample with $x = 0.186$: *1* and *2* are experimental spectra; *3–5* are the results of calculations (*3*, *4*) with and (*5*) without consideration of upper bands. T = (*1*, *3*, *5*) 300 and (*2*, *4*) 80 K.

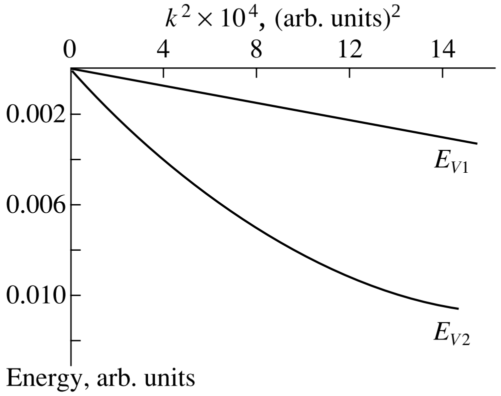

Fig. 2. Structure of $Mn_xHg_{1-x}Te$ ($x = 0.186$) valence band: E_{V1} is the heavy-hole band, E_{V2} is the light-hole band.

The MMT samples with p-type conduction and with $x > 0.12$ were chosen for studies, because the absorption due to charge carrier transitions between subbands of heavy and light holes, $V1 \longrightarrow V2$, is not obscured for these compositions by the edge of the fundamental band (band-to-band transitions). The absorption coefficient (α spectra) for one of the samples with $x = 0.186$ are shown in Fig. 1; the electrical parameters of this sample are presented in Table 1. The concentration and mobility of holes were determined from the measurements of the Hall coefficient R_H and conductivity σ by the Van der Pauw method; the band gap E_g and the content of Mn x were determined from optical measurements and the dependence $E_g(x, T)$ [2]. As can be seen from Fig. 1, in the region of free carrier absorption (at the wavelength $\lambda > 4$ μm), an additional absorption is observed. As the temperature is lowered, the absorption is enhanced and has a more complex structure. To some extent, this is caused by the fact that, as the temperature decreases, the degree of acceptor level ionization decreases and the role of impurity absorption with participation both of conduction and valence bands increases.

Table 1. Electrical parameters of p-$Mn_xHg_{1-x}Te$ sample

x	T, K	E_g, eV	$1/eR_H$, cm^{-3}	σR_H, cm^2 V^{-1} s^{-1}
0.186	300	0.387	3.6×10^{16}	2.0×10^2
	77	0.376	3.3×10^{16}	1.5×10^2

We carried out calculations of the absorption coefficient related to the charge-carrier transitions between the subbands of heavy and light holes $V1 \longrightarrow V2$. Calculations were carried out according to Kane's theory ($E_g < \Delta$) taking into account the nonparabolicity of the light-hole band and corrections to the dispersion laws of holes in bands $V1$ and $V2$; these corrections account for the effect of more remote bands located above the conduction band and below the valence band. The effects of upper and lower bands were estimated according to the second-order perturbation theory. Calculations were carried out similarly to those in [7, 8]. According to Kane's theory, band $V2$ is nonparabolic and the value of m_2 was defined as [9]

$$m_2 = \left(\frac{\hbar^3 k}{2\sqrt{2}} \frac{1}{\sqrt{E_{V2}}(dE_{V2}/dk^2)} \right)^{2/3},$$

where E_{V2} is the dispersion law of light holes and k is the absolute value of the wave vector.

For the $Mn_xHg_{1-x}Te$ solid solution, several sets of band parameters have been reported, in which the effect of remote bands on the main bands, as well as the interaction of the conduction band and valence band via the other bands, has been taken into account. On the basis of experimental data, the band parameters were determined in [10] for $x = 0.005$, and in [5], for $x = 0.20$–0.22. In review [1], the values of band parameters for $x = 0.155$ obtained by calculations in [11] are given: $\gamma_1 = 27.5$, $\gamma_2 = \gamma_3 = 12.5$, $\chi = 15$ (in the Luttinger notation). Calculations were carried out with three sets of band parameters. We have achieved the best agreement between theory and experiment by using the band parameters presented in [1] (Fig. 1, curves *3* and *4*). The values of density-of-states effective masses for heavy and light holes are calculated. The results of calculations in the vicinity of the Γ point for compositions with $x = 0.119$, 0.135, and 0.186 at $T = 300$ and 80 K are listed in Table 2. The dispersion laws of heavy and light

Table 2. Band parameters of p-Mn$_x$Hg$_{1-x}$Te ternary solid solutions

x	T, K	m_1/m_0	m_2/m_0	E_g, eV	E_a, eV
0.199	300	0.27	0.0286	0.217	
	80		0.0261	0.175	0.062
0.135	300	0.27	0.0320	0.253	
	80		0.0304	0.228	0.073
0.186	300	0.27	0.0446	0.387	
	80		0.0435	0.376	0.128

holes as a function of wave-vector squared for a MMT solid solution with $x = 0.186$ are illustrated in Fig. 2.

As can be seen from Fig. 1, the calculated spectra at $T = 300$ K for transitions $V1 \longrightarrow V2$ satisfactorily describe the experiment. The absorption spectra at $T = 80$ K in the region of $\lambda = 5$–10 μm have features which are not described by intersubband transitions $V1 \longrightarrow V2$. We assumed that this structure was caused by charge-carrier transitions from the acceptor level either to the conduction band or to the subband of light holes. The analysis of low-temperature spectra allowed us to estimate the ionization energy E_a of an acceptor level as a function of the composition (see Table 2).

Thus, the analysis of the absorption spectra for the long-wavelength side of the fundamental band of epitaxial layers of p-Mn$_x$Hg$_{1-x}$Te ternary solutions with $x = 0.12$–0.19 was carried out at 300 and 80 K. The dispersion laws and the values of the effective masses of heavy and light holes are calculated as functions of composition and temperature; the estimate of ionization energy at $T = 80$ K as a function of the composition is carried out.

ACKNOWLEDGMENTS

We thank M.P. Mezentseva and T.V. Chugunova for providing us with the samples.

REFERENCES

1. I. I. Lyapilin and I. M. Tsidil’kovskiĭ, Usp. Fiz. Nauk **146** (1), 35 (1985) [Sov. Phys. Usp. **28**, 349 (1985)].
2. J. Kaniewski and A. Mycielski, Solid State Commun. **41**, 959 (1982).
3. A. Rogalski, Infrared Phys. **31**, 117 (1991).
4. P. I. Baranskii, O. P. Gorodnichii, and N. V. Shevchenko, Infrared Phys. **30**, 259 (1990).
5. E. I. Georgitsé, V. I. Ivanov-Omskiĭ, and D. I. Tsypishka, Fiz. Tekh. Poluprovodn. (St. Petersburg) **32**, 450 (1998) [Semiconductors **32**, 401 (1998)].
6. A. M. Belykh, O. V. Romanov, N. N. Semenov, and V. I. Kalenik, in *Proceedings of the II All-Union Workshop “Impurities and Defects in Narrow-Gap Semiconductors”, Pavlodar, 1989*, Part I, p. 20.
7. I. M. Nesmelova, *Optical Properties of Narrow-Gap Semiconductors* (Nauka, Novosibirsk, 1992).
8. I. M. Nesmelova, Z. K. Tulvinskaya, and N. S. Baryshev, Zh. Prikl. Spektrosk. **50**, 480 (1989).
9. O. Madelung, *Physics of III–V Compounds* (Wiley, New York, 1964; Mir, Moscow, 1967).
10. K. Takita, T. Uchino, T. Gochou, and K. Masuda, Solid State Commun. **61**, 535 (1987).
11. T. R. Gawron and Y. Trylski, in *Proceedings of the 4th International Conference on Physics of Narrow Gap Semiconductors, Linz, Austria, 1981* (Springer-Verlag, Berlin, 1982), p. 312.

Translated by T. Galkina

Semiconductors, Vol. 36, No. 1, 2002, pp. 48–53. Translated from Fizika i Tekhnika Poluprovodnikov, Vol. 36, No. 1, 2002, pp. 52–58.
Original Russian Text Copyright © 2002 by Kuz'menko, Ganzha, Domashevskaya.

SEMICONDUCTOR STRUCTURES, INTERFACES, AND SURFACES

A Combined Technique for Studying the Multicomponent Spectra of Photoreflection from Semiconductors

R. V. Kuz'menko*, A. V. Ganzha, and É. P. Domashevskaya
Voronezh State University, Universitetskaya pl. 1, Voronezh, 394893 Russia
** e-mail: roman@ftt.vsu.ru*

Submitted April 26, 2001; accepted for publication May 11, 2001

Abstract—A new technique for studying the multicomponent photoreflection spectra in semiconductors involves spectra measurements at different laser fluences and wavelengths in combination with spectrum phase analysis. To demonstrate the possibilities offered by the technique, the multicomponent photoreflection spectrum of the passivated homoepitaxial Si_3N_4/n-GaAs/n^+-GaAs wafer is analyzed. *© 2002 MAIK "Nauka/Interperiodica".*

Photoreflection (PR) is a widely used modulation-optical technique for studying the electronic properties of semiconductors. On the one hand, the method is simple to realize in experiment and, on the other, it provides a great variety of data. This advantageous combination motivated its widespread use. However, the PR spectra measured in experiment can only be interpreted using qualitative analysis, which implies simulation (fitting) of the entire spectrum line.

As has been shown [1–4], the PR spectra of a single GaAs crystal measured at room temperature in the fundamental transition region E_0 are generally multicomponent. This fact is due to a set of closely spaced electron-optical transitions of various natures in the vicinity of the E_0 transition, as well as to the diversified processes accompanying the photogeneration of the high-density nonequilibrium plasma of charge carriers. Another problem for PR measurements in homoepitaxial and heteroepitaxial structures is associated with the interfaces buried as deep as 5–10 μm, which may, under certain conditions, contribute to the PR spectrum. Therefore, for high-precision quantitative analysis of multicomponent PR spectra, one should determine the number of spectral components, the measurability energy range for each of the components, the corresponding electron-optical transition type, and the modulation mechanism responsible for the component.

Phase analysis (PA) is one of the most powerful methods for studying multicomponent PR spectra [4, 5]. For different characteristic time constants, which in the first approximation are the delay time of the modulated reflection signal with respect to the excitation one, the multicomponent PR spectrum structure can be determined on the basis of a phase diagram. In one-component spectral regions, the corresponding phase diagram appears as a straight line with its tilt angle directly related to the characteristic time constant of the component. In certain cases, comparing the characteristic time constants obtained by PA may help to clarify the nature of the modulation mechanism or to localize the regions of the component's origin. For two-component PR spectra, one can suppress either of the components in the *x* or *y* direction by choosing a certain phase of the phase-sensitive amplifier and, thus, yield the true spectral line of the remaining component. However, the PA gives no means for the separation of overlapping components with close or equal time constants. The PA technique is also ineffective if three or more spectral components overlap. Therefore, the opportunities that PA offers for studying multicomponent spectra are generally limited.

Another possibility for studying the multicomponent spectra of PR is opened by varying the laser excitation wavelength. The reflection modulation associated with the laser-induced nonequilibrium carriers can be due to (1) the direct generation of nonequilibrium carriers in the PR origination region and (2) the diffusion or drift of the generated minority carriers towards the PR origination region. For a component that arises from a deeply buried interface, the first modulation mechanism can be excluded by a decrease in the laser wavelength. A further decrease in the wavelength may give rise to a situation where the nonequilibrium carriers are mainly generated in the space-charge region near the surface. In this case, only an insignificant number of nonequilibrium minority carriers reach the interface, and the PR signal appearing in this region will be attenuated or completely suppressed. In contrast, the use of short-wavelength laser radiation should amplify spectral components originating in the surface region. Hence, variation in the laser excitation wavelength seems to be one of the most reliable means of determining the spatial origin of the modulation components.

An interesting opportunity is provided by the permanent illumination of a sample with one of the lasers. For example, short-wavelength illumination together with modulating long-wavelength irradiation should reduce the spectral contribution of the sample surface [6, 7].

The third technique connected with multicomponent PR spectrum analysis is the detection of the spectral series as a function of laser excitation density [8]. Since the excitation density governs the number of nonequilibrium carriers generated and since the components of a multicomponent PR spectrum originate from the region of different electron-optical transitions or from the different spatial regions, it seems reasonable that the same variation in the excitation density produces a different change in the parameters of the corresponding modulation process and, therefore, in the spectral contribution of various photoreflection components [9–11]. Consequently, tracing the behavior of a spectral line in the spectral series measured for the different excitation densities, in most cases, allows one to infer the energy range of the components, as well as the modulation mechanism responsible for their appearance.

A technique combining the PA and the PR spectra measurements for different laser wavelengths and excitation densities within a single experimental procedure may not only yield the number of the spectral components and their energy ranges but may also suggest the modulation mechanisms. This is conducive to the choice of an adequate model for the component spectral shape and, thus, significantly improves the reliability of the quantitative analysis of the multicomponent PR spectrum.

We will demonstrate the potential of the combined technique by the example of the E_0 spectrum of PR from a (100) Si_3N_4/n-GaAs/n^+-GaAs wafer with the electron densities in the GaAs epilayer and the substrate $n = 7 \times 10^{15}$ cm^{-3} and $n^+ = 3 \times 10^{18}$ cm^{-3}, respectively; E_0(GaAs) = 1.424 eV. The homoepitaxial wafer was produced by molecular-beam epitaxy; a Si_3N_4 layer was then formed by the chemical-plasma deposition. The GaAs epilayer thickness specified by the manufacturer (Institute of Solid-State Physics, Technical University, Berlin, Germany) was 1 μm; the Si_3N_4 layer was about 100 nm thick. The experiments were carried out at room temperature using the setup described in detail elsewhere [11]. An SR850 two-channel phase-sensitive amplifier was employed for the phase analysis. Laser excitation was in the range of $L = 0.1$–1 W/cm^2. The modulation frequency varied within 50–500 Hz.

Figure 1 shows (a) the experimental photoreflection spectrum $\Delta R/R = f(E)$ measured while being modulated by a red He–Ne laser (wavelength $\lambda = 632.8$ nm, absorption depth in GaAs $1/\alpha = 250$ nm) with $L = 1$ W/cm^2 and (b) the corresponding $x'y'$ phase diagram (see [5]). As can be seen from Fig. 1a, the PR spectrum structure is rather complex. The low-energy region features the so-called low-energy oscillations. According to [12], the oscillations stem from the contribution of a broadened electromodulation E_0 component that originates near the n-GaAs/n^+-GaAs interface on the heavily doped substrate side. During the epitaxial growth of the n-GaAs films on n substrates, the Fermi level becomes pinned to the states of traps located near the interface. The Fermi level is assumed [7] to be located by ~0.5 eV below the conduction band edge. This value points to the capture of the minority carriers by the electric field near the n-GaAs/n^+-GaAs interface. Therefore, the observation of the components that originated in the vicinity of the n-GaAs/n^+-GaAs interface is not surprising.

Franz–Keldysh oscillations observed in the high-energy spectral range indicate the presence of a midfield electromodulation E_0 component that originates in the space-charge region of the GaAs epitaxial film near the Si_3N_4/n-GaAs interface. However, the disruption of continuous oscillations suggests the presence of another component in the energy range concerned. The phase diagram (Fig. 1b) also unambiguously confirms the spectrum's multicomponent character (loop structures) but gives no idea of the number of components.

As a next step, we attempted to suppress the components originating from the interface region by using a blue He–Cd laser (wavelength $\lambda = 442.5$ nm, absorption depth in GaAs $1/\alpha = 30$ nm). The results obtained for two densities of excitation are presented in Figs. 1c and 1d. Low-energy oscillations are seen to be completely suppressed, which indicates that the near-interface region does not contribute to the spectrum. An unexpected considerable simplification of the PR spectrum structure occurs in the region of Franz–Keldysh oscillations. Therefore, the distortion of the Franz–Keldysh oscillations, which was observed with the red laser irradiation, is due to the superposition of a component that originated from the homoepitaxial n-GaAs/n^+-GaAs interface. The corresponding phase diagram (Fig. 1d) remains complex, demonstrating that the spectrum is multicomponent. Nevertheless, a change in the main peak structure with the excitation density (a "shoulder" structure appears) indicates the presence of an exciton component, which stems from electromodulation (for details, see [4, 11, 13]). Two-component simulation data confirm the presence of the midfield electromodulation and the exciton components. Hence, using the blue laser, we managed to identify the PR spectrum components originating from the sample surface region.

We pursue our identification of the spectrum components using the red He–Ne laser for modulation and the blue He–Cd laser for steady illumination. Illumination makes it possible to decrease the electric-field strength near the Si_3N_4/n-GaAs interface or even to suppress it completely, which results in attenuation or extinction of components from this region. The results of measurements are shown in Fig. 2. In our opinion, the PR spectrum shown originates near

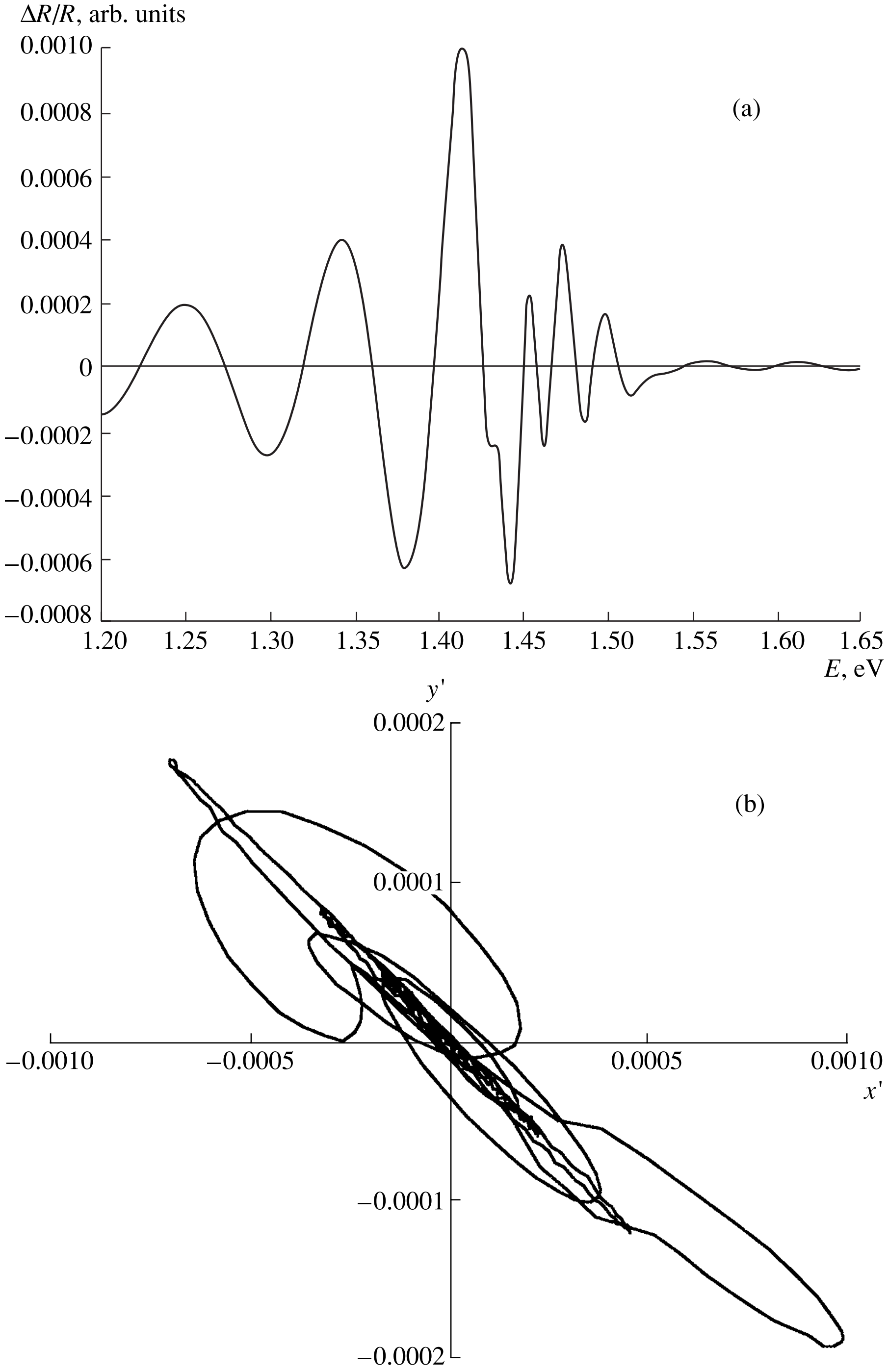

Fig. 1. (a, c) Photoreflection spectra and (b, d) phase diagrams of Si_3N_4/GaAs/GaAs. (a, b) He–Ne laser modulation, $L = 1$ W/cm^2. (c, d) He–Cd laser modulation, L = (the solid line) 0.2 and (dashed line) 0.5 W/cm^2.

the *n*-GaAs/n^+-GaAs interface and consists of the midfield and the broadened electromodulation components. Interfering in the film, the latter gives rise to the low-energy oscillations. This conclusion is supported by the following reasoning. Since the midfield electromodulation component features a great number of Franz–Keldysh oscillations, its energy broadening is actually small [14]. Therefore, this component cannot cause the low-energy oscillations; moreover, it cannot originate in the space-charge region of the substrate, since a heavily doped substrate gives rise to the spectra with large energy broadening γ. Hence, this component originates from the region of the homoepitaxial *n*-GaAs/n^+-GaAs interface in the epilayer space-

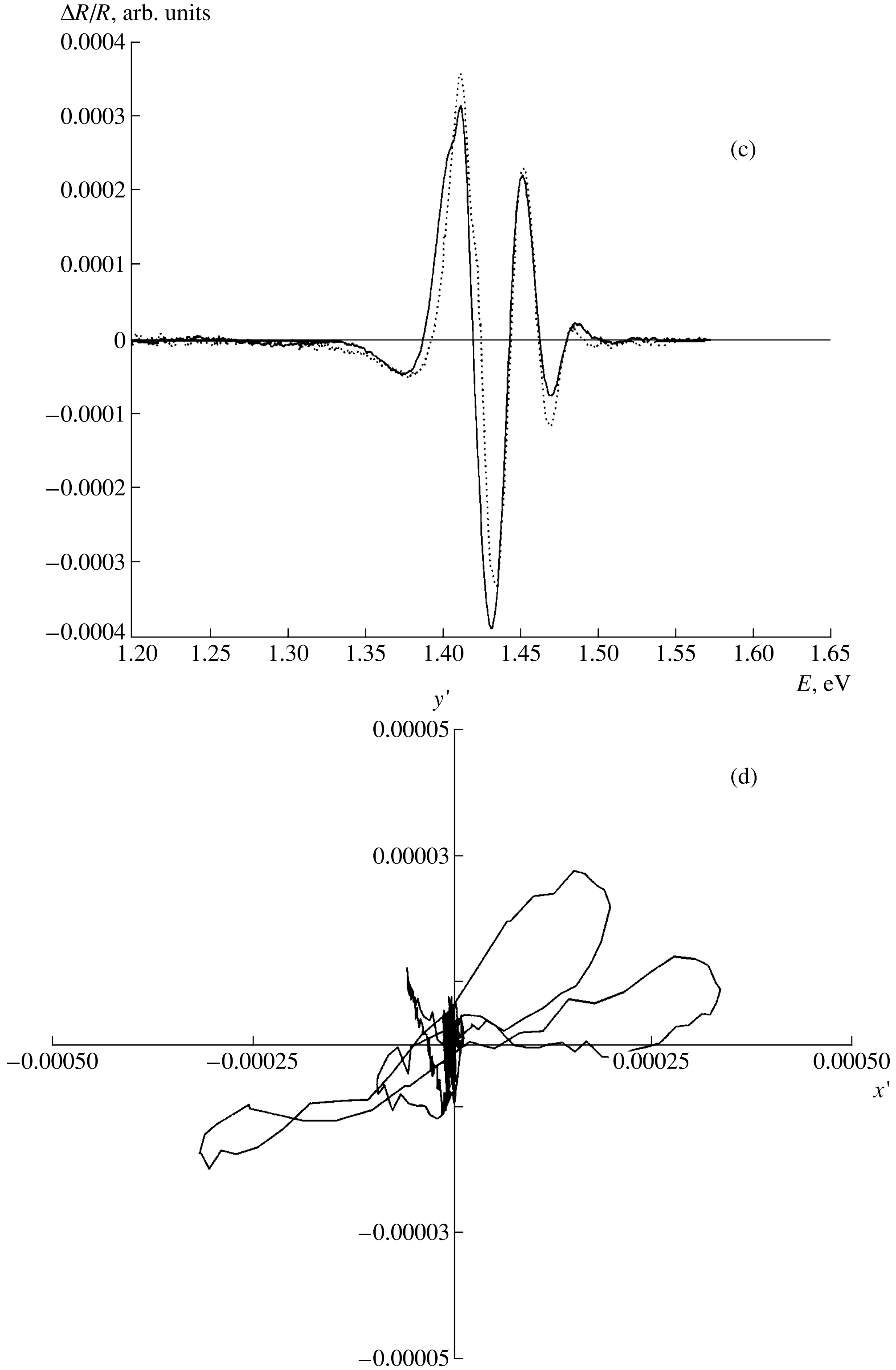

Fig. 1. (Contd.)

charge region. On the other hand, only a structure with a high broadening energy is capable of producing low-energy oscillations. Such a structure may appear in the substrate region only.

As is evident from the foregoing, the n-GaAs/n^+-GaAs interface makes two contributions to the resultant spectrum. Within the limits of experimental error, the phase diagram of the measured PR spectrum is represented by

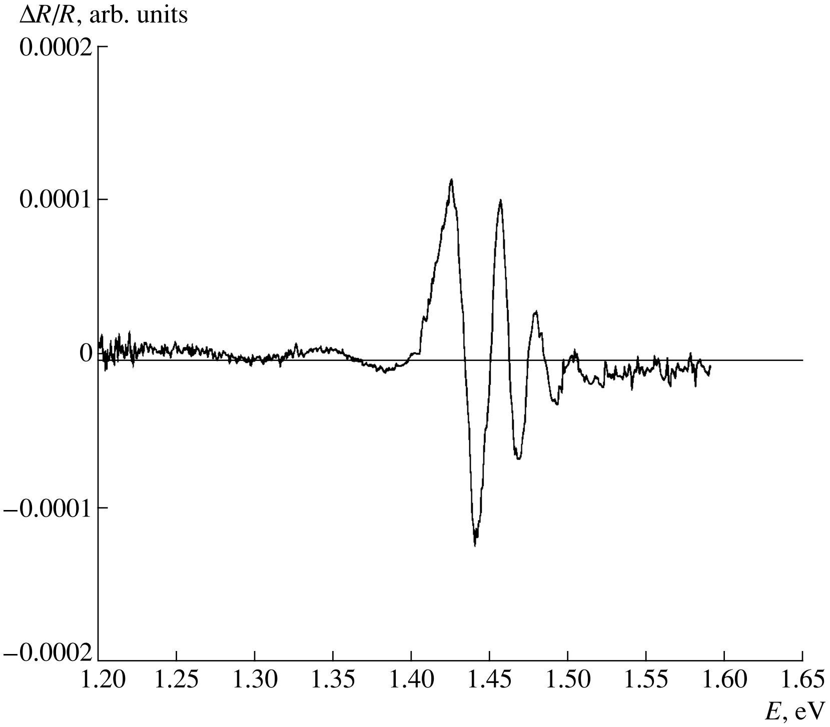

Fig. 2. Photoreflection spectrum for Si_3N_4/GaAs/GaAs structure with He–Ne laser modulation and He–Cd laser steady illumination.

a straight line, which indicates that characteristic time constants of electromodulation processes are identical on either side of the interface.

The experimentally observed line shape of the midfield electromodulation component, which originates from a deeply lying interface, may evidently be distorted by the interference in the epilayer. However, the interference effect on the energies of the Franz–Keldysh oscillations should not be considerable. This circumstance enabled the main parameters of the midfield component to be evaluated [14]. The electric-field strengths at the Si_3N_4/n-GaAs and n-GaAs/n^+-GaAs interfaces are nearly equal: $F_s = 4.23 \times 10^6$ V/m and $F_i = 3.87 \times 10^6$ V/cm. The midfield component originating near the Si_3N_4/n-GaAs interface is shifted to the lower energies (the respective transition energies E_0 were estimated at 1.415 and 1.424 eV) and has a much greater broadening energy, $\Gamma_s = 16.5$ meV and $\Gamma_i = 4.5$ meV. The lower broadening energy typical of the deeply buried interface can be attributed to the structure characteristics of the buried interface, which are superior to those of the Si_3N_4/n-GaAs surface region. The low-energy shift of the component that originated from the Si_3N_4/n-GaAs surface region will be discussed below.

Thus, our analysis suggests that the spectrum measured in the sample (Fig. 1a) is a superposition of four components: two midfield electromodulation components, which originated in the epitaxial film in the space-charge region near the Si_3N_4/n-GaAs and n-GaAs/n^+-GaAs interfaces; an exciton component originating from the homoepitaxial film surface; and an electromodulation component, which originated at the homoepitaxial n-GaAs/n^+-GaAs interface in the space-charge region of the heavily doped substrate.

In order to check the results, we carried out layer-by-layer etching of the wafer (etching step of 200 nm) and measured the spectra under red He–Ne laser illumination. The corresponding spectra are plotted in Fig. 3. Spectrum *1* was measured prior to etching. The shift of the PR spectrum to higher energies (curve *2*) after the etching of the Si_3N_4 layer is due to the relief of the stress that had been present near the heteroepitaxial Si_3N_4/GaAs interface. An increase in the low-energy oscillations period (spectra *2*–*4*) is indicative of a decrease in the GaAs homoepilayer thickness. With further etching, the low-energy oscillations vanish, and, then, the midfield and the exciton components vanish from the surface region. Concurrently, the contribution of the broadened spectral structure that originates in the substrate space-charge region (spectra *4*–*6*) increases. Additional etching leaves the spectrum unchanged. Spectrum *6*, characterized by a one-component phase diagram, was associated with a broadened midfield electromodulation E_0 component. Qualitatively, it featured extremely high values of the electric-field strength ($F > 10^7$ V/m) and the broadening energy ($\Gamma >$ 50 meV). Furthermore, this component has a broad low-energy "tail", whose presence is necessary for the low-energy oscillations to occur.

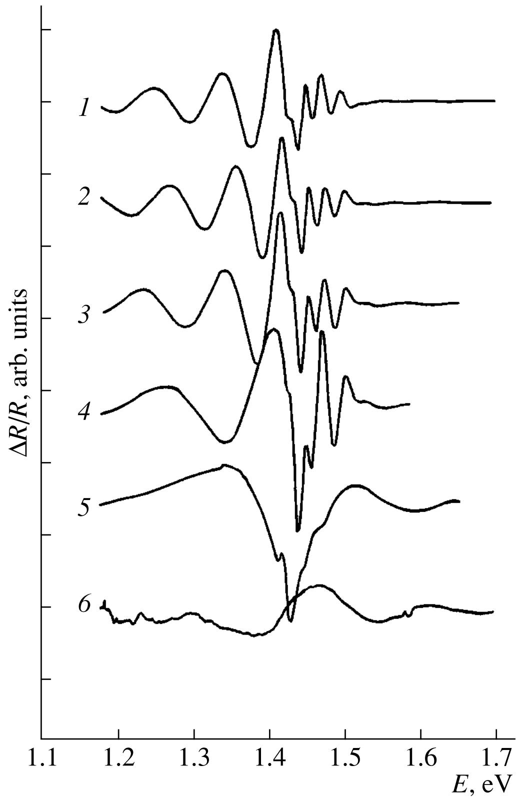

Fig. 3. Photoreflection spectra of a Si_3N_4/GaAs/GaAs structure subjected to layer-by-layer etching.

Of course, the broadened electromodulation component considered above also contributes somewhat to the high-energy region of the resultant spectrum taken from the initial homoepitaxial wafer. However, in the context of our analysis, this contribution is small and can be disregarded.

Our data support the assumption that the low-energy oscillations stem from the modulation of the substrate space-charge region, while the two midfield components stem from the modulation of the space-charge regions of the epilayer. It should be noted that the data obtained by etching does not yield any additional information except for the partial confirmation of data that were obtained within the scope of the combined study.

In conclusion, we suggest a new technique for studying multicomponent PR spectra. Our method combines measurements of spectra for different laser excitation densities and wavelengths with phase analysis. This combined technique allows one to determine the number of spectral components, their measurable energy ranges, the spatial regions of their origin, the relevant electron-optical transition type, and the associated modulation mechanism. The multicomponent PR spectrum of a homoepitaxial GaAs wafer was considered to demonstrate the potential of this method.

REFERENCES

1. J. M. A. Gilman, A. Hamnett, and R. A. Batchelor, Phys. Rev. B **46**, 13363 (1992).
2. O. J. Glembocki, N. Bottka, and J. E. Furneaux, J. Appl. Phys. **57** (2), 432 (1985).
3. E. G. Seebauer, J. Appl. Phys. **66**, 4963 (1989).
4. R. Kuz’menko, A. Ganzha, J. Schreiber, and S. Hildebrandt, Fiz. Tverd. Tela (St. Petersburg) **39**, 2123 (1997) [Phys. Solid State **39**, 1900 (1997)].
5. A. V. Garzha, V. Kircher, R. V. Kuz’menko, *et al.*, Fiz. Tekh. Poluprovodn. (St. Petersburg) **32**, 272 (1998) [Semiconductors **32**, 245 (1998)].
6. M. Sydor, A. Badakhshan, J. R. Engholm, and D. A. Dale, Appl. Phys. Lett. **58**, 948 (1991).
7. Y. Mochizuki, T. Ishii, and M. Mizuta, Jpn. J. Appl. Phys., Part 1 **34**, 6106 (1995).
8. R. E. Nahory and J. L. Shay, Phys. Rev. Lett. **21**, 1569 (1968).
9. R. Ditchfield, D. Llera-Rodriguez, and E. G. Seebauer, Phys. Rev. B **61**, 13710 (2000).
10. E. R. Wagner and A. Manselis, Phys. Rev. B **50**, 14228 (1994).
11. S. Hildebrandt, M. Murtagh, R. Kusmenko, *et al.*, Phys. Status Solidi A **152**, 147 (1995).
12. R. V. Kuz’menko, A. V. Ganzha, and É. P. Domashevskaya, Opt. Spektrosk. **89**, 601 (2000).
13. R. V. Kuz’menko, A. V. Ganzha, O. V. Bochurova, *et al.*, Fiz. Tekh. Poluprovodn. (St. Petersburg) **34**, 73 (2000) [Semiconductors **34**, 73 (2000)].
14. R. Kuz’menko, A. Ganzha, É. P. Domashevskaya, *et al.*, Fiz. Tekh. Poluprovodn. (St. Petersburg) **34**, 1086 (2000) [Semiconductors **34**, 1045 (2000)].

Translated by A. Sidorova-Biryukova

Semiconductors, Vol. 36, No. 1, 2002, pp. 54–59. Translated from Fizika i Tekhnika Poluprovodnikov, Vol. 36, No. 1, 2002, pp. 59–64.

Sulfide Passivating Coatings on GaAs(100) Surface under Conditions of MBE Growth of ⟨II–VI⟩/GaAs

I. V. Sedova*, T. V. L'vova, V. P. Ulin, S. V. Sorokin, A. V. Ankudinov, V. L. Berkovits, S. V. Ivanov, and P. S. Kop'ev

Ioffe Physicotechnical Institute, Russian Academy of Sciences,
Politekhnicheskaya ul. 26, St. Petersburg, 194021 Russia
** e-mail: irina@beam.ioffe.rssi.ru*

Submitted May 21, 2001; accepted for publication May 31, 2001

Abstract—Atomic-force microscopy was applied to compare the topographies of naturally oxidized surfaces of GaAs(100) substrates and those substrates treated with aqueous solutions of sodium sulfide in various stages of their preparation for growth of ZnSe-based heterostructures by molecular beam epitaxy (MBE). It was found that annealing of oxidized substrates strongly disrupts the surface planarity and leads to the appearance of pits with density of 10^{10} cm^{-2}. The pit density can be reduced by two orders of magnitude by treating the substrate surface with an aqueous solution of Na_2S. Transmission electron microscopy demonstrated that sulfidation of GaAs substrates makes it possible to reduce the number of stacking faults at the ZnSe/GaAs interface to $\sim 3 \times 10^5$ cm^{-2} and, correspondingly, to improve the structural perfection of MBE-grown II–VI layers and heterostructures. *© 2002 MAIK "Nauka/Interperiodica".*

1. INTRODUCTION

Semiconducting II–VI compounds are being widely used to create light-emitting and photodetector quantum-well structures operating in the green-blue spectral range. To design heterostructures with desired electronic and optical properties, structurally perfect epitaxial layers of a prescribed chemical composition need to be obtained. The structural perfection of heteroepitaxial layers largely depends on the density of defects appearing at the interface in the initial stage of epitaxial layer growth [1]. The main reason for the appearance of defects at the ⟨II–VI⟩/⟨III–V⟩ interface in molecular beam epitaxy (MBE) is the chemical reaction of the substrate with Group VI element vapor to give chalcogenide compounds of Group III elements. For example, the MBE of ZnSe-based compounds onto GaAs substrates poses a problem concerning the possibility of a chemical reaction of residual selenium vapor with the substrate surface prior to epitaxy. After high-temperature annealing of a GaAs surface covered with natural oxide, the surface layer is enriched in gallium, and the reaction between the gallium phase and selenium vapor leads to the formation of a defect layer, which is coherent with the substrate and close in composition to Ga_2Se_3 [2].

The density of growth defects can be substantially reduced by introducing a buffer GaAs epitaxial layer grown on a substrate in a separate MBE chamber, with the substrate then transferred into the chamber for the growth of II–VI compounds via a high-vacuum line. This gives, without additional annealing, a clean As-stabilized surface with (2 × 4) reconstruction recorded by the high-energy electron diffraction (HEED) technique and lowers the probability of Ga_2Se_3 layer formation [3].

An alternative way to prevent the reaction of the GaAs substrate with selenium vapor is to create, on its surface, coherent coatings composed of Group VI elements, i.e., to perform chemical passivation. Passivation of the GaAs surface with aqueous solutions of sodium or ammonium sulfide is presently being intensively studied [4]. In [5], GaAs substrates treated with $(NH_4)_2S$ solutions were used for MBE of ZnSe layers. It was found that the formation of a passivating layer in ammonium sulfide requires a long time (tens of hours), and the obtained adsorption coatings contain a considerable amount of oxygen. Moreover, a thick, physically adsorbed layer of sulfur may be formed on the surface during treatment in ammonium sulfide solution. The presence of this layer may result, in the course of annealing, in the undesirable reaction of sulfur with the GaAs surface, giving rise to a defective surface phase and to the doping with sulfur of the surface layer of the substrate.

The chemical processes occurring on the GaAs surface in Na_2S and $(NH_4)_2S$ and the compositions of the coatings formed were analyzed in detail in [6]. It was found that treatment in strongly alkaline solutions of Na_2S yields a GaAs(100) surface coated with a solid layer of chemisorbed sulfur atoms occupying bridging positions between arsenic atoms in the surface layer of the crystal. This suggests that GaAs(100) crystals treated in Na_2S solutions can be used as substrates for MBE growth of ZnSe layers. Previously, we found that preliminary passivation of III–V substrates in aqueous solutions of sodium sulfide or disulfide enables the substantial improvement of the interface quality in LPE-grown heterostructures based on AlGaAs solid solutions [7].

The aim of this study was to analyze in detail the physicochemical properties of the surface of GaAs(100) substrates treated with aqueous solutions of Na_2S and the possibility of their use in the MBE growth of ZnSe-based heterostructures. In the context of this task, the following investigations were carried out.

(a) Atomic-force microscopy (AFM) was applied to study the surface morphology of unpassivated and passivated GaAs substrates before and after annealing in an ultrahigh vacuum.

(b) Transmission electron microscopy (TEM) was used to determine the nature and density of growth defects formed at interfaces of ZnSe/GaAs heterostructures grown on passivated and unpassivated substrates.

2. EXPERIMENTAL

n^+-GaAs(100) substrates were used in all experiments. In order to reveal the influence exerted by the chemical composition of the substrate surface and its morphology on the quality of the ZnSe/GaAs interface, two groups of samples were studied.

The substrates of the first group were processed only using the conventional technique for pre-epitaxial treatment of gallium arsenide for MBE, which includes etching in a $H_2SO_4 : H_2O_2 : H_2O$ (6 : 1 : 1) solution to remove mechanical surface disruptions. The second group, in addition to the conventional processing, was treated with aqueous solutions of $Na_2S \cdot 9H_2O$. Substrates of both groups were then glued with indium solder to a molybdenum holder in an atmosphere of nitrogen and annealed under high-vacuum conditions in the growth chamber until a clear striped HEED pattern appeared. To select the optimal mode of sulfidation, the solution concentration and treatment time were varied.

The surface morphology of samples belonging to both groups was analyzed after each pretreatment stage by the AFM method under atmospheric conditions on a domestic instrument manufactured by NT-MDT Co., operating in the contact mode with an Si_3N_4 microcantilever with rigidity coefficients of 0.16 and 0.68 N/m, and a needle tip curvature diameter of less than 20 nm was used as a probe. The statistical processing of AFM topography was done using SPM Image Magic software [8].

ZnSe-based heterostructures were MBE-grown at 270–280°C without an epitaxial buffer layer using a domestic EP-1203 MBE machine. As sources, we used special purity Zn, Se, Cd, Mg, and ZnS. The epitaxy was started by keeping the GaAs surface in a Zn flow for 2 min. Then, a 20-nm buffer layer of ZnSe was grown under Se-enriched conditions, with the HEED pattern corresponding to (2×1) reconstruction.

The structural perfection of the ZnSe/GaAs interface was analyzed by TEM on a JEM-100C microscope in cross-sectional arrangement. Samples were prepared by chemical polishing in a $H_2SO_4 : H_2O_2 : H_2O$ (3 : 1 : 1) solution at $T = 40$°C with subsequent thinning by Ar^+ ions.

3. RESULTS

Visual inspection of the starting GaAs substrates shows their mirror-smooth surface with rms surface roughness amplitude equal to 0.15 nm according to AFM. After etching, the rms roughness amplitude increases to 0.18 nm and becomes 0.14 nm after etching and passivation.

Figure 1 shows typical AFM images of the surface topography of the substrates under study after they were annealed in ultrahigh vacuum until the appearance of a clear HEED pattern. It can be seen that annealing strongly changes the surface topography of samples belonging to both the first and the second groups. Elongated pits with a depth up to 10 nm and density $n \approx 10^{10}$ cm^{-2} are formed on the surface of samples belonging to the first group (Fig. 1a). It should be noted here that the topographic images of the annealed surfaces of samples of the first group and starting substrates not subjected to any pretreatment are virtually identical. Pits are also present on the surface of substrates of the second group (Fig. 1b), but their density is three times lower and their depth decreases to 5 nm, with the pit shape becoming rounded rather than elongated. Separately, the effect of prepassivation etching on the surface topography upon annealing was studied. For this purpose, samples were fabricated which were only treated with a sulfide solution but not etched. In this case, the pit density decreases by two orders of magnitude to 10^8 cm^{-2}, the pit depth does not exceed 3 nm, and the pits are rounded (Fig. 1c).

It should be noted that the temperature of annealing in the vacuum chamber until the appearance of clear HEED patterns is much higher for samples of the first group (T_{ann} = 530–540°C) compared with that for sulfided samples (T_{ann} = 500–510°C). It is also noteworthy that annealing of samples subjected to prolonged sulfide treatment (>10 min) gave no clear diffraction pattern.

Thus, preepitaxial annealing of substrates causes distortion of their surface planarity, which is most pronounced when the surface is oxidized. It would be expected that oxidized substrates are the least suitable for MBE.

Figure 2 presents cross-sectional TEM images of the interface in ZnSe/GaAs structures grown on a substrate subjected to sulfuric acid etching (Fig. 2a), those treated after etching with a 1 M Na_2S solution (Fig. 2b), and those treated only with a sodium sulfide solution without preliminary etching (Fig. 2c). Figure 2a clearly shows pits on the substrate surface, which give rise to

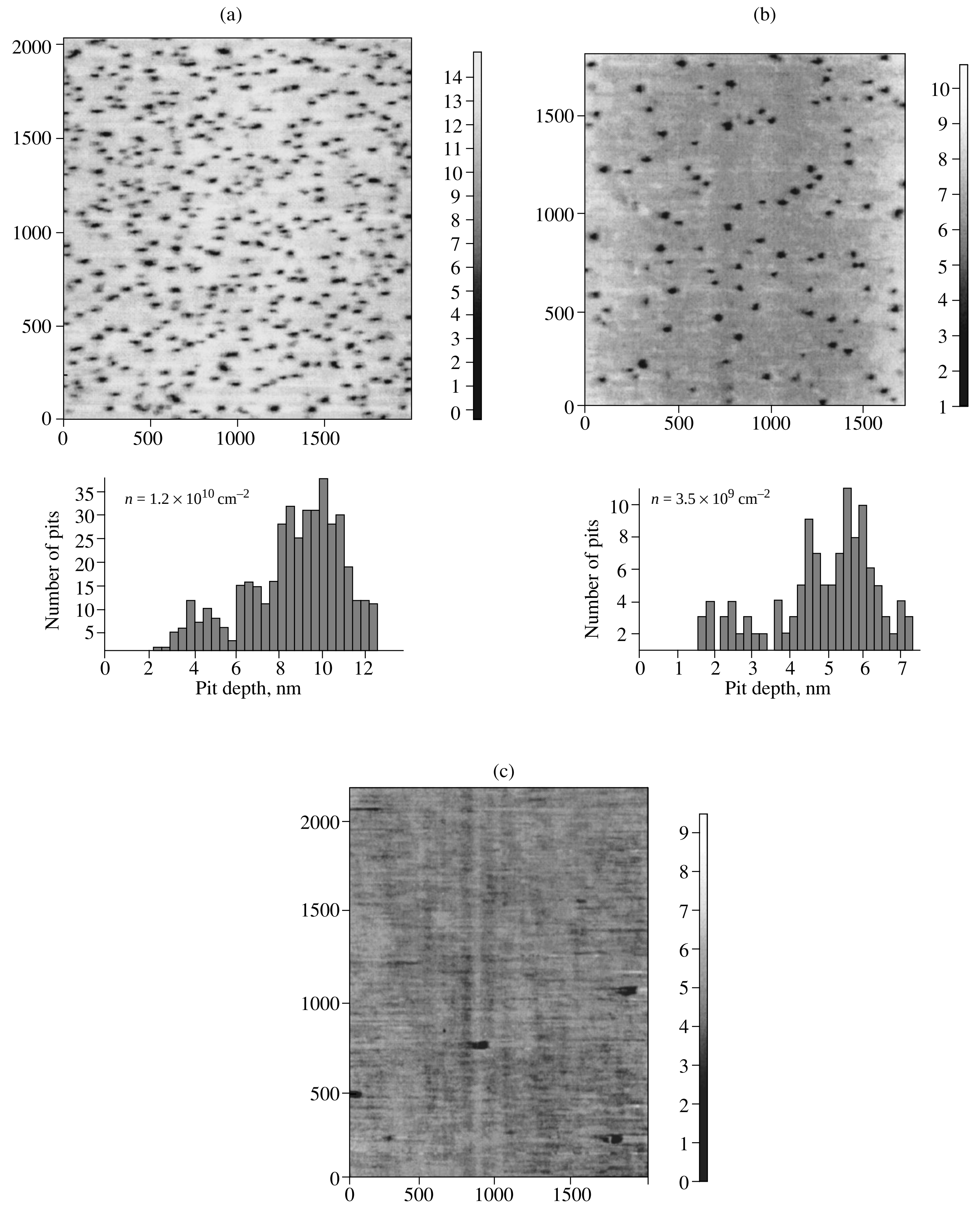

Fig. 1. AFM images of the surface of substrates annealed in a high vacuum until the appearance of a clear striped HEED pattern. (a) GaAs substrate processed by the standard technique, (b) that treated both with a sulfuric acid etchant and sodium sulfide solution, and (c) that treated only with a passivating solution. Measurement units in (a), (b), and (c) are nanometers.

microcracks and stacking faults in the ZnSe layer. The total density of defects greatly exceeds 10^8 cm^{-2}. Figure 2b shows only pits whose slopes extend into the layer in the form of stacking faults, with the defect density decreasing to 7×10^6 cm^{-2}.

Figure 2c presents a cross-sectional TEM image of a structure formed by three ZnCdSe quantum wells with different thicknesses confined between ZnMgSSe layers. The annealing temperature was 500°C, the reconstruction of the initial substrate surface was, according to HEED, (4×1), and the initial growth stage proceeded by the two-dimensional layer-by-layer mechanism. The TEM image demonstrates a planar interface without any stacking fault or dislocation nucleation centers. The density of the stacking fault defects, measured by the cathodoluminescence method [9], was $\sim 3 \times 10^5$ cm^{-2}.

Thus, layers with the best structural perfection were grown on substrates with the lowest pit density, i.e., on substrates that were only treated in a sulfide solution without preliminary etching. This suggests that pits formed in sample annealing are sources of defects growing into the epitaxial layer.

4. DISCUSSION

In this section, we analyze qualitatively the mechanisms causing distortion of the (100) surface planarity in annealing of passivated and unpassivated substrates. As is known, a 12- to 30-Å-thick amorphous oxide layer composed of $As_2O_3 \cdot Ga_2O_3$ is present on the GaAs surface upon etching [10, 11]. On heating to 300°C, the oxide layer decomposes into two components: volatile As_2O_3 and nonvolatile Ga_2O_3. The second component is a thermally stable compound which can be removed from the surface at higher temperatures as a monoxide (Ga_2O) formed from Ga_2O_3 and the substrate material by the reaction

$$Ga_2O_3 + 4GaAs \longrightarrow 3Ga_2O\uparrow + As_4\uparrow. \qquad (1)$$

Reaction (1) leads to reactive etching of the substrate and gives rise to the initial microrelief on the (100) surface. Since complete removal of Ga_2O_3 from the GaAs surface in a vacuum occurs at a temperature higher than the temperature of congruent evaporation of GaAs, the surface layer is depleted of As. Prolonged annealing leads to the appearance of gallium clusters that merge together to produce microdrops, in which arsenic dissolves. It is significant that the rate of arsenic evaporation from a drop exceeds the rate of the joint evaporation of arsenic and gallium from the GaAs surface. This process leads to the further development of the surface microrelief and the formation of pits with faceted walls. The pits become deeper with increasing temperature or annealing duration. The thermal etching pits are elongated along the directions $\langle 1\bar{1}0 \rangle$, which reflects the anisotropic nature of GaAs dissolution in microdrops of liquid Ga.

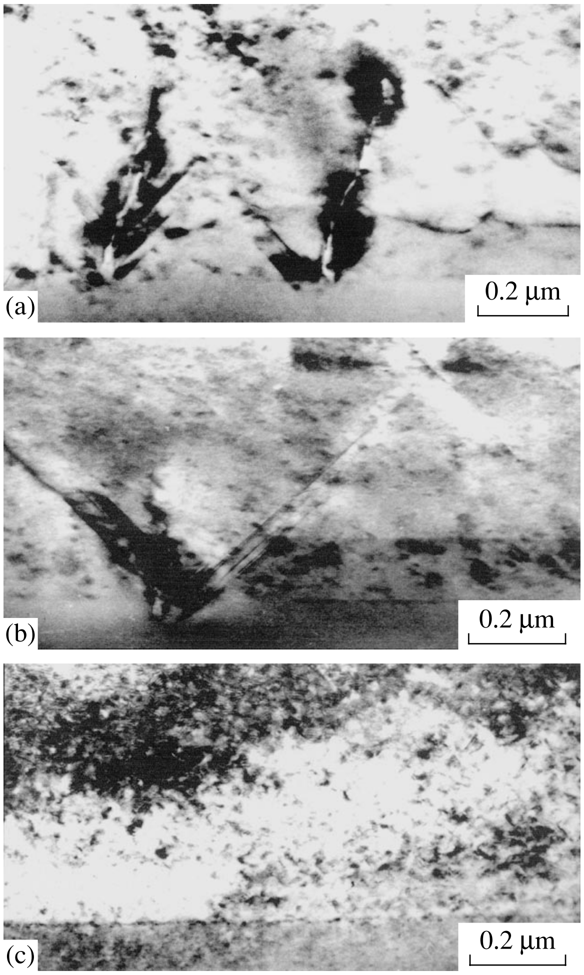

Fig. 2. Cross-sectional TEM images of the interface in ZnSe/GaAs heterostructures MBE-grown on GaAs substrates (a) processed by the standard technique, (b) treated both with sulfuric acid etchant and sodium sulfide solution, and (c) treated only with passivating solution.

Let us now consider the processes occurring on the surface of GaAs(100) crystals in the course of sulfidation and subsequent thermal treatment.

4.1. Processes Occurring on the Exposure of Crystals to Aqueous Sodium Sulfide Solution

We have shown previously that two processes occur in parallel in treatment of GaAs(100) crystals in strongly alkaline Na_2S solutions: layer-by-layer etching and passivation proceeding via gradual accumulation of adsorbed sulfur atoms occupying a bridging position between As atoms on arsenic terraces. The layer-by-layer etching occurs at the edges of unit steps formed by Ga atoms, with hydroxyl OH^- groups adsorbed on them. Raising the exposure of (100) surfaces in a sulfide solution makes the unit steps denser and enhances the microroughness of the crystal surface. Minimizing this effect requires that the treatment be made shorter.

Nevertheless, oxide removal and formation of a primary adsorption coating composed of SH groups adsorbed onto As atoms takes several minutes. In the course of drying and low-temperature annealing, a reaction occurs in such an adsorption layer, which also leads to the formation of a passivating sulfide coating:

$$2SH_{ad} \longrightarrow S_{ad} + H_2S\uparrow. \quad (2)$$

The monolayer of chemisorbed undimerized sulfur atoms, which appears as a result of reaction (2), forms a two-dimensional lattice with symmetry (1×1) on the surface of (100)As terraces. As shown by our investigations, the time of treatment in an aqueous solution of Na_2S should be short (5 min) in order to reduce the microroughness of the surface being treated to the maximum possible extent.

4.2. Processes Occurring on the Crystal Surface in the Course of Annealing in Vacuum Chamber

Heating a sulfided surface in a vacuum to more than 400°C leads to a substitution reaction in the surface layer, in which sulfur atoms substitute underlying arsenic atoms to form new Ga–S adsorption bonds. In the process, the arsenic atoms of the substituted layer, which originally had saturated hybridized sp^3 bonds, pass into a molecular form, acquiring a structure with five electrons per atom, and are desorbed. Simultaneously, sulfur atoms lose one of the six valence electrons and form dimers with five electrons per atom, with the total charge of the crystal remaining unchanged. The process of substitution by the above mechanism is thermodynamically favorable, since it leads to the formation of, on the whole, stronger chemical bonds [12]:

$$\begin{gathered} 4E_{\text{Ga–As}} + 4E_{\text{As–S}} < 4E_{\text{Ga–S}} + 3E_{\text{As–As}} + E_{\text{S–S}} \\ \approx 4 \times 37.8 + 4 \times 61.6 \\ < 4 \times 57.9 + 3 \times 40 + 63 \text{ kcal/mol.} \end{gathered}$$

Thus, in the course of annealing, GaAs(100) crystals must acquire a surface that ends with Ga atoms bound to adsorbed S atoms. The HEED pattern of such a surface corresponds in this case to (2×1) reconstruction.

At places of sulfide film discontinuity at edges of unit steps and facets formed by them, oxygen bound to gallium is retained. This leads, in the course of annealing, to the formation of pits on the GaAs surface by the same mechanism as in the case of the oxidized surface. However, the development of pits on passivated surfaces is limited by the presence of a sulfide film around them. As a result, the density and depth of the pits decrease, and their shape becomes rounded rather than elongate (Fig. 1b).

It is noteworthy that making the passivation longer (>10 min) leads to the growth of thick layers of physically adsorbed sulfur atoms on the initial surfaces. In the course of annealing, the reaction between elementary sulfur that has no time to be desorbed and GaAs leads to the formation of a Ga_2S_3 layer incoherent with the substrate material. This results in the absence of a clear HEED pattern. Making the treatment shorter diminishes the accumulation of polysulfide groups in the adsorption layer and hinders deposition of an amorphous coating composed of elementary sulfur and thioarsenious acid (a product of GaAs etching).

At the same time, annealing of GaAs surfaces subjected to short-time treatment in a sodium sulfide solution and lacking a solid layer of physically adsorbed sulfur cannot ensure formation of a solid Ga–S monolayer coating since, as a result of the photostimulated dissociation of As–S bonds on the GaAs surface [13], part of the chemisorbed S atoms have enough time to be desorbed and are not involved in the substitution reaction. In this case, a mixed Ga–(S_xAs_y) monolayer can be formed on annealed surfaces, which must lead to the appearance of more complex $(n \times 1)$ surface reconstructions.

5. CONCLUSION

The AFM technique was used to perform a comparative analysis of the topography of naturally oxidized surfaces of GaAs substrates with that of substrates treated with aqueous sodium sulfide solutions in different stages of their preparation for MBE growth of II–VI layers. It is established that conventional annealing of unpassivated substrates without arsenic flow leads to rather strong distortion of the surface planarity. The appearance of numerous pits on surfaces of this kind is attributed to reactive etching of GaAs in the course of gallium oxide removal and subsequent thermal etching with gallium of the substrate surface. Treatment of substrates with sodium sulfide makes it possible to substantially reduce the density and depth of pits formed in annealing and lowers the required temperature of pre-epitaxial annealing.

TEM was used to establish a direct relationship between the number of defects in the layers grown and the density of pits. Layers and heterostructures with the best structural perfection were obtained in epitaxy onto GaAs substrates treated for 5 min in a 1 M Na_2S solution without preliminary etching. The investigations performed clearly indicate that the sulfidation of GaAs substrates substantially reduces the number of defects originating at the ZnSe/GaAs interface.

Thus, sulfide passivation of GaAs substrates makes it possible to substantially reduce the defectiveness of interfaces and improve the crystal perfection of epitaxial ZnSe layers. The results obtained in this study demonstrate that the use of passivating chemisorbed coatings is a possible alternative to the growth of a buffer GaAs layer with an arsenic coating in a separate MBE chamber.

ACKNOWLEDGMENTS

This study was supported by the Program of the Ministry of Science "Physics of Solid-State Nanostructures" (grant no. 99-2035), the Russian Foundation for Basic Research (project no. 99-02-17097), and the Volkswagen Foundation.

We thank A.N. Titkov for assistance in performing AFM experiments; A.A. Sitnikov and R.V. Zolotareva, for TEM measurements; and A.G. Kop'eva, for his help in the chemical treatment of substrates.

REFERENCES

1. S. Guha, H. Munekata, F. K. LeGoues, and L. L. Chang, Appl. Phys. Lett. **60**, 3220 (1992).
2. A. Krost, W. Richter, and D. R. T. Zahn, Appl. Surf. Sci. **56–58** (1–4), 691 (1992).
3. R. L. Gunshor, L. A. Kolodziejski, M. R. Melloch, *et al.*, Appl. Phys. Lett. **50**, 200 (1987).
4. V. H. Wu, T. Toyda, Y. Kawakami, *et al.*, Jpn. J. Appl. Phys. **29**, L1441 (1990).
5. J. Wang, X. H. Liu, Z. S. Li, *et al.*, Appl. Phys. Lett. **67**, 2043 (1995).
6. V. L. Berkovits, V. P. Ulin, D. Paget, *et al.*, J. Vac. Sci. Technol. A **16** (4), 2528 (1998).
7. V. L. Berkovits, V. M. Lantratov, T. V. L'vova, *et al.*, Appl. Phys. Lett. **63**, 970 (1993).
8. http://members.xoom.com/AlexKryzh.
9. V. A. Solov'ev, S. V. Sorokin, I. V. Sedova, *et al.*, J. Cryst. Growth **200/201**, 481 (1999).
10. W. Monch, in *Semiconductor Surfaces and Interfaces* (Springer-Verlag, Berlin, 1993), Part 17, p. 276.
11. A. V. Ankudinov, V. P. Evtikhiev, V. E. Tokranov, *et al.*, Fiz. Tekh. Poluprovodn. (St. Petersburg) **33**, 594 (1999) [Semiconductors **33**, 555 (1999)].
12. *Thermodynamic Properties of Individual Substances: Handbook*, Ed. by V. P. Glushko (Moscow, 1971), Vol. 5.
13. V. L. Berkovits, A. O. Gusev, V. M. Lantratov, *et al.*, Phys. Low-Dimens. Struct. **12**, 293 (1995).

Translated by M. Tagirdzhanov

Semiconductors, Vol. 36, No. 1, 2002, pp. 60–64. Translated from Fizika i Tekhnika Poluprovodnikov, Vol. 36, No. 1, 2002, pp. 65–69.
Original Russian Text Copyright © 2002 by Antonova, Stano, Nikolaev, Naumova, Popov, Skuratov.

SEMICONDUCTOR STRUCTURES, INTERFACES, AND SURFACES

Transformation of Interface States in Silicon-on-Insulator Structures under Annealing in Hydrogen Atmosphere

I. V. Antonova*, Ĭ. Stano, D. V. Nikolaev*, O. V. Naumova*,**
V. P. Popov*, and V. A. Skuratov**

** Institute of Semiconductor Physics, Siberian Division, Russian Academy of Sciences,*
pr. Akademika Lavrent'eva 13, Novosibirsk, 630090 Russia
*** Joint Institute for Nuclear Research, Dubna, Moscow oblast, 141980 Russia*

Submitted May 8, 2001; accepted for publication June 5, 2001

Abstract—Changes induced by annealing the spectrum of states on a Si/SiO$_2$ interface obtained by direct bonding and on a Si(substrate)/⟨thermal SiO$_2$⟩ interface in silicon-on-insulator (SOI) structures were investigated by charge-related deep-level transient spectroscopy. The structures were formed by bonding silicon wafers and slicing one of the wafers along a plane weakened by hydrogen implantation. The SOI structures were annealed at 430°C for 15 min in hydrogen, which corresponded to the conventional mode of passivation of the Si/SiO$_2$-interface states. The passivation of interface states by hydrogen was shown to take place for the Si/⟨thermal SiO$_2$⟩ interface, as a result of which the density of traps substantially decreased, and the continuous spectrum of states was replaced by a band of states in the energy range E_c = 0.1–0.35 eV within the entire band. For the traps on the bonded Si/SiO$_2$ interface, the transformation of the centers occurs; namely, a shift of the energy-state band is observed from E_c = 0.17–0.36 to 0.08–0.22 eV. The trapping cross section decreases by about an order of magnitude, and the density of traps observed increases slightly. *© 2002 MAIK "Nauka/Interperiodica".*

1. INTRODUCTION

The trap-level spectrum for interfaces in silicon-on-insulator (SOI) structures plays an important role in designing devices, especially if the thickness of the split-off layer is less than 0.2–0.3 μm. The annealing of MIS structures prepared on bulk silicon is known to lead to an appreciable (approximately, an order of magnitude) decrease in the density of surface states on the SiO$_2$/Si interface [1, 2]. A conventional method for such passivation of the interface states is annealing at a relatively low temperature (~450°C) in a hydrogen atmosphere. A widely used method for the formation of SOI structures is bonding Si wafers and slicing one of the wafers along a plane weakened by hydrogen implantation [3, 4]. Because hydrogen implantation is used in the formation of SOI structures and because hydrogen is present at both interfaces at relatively high concentrations (10^{20}–10^{21} cm^{-3}) [5], the effect of repeated low-temperature thermal treatment in hydrogen on interface states can differ radically from the effect exerted by the primary annealing of these structures. Furthermore, one of the Si/SiO$_2$ interfaces in such structures is formed by bonding rather than by thermal oxidation. How the thermal treatments in hydrogen affect the states at such an interface was unknown until now. The purpose of this study is to verify the possibility of passivating the traps at the SOI-structure interfaces using the regime conventional for bulk silicon.

2. EXPERIMENTAL

To form the SOI structures, we used wafers of 100 mm in diameter fabricated from Czochralski-grown silicon. In Table 1, we list the charge-carrier concentrations in the film and the substrate of the SOI structures measured by the capacitance–voltage (C–V) method. Carrier concentrations before and after hydrogen annealing virtually coincided both in the film and in the substrate. The thickness of the Si split-off layer in the structures amounted to 0.5 μm, and the buried-insulator thickness was 0.28–0.4 μm. In particular cases, the split-off silicon layer was additionally implanted with phosphorus (ion energy E = 300 keV, dose D = 10^{12} cm^{-2}) with subsequent annealing at 1000°C for the activation of the implanted impurity. In the investigated structures, the ⟨split-off silicon layer⟩/⟨buried oxide⟩ interface is a bonding boundary, whereas the substrate/⟨buried oxide⟩ interface is the boundary between Si and a ther-

Table 1. Parameters of the initial material and the combination of wafers in the silicon-on-insulator (SOI) structures

Designation of the SOI structures	Split-off silicon layer; concentration, cm^{-3}	Substrate; concentration, cm^{-3}
SOI-I	n-Si; 3×10^{15}	n-Si; 1.5×10^{15}
SOI-II	n-Si; 5×10^{15}	n-Si; 1.5×10^{15}
SOI-III	n-Si; 2×10^{16}	n-Si; 3×10^{14}

mally grown oxide. An additional thermal treatment was performed at a temperature of 430°C for 15 min in hydrogen. For the investigations, we measured the capacitance–voltage (*C*–*V*) characteristics at frequencies of 1 MHz and 100 kHz and the components of the complex conductivity of structures (*G*–*V* characteristics) and used the deep-level transient spectroscopy (DLTS) method. From the available varieties of DLTSs, we used the so-called charge-related DLTS (*Q*-DLTS) method [6] with wider capabilities for investigating the interfaces in the metal–insulator–semiconductor (MIS) structures. The operating frequency in the *Q*-DLTS measurements amounted to 1 kHz. The time window varied within 10^{-4}–2×10^{-3} s, and the filling-pulse duration was 10^{-5}–2×10^{-4} s. All the measurements were carried out using the mesa structures. The contacts were formed using Al deposition. The mesa area varied within 0.5–1 mm^2.

3. RESULTS AND DISCUSSION

In Fig. 1, we show the typical *C*–*V* characteristics for *n*-Si/SiO$_2$/*n*-Si structures. In Fig. 1, it is possible to isolate voltage intervals I and II in which the high-frequency capacitance is modulated from a maximum value to a minimum one. The voltage region from interval I corresponds to the case when the substrate is depleted and the silicon film is enriched. Precisely in this voltage interval, the recharging of states at the film/oxide interface and the deep levels in the substrate can be observed in the DLTS measurements. For the voltages from interval II, the film is depleted, and the substrate is enriched. Selecting the voltages from this interval, we can observe the recharging of states at the film/oxide interface and deep levels in the film.

In Fig. 1, we show the *C*–*V* and *G*–*V* characteristics for the SOI-II structure measured at a frequency of 100 kHz before and after the annealing of the structure in hydrogen. A voltage shift of regions I and II (after annealing) towards $V = 0$ corresponds to a certain decrease in the charge of the buried insulator, but such an effect is observed only in particular cases. As a rule, the charge fixed in the insulator varied insignificantly (Table 2). For an initial SOI structure, the conductivity peaks associated with each of the structure interfaces can be seen in Fig. 1. The annealing in hydrogen led to the virtually complete passivation of traps at the lower substrate–buried-oxide interface, whereas, at the upper SiO$_2$/Si interface, only a transformation of traps took place and was accompanied even with a certain increase in the height of the peak in the *G*–*V* characteristic. Furthermore, for the upper interface, the carrier capture cross sections are changed (decreased) for the interface states. This follows from the fact that the *C*–*V* dependence for this interface changed from the shape characteristic of high frequencies to the low-frequency type. For the substrate–buried-insulator interface, no similar changes occur. In Table 2, we list the data on charge values in the buried insulator and the trap densities at the interfaces obtained from *C*–*V* and *G*–*V* measurements.

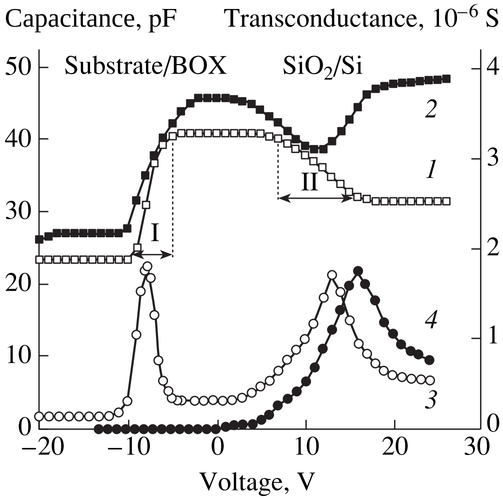

Fig. 1. Typical *C*–*V* (*1*, *2*) and *G*–*V* (*3*, *4*) characteristics for the silicon-on-insulator structure measured at a frequency of 100 kHz. The data are displayed for the SOI-II structure (*1*, *3*) before and (*2*, *4*) after annealing at 430°C for 15 min in hydrogen. BOX stands for buried oxide.

In Fig. 2, we show the DLTS spectra for the SOI-I structure taken before and after annealing in hydrogen for the voltages from interval II (the depletion mode, see Fig. 1) when the interface between the split-off silicon layer and the buried insulator is probed. The *E* peak in the spectra, obtained for the initial SOI structures, belongs to the deep-level centers, which are localized in the near-surface part of the split-off Si layer, and their parameters are $E_c - E = 0.58$ eV, $\sigma = 4 \times 10^{-14}$ cm^2, and $N = (3–5) \times 10^{15}$ cm^{-3} [7]. As can be seen from Fig. 2, in the hydrogen-annealed sample, a peak associated with a deep-level center in the film is virtually not observed, while the peaks associated with traps at the interface are shifted to lower temperatures.

Similar changes in the spectra are also observed for other investigated SOI structures. On the substrate/⟨buried insulator⟩ interface, we also observed only the peaks related to the interface states, but which were shifted to lower temperatures.

In order to construct the distribution of the surface-state density in the Si band gap based on the spectra obtained, we used the method suggested in [8]. In this method, the conventional equation describing the charge exchange of deep centers is used:

$$1/\tau = \nu\sigma N_c \exp(-E_c - E)/kT,$$

where conventional notation is used. In order to calculate the energy of centers, which mainly contribute to the DLTS signal for the specified temperature and time window, we measure the DLTS spectrum corresponding to the recharging of deep centers within the entire

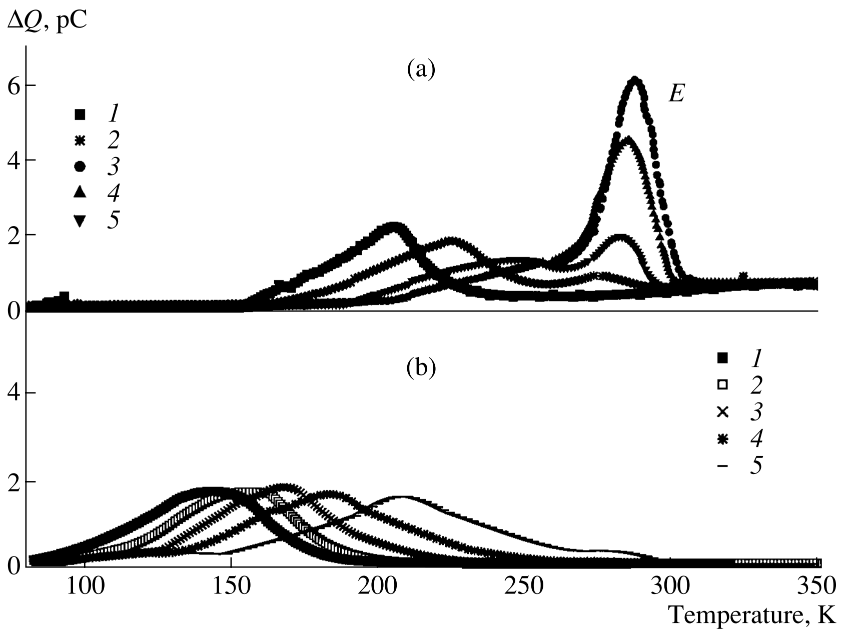

Fig. 2. Q-DLTS spectra for the SOI-I structure (a) before and (b) after annealing in hydrogen obtained using voltages from the interval II (see Fig. 1) when the split-off silicon layer and its interface with oxide are tested. A filling-pulse amplitude $U_1 = -2.0$ V. A bias voltage U_2 applied across the structure during the measurements was equal to (a) (*1*) 8, (*2*) 10, (*3*) 12, (*4*) 14, and (*5*) 16 V; (b) (*1*) 2, (*2*) 4, (*3*) 6, (*4*) 8, and (*5*) 10 V.

voltage interval I (or II) (see Fig. 1), from which we determine the distribution of states over the band gap:

$$E_c - E = kT\ln(\sigma v N_c \tau).$$

For this method, it is necessary to know the capture cross sections for a level; these cross sections can be estimated from the DLTS spectra. For determining the carrier-capture cross sections by a level, it is convenient to use the DLTS spectra measured for a relatively small filling-pulse amplitude, when the traps are recharged in a relatively narrow energy range, and the peaks obtained can be approximately described using the expressions for the centers with a fixed energy and cross section.

Our estimates for the states at the substrate/⟨buried insulator⟩ interface showed that the value of the cross section amounts to 10^{-18} cm^2 for the entire spectrum of traps and changes insignificantly during the annealing in hydrogen. The obtained distribution of states at the substrate/⟨thermal oxide⟩ interface is shown in Fig. 3. The density of states after the annealing (curves *2*, *3*) decreases, and the wide spectrum of traps is replaced by traps localized in a relatively narrow energy range. In Table 2, we list the integrated values of the density of

Table 2. Fixed charge (Q) in the buried insulator referred to one of the interfaces in the silicon-on-insulator structure determined from the C–V characteristics measured at a frequency of 1 MHz, and a density of interface states determined from the G–V and DLTS measurements (D_{it}^{GV} and $D_{\text{it}}^{\text{DLTS}}$, respectively)

Designation of structures		Substrate/SiO$_2$			Si/SiO$_2$		
		Q, cm^{-2}	D_{it}^{GV}, cm^{-2}	$D_{\text{it}}^{\text{DLTS}}$, cm^{-2}	Q, cm^{-2}	D_{it}^{GV}, cm^{-2}	$D_{\text{it}}^{\text{DLTS}}$, cm^{-2}
SOI-I	1	3.7×10^{11}	2×10^{11}	1.7×10^{10}	1.4×10^{11}	2×10^{11}	5.3×10^{9}
	2	4×10^{11}	$\lesssim 5 \times 10^{10}$	6×10^{8}	10^{11}	1.7×10^{11}	9.3×10^{9}
SOI-II	1	3×10^{11}	7×10^{11}	1.8×10^{10}	1.6×10^{11}	2×10^{11}	5×10^{9}
	2	8×10^{10}	$\lesssim 5 \times 10^{10}$	3.6×10^{9}	5.3×10^{10}	8×10^{11}	1.7×10^{10}
SOI-III	1	5×10^{10}	–	–	2×10^{11}	–	2.2×10^{9}
	2	6×10^{10}	–	–	2.1×10^{11}	–	5.3×10^{9}

Note: (1) Initial structures; (2) structures annealed in hydrogen.

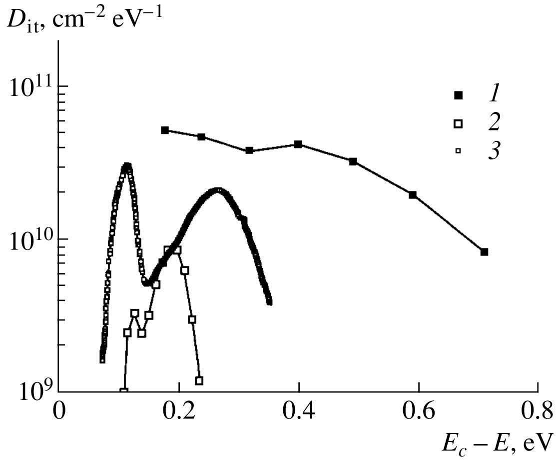

Fig. 3. Distribution of density of states D_{it} at the substrate/⟨thermal oxide⟩ interface obtained for (*1*, *2*) SOI-I and (*3*) SOI-II structures. A value of the trapping cross section in (*1*) initial and (*2*, *3*) annealed structures amounted to 10^{-18} cm^2.

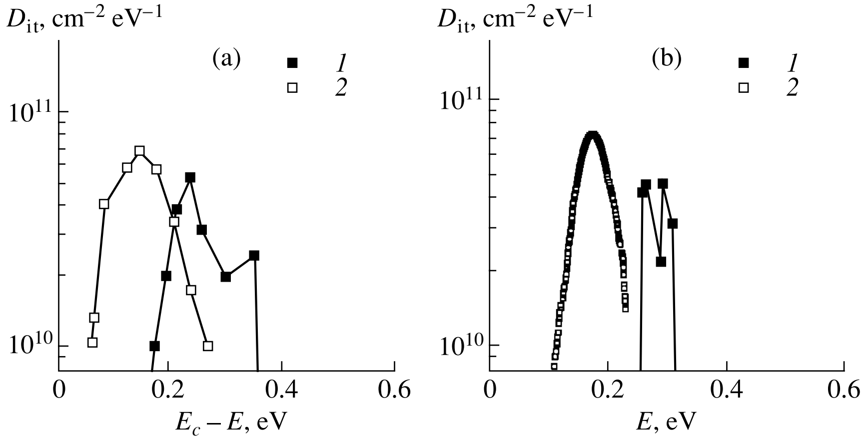

Fig. 4. Distribution of states at the bonded Si/SiO$_2$ interface for (2) SOI-I and (b) SOI-II structures. A value of the trapping cross section amounted to 10^{-18} cm^2 in the initial structures and 10^{-19} cm^2 after annealing. (*1*) initial structures, and (*2*) annealed structures.

states at the given interface before (samples 1) and after (samples 2) annealing.

The processing of the DLTS spectra for the ⟨split-off silicon layer⟩/⟨buried insulator⟩ interface shows that the peaks observed even in the initial structures correspond to a relatively narrow energy range in the Si band gap. The estimates of the carrier-trapping cross section for the upper interface show that the cross section was on the order of 10^{-18} cm^2 before the annealing. A value of the capture cross section for the traps in the annealed samples decreased and came to equal approximately 10^{-19} cm^2. In Fig. 4, we show the energy distributions of states both in initial (curves *1*) and annealed (curves *2*) SOI-I and SOI-III structures. After annealing, we observe a shift of trap energies to the region of lower values and a certain increase in the peak of distribution. The integrated values of the density of states at this interface before and after annealing are also listed in Table 2.

The results obtained show that annealing SOI structures in hydrogen has varying effects on the interface states. At the substrate/⟨buried insulator⟩ interface formed by thermal oxidation, a conventional passivation of centers occurs. During this passivation, some traps disappear, while the parameters of the remaining traps remain unchanged (in particular, the trapping cross section). On the bonded Si/SiO$_2$ interface, the reconstruction of states apparently takes place. As a result of this reconstruction, both the energy and the capture cross section change, and even the trap concentration somewhat increases.

4. CONCLUSION

Annealing in hydrogen is shown to lead to the passivation of an appreciable fraction of traps on the substrate/⟨thermal SiO$_2$⟩ interface in silicon-on-insulator structures. At the same time, at the Si/SiO$_2$ interface obtained by bonding, a transformation of the traps observed occurs: the state-energy band is shifted from E_c = (0.17–0.36) eV to E_c = (0.08–0.22) eV, the trapping cross section decreases approximately by an order of magnitude, and the density of traps increases slightly.

ACKNOWLEDGMENTS

We thank B.I. Fomin for his help in carrying out the *G–V* measurements. This study was supported by the Russian Foundation for Basic Research, project no. 01-02-16986.

REFERENCES

1. P. V. Gray, IEEE Trans. Electron Devices **8**, 88 (1969).
2. S. Sze, *Physics of Semiconductor Devices* (Wiley, New York, 1981; Mir, Moscow, 1984).
3. M. Bruel, Electron. Lett. **31**, 1201 (1995).
4. V. P. Popov, I. A. Antonova, V. F. Stas, L. V. Mironova, E. P. Neustroev, A. K. Gutakovskii, A. A. Franzusov, and G. N. Feofanov, in *Perspectives, Science and Technologies for Novel Silicon-on-Insulator Devices*, Ed. by P. L. F. Hemment *et al.* (Kluwer, Dordrecht, 2000), p. 47.
5. I. V. Antonova, V. F. Stas’, V. P. Popov, *et al.*, Fiz. Tekh. Poluprovodn. (St. Petersburg) **34**, 1095 (2000) [Semiconductors **34**, 1054 (2000)].
6. J. W. Farmer, C. D. Lamp, and J. M. Meese, Appl. Phys. Lett. **41**, 1064 (1982).
7. I. V. Antonova, J. Stano, D. V. Nikolaev, *et al.*, Fiz. Tekh. Poluprovodn. (St. Petersburg) **35** (8), 948 (2001) [Semiconductors **35**, 912 (2001)].
8. K. Hofmann and M. Schulz, J. Electrochem. Soc. **132**, 2201 (1985).

Translated by V. Bukhanov

Semiconductors, Vol. 36, No. 1, 2002, pp. 65–73. Translated from Fizika i Tekhnika Poluprovodnikov, Vol. 36, No. 1, 2002, pp. 70–78.
Original Russian Text Copyright © 2002 by Shelykh, Bagraev, Ivanov, Klyachkin.

Spontaneous Spin Polarization of Electrons in Quantum Wires

I. A. Shelykh*, N. T. Bagraev, V. K. Ivanov*, and L. E. Klyachkin****
** St. Petersburg State Technical University, St. Petersburg, 195251 Russia*
*** Ioffe Physicotechnical Institute, Russian Academy of Sciences, St. Petersburg, 194021 Russia*
e-mail: impurity.dipole@pop.ioffe.rssi.ru

Submitted April 10, 2001; accepted for publication April 10, 2001

Abstract—The quantum conductance staircase of the one-dimensional (1D) channel is analyzed for a weak filling of the lower 1D subbands, when the exchange electron–electron interaction of carriers dominates over their kinetic energy. Main attention is paid to considering the behavior of the "$0.7(2e^2/h)$" feature split off from the first quantum step, which is identified as a result of the spontaneous spin polarization of the 1D electronic gas through exchange interaction at zero magnetic field. The critical linear concentration of electrons above which fully polarized electron gas starts to depolarize, with the resulting evolution of the split-off substep height from e^2/h to $2e^2/h$, is determined within the framework of phenomenological theory. Moreover, the temperature dependence of the height of this substep at the range $0.5(2e^2/h) – 0.75(2e^2/h)$, resulting from the partial depolarization of the electron gas near the 1D subband bottom, is predicted. The quantum-mechanical consideration carried out analytically in the context of the Hartree–Fock–Slater approximation with localized exchange potential shows that consideration of the electron–electron interaction in a quantum wire with an arbitrary carrier density leads to spontaneous polarization of the quasi-1D electronic gas in zero magnetic field at small linear concentrations of carriers. © *2002 MAIK "Nauka/Interperiodica".*

1. INTRODUCTION

The development of modern nanotechnology makes it possible to obtain quantum wires and quantum point contacts which are one-dimensional (1D) channels connecting two-dimensional (2D) electronic gas reservoirs inside heterojunctions and single quantum wells (QW) [1–7]. The study of the quasi-one-dimensional (Q1D) transport in such systems has shown that if the 1D channel length is less than the mean free path, the carriers demonstrate ballistic properties resulting in quantization of the conductance in units of $2e^2/h$ [2, 3, 8, 9]. The observation of quantized conductance became possible due to the use of electrostatically compressed 1D channels. These ballistic 1D channels appear at the negative voltage applied to the pair of separated gates, which are created in 2D structures using electron beam nanolithography [1–3]. An increase of the gate voltage U_g increases the electron density inside the quantum wire and thereby stimulates filling of a larger number of 1D subbands. The $G(U_g)$ dependence is a series of the 1D conductance plateaus separated by steps of the height $2e^2/h$, since the 1D channel conductance changes abruptly each time the Fermi level coincides with one of the 1D subbands:

$$G = G_0NT, \tag{1}$$

where $G_0 = 2e^2/h$; N is the number of 1D subbands, which can be varied by changing U_g and corresponds to the number of the upper occupied subband; T is the transmission coefficient, which is equal to unity if the elastic scattering length is larger than the length of the ballistic channel.

Thus, the observation of the quantum conductance staircase, $G(U_g)$, identifies adiabatic transparency of the spin-nondegenerate 1D subbands [2, 3].

Of particular interest is the study of the quantum conductance staircase at low filling of 1D subbands when electron–electron interactions, which lead to the formation of crystalline [10, 11] and liquid [12–14] states of Q1D electrons and to their spontaneous spin polarization [15–24], start to dominate. The Tomonaga–Luttinger model of electronic liquid [12, 13] is the most suitable for estimating the effect of the local interaction between carriers on features of the Q1D transport [14]. In this case, the height of the first step of the quantum staircase $G_0 = K(2e^2/h)$ can increase or decrease, respectively, in the case of the dominant attraction ($K > 1$) or repulsion ($K < 1$) component of the electron–electron interaction ($K = 1$ for noninteracting electron gas). In particular, the modified Tomonaga–Luttinger liquid model made it possible to explain the enhancement [4] and suppression [14] of the first quantum step in long (>2 μm) quantum wires, as well as oscillations of the 1D conductance plateau because of carrier scattering by an impurity center located near quantum wire boundaries [12, 14].

However, this and other models of 1D channels, taking into account the contact phenomena at channel boundaries [25–27] and spin–orbit interaction [28], define the change in characteristics of the first quantum step as only resulting from elastic backscattering of carriers and decoherence of the 1D transport. At the same time, it is not possible to interpret, in terms of these models, the behavior of the "$0.7(2e^2/h)$" feature split-off from the first quantum step, which is identified as a consequence of the spontaneous spin polarization of the 1D electronic gas in zero magnetic field [6, 15–24]. We notice two important experimental facts that provide evidence of the presence of spontaneous spin-polarization in 1D channels, notwithstanding the general theoretical prediction of the impossibility of a ferromagnetic state in ideal ferromagnetic systems in the absence of a magnetic field [29]. First, the electron g-factor is found to increase severalfold ($0.4 \longrightarrow 1.3$) with a decreasing number of occupied 1D subbands [15]. Second, the "$0.7(2e^2/h)$" feature of the first quantum step tends toward a value $0.5(2e^2/h)$ with increasing external magnetic field applied along the quantum wire [15, 18]. These results have stimulated the consideration of possible spontaneous electronic spin polarization, enhanced by disorder in the 1D channel [17, 30]. These mechanisms were developed within the framework of the spin-polaron concept in conditions of the Wigner crystallization [11] and for the 1D transport at an ultralow linear concentration of carriers, when the exchange interaction begins to exceed their kinetic energy in zero magnetic field [19–24]. In the latter case, the numerical calculations conducted in the Kohn–Sham mean-field approximation [19–21] describe qualitatively the current–voltage characteristic of the polarized 1D channel. However, up to now, no analytic proof of the existence of the electron spin-polarization in the 1D channel has been presented. Besides, no analytic expression describing the linear carrier concentration dependence of the "$0.7(2e^2/h)$" feature has been derived, which significantly complicates analysis of the spontaneous electron spin polarization in 1D channels at finite temperature.

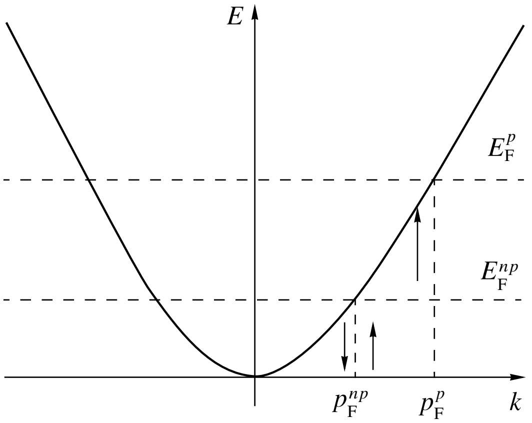

Fig. 1. The model of filling of the energy states by the partially polarized electron gas. The states near the 1D subband bottom are unpolarized. The polarization appears near the Fermi level.

The Hartree–Fock–Slater approximation with the localized exchange potential was used in the present work in order to solve this problem. Taking the electron–electron interaction into account is shown to lead to a spontaneous spin polarization of the Q1D electron gas at a small linear density of carriers. First, the appearance of spontaneous electron spin polarization in a 1D channel is considered in the context of phenomenological theory, which allows for the determining of a range of exchange-interaction prevalence over the kinetic energy in dependence on the linear carrier density. One of the main results of phenomenological theory is the determination of the critical carrier linear density below which the 1D channel is fully polarized. This completely lifts the spin degeneracy for the first quantum conductance step $G = e^2/h$. However, as soon as the carrier density in the 1D channel exceeds the critical value, the spontaneous electron spin-polarization becomes partial, which leads to an increase of the first quantum step up to the standard value $2e^2/h$. In addition, phenomenological theory predicts the temperature dependence of the split-off substep in the range $0.5(2e^2/h) - 0.75(2e^2/h)$. Further, a quantum-mechanical consideration of the electron spin polarization through exchange interaction in a quantum wire with an arbitrary carrier density is carried out within the framework of the Hartree–Fock–Slater approximation with localized exchange interaction. Comparing energy densities for spin-polarized and unpolarized electron gas in a 1D channel, one can conclude that, in the zero magnetic field case, the polarized and unpolarized states are energetically favorable at, respectively, small and large carrier densities.

2. SPONTANEOUS SPIN POLARIZATION OF CARRIERS THROUGH EXCHANGE INTERACTION IN QUANTUM WIRES: PHENOMENOLOGICAL THEORY

Spin-polarization of carriers in quantum wires appears basically similarly to processes in multielectron atoms, where, due to exchange interaction, each subshell is filled so that the total spin is maximal. The quantum-mechanical theory of the forming of the spin-polarized state in a quantum wire will be presented in the next section. First, we investigate the possibility of the appearance of a spontaneous spin polarization in 1D channels within the framework of phenomenological theory.

Let us consider a wire of length L containing N electrons, with N_p of these polarized. Consequently, the wire contains $N_\uparrow = (N - N_p)/2$ electrons with one spin direction and $N_\downarrow = (N + N_p)/2$ electrons with another. Let us assume that the unpolarized component occupies energy levels in the range $[0; E_F^{np}]$ and that the polarized component occupies energy levels in the range $[E_F^{np}; E_F^p]$ (see Fig. 1).

The energy of the partially polarized electronic liquid is given by

$$E = E_{\text{kin}}(N, N_p) + E_{\text{Coul}}(N) + E_{\text{ex}}(N_p). \tag{2}$$

The first term $E_{\text{kin}} > 0$ is related to the kinetic energy that depends both on the total number of electrons and on the polarized component density. E_{kin} will naturally increase with an increasing degree of polarization because of an increase of the number of levels, each occupied by a single electron.

The second term $E_{\text{Coul}} > 0$ describes the contribution of the Coulomb interaction, which depends only on the total number of electrons.

The third term $E_{\text{ex}} < 0$ accounts for the exchange interaction energy. We assume that this energy depends only on the polarized component density, which looks rather natural since the exchange interaction takes place only between electrons with the same spin direction.

The polarized component density is determined from the condition that the energy as a function of N_p should be at a minimum in the range $N_p \in [0; N]$. Since the Coulomb interaction energy does not depend on the spin state, in what follows it is enough to take into account only the first and third terms in (2):

$$W = E_{\text{kin}}(N, N_p) + E_{\text{ex}}(N_p). \tag{3}$$

In its turn, the kinetic energy of the partially polarized electronic liquid is the sum of the kinetic energies of the polarized and unpolarized components:

$$E_{\text{kin}} = E^{np}_{\text{kin}}(N, N_p) + E^{p}_{\text{kin}}(N, N_p). \tag{4}$$

The unpolarized component energy reads

$$E^{np}_{\text{kin}} = \frac{g_s}{2m}\sum_{|p| < p^{np}_{\text{F}}} p^2 = \frac{g_s}{2m}\frac{L}{2\pi\hbar}\int_{-p^{np}_{\text{F}}}^{p^{np}_{\text{F}}} p^2 dp = \frac{g_s L}{2\pi\hbar m}\frac{(p^{np}_{\text{F}})^3}{3}. \tag{5}$$

Here, $g_s = 2$ is the spin g-factor, and p^{np}_{F} is determined from the condition

$$2g_s p^{np}_{\text{F}} L = 2\pi\hbar(N - N_p), \qquad p^{np}_{\text{F}} = \frac{\pi\hbar}{g_s}(n - n_p), \tag{6}$$

where $n = N/L$ is the linear carrier density. Thus,

$$E^{np}_{\text{kin}} = \frac{\pi^2\hbar^2}{6g_s^2 m}(n - n_p)^3 L = \frac{\pi^2\hbar^2}{24m}(n - n_p)^3 L. \tag{7}$$

The polarized component energy is determined similarly:

$$E^{p}_{\text{kin}} = \frac{1}{2m}\sum_{p^{np}_{\text{F}} < |p| < p^{p}_{\text{F}}} p^2 = \frac{L}{2\pi\hbar m}\int_{p^{np}_{\text{F}}}^{p^{p}_{\text{F}}} p^2 dp = \frac{g_s L}{2\pi\hbar m}\frac{(p^{p}_{\text{F}})^3 - (p^{np}_{\text{F}})^3}{3}, \tag{8}$$

where p^{p}_{F} is determined from the condition

$$2(p^{p}_{\text{F}} - p^{np}_{\text{F}})L = 2\pi\hbar N_p, \qquad p^{p}_{\text{F}} = p^{np}_{\text{F}} + \pi\hbar n_p = \pi\hbar(n + n_p)/2. \tag{9}$$

Thus,

$$E^{p}_{\text{kin}} = \frac{\pi^2\hbar^2}{48m}[(n + n_p)^3 - (n - n_p)^3]L, \tag{10}$$

which determines the linear density of the kinetic energy per unit of quantum-wire length

$$\varepsilon_{\text{kin}} = E_{\text{kin}}/L = \frac{\pi^2\hbar^2}{48m}[2n^3 + 6nn_p^2]. \tag{11}$$

The exchange interaction energy density can be presented in the form

$$\varepsilon_{\text{ex}} \approx -a_1 n_p - b_1 n_p^2, \tag{12}$$

which corresponds to the retaining of the first two terms in the Taylor series. Thus, a minimum of the total energy as a function of n_p in the range $n_p \in [0; n]$ should be found in order to find the density of the polarized component of the electron gas in the 1D channel:

$$\varepsilon = \varepsilon_{\text{kin}} + \varepsilon_{\text{ex}} = \frac{\pi^2\hbar^2}{48m}[2n^3 + W(n_p)], \tag{13}$$

where

$$W(n_p) = (6n - b)n_p^2 - an_p, \qquad a = 48ma_1/\pi^2\hbar^2, \quad b = 48mb_1/\pi^2\hbar^2. \tag{14}$$

Three cases should be considered.

1. $6n < b$. The $W(n_p)$ plot is depicted in Fig. 2. The function W steadily decreases in the range $[0; n]$; the minimum is reached at $n = n_p$. Thus, the system is completely polarized.

2. $n > b$, $\dfrac{a}{12(n - b)} > n$. The $W(n_p)$ plot is given in Fig. 3. The minimum is also reached at $n = n_p$. Thus, if the linear electron density does not exceed the value

$$n < n_{\text{crit}} = \frac{1}{2}(b + \sqrt{b^2 + (a/3)}), \tag{15}$$

the system remains completely polarized.

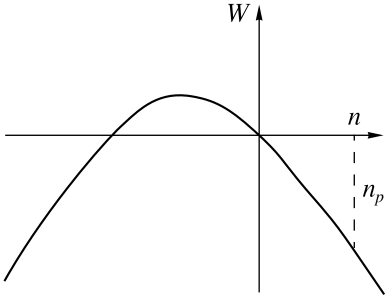

Fig. 2. Dependence of the function W on the density of the polarized component n_p at low total linear carrier density ($n < b$).

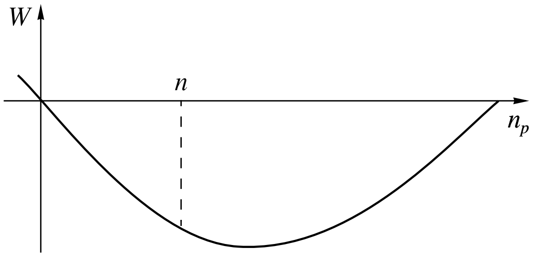

Fig. 3. Dependence of the function W on the polarized-component density n_p at high total linear carrier density ($n > b$).

3. $n > n_{\text{crit}}$. The function $W(n_p)$ has a minimum in the range $[0; n]$ at the point

$$n_p = \frac{a}{12(n-b)}, \tag{16}$$

which determines the density of the polarized component of the electron gas in the 1D channel. It can be seen that its fraction decreases with increasing total carrier density. The corresponding density dependence of the polarization degree $\alpha = n_p(n)/n$ is shown in Fig. 4.

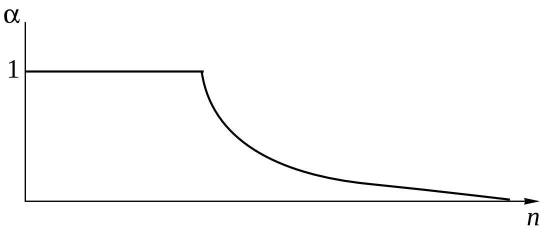

Fig. 4. Dependence of the degree of polarization, α, on the total linear carrier density n in a quantum wire.

Let us assume that the momentum dependence of the state occupancy is given by the following expression:

$$Q(p, T) = g_s(T, \varepsilon(p) - \mu^{np}) f(T, \varepsilon(p) - \mu^p), \tag{17}$$

where $1 < g_s < 2$ is the spin g-factor corresponding to the average number of electrons in a k space cell, which depends on temperature and chemical potential of the unpolarized component μ^{np}; $f(p, T, \mu^p)$ is the Fermi distribution. Then, the conductance of the quantum wire with a partially polarized electron gas equals

$$\begin{aligned} G = \frac{e}{hnV}\int_0^\infty p\{&g_s(T, \varepsilon(p) - \mu^{np}) f(T, \varepsilon(p) - \mu^p) \\ &- g_s(T, \varepsilon(p) - \mu^{np} + eV) f(T, \varepsilon(p) - \mu^p + eV)\}dp, \end{aligned} \tag{18}$$

where V is the longitudinal (pulling) voltage (source–drain voltage, V_{ds}, applied along the 1D channel, which is electrostatically compressed using the split-gate technique [1–3]). In the limit of small V, we have

$$\begin{aligned} G &= \frac{e^2}{hm}\int_0^\infty p\left\{g_s(T, \varepsilon(p) - \mu^{np})\frac{\partial f(T, \varepsilon(p) - \mu^p)}{\partial \mu^p}\right. \\ &\qquad \left. + f(T, \varepsilon(p) - \mu^p)\frac{\partial g_s(T, \varepsilon(p) - \mu^{np})}{\partial \mu^{np}}\right\}dp \\ &= -\frac{e^2}{h}\int_0^\infty \left\{g_s(T, \varepsilon - \mu^{np})\frac{\partial f(T, \varepsilon - \mu^p)}{\partial \varepsilon}\right. \\ &\qquad \left. + f(T, \varepsilon - \mu^p)\frac{\partial g_s(T, \varepsilon - \mu^{np})}{\partial \varepsilon}\right\}d\varepsilon. \end{aligned} \tag{19}$$

At zero temperature, $\mu^{np} \equiv E_{\text{F}}^{np}$, $\mu^p \equiv E_{\text{F}}^p$, so that

$$\begin{aligned} f(T, \varepsilon(p) - \mu^{np}) &= \theta(\mu^p - \varepsilon), \\ g_s(T, \varepsilon(p) - \mu^{np}) &= 1 + \theta(\mu^{np} - \varepsilon), \\ \frac{\partial f(T, \varepsilon - \mu^p)}{\partial \varepsilon} &= \delta(\varepsilon - \mu^p), \\ \frac{\partial g_s(T, \varepsilon - \mu^{np})}{\partial \varepsilon} &= \delta(\varepsilon - \mu^{np}), \end{aligned} \tag{20}$$

and the conductance equals

$$G|_{T=0} = \begin{cases} \dfrac{e^2}{h} = \dfrac{1}{2}G_0, & n_p = n, \\ 2\dfrac{e^2}{h} = G_0, & n_p < n. \end{cases} \tag{21}$$

Thus, the system remains fully polarized at small linear carrier densities $n < n_{\text{crit}}$, which results in the quantum step height being equal to half the standard value. As soon as the carrier density exceeds the critical value, the spontaneous spin polarization becomes partial, which is manifested in an abrupt change in conductance to the standard level ($G_0 = 2e^2/h$).

It is reasonable to assume at finite temperature ($T \neq 0$) that, with decreasing energy, g_s decreases from 2 to 1 smoothly rather than stepwise (Fig. 5):

$$g_s = 1 + f(T, \varepsilon - \mu^{np}). \qquad (22)$$

If the temperature is sufficiently low, then it may be assumed that

$$\mu^{np} \approx -\xi + E_{\rm F}^{np}(n), \qquad (23)$$

where the small negative addition $-\xi$ to the Fermi energy of the unpolarized component depends weakly on the carrier density. It reflects the absence of an abrupt change in the derivative $\frac{\partial g_s}{\partial \varepsilon}$ at $\varepsilon = 0$, $T = 0$ for the fully polarized gas.

Let us consider the case when the system is fully polarized at zero temperature. Then, $F_{\rm F}^{np} \equiv 0$, and $\mu^{np} = -\xi$ is a negative constant. Including temperature into our consideration leads in this case to the partial depolarization of the low-energy states with the probability $\left(1 + \exp\left(\frac{\varepsilon + \xi}{kT}\right)\right)^{-1}$. Then we can put $g_s(T, \varepsilon - \mu^{np}) = 1$ and $f(T, \varepsilon - \mu^p) = 1$ in (19). Therefore, taking into consideration the behavior of the spin g-factor at finite temperature (22), we obtain for the 1D channel conductance

$$\begin{aligned} G &= -\frac{e^2}{h}\int_0^{\infty}\left\{\frac{\partial f(T, \varepsilon - \mu^p)}{\partial \varepsilon} + \frac{\partial f(T, \varepsilon + \xi)}{\partial \varepsilon}\right\}d\varepsilon \\ &= \frac{e^2}{h}\left\{\frac{1}{e^{-\mu^p/kT} + 1} + \frac{1}{e^{\xi/kT} + 1}\right\}. \end{aligned} \qquad (24)$$

At moderate temperatures, when $\mu^p/kT \gg 1$ (but it is not necessary that $\xi/kT \gg 1$), the exponential function in the denominator of the first term in (24) can be neglected and the expression can be rewritten as

$$G = \frac{e^2}{h}\left\{1 + \frac{1}{e^{\xi/kT} + 1}\right\}. \qquad (25)$$

This formula describes the conductance of a fully polarized electron gas within a quantum wire at a nonzero temperature. Passing to the limit $T \longrightarrow 0$, we have $G = e^2/h$, which agrees with the result obtained above. An increase in the temperature at the condition $\xi/kT \ll 1$ leads to an increase of the conductance up to the value of $g = 3/2\ (e^2/h)$.

Thus, the presented phenomenological theory predicts a temperature dependence of the substep height in the range from $0.5G_0$ to $0.75G_0$. The obtained temperature dependence of the conductance of the partially polarized gas explains the stable observation of the unified "$0.7(2e^2/h)$" feature of the first quantum step in studies of quantum wires with various characteristics [6, 15–24]. These experiments were probably carried out at temperatures that were not sufficiently low to ensure, with account taken of the width of the quantum wires studied, suppression of the electron depolarization near the bottom of the first 1D subband. At this subband, the transformation of the "$0.7(2e^2/h)$" feature into the $0.5(2e^2/h)$ substep occurs only with the appropriate increase of the Boltzmann factor, which is achieved by lowering the temperature [31], raising the magnetic field [15], or by using narrow [6] or slightly disordered [17, 30] quantum wires.

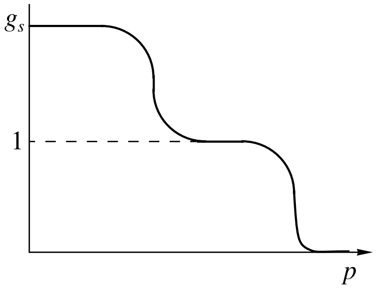

Fig. 5. Dependence of the mean electron number in the k-space cell on the momentum.

We can represent the conductance of a partially polarized gas as

$$G = \frac{e^2}{h}\left\{1 + \frac{1}{e^{(\xi - E_{\rm F}^{np}(n))/kT} + 1}\right\}. \qquad (26)$$

Hence, it follows that when the carrier density increases to the level satisfying the inequality $E_{\rm F}^{np}(n)/kT \gg 1$, the conductance increases to the standard value $(2e^2/h)$. It is precisely this effect that is realized in experiments on the study of the quantum conductance staircase in the case of increasing 1D subband filling accompanied by quenching of the "$0.7(2e^2/h)$" feature [6, 15, 17, 18].

3. SPONTANEOUS SPIN POLARIZATION OF CARRIERS THROUGH EXCHANGE INTERACTION IN QUANTUM WIRES: QUANTUM-MECHANICAL CONSIDERATION

Let us now show, using methods of quantum mechanics, that exchange interaction can indeed lead to the forming of the spin-polarized state of the electron gas in a quantum wire. We consider two examples.

3.1. Singlet and Triplet States of a Two-Electron System in a Quantum Wire

Let us consider a wire of length L containing a pair of particles. We assume that the particles are located in a single quantum-well subband. In the absence of interaction, particles 1 and 2 have the wave functions

$$\begin{aligned}\psi_1 &= \frac{1}{\sqrt{L}}e^{ik_1z}\varphi(x, y)\chi_1,\\ \psi_2 &= \frac{1}{\sqrt{L}}e^{ik_2z}\varphi(x, y)\chi_2,\end{aligned} \tag{27}$$

where $k_1 = \frac{\pi n_1}{L}$, $k_2 = \frac{\pi n_2}{L}$, $\varphi(x, y)$ is the wave function in the xy plane normal to the wire axis z, and χ is the spin component of the wave function.

The energy of the pair of noninteracting particles is equal to

$$E = 2E_0 + \frac{\pi^2\hbar^2}{2mL^2}(n_1^2 + n_2^2). \tag{28}$$

The total wave function of the system must be antisymmetric. Disregarding the spin–orbit interaction, the wave function factorizes into a product of the coordinate and spin components:

$$\Psi = \Phi(\mathbf{r}_1, \mathbf{r}_2)X(s_1, s_2). \tag{29}$$

If the total spin equals unity, the spin part X is symmetric relative to the transposition of arguments. Therefore, the coordinate part must be antisymmetric in this case. If the total spin is zero, the coordinate part must be, by contrast, symmetric. We can write in the zero approximation

$$\begin{aligned}\Phi_{\uparrow\uparrow} &= \frac{\varphi(x_1, y_1)\varphi(x_2, y_2)}{L\sqrt{2}}[e^{i(k_1z_1 + k_2z_2)} - e^{i(k_1z_2 + k_2z_1)}],\\ \Phi_{\uparrow\downarrow} &= \frac{\varphi(x_1, y_1)\varphi(x_2, y_2)}{L\sqrt{2}}[e^{i(k_1z_1 + k_2z_2)} + e^{i(k_1z_2 + k_2z_1)}].\end{aligned} \tag{30}$$

Let us assume that electrons in the singlet state occupy the level with the lower kinetic energy ($k = 0$). For the triplet state, we assume that the momentum of one of electrons is zero, and that of the other electron, arbitrary. Then

$$\begin{aligned}\Phi_{\uparrow\uparrow} &= \frac{\varphi(x_1, y_1)\varphi(x_2, y_2)}{L\sqrt{2}}[e^{ikz_1} - e^{ikz_2}],\\ \Phi_{\uparrow\downarrow} &= \frac{1}{L}\varphi(x_1, y_1)\varphi(x_2, y_2).\end{aligned} \tag{31}$$

Let us now assume that electrons repel one another, and the repulsion potential is $V(\mathbf{r}_1, \mathbf{r}_2)$. To a first order of the perturbation theory, we have

$$\begin{aligned}E_{\uparrow\uparrow} &= 2E_0 + \frac{\hbar^2k^2}{2m} + \langle\Phi_{\uparrow\uparrow}|V|\Phi_{\uparrow\uparrow}\rangle = 2E_0 + \frac{\hbar^2k^2}{2m}\\ &+ \frac{1}{L}\int\varphi^*(x_1, y_1)\varphi^*(x_2, y_2)V(\mathbf{r}_1, \mathbf{r}_2)\\ &\times\varphi(x_1, y_1)\varphi(x_2, y_2)d\mathbf{r}_1d\mathbf{r}_2 - \frac{1}{L}\int\varphi^*(x_1, y_1)\varphi^*(x_2, y_2)\\ &\times V(\mathbf{r}_1, \mathbf{r}_2)e^{ik(z_1 - z_2)}\varphi(x_1, y_1)\varphi(x_2, y_2)d\mathbf{r}_1d\mathbf{r}_2,\\ E_{\uparrow\downarrow} &= 2E_0 + \langle\Phi_{\uparrow\downarrow}|V|\Phi_{\uparrow\downarrow}\rangle\\ &= 2E_0 + \frac{1}{L}\int\varphi^*(x_1, y_1)\varphi^*(x_2, y_2)\\ &\times V(\mathbf{r}_1, \mathbf{r}_2)\varphi(x_1, y_1)\varphi(x_2, y_2)d\mathbf{r}_1d\mathbf{r}_2.\end{aligned} \tag{32}$$

Let us introduce the short-range repulsive potential

$$V(\mathbf{r}_1, \mathbf{r}_2) = \alpha\delta(\mathbf{r}_1 - \mathbf{r}_2). \tag{33}$$

Then we obtain

$$\begin{aligned}E_{\uparrow\uparrow} &= E_0 + \frac{\hbar^2k^2}{2m},\\ E_{\uparrow\downarrow} &= 2E_0 + \langle\Phi_{\uparrow\downarrow}|V|\Phi_{\uparrow\downarrow}\rangle = 2E_0 + \alpha\int|\varphi(x, y)|^4dxdy.\end{aligned} \tag{34}$$

The first-order correction vanishes for the triplet state and is positive for the singlet state. It can be seen from the formula that, if the wave number k is small enough and the “power” a of the repulsive potential is high enough, so that

$$\frac{\hbar^2k^2}{2m} < \alpha\int|\varphi(x, y)|^4dxdy, \tag{35}$$

then, with perturbation taken into account, the triplet state becomes more favorable than the singlet one.

Undoubtedly, the actual potential of the electron–electron repulsion is Coulombic, rather than delta-like. However, we assume that taking this factor into consideration will not change the situation drastically. It would be expected that in narrow wires, where electrons are arranged more densely, the Coulomb interaction matrix element will be larger than in wide wires, which will lead to an increase of the formation probability of the triplet state, i.e., the state with a maximum spin.

3.2. Consideration of the Exchange Interaction in Electron Gas inside a Quantum Wire

The number of electrons in quantum wires always exceeds 2. Therefore, it is interesting to consider effects resulting from the exchange interaction in the case of an arbitrary number of electrons N in a quantum wire.

Let us first consider the case of a fully polarized system. Then, the coordinate part of the total wave function is antisymmetric with respect to any pair of indices. We use the Hartree–Fock–Slater approximation for the one-particle wave functions to obtain

$$\begin{aligned}&\left[-\frac{\hbar^2}{2m}\nabla^2 + U(\boldsymbol{\rho}) + U_\mathrm{b}\right]\psi_j(\mathbf{r})\\&+ e^2\sum_{l=1}^{N}\int\frac{\psi_l(\mathbf{r}')\psi_l(\mathbf{r}')\psi_j(\mathbf{r}) - \psi_l(\mathbf{r}')\psi_j(\mathbf{r}')\psi_l(\mathbf{r})}{|\mathbf{r}-\mathbf{r}'|}d\mathbf{r}'\\&= \varepsilon_j\psi_j(\mathbf{r}),\end{aligned} \tag{36}$$

where $U(\boldsymbol{\rho})$ is the confining potential in the plane perpendicular to the wire axis, and U_b is the potential of interaction with the positive background. The motion along the quantum wire axis z is free. Thus,

$$\psi_j(\mathbf{r}) = \frac{1}{\sqrt{L}}e^{ik_jz}\varphi(\boldsymbol{\rho}), \quad \boldsymbol{\rho} = (x, y). \tag{37}$$

We have

$$\begin{aligned}&\left[-\frac{\hbar^2}{2m}\nabla^2 + U(\boldsymbol{\rho}) + U_\mathrm{b}\right]\varphi_j(\boldsymbol{\rho}) + \frac{e^2}{L}\sum_{l=1}^{N}\\&\times\int\frac{\varphi_l(\boldsymbol{\rho}')\varphi_l(\boldsymbol{\rho}')\varphi_j(\boldsymbol{\rho}) - \varphi_l(\boldsymbol{\rho}')\varphi_j(\boldsymbol{\rho}')\varphi_l(\boldsymbol{\rho})e^{ik_j(z'-z)+ik_l(z-z')}}{|\mathbf{r}-\mathbf{r}'|}\\&\times d\mathbf{r}' = \left(\varepsilon_j - \frac{\hbar^2k_j^2}{2m}\right)\varphi_j(\boldsymbol{\rho}).\end{aligned} \tag{38}$$

The interaction term depends on the coordinate z along the wire, which leads to a nonharmonic dependence of one-particle wave functions on this coordinate. However, it can be readily seen that this dependence disappears for an infinitely long wire, since a shift by z along the z'-axis is unimportant in this case. Then, we have in the thermodynamic limit ($L \longrightarrow \infty$, $n = N/L = \mathrm{const}$)

$$\begin{aligned}&\left[-\frac{\hbar^2}{2m}\nabla^2 + U(\boldsymbol{\rho}) + U_\mathrm{b}\right]\varphi_j(\boldsymbol{\rho})\\&+ U_\mathrm{H}\varphi_j(\boldsymbol{\rho}) + U_\mathrm{HF}[\varphi_j(\boldsymbol{\rho})] = \left(\varepsilon_j - \frac{\hbar^2k_j^2}{2m}\right)\varphi_j(\boldsymbol{\rho}),\end{aligned} \tag{39}$$

where U_H corresponds to the local Hartree potential

$$U_\mathrm{H} = \lim_{L\to\infty}\left\{\frac{e^2}{L}\sum_{l=1}^{nL}\int_{-L/2}^{L/2}dz'\int\frac{\varphi_l^*(\boldsymbol{\rho}')\varphi_l(\boldsymbol{\rho}')}{|\mathbf{r}-\mathbf{r}'|}d\boldsymbol{\rho}'\right\}, \tag{40}$$

and U_HF is the nonlocal Fock addition; i.e., it is related to the consideration of the exchange interaction

$$\begin{aligned}U_\mathrm{HF}[\varphi_j] = \lim_{L\to\infty}&\left\{\frac{e^2}{L}\sum_{l=1}^{nL}\int_{-L/2}^{L/2}\frac{dz'e^{i(k_j+k_l)z'}}{\sqrt{(\boldsymbol{\rho}-\boldsymbol{\rho}')+z'^2}}\right.\\&\left.\times\int\varphi_l^*(\boldsymbol{\rho}')\varphi_j(\boldsymbol{\rho}')\varphi_l(\boldsymbol{\rho})d\boldsymbol{\rho}'\right\}.\end{aligned} \tag{41}$$

Now we introduce one serious simplification. We assume that all electrons are in a single quantum-well subband and that the one-particle wave function does not depend on the electron momentum. Then, the equation under consideration must be independent of k_j. In order to satisfy this condition, we assume that $e^{ik_j(z'-z)} \approx 1$. The exchange term can then be rewritten approximately in the local form:

$$\begin{aligned}U_\mathrm{HF}(\varphi) = \varphi(\boldsymbol{\rho})\lim_{L\to\infty}&\left\{\frac{e^2}{L}\sum_{l=1}^{N}\int_{-L/2}^{L/2}dz\frac{e^{-ik_lz'}}{\sqrt{(\boldsymbol{\rho}-\boldsymbol{\rho}')^2+z'^2}}\right.\\&\left.\times\int\varphi^*(\boldsymbol{\rho}')\varphi(\boldsymbol{\rho}')d\mathbf{r}'\right\} = 2\varphi(\boldsymbol{\rho})\end{aligned} \tag{42}$$

$$\times\lim_{L\to\infty}\left\{\frac{e^2}{L^2}\int_{-L/2}^{L/2}dz'\frac{\sum\limits_{k_l>0}\cos(k_lz')}{\sqrt{(\boldsymbol{\rho}-\boldsymbol{\rho}')^2+z'^2}}\int\frac{\varphi^*(\boldsymbol{\rho}')\varphi(\boldsymbol{\rho}')}{|\mathbf{r}-\mathbf{r}'|}d\mathbf{r}'\right\}.$$

Now we replace summation over k_l by integration using the substitution

$$\sum_{k_l} \Rightarrow \frac{L}{2\pi}\int dk. \tag{43}$$

Then,

$$\begin{aligned}U_\mathrm{HF}(\boldsymbol{\rho}) = \frac{e^2}{\pi}\lim_{L\to\infty}&\left\{\int_{-L/2}^{L/2}dz'\frac{\sum\limits_{k_l>0}\cos[k_lz']}{\sqrt{(\boldsymbol{\rho}-\boldsymbol{\rho}')^2+z'^2}}\right.\\&\left.\times\int\varphi^*(\boldsymbol{\rho}')\varphi(\boldsymbol{\rho}')d\boldsymbol{\rho}'\right\}\end{aligned} \tag{44}$$

$$= \frac{e^2}{\pi}\int_{-\infty}^{+\infty}dz'\frac{\sin[k_\mathrm{max}z']}{z'\sqrt{(\boldsymbol{\rho}-\boldsymbol{\rho}')^2+z'^2}}\int\varphi^*(\boldsymbol{\rho}')\varphi(\boldsymbol{\rho}')d\boldsymbol{\rho}'.$$

This integral can be expressed in terms of hypergeometric functions. The cutoff momentum is determined from the condition

$$\begin{aligned} 2k_{\max}L &= 2\pi N, \\ k_{\max} &= \pi n, \end{aligned} \tag{45}$$

where $n = N/L$ is the linear electron density. At large linear densities, we have

$$\begin{aligned} U_{\mathrm{HF}}(\boldsymbol{\rho}) &= e^2 \lim_{L \leftarrow \infty}\left\{\frac{1}{L}\int_{-L/2}^{L/2} dz\delta(z-z')\int\frac{\varphi(\boldsymbol{\rho}')\varphi(\boldsymbol{\rho}')}{|\mathbf{r}-\mathbf{r}'|}d\mathbf{r}'\right\} \\ &= e^2\int\frac{\varphi^*(\boldsymbol{\rho}')\varphi(\boldsymbol{\rho}')}{|\boldsymbol{\rho}-\boldsymbol{\rho}'|}d\boldsymbol{\rho}'. \end{aligned} \tag{46}$$

Thus, in the limit of high linear carrier densities, the exchange term does not depend on n.

At a low linear concentration, when $n \ll |\boldsymbol{\rho}-\boldsymbol{\rho}'|$, i.e., at a distance between carriers smaller than the wire diameter, the integral in (44) can be estimated as follows:

$$U_{\mathrm{HF}}(\boldsymbol{\rho}) = \frac{\pi^{3/2}}{4}e^2 n\int\varphi^*(\boldsymbol{\rho}')\varphi(\boldsymbol{\rho}')d\boldsymbol{\rho}' = \frac{\pi^{3/2}}{4}e^2 n. \tag{47}$$

In this case, the exchange interaction does not affect the self-consistent wave functions, but leads to the appearance of a negative addition to the system energy.

Let us now consider the term U_{H}:

$$\begin{aligned} U_{\mathrm{H}} &= \lim_{L\to\infty}\left\{\frac{e^2}{L}\sum_{l=1}^{nL}\int_{-L/2}^{L/2}\frac{dz'}{\sqrt{(\boldsymbol{\rho}-\boldsymbol{\rho}')^2+z'^2}} \times\int\varphi_l^*(\boldsymbol{\rho}')\varphi_l(\boldsymbol{\rho}')d\boldsymbol{\rho}'\right\} \\ &= ne^2\lim_{L\to\infty}\left\{\int_{-L/2}^{L/2}\frac{dz'}{\sqrt{(\boldsymbol{\rho}-\boldsymbol{\rho}')^2+z'^2}}\int\varphi_l^*(\boldsymbol{\rho}')\varphi_l(\boldsymbol{\rho}')d\boldsymbol{\rho}'\right\} \\ &= 2ne^2\lim_{L\to\infty}\left\{\int\operatorname{arcsinh}\left(\frac{L}{|\boldsymbol{\rho}-\boldsymbol{\rho}'|}\right)\varphi_l^*(\boldsymbol{\rho}')\varphi_l(\boldsymbol{\rho}')d\boldsymbol{\rho}'\right\}. \end{aligned} \tag{48}$$

It is easy to see that, in the limit of infinite L, we have a logarithmic divergence associated with the long-range character of the Coulomb potential. However, according to the general theorem, Hartree's term will always be fully compensated by the interaction with the positive background:

$$U_{\mathrm{H}} + U_{\mathrm{b}} = 0. \tag{49}$$

The general equation for the one-particle wave function coincides at low densities with the one-particle Schrödinger equation in the absence of electron–electron interaction (surely, with allowance for the negative addition to the energy due to the exchange)

$$\begin{aligned} &\left[-\frac{\hbar^2}{2m}\nabla^2 + U(\boldsymbol{\rho})\right]\varphi_j(\mathbf{r}) \\ &= \left(\varepsilon - \frac{\hbar^2 k_j^2}{2m} + \frac{\pi^{3/2}}{4}e^2 n\right)\varphi_j(\mathbf{r}). \end{aligned} \tag{50}$$

The energy density equals

$$\begin{aligned} \varepsilon &= \frac{1}{2}[\varepsilon_{\mathrm{kin}} + \sum\varepsilon_j] \\ &= \varepsilon_0 n + \frac{\pi^2\hbar^2}{6m}n^3 - \frac{\pi^{3/2}}{8}e^2 n^2, \end{aligned} \tag{51}$$

where the first term corresponds to the constant addition to the energy of each one-particle level; the second, to the density of the kinetic energy; and the third, to the exchange interaction energy.

At a high linear density, the one-particle wave functions are determined from the following equation:

$$\begin{aligned} &\left[-\frac{\hbar^2}{2m}\nabla^2 + U(\boldsymbol{\rho}) - \frac{e^2}{\pi}\int\frac{\varphi^*(\boldsymbol{\rho}')\varphi(\boldsymbol{\rho}')}{|\boldsymbol{\rho}-\boldsymbol{\rho}'|}d\boldsymbol{\rho}'\right]\varphi_j(\mathbf{r}) \\ &= \left(\varepsilon - \frac{\hbar^2 k_j^2}{2m}\right)\varphi_j(\mathbf{r}). \end{aligned} \tag{52}$$

The term describing the exchange interaction is a negative addition leading to a downward shift of the one-particle energies. The magnitude of this shift does not depend on the density. The energy density equals

$$\varepsilon = \tilde{\varepsilon}_0 n + \frac{\pi^2\hbar^2}{6m}n^3, \tag{53}$$

where $\tilde{\varepsilon}_0$ stands for the one-particle energy with a correction for exchange; the second term is related to the kinetic energy.

Let us now consider the unpolarized system, which can be represented as a combination of two polarized systems with opposite spins. The exchange interaction then shows itself only among the electrons of one subsystem. Thus, at small carrier densities, the energy density for the unpolarized gas is given by

$$\varepsilon = \sum\varepsilon_j = \varepsilon_0 n + \frac{\pi^2\hbar^2}{24m}n^3 - \frac{\pi^{3/2}}{16}e^2 n^2. \tag{54}$$

At high densities, when the exchange term does not depend on the density, the equation for one-particle wave functions in the unpolarized gas coincides with the one for the polarized gas. The energy density for the unpolarized gas is then given by

$$\varepsilon = \tilde{\varepsilon}_0 n + \frac{\pi^2\hbar^2}{24m}n^3. \tag{55}$$

Comparing energy densities for the polarized and unpolarized gas, we conclude that the polarized state is energetically favorable at small linear carrier densities, and the unpolarized state of the electron gas in 1D channels, at high concentrations.

4. CONCLUSION

Thus, consideration of the electron–electron interaction in the Hartree–Fock–Slater approximation with localized exchange potential may lead to the spontaneous spin polarization of the Q1D electronic gas at small linear carrier densities, whereas the unpolarized state dominates at large linear densities. This effect of the exchange interaction shows itself in the splitting of the first quantum step at zero magnetic field. The obtained temperature dependence of the height of the substep split-off, as a result of the spontaneous polarization, predicts its transformation from e^2/h to $(3/2(e^2/h))$, due to the partial depolarization of the electron gas near the 1D subband bottom. The proposed model accounts for the stable observation of the unified "$0.7(2e^2/h)$" feature of the first quantum step when studying various quantum wires, whose large width prevents the suppression of the depolarization process even at ultralow temperatures.

ACKNOWLEDGMENTS

We thank V.I. Perel and V.V. Kveder for their helpful participation in discussions.

This study was supported by the programs "Physics of Solid-State Nanostructures" (FTNS, project no. 97-1040) and "Fullerenes and Atomic Clusters" (project no. 3-1-98).

REFERENCES

1. T. J. Thornton, M. Pepper, H. Ahmed, *et al.*, Phys. Rev. Lett. **56**, 1198 (1986).
2. D. A. Wharam, T. J. Thornton, R. Newbury, *et al.*, J. Phys. C **21**, L209 (1988).
3. B. J. van Wees, H. van Houten, C. W. J. Beenakker, *et al.*, Phys. Rev. Lett. **60**, 848 (1988).
4. A. Yakoby, H. L. Stormer, Ned S. Wingreen, *et al.*, Phys. Rev. Lett. **77**, 4612 (1996).
5. J. I. Pascual, J. Mendez, J. Gomez-Herrero, *et al.*, Phys. Rev. Lett. **71**, 1852 (1993).
6. N. T. Bagraev, L. E. Klyachkin, A. M. Malyarenko, and W. Gehlhoff, Superlattices Microstruct. **23**, 1333 (1998).
7. N. T. Bagraev, W. Gehlhoff, V. K. Ivanov, *et al.*, Fiz. Tekh. Poluprovodn. (St. Petersburg) **34**, 477 (2000) [Semiconductors **34**, 462 (2000)].
8. R. Landauer, IBM J. Res. Dev. **1**, 233 (1957).
9. M. Büttiker, Phys. Rev. Lett. **57**, 1761 (1986).
10. L. I. Glazman, I. M. Ruzin, and B. I. Shklovskii, Phys. Rev. B **45**, 8454 (1992).
11. B. Spivak and Fei Zhou, Phys. Rev. B **61**, 16730 (2000).
12. Masao Ogata and Hidetoshi Fukuyama, Phys. Rev. Lett. **73**, 468 (1994).
13. Takashi Kimura, Kazuhiko Kuroki, and Hideo Aoki, Phys. Rev. B **53**, 9572 (1996).
14. Seigo Tarucha, Takashi Honda, and Tadashi Saku, Solid State Commun. **94**, 413 (1995).
15. K. J. Thomas, J. T. Nicholls, M. Y. Simmons, *et al.*, Phys. Rev. Lett. **77**, 135 (1996).
16. K. J. Thomas, J. T. Nicholls, N. J. Appleyard, *et al.*, Phys. Rev. B **58**, 4846 (1998).
17. K. J. Thomas, J. T. Nicholls, M. Pepper, *et al.*, Phys. Rev. B **61**, 13365 (2000).
18. K. S. Pyshkin, C. J. B. Ford, R. H. Harrell, *et al.*, Phys. Rev. B **62**, 15842 (2000).
19. Chuan-Kui Wang and K.-F. Berggren, Phys. Rev. B **54**, 14257 (1996).
20. Chuan-Kui Wang and K.-F. Berggren, Phys. Rev. B **57**, 4552 (1998).
21. A. M. Bychkov, I. I. Yakymenko, and K.-F. Berggren, in *Proceedings of the 8th International Symposium "Nanostructures: Physics and Technology", St. Petersburg, Russia, 2000*, p. 391.
22. Kenji Hirosi, Shu-Shen Li, and N. S. Wingreen, Phys. Rev. B **63** (3), 033315 (2001).
23. A. Gold and L. Calmels, Philos. Mag. Lett. **74**, 33 (1996).
24. A. Gold and L. Calmels, in *Proceedings of the 23rd ICPS, Berlin, Germany, 1996*, Ed. by M. Scheffler and R. Zimmermann (World Scientific, Singapore, 1996), p. 1229.
25. A. Yu. Alekseev and V. V. Cheianov, Phys. Rev. B **57**, 6834 (1998).
26. D. L. Maslov and M. Stone, Phys. Rev. B **52**, 5539 (1995).
27. I. Safi and H. J. Schulz, Phys. Rev. B **52**, 17040 (1995).
28. G. E. Pikus, W. Knap, and C. Skierkiszewski, in *Proceedings of the 23rd ICPS, Berlin, Germany, 1996*, Ed. by M. Scheffler and R. Zimmermann (World Scientific, Singapore, 1996), p. 2435.
29. E. Lieb and D. Mattis, Phys. Rev. **125**, 164 (1962).
30. A. V. Andreev and A. Kamenev, Phys. Rev. Lett. **81**, 3199 (1998).
31. L. G. Glazman and A. V. Khaetskii, J. Phys.: Condens. Matter **1**, 5005 (1989).

Translated by S. Ktitorov

Semiconductors, Vol. 36, No. 1, 2002, pp. 74–80. Translated from Fizika i Tekhnika Poluprovodnikov, Vol. 36, No. 1, 2002, pp. 79–88.
Original Russian Text Copyright © 2002 by Evtikhiev, Konstantinov, Matveentsev, Romanov.

LOW-DIMENSIONAL SYSTEMS

Light Emission by Semiconductor Structure with Quantum Well and Array of Quantum Dots

V. P. Evtikhiev, O. V. Konstantinov, A. V. Matveentsev, and A. E. Romanov
Ioffe Physicotechnical Institute, Russian Academy of Sciences, St. Petersburg, 194021 Russia

Submitted July 17, 2000; accepted for publication May 17, 2001

Abstract—A new type of composite active region of a laser, which contains an $In_{0.2}Ga_{0.8}As$ quantum well (QW) and an array of InAs quantum dots (QDs) embedded in GaAs is studied. The QW acts as accumulator of injected carriers, and the QD array is the emitting system located in tunneling proximity to the QW. A theory for the calculation of electron and hole energy levels in the QD is developed. Occupation of the QDs due to the resonance tunneling of electrons and holes from the QW to the QD is considered; the conclusions are compared with the results obtained in studying an experimental laser with a combined active region. *© 2002 MAIK “Nauka/Interperiodica”.*

1. INTRODUCTION

Lasers based on arrays of quantum dots (QDs) were repeatedly described in the literature. In particular, lasers on InAs QDs embedded in GaAs, emitting in the photon energy range of 1.2–1.3 eV, are known [1]. Their distinctive feature is the rather low threshold current of about 200 A/cm^2 at room temperature. These lasers contain one or a few sheets of QDs in the undoped part of the *p*–*n* structure. A preliminary experimental study shows that certain advantages appear if a quantum well (QW) is located in the tunneling proximity to the QD array. The quantum yield of emission from such a structure hardly depends on the driving current. The possibility of increasing the carrier capture rate, since the related cross section is significantly larger for a QW than for a QD, represents an obvious advantage of this structure. Moreover, thermal equilibrium inside the QW is also bound to be attained faster than in the QD array.

This work is dedicated to developing a theoretical approach for the calculation of the electron and hole energy in a QD. The aim of this study is to establish the condition for coincidence of the energies of ionization of electron and hole states in the QW and QD. This resonance essentially facilitates tunneling from the QW into QDs and accelerates filling of the latter.

A semiconductor *p*–*n* heterostructure laser is considered. It comprises a QW—a layer of the $In_xGa_{1-x}As$ solid solution with a thickness *W*, and an array of InAs QDs embedded in GaAs in tunneling proximity to the QW. Experiments show that the distance between the QD array and the QW must be about 40 Å. As mentioned above, the QW plays the role of the reservoir, accumulating electrons and holes when the forward current is passed through the structure. When the distance between the QW and the QD sheet is small, carriers can easily tunnel from the QW to the QD under resonance conditions. As will be shown below, the QW with a thickness $W = 80$ Å and a $In_{0.2}Ga_{0.8}As$ composition will have a hole ground state ionization energy approximately coinciding with that for the unoccupied QD. The electron energy level in the unoccupied QD is 0.03 eV higher than in the QW. However, when a QD is occupied by a hole, the electron level in the QD decreases by an approximately similar value due to the electron–hole Coulomb interaction. The possibility of a free resonance electron tunneling from the QW to the QD occupied by a hole then appears. An electron and a hole form a bound exciton in the QD, with only singlet excitons emitting light. The triplet excitons with parallel electron and hole spins recombine nonradiatively due to the Auger effect. That is why the quantum yield (at relatively low current value) will be, at most, 25%, and this agrees with observations.

2. CARRIER DISPERSION LAWS

The heavy hole energy spectrum in the InAs crystal is well described by the quadratic approximation within a rather wide range. According to the data presented in the handbook [2] and in [3], this approximation holds when the hole energy is lower than 0.4 eV. The dispersion law was calculated there using the nonlocal pseudopotential method, which gives the most reliable results. Based on these, we assume that the hole energy is given by the quadratic dispersion law:

$$E_v(k) = \frac{\hbar^2 k^2}{2m_v}, \qquad (1)$$

where k is the hole wave vector, and $m_v = 0.41m_0$ is the tabulated hole effective mass in InAs. The energy is given in electron volts in [3], and the wave vector in fractions of its maximum value in the [001] direction, ($k' = ka/2\pi$), where $a = 6.06$ Å is the InAs lattice constant. One can judge to what extent (1) is satisfied by inspecting the plots presented in the lower part of the figure. The two dotted lines describe the band structure calculation results [3] for the [100] direction (lower dotted line) and the [111] direction (upper dotted line). The solid line is a standard quadratic dispersion law with the tabulated effective mass given by (1). It is seen that this curve is located exactly in the middle between the two dashed lines. The discrepancy between the dotted lines is due to corrugation of the heavy-hole energy surface.

The quadratic approximation for the electron energy spectrum is valid only within an exceedingly narrow energy range. We have found that the semiempirical expressions, similar to the Kane formulas [4], give an adequate analytic description of the numerical results obtained in [3]. This approximation for the electronic energy in the conductance band reads

$$E_c(k) = \frac{E_g}{2}\left(\sqrt{1 + \frac{2\hbar^2 k^2}{m_c E_g}} - 1\right). \qquad (2)$$

Here, $E_g = 0.356$ eV is the energy gap for InAs, and m_c is the electron effective mass that is considered as a fitting parameter for which the value $m_c = 0.057m_0$ is obtained. This value gives the dependence calculated using (2), which is presented in the upper part of the figure by a thick solid line; the dotted line, presenting the results of [3], practically coincides with it. Moreover, the thin solid line in the figure depicts the standard quadratic approximation for the conduction band with the tabulated electron effective mass $m_c = 0.027m_0$. This approximation obviously leads to a significant inaccuracy when the electron energy exceeds 0.05 eV. Notice that, in accordance with calculations [3], the electronic energy spectrum is isotropic up to an energy $E_c \approx 1$ eV, at which the anisotropy, due to a distinction between the L and X valleys, becomes essential.

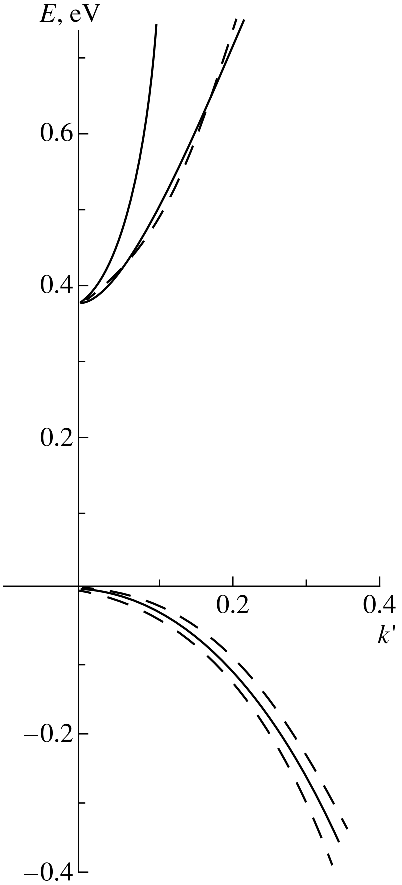

Dispersion laws in the valence (lower part) and conduction bands (upper part). Dotted lines represent the carrier dispersion laws obtained by the pseudopotential method in [3]. Thick solid lines show the dispersion laws obtained from the approximating expressions derived in this study: formula (1) for holes and formula (2) for electrons. Thin solid line in the upper part of the figure represents the quadratic dispersion law.

3. SPHERICAL MODEL OF QD

Formula (2) for the nonparabolic dispersion law is related to the case of a plane wave in an infinite medium. The InAs QWs embedded in GaAs have a truncated cone form with the rounded vertex 15 Å in diameter. The base of the cone is elliptic with axes 150 and 170 Å; the height equals 20 Å. The nonparabolic Hamiltonian in the effective mass approximation is absent for an object of such complex shape; such a Hamiltonian can be constructed only for a spherical microscopic object. The optimal diameter of a sphere modeling the cone is chosen in [5], so that its value lies between the diameter of a sphere inscribed in the cone and the diameter of a sphere whose surface passes through the vertex and is tangent to the base. The cone is similar in shape to the sporting discus; therefore, these two spheres have very close diameters. Here we assume that the optimal diameter equals the height of an untruncated pyramid, i.e., the diameter of the sphere whose surface passes through the vertex and is tangent to the base of the cone, $d = 22.2$ Å. It is noteworthy that the energy levels of electrons in a spherical QD lie higher than those in the cone.

Inside the sphere, at distances $r < d/2$, the wave equation has the following form both for electrons and holes:

$$T\Psi_1 = E\Psi_1. \qquad (3)$$

The energy is reckoned from the bottom of the corresponding band in the InAs crystal. Here, T is the kinetic energy operator, which is obtained from (2) for electrons and from (1) for holes by substituting the operator $(-i\nabla)$ for the wave vector k. Let us consider the square root of the operator expression obtained for electrons from (2). We understand the radical operator as a power series expansion of the radical (2) in k^2 with the following substitution of k^2 by the operator $(-\nabla^2)$:

$$T\Psi_1 = -\frac{E_g}{4}\left(y\nabla^2 + \frac{1}{4}y^2\nabla^4 + \frac{1.3}{4.6}y^3\nabla^6 + \dots\right)\Psi_1,$$
$$y = \frac{2\hbar^2}{m_c E_g}. \tag{4}$$

The bound carrier wave function Ψ_2 is described outside the sphere $r > d/2$ (in GaAs crystal) by the equation corresponding to the parabolic approximation for the kinetic energy

$$\left(-\frac{\hbar^2}{2m_2}\nabla^2 + U\right)\Psi_2 = E\Psi_2, \quad U = \Delta E. \tag{5}$$

Here, m_2 is the carrier effective mass in the GaAs crystal; the potential energy U is equal to the conduction or valence band discontinuity ΔE for electrons and holes, respectively.

Let us now consider the boundary conditions at $r = d/2$, which will be discussed in detail below. Here, we only note that the boundary conditions, in fact, constitute an independent part of the mathematical model of the QD. To describe the bound states, they are chosen in the form

$$\Psi_1 = \Psi_2; \quad \frac{d\Psi_1}{dn} = \frac{d\Psi_2}{dn}. \tag{6}$$

These conditions mean the continuity of the wave function and its derivative along the normal n to the interface. In the spherical model case, the second condition represents the continuity of the radial component of the wave function gradient. It is easy to see that the solutions to (3) or (5) read

$$\Psi_1 = \frac{\sin(kr)}{r}, \quad \Psi_2 = D\frac{e^{-qr}}{r}. \tag{7}$$

This solution is well known for the parabolic dispersion law (holes in InAs and both types of carriers in GaAs). The wave function decay parameter for GaAs is given by the expression

$$q^2 = \frac{2m_2}{\hbar^2}[\Delta E - E(k)]. \tag{8}$$

Parameters k and D can be found from the boundary conditions (6). However, in the case of electrons in InAs with nonparabolic dispersion law, we must make sure that the function Ψ_1 in (7) is an eigenfunction of the operator T from (4). To this end, we use the relations

$$\nabla^2\Psi_1 = \frac{1}{r}\frac{d^2}{dr^2}(r\Psi_1) = -k^2\Psi_1,$$
$$\nabla^4\Psi_1 = \nabla^2\nabla^2\Psi_1 = k^2\Psi_1 \quad \text{etc.} \tag{9}$$

Thus, we obtain the result of action of an arbitrary power of the Laplacian

$$\nabla^{2n}\Psi_1 = (-1)^n k^{2n}\Psi_1. \tag{10}$$

Then the operator series (4) transforms into a power series, which is an expansion of the radical (2) in k^2. Thus, we have shown that Ψ_1 is an eigenfunction, and the eigenvalue $E(k)$, as a function of the wave vector, is given by (2). Now, we use two boundary conditions (6) in order to obtain two values: the wave vector k [or energy $E(k)$] and the constant D, appearing in the wave function Ψ_2 for the outer region. This leads to the transcendent equation for the wave vector (or energy):

$$k\cot\left(\frac{kd}{2}\right) = -q, \tag{11}$$

where the decay parameter q is given by (8). This equation is well known in the literature. The new point is that the electron energy $E(k)$ appearing in (8) is described by the nonparabolic law (2). Equation (11) may have a few solutions related to different branches of the cotangent. We rewrite (11) to make it obvious:

$$k\tan\left(\frac{kd}{2} - \frac{M\pi}{2}\right) = q. \tag{12}$$

Here, the integer number M assumes odd values $M = 1, 3, 5\dots$ to which correspond different solutions of the transcendent equation. The modulus of the tangent argument $(kd - M\pi)/2$ is less than $\pi/2$. It is noteworthy that (12) is valid also for the flat geometry, i. e., for QW if the boundary conditions (6) are satisfied. In this case, however, the sphere diameter must be substituted by the QW thickness W. Moreover, the quantum number M assumes all whole values, both odd and even, including zero in the flat geometry case. We note that the similar form of the dispersion equation both for the spherical and flat geometry is only obtained in the case of derivative continuity at the sphere surface.

4. CHANGE IN THE ENERGY GAP IN A STRAINED STRUCTURE

The QW material is a solid solution containing 20% In. The lattice constant of the virtual crystal is larger than for the GaAs matrix. Therefore, the QW material will be compressed. This effect must be particularly strong for the InAs QD in GaAs, since, in this case, the mismatch between the cluster and matrix lattices is very large. The compression induces an increase of the material band gap. According to experimental data summed up in the monograph [6], the gap change δE_g for most of the III–V semiconductors increases with increasing pressure p at pressures less than 20 kbar with the proportionality coefficient K = 12 meV/kbar, i.e.,

$$\delta E_g\ [\text{eV}] = 0.12p\ [\text{GPa}]. \tag{13}$$

A formula can be derived (and this is done below) according to which the pressure is related to the relative lattice mismatch $f = \Delta a/a$ by the similar relations for both the spherical QD and the flat QW:

$$p = \frac{2}{3}\frac{E}{1-\nu}f, \tag{14}$$

where E is Young's modulus, and ν is the Poisson ratio. We assume the following for solid solutions on the basis of InAs: E = 50 GPa, and ν = 1/3 [7]. Both of these values are approximate with an accuracy of 10%. Taking into account the magnitudes of E and ν, we have

$$p = 50f, \tag{15}$$

and we arrive at the formula for an increase of the bound gap, with pressure eliminated:

$$\delta E_g\ [\text{eV}] = 6f. \tag{16}$$

Let us discuss the magnitude of the lattice mismatch f. The lattice constant for components of the InAs/GaAs heterointerface are equal to 6.058 and 5.653 Å that gives $f = 0.067$. In the case of the $In_{0.2}Ga_{0.8}As$/GaAs interface, the In content in the solid solution is 5 times less. This means that the lattice mismatch between the virtual crystal and the GaAs crystal will also be 5 times less, i.e., $f = 0.0133$. According to (16), the energy gap in the $In_{0.2}Ga_{0.8}As$ QW increases by 0.08 eV due to the compression. The increase of the energy gap inside the InAs QD is 0.40 eV, which exceeds the initial gap value of 0.356 eV. Therefore, no pseudomorphic state appears at the boundary of the cluster, which is a QD. We shall discuss below, in detail, various aspects of the discrepancy between experimental data with the estimate given here for the QD. Here, we only notice that the electronic level must not exist in such a QD, but this conclusion contradicts the experiment. Perhaps, this is related to the growth conditions of the QD cone, whose wide base lies on the wetting layer of InAs. When the wetting layer is gradually overgrown with GaAs, the cone is gradually "flooded" with gallium arsenide. This is our explanation of the absence of a stretched GaAs crystal, in which the cone is embedded, due to forming of the amorphous layer at the cone surface.

5. CALCULATION OF ENERGY LEVELS

Let us square both the left- and right-hand sides of the characteristic Eq. (12). It then takes the form

$$E(k) + I(k) = \Delta E. \tag{17}$$

The carrier energy $E(k)$ is reckoned from the edge of the respective band inside the spherical or flat potential well; $I(k)$ is the ionization potential for a carrier in the well. Since Eq. (17) is valid for both of the well types, the ionization potential is given by the same expression in both cases:

$$I(k) = \frac{\hbar^2 k^2}{2m_2}\tan^2\left(\frac{kd}{2} - \frac{M\pi}{2}\right). \tag{18}$$

Let us consider conditions for the appearance of a single electron level at the QD. At $M = 1$ and $k = \pi/d$, the equality (17) yields the threshold value of the conduction band discontinuity:

$$\Delta E_{te} = E_c(k) = \frac{E_g}{2}\left(\sqrt{1 + 2\hbar^2\frac{k^2}{m_c E_g}} - 1\right). \tag{19}$$

Assuming that $d = 2.22$ nm, $E_g = 0.356$ eV, and $m_c = 0.057m_0$, we obtain $\Delta E_{te} = 0.53$ eV.

Let us now consider the conduction band discontinuity ΔE_c at the boundary of the QD. We take into account the material strain due to the lattice mismatch and use the standard values for the conduction and valence band discontinuities: $\Delta E_c = 0.65\Delta E_g$, and $\Delta E_v = 0.35\Delta E_g$ (ΔE_g is the difference of the energy gaps). In the case of the QD under consideration, $E_g = 0.356$ eV + 0.40 eV ≈ 0.76 eV; therefore, $\Delta E_g = 1.43$ eV – 0.76 eV = 0.67 eV, and, therefore, $\Delta E_c = 0.44$ eV. The obtained discontinuity is noticeably less than the threshold value $\Delta E_{te} = 0.53$ eV. Thus, no bound electronic state exists in the QD.

For the valence band discontinuity, we obtain $\Delta E_v = 0.23$ eV. The critical hole energy with respect to bound state formation, reckoned from the valence band top, is given by

$$E_{th} = \frac{\hbar^2\pi^2}{2m_v d^2} \tag{20}$$

and equals 0.17 eV. This value is less than the valence band discontinuity of 0.23 eV. Therefore, a bound hole state exists in the QD.

An electron can be theoretically bound at a bound hole because of the Coulomb electron–hole interaction. However, the electron binding energy will be of the order of the exciton binding energy in GaAs, i.e., 0.006 eV. All such bound excitons will be almost completely ionized at room temperature. Thus, the emission line due to the electron-hole recombination in the QD should not be observed. This conclusion contradicts the experimental data. Therefore, the stress at the QD surface must somehow relax. We believe that the most likely mechanism of this relaxation may be related to the amorphous layer appearing near the cluster surface. That is why we will assume later that the pressure-induced increase of the gap in the QD is absent and calculate the energy levels on this assumption.

Let us introduce the dimensionless variable

$$x = \frac{kd}{2} \tag{21}$$

and use it in Eq. (17). The numerical solving of the transcendent Eq. (17) for holes yields $x = 2.02$, which leads to the following hole ionization energy [using (18)]: $I_h = 0.07$ eV. A similar procedure yields $x = 1.78$ for electrons from whence follows the electron ionization energy $I_e = 0.07$ eV. These ionization energies are related to the case of a QD occupied by only a hole or an electron. The following electron and hole effective masses were used: $m_c = 0.057m_0$ and $m_v = 0.41m_0$ for InAs and $m_c = 0.065m_0$ and $m_v = 0.45m_0$ for GaAs. The diameter of the sphere approximating the QD is equal $d = 22.2$ nm. The critical values $x = x_1$, etc. are equal to, respectively, $\pi/2$, $3\pi/2$, etc. They correspond to the appearance of new energy levels in the well. Values of x, which are solutions to (17) both for electrons and holes, are located within the interval $(\pi/2, 3\pi/2)$, which implies the presence of a single level only.

Let us now consider electron and hole energy levels in the accumulating QW. To this end, we shall find parameters of the $In_{0.2}Ga_{0.8}As$ QW. The band gap in the unstressed $In_xGa_{1-x}As$ material, calculated with the use of the known empirical formula [2]

$$E_g = 0.324 + 0.7x + 0.4x^2, \tag{22}$$

is equal to $E_g = 1.14$ eV at $x = 0.8$. Formula (22) is accurate enough at $x \approx 1$, but it gives too large an error near $x = 0$. This is not important for us, since we are interested only in the energy gap at $x = 0.8$. We have mentioned above that the pressure-induced increase of the gap must be about 0.08 eV. Thus, the total width of the energy gap is $E_g(f) = 1.14$ eV + 0.08 eV = 1.22 eV, with discontinuities $\Delta E_c = 0.14$ eV and $\Delta E_v = 0.07$ eV. Since the band discontinuities are small and the well is wide enough, the parabolic approximation is applicable. We obtain, using linear interpolation, the following effective masses: $m_c = 0.057m_0$ and $m_v = 0.0442m_0$. The width of this well is $a = 8$ nm. Solving (12) numerically gives two solutions for electrons [$x_1^e = 1.01$, $x_2^e = 1.79$ ($M = 0.1$)] and three solutions for holes [$x_1^h = 1.24$, $x_2^h = 2.4$, $x_3^h = 3.5$ ($M = 0, 1, 2$)]. We are interested in the ground state levels for electrons and holes: $E_0^e = 0.04$ eV and $E_0^h = 0.01$ eV. The corresponding ionization levels are $I_e^0 = 0.1$ eV and $I_0^h = 0.06$ eV.

Notice that the ionization energy for a hole in a QW is close to the ionization energy for a hole in a QD. This means that there is a resonance for a hole tunneling between a QW and an unoccupied QD. The ionization energy for an electron in a QW is 0.03 eV larger than that for a QD. This means that the resonance electron tunneling from the QW into the empty QD is hindered. However, if the QD is occupied by a hole, the situation changes, since the Coulomb interaction between the tunneling electron and hole appears [8].

Let us estimate the energy of the Coulomb interaction between an electron and a hole in a QD. To this end, we consider the change of the potential energy of an electron transferred from the QW boundary toward a QD occupied by a hole. This potential energy can be considered as the Coulomb interaction energy of two point charges only if the distance between the electron and the QD center is much larger than the effective radius of the hole wave function localized in the QD. When the electron approaches the QD boundary, its potential energy drops on

$$\Delta U = \frac{1}{\varepsilon}\frac{e^2}{l}, \tag{23}$$

where e is the electron charge, $\varepsilon = 12.9$ is the dielectric constant of GaAs filling the space between the QW and the QD, and l is the distance between boundaries of the QW and QD. We assume that $l = 4$ nm; i.e., we believe that it equals the distance between the QW boundary and the QD sheet plane. We then obtain $\Delta U = 0.03$ eV; and resonance of electronic levels in the QW and the QD occupied by the hole occurs. When the QD is occupied by an electron and hole, a violation of the resonance of electronic levels takes place and the hole resonance is restored, which facilitates capture of the second hole. If radiative recombination does not occur before the second hole is captured, then the nonradiative Auger recombination takes place with overwhelming probability. Notice that, according to the calculations carried out above, the total energy of ionization for an electron and a hole ionization in a QD equals 0.17 eV, and the emitted photon energy is 1.26 eV; this agrees with the experimental data and confirms the validity of the used model.

Let us now discuss the boundary conditions for the wave function at the heterointerface. One condition is usual and indisputable: the continuity of the wave function $\Psi_1 = \Psi_2$. The second condition must relate the normal to the boundary derivatives of these functions. In the literature, these derivatives are usually assumed to be equal. This is postulated without comments in some monographs; some proof is given in others. Band bottom discontinuity and absence of effective mass discontinuity are generally assumed. We will temporarily substitute the steplike change in $U(x)$ by a smooth function. Carrying out the standard procedure similar to the proof of continuity for the normal component of induction in electrostatics, we obtain the continuity condition for the normal derivative of the wave function. In the presence of the effective mass discontinuity, new possibilities for derivative matching appear. In addition to the equality of the derivatives, a new relation appears:

$$\frac{1}{m_1}\frac{d\Psi_1}{dn} = \frac{1}{m_2}\frac{d\Psi_2}{dn}. \tag{24}$$

We can give an example when this boundary condition gives a reasonable result: the problem of the above-barrier transport of an electron across a heterointerface with conduction-band bottom and effective mass discontinuities.

It is easy to see that the conservation of particle flux across a single heterointerface is violated if the condition $d\Psi_1/dn = d\Psi_2/dn$ is used. Condition (24) must be used to obey this law. This can be verified by direct calculation. The boundary condition can be chosen arbitrarily, since it is a part of the mathematical model of the physical problem under consideration. If the problem of the above-barrier transport of an electron across a single heterointerface is considered, condition (24) must be used; however, if the bound state problem at the double heterointerface is considered (QW), the derivative continuity is preferable, since the particle flux equals zero in this case. If it is invalid, only experiment can suggest a correct substitution.

6. CONCLUSION

1. The electronic level in an unoccupied QD is higher than that in a QW. This level is lowered upon occupation of the QD by the hole with a value of the same order due to the Coulomb electron-hole interaction, which provides its resonance with the electronic level in the QW.

2. The electron and the hole in the QD form the bound exciton, and only singlet bound excitons emit light, while the triplet ones recombine nonradiatively via the Auger recombination process. This is the reason why the quantum yield (at relatively small currents) does not exceed 25 %.

3. The position of the electronic level in the QD critically depends on the choice of the electronic dispersion law. If the parabolic approximation is used with the tabulated effective mass $m_c = 0.027m_0$, the bound electron state in an unoccupied QD does not exist. Similarly, it is absent in the nonparabolic dispersion (2) case with the same effective mass. If a hole is captured, a bound electronic state appears [8] with an energy about 6 meV, which is characteristic for the exciton. Electrons, however, cannot survive at so shallow a level at room temperature and, therefore, lasers could not function at such conditions. This conclusion contradicts the experimental data, which suggests that the nonparabolic dispersion law with $m_c = 0.057m_0$ be taken into account. This reasoning causes us to disregard the hydrostatic compression of the InAs clusters and consider it only for $In_{0.2}Ga_{0.8}As$ QWs.

APPENDIX

ELASTIC FIELDS OF QDs AND QWs

Let the crystal lattices of the quantum structure and the embedding matrix be characterized, respectively, by parameters a_1 and a_2. The strain fields due to the mismatch $\Delta a = a_1 - a_2$ are proportional to the mismatch parameter $f = \Delta a/a_1$.

1. Spherical QD

The spherical QD with radius R_0 can be represented as an elastic dilatation inclusion. It is assumed, in this case [9, 10], that an elastic sphere of radius R_0 is put into the spherical void whose volume is smaller than the inclusion volume by ΔV. By virtue of the symmetry, the field of displacements both inside, $\mathbf{u}^{(1)}$, and outside, $\mathbf{u}^{(2)}$, the sphere has only the radial component depending only on the radial coordinate r [9]:

$$u_r^{(1)} = -\frac{2(1-2\nu)}{(1+\nu)}\frac{C}{R_0^3}r, \qquad \text{(A.1)}$$

$$u_r^{(2)} = \frac{C}{r^2}, \qquad \text{(A.2)}$$

where ν is the Poisson ratio (the elastic moduli of the QD and the embedding matrix are assumed equal), and the constant C is determined from the boundary condition

$$\pi R_0^3(u_r^{(2)} - u_r^{(1)})\big|_{r=R_0} = \Delta V \qquad \text{(A.3)}$$

and is equal to

$$C = \frac{1+\nu}{12\pi(1-\nu)}\Delta V,$$

or

$$C = \frac{1+\nu}{3(1-\nu)}R_0^3 f. \qquad \text{(A.4)}$$

In the second equality, we took into account that the volume change ΔV is related to the mismatch parameter f by the equation

$$\Delta V = 4\pi R_0^3 f. \qquad \text{(A.5)}$$

The displacement field (A.1) and (A.2) determines the following components of the strain tensor (in spherical coordinates):

$$\varepsilon_{rr}^{(1)} = \varepsilon_{\varphi\varphi}^{(1)} = \varepsilon_{\theta\theta}^{(1)} = -\frac{2(1-2\nu)}{3(1-\nu)}f, \qquad \text{(A.6)}$$

$$\left.\begin{aligned} \varepsilon_{rr}^{(2)} &= -\frac{2(1+\nu)}{3(1-\nu)}\frac{R_0^3}{r^3}f, \\ \varepsilon_{\varphi\varphi} &= \varepsilon_{\theta\theta} = \frac{1+\nu}{3(1-\nu)}\frac{R_0^3}{r^3}f. \end{aligned}\right. \qquad \text{(A.7)}$$

The dilatation $\delta = \sum_k \varepsilon_{kk}$ is obviously constant inside the QD

$$\delta^{(1)} = -\frac{2(1-2\nu)}{(1-\nu)}f \qquad \text{(A.8)}$$

and vanishes outside the QD

$$\delta^{(2)} = 0. \qquad \text{(A.9)}$$

We determine the elastic strain field from (A.6) and (A.7) and from the Hooke law:

$$\sigma_{rr}^{(1)} = \sigma_{\varphi\varphi}^{(1)} = \sigma_{\theta\theta}^{(1)} = -\frac{2E}{3(1-\nu)}f, \qquad (A.10)$$

$$\sigma_{rr}^{(2)} = -\frac{2E}{3(1-\nu)}f, \quad \sigma_{\varphi\varphi}^{(2)} = \sigma_{\theta\theta}^{(2)} = -\frac{1}{2}\sigma_{rr}^{(2)}, \qquad (A.11)$$

where E is Young's modulus. Correspondingly, the pressures $p = 1/3\sum_k \sigma_{kk}$ inside and outside the QD are the following:

$$p^{(1)} = \frac{2E}{3(1-\nu)}f, \qquad (A.12)$$

$$p^{(2)} = 0. \qquad (A.13)$$

2. Quantum well

Let us choose the Cartesian coordinates so that the *y*-axis is perpendicular to the QW boundaries. The *x* and *y* axes are parallel to these surfaces and to the crystallographic planes, along which the mismatch *f* is set. Elastic strains and stresses outside the QW are absent. Inside the QW, they are given by

$$\varepsilon_{xx} = \varepsilon_{zz} = -f, \quad \varepsilon_{yy} = \frac{2\nu}{1-\nu}f; \qquad (A.14)$$

$$\sigma_{xx} = \sigma_{zz} = -\frac{E}{1-\nu}f, \quad \sigma_{yy} = 0. \qquad (A.15)$$

Correspondingly, the dilatation and the pressure inside the QW are as follows:

$$\delta = \frac{2(1-2\nu)}{1-\nu}f, \qquad (A.16)$$

$$p = \frac{2E}{3(1-\nu)}f. \qquad (A.17)$$

Thus, the pressure inside the compressed QW and QD is described by the same expression, (A.17) or (A.12).

ACKNOWLEDGMENTS

We thank R.A. Suris, a corresponding member of the Russian Academy of Sciences, and Prof. A.V. Subashiev for constructive criticism.

REFERENCES

1. I. V. Kudryashov, V. P. Evtikhiev, V. E. Tokranov, *et al.*, J. Cryst. Growth **201/202**, 1158 (1999).
2. *Landolt-Bornstein: Numerical Data and Functional Relationships in Science and Technology, New Series* (Springer-Verlag, Berlin, 1987), Group III, Vol. 22a.
3. J. R. Chelikowsky and M. L. Cohen, Phys. Rev. B **14** (2), 556 (1976).
4. K. Seeger, *Semiconductor Physics* (Springer-Verlag, Berlin, 1974; Mir, Moscow, 1977).
5. L. V. Asryan and R. A. Suris, Semicond. Sci. Technol. **11**, 554 (1996).
6. R. A. Smith, *Semiconductors* (Cambridge Univ. Press, Cambridge, 1978; Mir, Moscow, 1982).
7. T. Benabbas, Y. Androussi, and A. Lefebvre, J. Appl. Phys. **86** (4), 1945 (1999).
8. V. E. Bugrov and O. V. Konstantinov, Fiz. Tekh. Poluprovodn. (St. Petersburg) **32** (10), 1235 (1998) [Semiconductors **32**, 1101 (1998)].
9. J. D. Eshelby, Solid State Phys. **3**, 79 (1956).
10. C. Teodosiu, *Elastic Models of Crystal Defects* (Springer-Verlag, Berlin, 1982; Mir, Moscow, 1985).

Translated by S. Ktitorov

Semiconductors, Vol. 36, No. 1, 2002, pp. 81–84. Translated from Fizika i Tekhnika Poluprovodnikov, Vol. 36, No. 1, 2002, pp. 87–90.
Original Russian Text Copyright © 2002 by Shamirzaev, Sokolov, Zhuravlev, Kobitski, Wagner, Zahn.

Changes in the Density of Nonradiative Recombination Centers in GaAs/AlGaAs Quantum-Well Structures as a Result of Treatment in CF_4 Plasma

T. S. Shamirzaev*, A. L. Sokolov*, K. S. Zhuravlev*, A. Yu. Kobitski*,
H. P. Wagner, and D. R. T. Zahn****

** Institute of Semiconductor Physics, Siberian Division, Russian Academy of Sciences,*
pr. Akademika Lavrent'eva 13, Novosibirsk, 630090 Russia

e-mail: timur@thermo.isp.nsc.ru

*** Institute für Physik, Technische Universität Chemnitz, D-09126 Chemnitz, Germany*

Submitted March 12, 2001; accepted for publication May 25, 2001

Abstract—The effect of low-energy CF_4 plasma treatment on the stationary photoluminescence (PL) spectra and PL kinetics in GaAs/AlGaAs quantum-well (QW) structures is investigated. Intensity of the PL from QWs located deeper than the surface layer damaged by plasma treatment increases. It is established that this is accompanied by an increase in the PL decay time at temperatures above 30 K. It is shown that the density of nonradiative recombination centers in the QW located below the damaged surface layer decreases by a factor of 30 after 40-s exposure to plasma. © *2002 MAIK “Nauka/Interperiodica”.*

Dry etching by means of low-energy-plasma treatment is widely used for selective mask removal in the fabrication of low-dimensional structures and microelectronic devices based on III–V compounds. To ensure the complete removal of the mask from the surface, it is overetched. To this end, the surface is bombarded with plasma ions, which damage the deeper layers of the semiconductor and leads to a substantial modification of their electrical and optical properties [1–12]. It was established that the density of the defects introduced by exposure to low-energy plasma is highest in the surface region of thickness from several tens to several hundreds of angstroms and gradually decreases into the depth of the structure; the electrical properties of the layers as deep as 1000 Å from the surface are affected. A convenient method to study the defects induced in the surface region by plasma treatment is based on the investigation of photoluminescence (PL) of GaAs/AlGaAs structures with several quantum wells (QWs) located at different depths beneath the surface [13, 14]. It was shown that, upon exposure of such structures to low-energy plasma, the intensity of the PL from the QWs located close to the surface decreases due to the formation and diffusion of point defects acting as nonradiative recombination centers.

In our previous studies, it was found that, along with a decrease in the intensity of the PL from the surface layers, exposure of GaAs/AlGaAs QW structures to low-energy CF_4, Ar, or Kr plasma results also in an enhancement of the PL from the QWs located deeper than the damaged region [10, 12]. It was suggested that this enhancement is a consequence of passivation of the defects acting as nonradiative recombination centers (introduced in the structure in the course of epitaxy) due to their binding into complexes with rapidly diffusing defects introduced by plasma treatment.

To evaluate quantitatively the variation in the density of nonradiative recombination centers in the QWs located below the plasma-damaged region of the structure, in this study we examine the temperature dependence of picosecond kinetics of the PL in GaAs/AlGaAs QW structures exposed to low-energy CF_4 plasma.

GaAs/$Al_{0.3}Ga_{0.7}As$ structures under study were grown by molecular-beam epitaxy on semi-insulating (100)-oriented GaAs substrates. They consisted of six GaAs QWs of thickness 2.2, 2.8, 3.4, 4.2, 5.6, and 8.5 nm, separated by 25-nm-thick $Al_{0.3}Ga_{0.7}As$ barriers. Thicker QWs were grown at greater distances from the surface. To prevent diffusion of impurities and defects from the substrate to the structure, the QWs were grown on a buffer consisting of a 1-μm-thick GaAs layer and a 0.5-μm-thick $Al_{0.3}Ga_{0.7}As$ layer; the latter incorporated a short-period GaAs/AlAs superlattice. To prevent oxidation of the upper $Al_{0.3}Ga_{0.7}As$ layer, the structure was capped by a 100-nm-thick GaAs layer. The samples were treated for 40 s in CF_4 plasma at a pressure of 0.07 Torr, a power density of 1 W/cm^2, and a

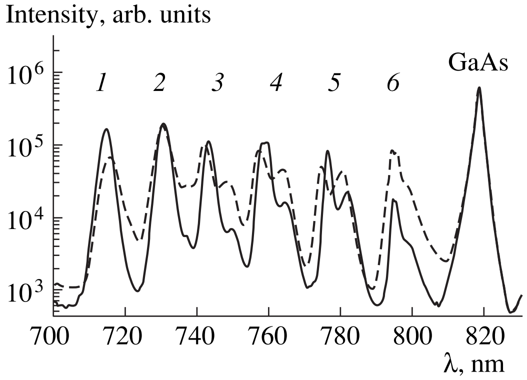

Fig. 1. Low-temperature (T = 6 K) PL spectra of the structure before (solid line) and after (dashed line) a 40-s treatment in CF_4 plasma.

self-bias potential of about –300 V. The stationary PL measurements were carried out using a setup described in [10]. A He–Ne laser operating at 632.8 nm was used for PL excitation, with the laser power density being 20 W/cm^2. At this wavelength, the absorption coefficients of GaAs and $Al_{0.3}Ga_{0.7}As$ at 4.2 K are 3×10^4 and 1×10^4 cm^{-1}, respectively; thus, about 3% of the excitation radiation is absorbed in each QW, which ensures their uniform excitation. The transient PL was excited by a pulsed dye laser operating at 580 nm and pumped by a mode-locked Ar$^+$ laser. The parameters of the dye-laser pulses are the following: duration, 20 ps; repetition rate, 4 MHz; and energy, 0.2 nJ. The PL signal was analyzed by a CROMEX 250IS spectrometer and detected by a Hamamatsu C4334 streak-camera, with the time resolution being 50 ps. The samples were installed in a closed-cycle CTI-Cryogenics cryostat.

The PL spectra of the structures before and after CF_4 plasma treatment, measured at 6 K, are shown in Fig. 1. Of the seven lines in the spectra, lines *1–6* correspond to the transitions between the ground electron and heavy-hole levels (1e–1h) in the QWs of different thickness; these lines are split into doublets due to the fluctuations of the QW width [15]. The line at 1.515 eV originates from exciton recombination in the GaAs buffer layer. One can see that, in the spectra of the as-grown structure, the intensities of the PL from the first five QWs are roughly the same, while the PL line corresponding to the sixth QW, most distant from the surface, is weaker by about an order of magnitude. Apparently, the low intensity of the PL from this QW is related to the high density of defects, which are introduced during the growth of the structure and act as nonradiative recombination centers. The 40-s exposure of the structure to low-energy CF_4 plasma has the following effect: the PL from the QW closest to the surface is weakened slightly, and the PL from the QW most distant from the surface is enhanced significantly and becomes comparable in intensity to the PL from the first five QWs.

The kinetics of the sixth QW PL line at 20 K, measured before and after the plasma treatment of the structure, is shown in Fig. 2. One can see that the characteristic PL decay time in both cases is $\tau \approx 600$ ps. In Fig. 3, we present the temperature dependences of the PL decay time τ in the sixth QW of the structure before and after plasma treatment. With a rise in temperature, the PL decay time in the as-grown structure increases insignificantly, while, in the plasma-exposed structure,

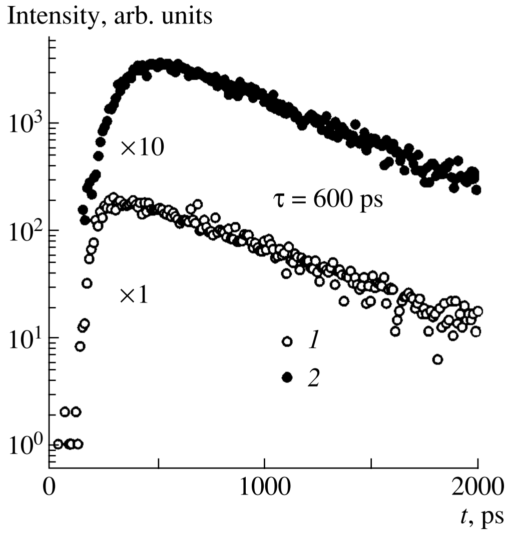

Fig. 2. The PL kinetics in the sixth QW of the structure (*1*) before and (*2*) after the plasma treatment. The measurement temperature was T = 20 K.

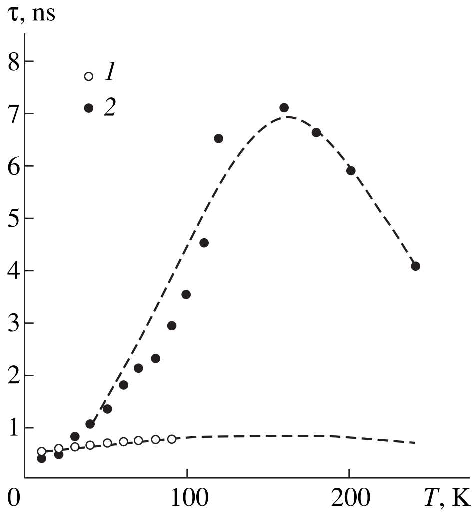

Fig. 3. Temperature dependences of the PL decay time in the sixth QW in (*1*) as-grown and (*2*) CF_4 plasma-exposed structure. The dashed lines show the results of calculations.

τ increases with T up to 150 K by more than an order of magnitude and then decreases somewhat.

It is known that the PL decay time in QWs is determined by the ratio between the rates of radiative and nonradiative recombination of free charge carriers and excitons. At low temperatures, nonradiative recombination is suppressed and the charge carriers are mostly bound into excitons; thus, the annihilation of excitons is the main recombination channel, and the PL decay time is determined by their lifetime. At elevated temperatures, two factors become important. On the one hand, thermal ionization of excitons leads to an increase in the density of unbound electron–hole pairs, whose lifetime exceeds considerably the exciton lifetime. On the other hand, the nonradiative recombination rate increases. Thus, depending on the density of nonradiative recombination centers in the QW, the temperature variation of the PL decay time can be described in the following terms. When this density is negligibly small, the PL decay time increases steadily with the temperature from the value determined by the exciton lifetime to that determined by the free charge carrier lifetime. At higher densities of nonradiative recombination centers, the PL decay time is determined by the rate of radiative recombination of excitons and electron–hole pairs at low temperatures and by the rate of their nonradiative recombination at high temperatures. Finally, when the number of nonradiative recombination centers in the QW is very large, the PL decay time equals the nonradiative recombination time in the whole temperature range.

An increase in the intensity of the peak corresponding to the sixth QW in the stationary PL spectrum indicates that the number of nonradiative recombination centers in the vicinity of this well is reduced. To evaluate quantitatively the variation in the density of these centers after plasma treatment, we used the following method developed recently [16]. In that paper, the formula relating the PL decay time τ in the QW with the temperature T and the total nonradiative recombination rate R_{nr} was obtained:

$$\tau(T) = [p_0 + n_c(T)]/[p_0 R_r(T) + n_c(T) R_{nr}(T)], \quad (1)$$

$$R_r(T) = B n_c(T) + R_x,$$

$$R_{nr}(T) = R_0 + R_s \exp(-E_A/kT),$$

$$n_c(T) = [m_e m_h/(m_e + m_h)](kT/\pi\hbar^2)\exp(-E_x/kT),$$

where R_r is the radiative-recombination probability; R_x is the exciton-recombination probability; B is the radiative-recombination coefficient for free charge carriers; R_0 is the temperature-independent contribution to the nonradiative-recombination probability (proportional to the density of nonradiative recombination centers); n_c is the ratio of the product of electron and hole densities to the exciton density; E_x is the exciton ionization energy; E_A is the thermal activation energy for nonradiative recombination; p_0 is the free hole density; and $m_e = 0.065m_0$ and $m_h = 0.5m_0$ are the electron and hole effective masses, respectively.

Temperature dependences of the PL decay time in the sixth QW in as-grown and plasma-treated structures were fitted by formula (1), and the results are shown in Fig. 3. The best fit to experimental data was obtained with the following set of parameters (the same for both curves): $E_x = 8$ meV, $E_A = 90$ meV, $B = 10^{-10}$ cm^2 s^{-1}, $p_0 = 5 \times 10^9$ cm^{-2}, $R_s = 1.2 \times 10^{10}$ s^{-1}, and $R_x = 1.8 \times 10^9$ s^{-1}. The parameter R_0, proportional to the density of nonradiative-recombination centers, changes from 1.17×10^9 s^{-1} in the as-grown structure to 4.2×10^7 s^{-1} in the CF$_4$ plasma-treated structure. This indicates that the number of nonradiative-recombination centers is reduced almost by a factor of 30. It should be noted that the above value for R_x, obtained from the fit, agrees well with that given in [16].

Similar calculations for the temperature dependence of the PL decay time in the fifth QW of the structure showed that here the density of nonradiative recombination centers changes after plasma exposure by no more than a factor of 2.

Thus, in this study we examined the effect of low-energy CF$_4$ plasma treatment of GaAs/AlGaAs QW structures on their PL spectra and kinetics. It is demonstrated that an increase in the intensity of the QW located beneath the surface region damaged by plasma treatment is accompanied by an increase in the PL decay time, which is more pronounced the higher the measurement temperature. It is established that the density of nonradiative-recombination centers in this QW is reduced by nearly a factor of 30 after the structure is exposed to plasma for 40 s.

REFERENCES

1. S. J. Fonash, Solid State Technol. **28**, 201 (1985).
2. S. J. Pearton, U. K. Chakrabarti, and F. A. Baiocchi, Appl. Phys. Lett. **55**, 1633 (1989).
3. W. Beinstingl, R. Christanell, J. Smoliner, *et al.*, Appl. Phys. Lett. **57**, 177 (1990).
4. K. L. Seaward, N. J. Moll, and W. F. Stickle, J. Electron. Mater. **19**, 385 (1990).
5. C. Juang, J. K. Hsu, I. S. Yen, and H. S. Shiau, J. Appl. Phys. **72**, 684 (1990).
6. S. J. Yun, S. J. Park, M. C. Paek, and J. Y. Lee, J. Electrochem. Soc. **137**, 2634 (1990).
7. K. Ohtsuka, T. Ohishi, Y. Abe, *et al.*, J. Appl. Phys. **70**, 2361 (1991).
8. K. S. Zhuravlev, V. A. Kolosanov, V. G. Plyukhin, and T. S. Shamirzaev, Zh. Tekh. Fiz. **64** (11), 185 (1994) [Tech. Phys. **39**, 1188 (1994)].

9. A. V. Murel’, A. P. Kasatkin, and V. M. Kogan, Izv. Akad. Nauk, Ser. Fiz. **56**, 161 (1992).
10. K. S. Zhuravlev, V. A. Kolosanov, I. I. Marahovka, and M. Holland, Fiz. Tekh. Poluprovodn. (St. Petersburg) **31**, 1436 (1997) [Semiconductors **31**, 1241 (1997)].
11. F. Ren, J. W. Lee, C. R. Abernathy, *et al.*, Appl. Phys. Lett. **70**, 2410 (1997).
12. K. S. Zhuravlev, A. L. Sokolov, and K. P. Mogil’nikov, Fiz. Tekh. Poluprovodn. (St. Petersburg) **32**, 1450 (1998) [Semiconductors **32**, 1293 (1998)].
13. H. F. Wong, D. L. Green, T. Y. Liu, *et al.*, J. Vac. Sci. Technol. B **6**, 1906 (1988).
14. B. S. Ooi, A. C. Bryce, C. D. W. Wilkinson, and J. H. Marsh, Appl. Phys. Lett. **64**, 598 (1994).
15. C. A. Warwick, W. Y. Jan, A. Ourmazd, and T. D. Harris, Appl. Phys. Lett. **56**, 2666 (1990).
16. S. Jin and A. Li, J. Appl. Phys. **81**, 7357 (1997).

Translated by M. Skorikov

Semiconductors, Vol. 36, No. 1, 2002, pp. 85–90. Translated from Fizika i Tekhnika Poluprovodnikov, Vol. 36, No. 1, 2002, pp. 91–96.
Original Russian Text Copyright © 2002 by Berashevich, Danilyuk, Kholod, Borisenko.

LOW-DIMENSIONAL SYSTEMS

Charge Effects Controlling the Current Hysteresis and Negative Differential Resistance in Periodic Nanodimensional Structures Si/CaF$_2$

Yu. A. Berashevich, A. L. Danilyuk, A. N. Kholod, and V. E. Borisenko
Belarussian State University of Information Science and Electronic Engineering, Minsk, 220013 Belarus

Submitted April 16, 2001; accepted for publication June 14, 2001

Abstract—A kinetic model for charge carrier transport in periodic nanodimensional Si/CaF$_2$ structures via localized states in the insulator was suggested. The appearance of the built-in electric charge in the insulator due to the polarization of the charge trapped by localized charge centers and the subsequent discharge of these centers were investigated. It was demonstrated that these phenomena explain the hysteresis of current–voltage (*I*–*V*) characteristics with a change of polarity of the applied external voltage. These phenomena bring about the portion of negative differential resistance (NDR) in these characteristics. Major factors ensuring the NDR appearance for the structures under investigation are the charge carrier density at the contacts and the charge voltage. At temperatures below 250 K, the NDR portion disappears. It was demonstrated that, in the course of recording the experimental *I*–*V* characteristics, the effect of the charging–discharging of localized centers should decrease. This decrease is in accordance with an increase in the time interval of measuring the current at a constant voltage and with an increase in the step of the applied voltage. This effect actually disappears for the measurement time of 20 s and the voltage step of 0.6 V. © *2002 MAIK “Nauka/Interperiodica”.*

1. INTRODUCTION

An interest in nanodimensional structures, which form a system of quantum wells (QWs), arose several decades ago in connection with the possibility of designing devices with a negative differential resistance (NDR) based on these structures. The NDR effect in nanodimensional structures appears due to the resonance tunneling of charge carriers [1]. This effect was originally discovered and subsequently investigated in detail for III–V semiconductor compounds [2].

At the present time, much attention is being given to Si-based nanodimensional structures, whose main advantage is associated with the well-developed technology of integrated circuit fabrication. Recently, the NDR effect was experimentally observed at room temperature in periodic nanodimensional Si/CaF$_2$ structures grown on single-crystal Si(111) substrates [3]. It was demonstrated that the observed effect is associated with the charge properties of Si–insulator systems [3, 4]. However, the mechanism of the emergence of this effect and the pattern of its manifestation were not described in detail theoretically.

The purpose of this study was to analyze the mechanism of charge carrier transport in periodic nanodimensional Si–insulator structures and to reveal the conditions for the emergence of the NDR effect in them. We also developed a model of charge carrier transport via localized states in the insulator with allowance made for the dynamics of carrier trapping at these states, the carrier transport, and detrapping.

2. THEORETICAL MODEL

Charge carrier transport is considered for the periodic nanodimensional Si–insulator structure [4]. This structure consists of *N* QWs of Si, which are separated by *N* + 1 potential barriers of CaF$_2$. It is assumed that the structure contains no impurities. It is also assumed that the charge carrier transport across this structure is accomplished owing to a series of electron processes. These are the injection of charge carriers from the contacts, carrier trapping at localized states in the insulator and depletion of these states, and recombination of nonequilibrium charge carriers in the semiconductor. The kinetics of charge variation in the *i*th QW of the structure is described by the following set of equations [5]:

$$\begin{aligned}\frac{dn_i}{dt} &= g^t_{n,\,i-1}(n_{i-1}, n_i) + g^t_{n,\,i+1}(n_{i+1}, n_i)\\ &\quad - g^t_{n,\,i}(n_i, n_{i-1}) - g^t_{n,\,i}(n_i, n_{i+1}) - \gamma_i n_i p_i,\end{aligned} \tag{1}$$

$$\begin{aligned}\frac{dp_i}{dt} &= g^t_{p,\,i+1}(p_{i+1}, p_i) + g^t_{p,\,i-1}(p_{i-1}, p_i)\\ &\quad - g^t_{p,\,i}(p_i, p_{i-1}) - g^t_{p,\,i}(p_i, p_{i+1}) - \gamma_i n_i p_i.\end{aligned} \tag{2}$$

Here, *i* is the period of the structure, ($i = 1\ldots N$), $n_i(p_i)$ is the electron (hole) density in the *i*th layer of the semiconductor, $g^t_{n(p),\,i}$ is the rate of electron (hole) transport through the *i*th insulator layer with the participation of traps, and γ_i is the coefficient of electron (hole) recombination in the *i*th layer of the semiconductor.

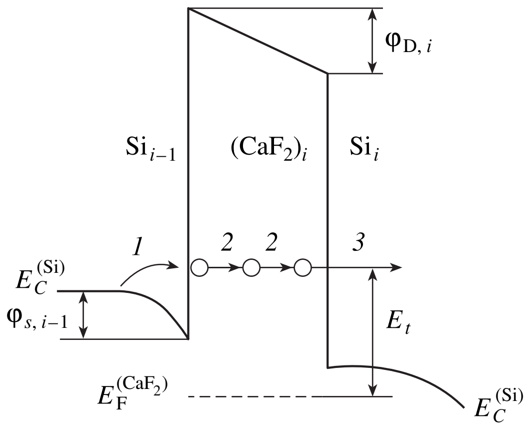

Fig. 1. Energy diagram of a period in the Si/CaF_2 structure and charge-carrier transport in this structure. (*1*) Charge carrier trapping from the conduction band of Si by the trap in the insulator, (*2*) charge carrier tunneling via the trap level in the insulator, and (*3*) carrier tunneling from the trap into the potential well.

The properties of localized states depend on the crystal lattice type of the material, and on the conditions and method for the formation of the structure. Major causes of the appearance of such states are the stoichiometric defects of the crystal lattice and structural defects, particularly those related due to dangling bonds [6]. The localized states manifest themselves as the traps, which are able to capture the charge carriers. Thus, they control the flux of charge carriers injected from the contacts and determine current–voltage (*I*–*V*) characteristics. For single crystals, the trap energy levels in the band gap are usually discrete and are characterized by the energy E_t.

The position of the trap level for periodic Si/CaF_2 structures was determined previously [7] from the slope of the curve ln(J/V) as a function of the inverse temperature T^{-1}, where J is the current, and V is the potential. In the absence of external bias, the energy of the level is equal to 0.35 eV and decreases linearly with increasing V, i.e., $E_a = E_{C(V)} - E_t - qV$, where q is the elementary charge. This is in disagreement with the Pool–Frenkel and Schottky models, according to which the activation energy of the trap is defined as $E_a = E_{C(V)} - E_t - \eta V^{1/2}$, where η is the coefficient of proportionality. In addition, for Si/CaF_2 structures, the potential barrier height is $U_n = 3.3$ and $U_p = 7.6$ eV for electrons and holes, respectively [8]. For this reason, if $E_a = 0.35$ eV, above-barrier activated transport via the traps is impossible because of its nearly zero probability. However, according to the experimental data, the current drops by several orders of magnitude as the temperature decreases from 300 to 150 K [7].

Based on the above data, we assume that the charge-carrier transport in nanodimensional periodic structures is conducted both by tunneling through potential barriers and via a system of localized states in the band gap of the insulator. In this case, the experimentally measured energy is simply the energy of thermally activated trapping of the charge carriers by traps in a QW. This energy is equal to $E_t - E_g/2 - q\varphi_{s,i}$ (for an intrinsic semiconductor), where $\varphi_{s,i}$ is the potential drop in the ith well of the semiconductor, and E_g is the band gap for Si. The motion of captured charge carriers in the insulator is carried out via trap-to-trap tunneling transitions. In this case, the distance between the defects, which generate the localized states, should be on the order of $a = (1/4)a_0$, where a_0 is the lattice parameter. Such a high defect concentration is characteristic of the intrinsic defects of the CaF_2 matrix, which are related, for example, to the dangling Ca–F bonds [9]. On applying an external voltage, the electron motion will be effected mainly along the direction of the external field. The aforementioned processes of charge carrier transport via the trap level in the insulator are illustrated in the energy diagram of the ith period of the Si/CaF_2 structure in Fig. 1. The direct tunneling of charge carriers across the barrier is not taken into account in the model. The reason is that the calculated estimates [5] and experimental data [7] demonstrate that the probability of tunneling is low compared to transport via the traps in the temperature range of 200–300 K.

The probability of the transition of trapped charge carriers across the ith layers of the insulator via the trap states and their subsequent transition into the ith QW is defined as [10]

$$D_{n(p),i}(\varphi_D) = \sum_{m=0}^{\infty} (p_m) m! \beta^m_{n(p),i}(\varphi_D), \qquad (3)$$

where

$$p_m = \frac{(H_a a^2 d_D)^m}{m!} \exp(-H_a a^2 d_D)$$

is the probability of arrangement of m traps along the trajectory of charge-carrier motion through the insulator;

$$\beta_{n(p),i}(-\varphi_D) = \left[-2m^*_{n(p)}\left(-qU_{n(p)} + E_t - q\varphi_{D,i}\frac{a}{d_D}\right)/\hbar^2\right]^{-0.5}/a$$

is the probability of the reverse tunneling transition of the captured charge carrier into the (i – 1)th well [10]; $m^*_{n(p)}$ is the effective electron (hole) mass; d_D is the insulator thickness; and $\varphi_{D,i}$ is the potential drop across the ith layer of insulator. The number of states along the trajectory of charge carrier motion via the trap level is related to the barrier width, the distance between the trapping centers, and the deviation of the trajectory from the straight line [10].

The kinetics of variation in the density of charge carriers, which are located in the ith layer of the insulator, due to the processes of charging and discharging of localized states in the insulator can be described using the following equations:

$$\frac{dn_i^t}{dt} = \alpha n_{i-1} n_i^t(\varphi_s)[1 - D_{n,i}(\varphi_D)] + \alpha n_i n_i^t(-\varphi_s)[1 - D_{n,i}(-\varphi_D)], \tag{4}$$

$$\frac{dp_i^t}{dt} = \alpha p_i p_i^t(\varphi_s)[1 - D_{p,i}(\varphi_D)] + \alpha p_{i-1} p_i^t(-\varphi_s)[1 - D_{p,i}(-\varphi_D)]. \tag{5}$$

Here, α is the coefficient of charge carrier capture by the traps, which is determined by the product of the capture cross section S and thermal velocity of charge carriers

$$v_T = \left(\frac{k_B T}{2\pi m^*_{n(p)}}\right)^{1/2},$$

where k_B is the Boltzmann constant; $n_i^t(\varphi_s)$ and $p_i^t(\varphi_s)$ are the densities of charge carriers captured by the traps, which depend on the density of empty traps and can be defined as

$$n_i^t(\varphi_s) = \frac{H_a D_i^t(\varphi_s)}{1 + D_i^t(\varphi_s)}, \tag{6}$$

where H_a is the total density of empty and filled trap states in the insulator; and $D_i^t(\varphi_s)$ is the function of filling the trap levels by charge carriers from the $(i - 1)$th QW with allowance made for their reverse transition into the same well for the case of homogeneous spatial distribution of traps, which is equal to [11]

$$D_i^t(\varphi_s) = \delta \exp\left(-\frac{E_t - E_g/2}{k_B T}\right) \exp\left(\frac{q\varphi_{s,i-1}}{k_B T}\right) \times [1 - \beta_{n(p),i}(-\varphi_D)], \tag{7}$$

where δ is the factor of degeneracy of trap levels ($\delta = 2$).

In view of Eqs. (4) and (5), the set of Eqs. (1) and (2), which describes the kinetics of variation in the electron and hole density in the ith well, takes the form

$$\frac{dn_i}{dt} = \alpha[n_{i-1} n_i^t(\varphi_s) D_{n,i}(\varphi_D) - n_i n_i^t(-\varphi_s) D_{n,i}(-\varphi_D) + n_{i+1} n_{i+1}^t(-\varphi_s) D_{n,i+1}(-\varphi_D) - n_i n_{i+1}^t(\varphi_s) D_{n,i+1}(\varphi_D)] - \gamma_i n_i p_i, \tag{8}$$

$$\frac{dp_i}{dt} = \alpha[p_{i+1} p_{i+1}^t(\varphi_s) D_{p,i+1}(\varphi_D) - p_i p_{i+1}^t(-\varphi_s) D_{p,i+1}(-\varphi_D) + p_{i-1} p_i^t(-\varphi_s) D_{p,i}(-\varphi_D) - p_i p_i^t(\varphi_s) D_{p,i}(\varphi_D)] - \gamma_i n_i p_i. \tag{9}$$

The charge accumulated in the thin insulator layer is redistributed and polarized by the applied external potential. We took this into account by introducing the Poisson equations for the insulator layer

$$\frac{d}{dx}\left(\frac{d\varphi_{D,i}}{dx}\right) = -\frac{q(n_i^t - p_i^t)}{\varepsilon_0 \varepsilon_D} \tag{10}$$

and the semiconductor layer

$$\frac{d}{dx}\left(\frac{d\varphi_{s,i}}{dx}\right) = \frac{q(n_i - p_i)}{\varepsilon_0 \varepsilon_s}. \tag{11}$$

Solutions to Eqs. (10) and (11) are joined at the interfaces with respect to the potential and field strength with allowance made for the complete potential drop across the structure:

$$\sum_{i=1}^{N+1} (\varphi_{D,i} + \varphi_{s,i}) = V_{bias}. \tag{12}$$

Here, V_{bias} is the external bias; ε_0 is the dielectric constant of free space; and ε_s and ε_D are the relative dielectric constants for the semiconductor and insulator, respectively.

The set of Eqs. (4), (5), (8)–(11) was solved for the case when the charge carrier capture by the trap states is the limiting process. In this situation, it is assumed that the thicknesses of the insulator and semiconductor layers, the coefficient of recombination, the energy position of localized states, and the relative dielectric constants for all materials are identical for all periods of the structure. The carrier density at the electron and hole contacts was assumed to be identical and equal n_c.

3. RESULTS OF CALCULATIONS AND DISCUSSION

It follows from the experimental data [3, 4, 7, 12] that the I–V characteristics $J(V_{bias})$ of the periodic Si/CaF_2 structure depend on its configuration, as well as on the conditions of electrical measurements such as the magnitude and time interval of varying the external bias. For this reason, the I–V characteristics were simulated with allowance made for the above factors. The parameters used in computations are given in the table.

The results of simulating the I–V characteristic of the structure, which consists of $N = 4$ Si/CaF_2 periods, are shown in Fig. 2. With a variation in the voltage from $-V_{max}$ to V_{max} and in the opposite direction, the hysteresis of the I–V characteristic is observed. This circumstance is associated with the appearance of internal fields in insulators during polarization of the trapped charge. Internal fields are directed oppositely to the external field. In this case, variation in the current direction occurs at the nonzero potential, when internal fields compensate for the external field.

In addition, the I–V curves are characterized by the pronounced NDR portion. The peak of the NDR current

Parameters used for simulating the charge-carrier transport in layered Si/CaF$_2$ structures

Parameter	Value
Thickness of the CaF$_2$ layer	2 nm
Thickness of the Si layer	1.5 nm
Number of periods	4–20
Effective electron mass	$0.35m_0$ [13]
Effective hole mass	$0.42m_0$ [13]
Relative dielectric constant for CaF$_2$	5 [14]
Relative dielectric constant for Si	7.5 [14]
Charge carrier density at contacts	10^{24}–10^{25} m^{-3}
Trap density	10^{26} m^{-3}
Cross-section of charge carrier capture by traps	10^{-21} m^2
Energy position of the trap level ($E_t - E_g/2$)	0.35 eV [7]
Time interval of maintaining the constant voltage	1–20 s
Voltage variation step	0.1–0.6 V

is located in the nonzero potential region. This peak diminishes and shifts to the region of positive voltages with an increase in the time step of varying the external bias (Fig. 3). With an increase in the step mentioned, the hysteresis of the *I–V* characteristic also becomes less pronounced.

In this case, the shift of the zero current and NDR formation are associated with charging–discharging of localized states in insulator layers of the periodic structure in the course of the step-by-step application of external bias. For a certain step of varying the bias, the charge trapped in the insulator has no time to disperse in a time of maintaining the fixed potential. Internal fields formed by carriers trapped appear in insulator layers of the structure. At a certain external bias, the internal field compensates the external one, and, in this case, the current reaches the smallest value. With a further decrease in the negative bias, the oppositely directed current begins to prevail due to the trap discharge. This current attains its maximum at the zero potential, which gives rise to the NDR. As the potential becomes positive, the current caused by the external bias begins to increase and compensates the discharge current. These currents are equalized for the smallest NDR value. The largest NDR current decreases, and this region smoothens (Fig. 3) as the time step of varying the external bias increases. This is caused by a decrease in the internal fields due to the charge density drop at localized states in the insulator. The reason for this is that the largest part of this charge has time to disperse, i.e., to escape from the traps.

An increase in the number of periods in the structure causes the NDR portion to disappear. The reason for this is that it leads to a decrease in the potential drop across one period of the structure and to a corresponding decrease in the charge accumulation in each insulator layer, notwithstanding the fact that the total capability of the structure to accumulate the charge does not vary, as shown in Fig. 4. With an increase in the number of periods, the NDR portion smoothens, and the largest current lowers.

The degree of filling the traps depends on the charge carrier density at the contacts and on the potential

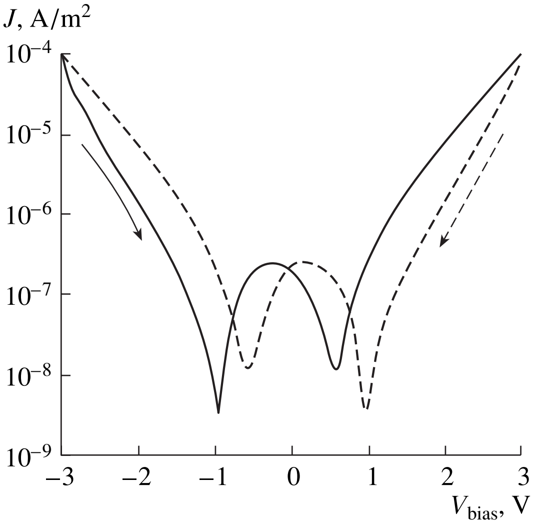

Fig. 2. Hysteresis of the *I–V* characteristic of the Si/CaF$_2$ structure with the change of polarity of the external bias. Parameters of computation: $t_s = 1$ s, $N = 4$, and $n_c = 5 \times 10^{24}$ m^{-3}.

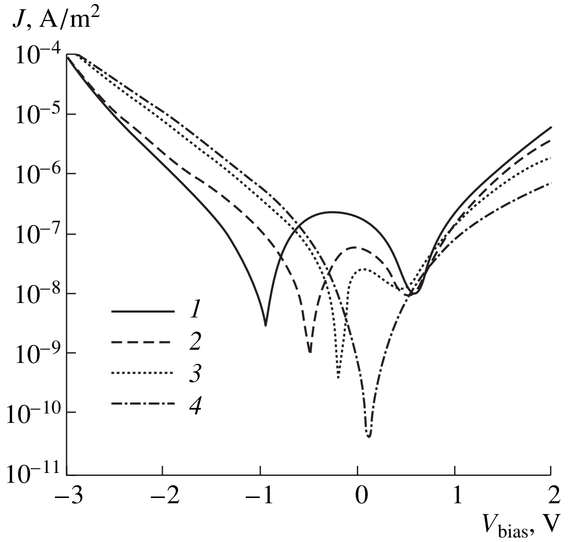

Fig. 3. Current–voltage characteristic of the Si/CaF$_2$ structure at time steps of varying the external bias t_s: (*1*) 1, (*2*) 3, (*3*) 10, and (*4*) 20 s. Parameters of computation: $N = 4$ and $n_c = 5 \times 10^{24}$ m^{-3}.

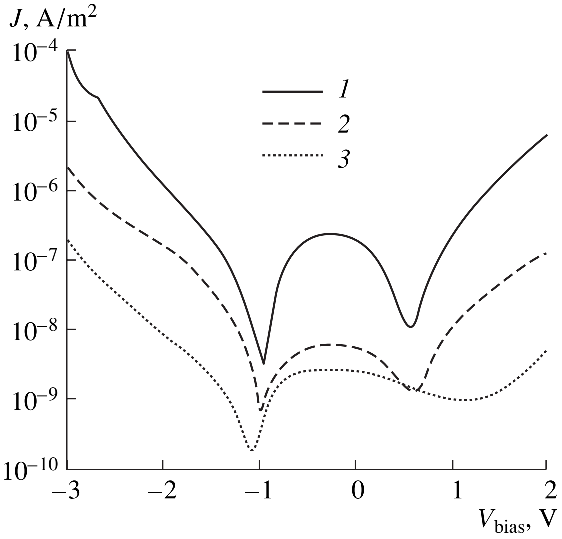

Fig. 4. Current–voltage characteristic of the Si/CaF$_2$ structure with varying the number of periods N: (*1*) 4, (*2*) 10, and (*3*) 20; t_s = 1 s, and $n_c = 5 \times 10^{24}$ m^{-3}.

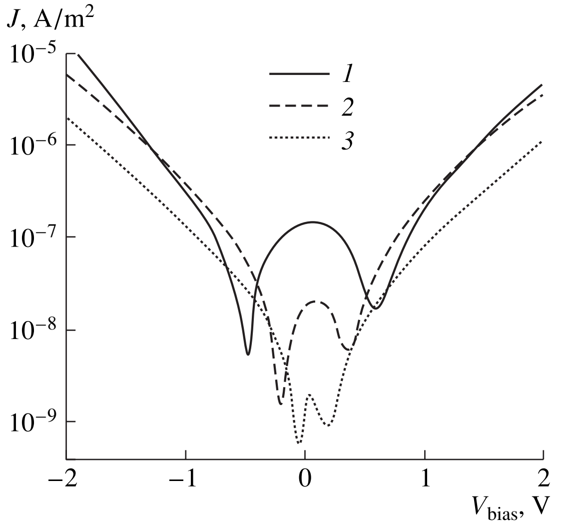

Fig. 5. Current–voltage characteristic of the Si/CaF$_2$ structure for the value of the initial bias V_{max} = –2 V and parameters: N = 4 and t_s = 1 s; n_c = (*1*) 10^{25}, (*2*) 5×10^{24}, and (*3*) 10^{24} m^{-3}.

applied. The results of calculating the *I–V* characteristics as a function of the carrier density at the contacts are shown in Fig. 5. We may conclude from the data obtained that the NDR region widens as the carrier density at the contacts increases. This is true if the trap density is substantially higher than the carrier density at the contacts. However, widening of the NDR portion is limited by the polarization of the insulator, which decreases with the increasing degree of filling the traps by charge carriers. If this condition is not satisfied, the hysteresis in the *I–V* characteristic becomes less pronounced and the NDR region does not widen.

In the computations carried out, the influence of the temperature on the *I–V* characteristic of the periodic Si/CaF$_2$ structure was also assessed. As the results obtained demonstrated, with the temperature decreasing from 300 to 150 K, the current exponentially decreases by a factor of 10^5. The NDR region diminishes with the temperature decreasing to 280 K and disappears at 250 K; the same is true of the hysteresis effect. This is caused by the exponential decrease in the probabilities of charge carrier trapping by localized states in the insulator and carrier accumulation on these states. A decrease in the insulator thickness also reduces the effect caused by the charge accumulation in the structure.

4. CONCLUSION

A model of charge carrier transport through the localized states in the insulator is suggested for periodic nanodimensional Si/CaF$_2$ structures. This model was used for the analysis of the mechanism of NDR origination, which is experimentally observed for such structures. The hysteresis of the *I–V* characteristics with changing polarity of applied external voltage is explained. It is caused by the emergence of the built-in field in the insulator due to the polarization of the charge trapped by localized states and the subsequent discharge of these states. These phenomena lead to the appearance of the NDR portion in *I–V* characteristics. It is demonstrated that the effect of the charging–discharging of localized states should decrease with an increase in the time interval of the current measurement to 20 s and a step of variation in the voltage applied to 0.6 V in the course of recording the *I–V* characteristics. The charge carrier density at the contacts, the density of trap centers, and the magnitude of the initial applied bias most strongly affect the appearance of NDR for the structures investigated. The decrease in temperature from 300 K to 250 K leads to the disappearance of the NDR portion. This takes place at room temperature if the structure consists of more than 25 periods.

ACKNOWLEDGMENTS

This study was carried out in the framework of the “Interuniversity Program on Nanoelectronics” and project T99-102 of the Foundation for Basic Research of the Republic of Belarus.

REFERENCES

1. L. L. Chang, P. J. Stiles, and L. Esaki, J. Appl. Phys. **38**, 4440 (1967).
2. L. Esaki, Phys. Rev. **109**, 63 (1958).
3. S. Ménard, A. N. Kholod, M. Liniger, *et al.*, Phys. Status Solidi A **181**, 424 (2000).

4. S. Ménard, M. Liniger, F. Bassani, *et al.*, in *Physics, Chemistry, and Application of Nanostructures*, Ed. by V. E. Borisenko *et al.* (World Scientific, Singapore, 1999), p. 365.
5. Yu. A. Berashevich, A. L. Danilyuk, A. N. Kholod, and V. E. Borisenko, Fiz. Tekh. Poluprovodn. (St. Petersburg) **35** (1), 110 (2001) [Semiconductors **35**, 112 (2001)].
6. E. H. Nicollian, J. Vac. Sci. Technol. **14**, 1112 (1977).
7. V. Ioannou-Sougleridis, T. Ouisse, A. G. Nassiopoulou, *et al.*, J. Appl. Phys. **89** (1), 610 (2001).
8. M. T. Cuberes, A. Bauer, H. J. Wen, *et al.*, J. Vac. Sci. Technol. B **12**, 2646 (1994).
9. V. Ioannou-Sougleridis, T. Tsakiri, A. G. Nassiopoulou, *et al.*, in *European Projects: Silicon Modules for Integrated Light Engineering, Marseilles, France, 2000*, p. 133.
10. V. Ya. Kirpichenkov, Zh. Éksp. Teor. Fiz. **113**, 1522 (1998) [JETP **86**, 833 (1998)].
11. K. C. Kao and W. Hwang, *Electrical Transport in Solids* (Pergamon, Oxford, 1981; Mir, Moscow, 1984), Vol. 1.
12. J. M. Shannon and B. A. Morgan, J. Appl. Phys. **86**, 1548 (1999).
13. C. Svensson and I. Lundström, J. Appl. Phys. **44**, 4657 (1973).
14. V. E. Borisenko, A. L. Danilyuk, and A. N. Kholod, Mikroélektronika **27**, 170 (1998).

Translated by N. Korovin

Semiconductors, Vol. 36, No. 1, 2002, pp. 91–97. From Fizika i Tekhnika Poluprovodnikov, Vol. 36, No. 1, 2002, pp. 97–103.
Original English Text Copyright © 2002 by Averkiev, Golub, Willander.

LOW-DIMENSIONAL SYSTEMS

Spin Relaxation in Asymmetrical Heterostructures[1]

N. S. Averkiev*, L. E. Golub, and M. Willander****
** Ioffe Physicotechnical Institute, Russian Academy of Sciences, St. Petersburg, 194021 Russia*
*** Physical Electronics and Photonics, Department of Physics,*
Chalmers University of Technology and Göteborg University, S-412 96 Göteborg, Sweden
e-mail: golub@coherent.ioffe.rssi.ru

Submitted April 3, 2001; accepted for publication April 5, 2001

Abstract—Electron spin relaxation by the D'yakonov–Perel' mechanism is investigated theoretically in asymmetrical III–V heterostructures. Spin relaxation anisotropy for all three dimensions is demonstrated for a wide range of structural parameters and temperatures. Dependences of spin relaxation rates are obtained both for a GaAs-based heterojunctions and triangular quantum wells. The calculations show a several-orders-of-magnitude difference between spin relaxation times for heterostructure parameters realized in experiments. © *2002 MAIK "Nauka/Interperiodica".*

1. INTRODUCTION

The degrees of freedom of spin have received a great deal of attention throughout the development of semiconductor physics. Recently, the spin properties of carries have been investigated intensely in low-dimensional semiconductor structures. In electronics, much interest in spin has been aroused by recent proposals to construct spin transistors and spin computers based on heterostructures [1, 2].

The spin–orbit interaction, governing the spin behavior, is much more complex in semiconductor heterostructures than in bulk systems. The bulk spin–orbit terms take a more interesting form in two-dimensional (2*D*) systems, and, in addition, new terms appear, which are absent in bulk.

In [3] we considered electron spin dynamics in asymmetrical heterostructures. A giant anisotropy of spin relaxation times caused by interference of different spin–orbit terms has been revealed. In this work, we calculate the spin relaxation rates in real asymmetrical structures. A heterojunction and a triangular quantum well (QW) are considered in detail. The effect of heteropotential asymmetry on spin relaxation is investigated in a wide range of electron concentrations and temperatures. We show that the giant spin relaxation anisotropy is governed by external parameters, and this opens up new possibilities for spin engineering.

2. THEORY

Let us consider a system with a spin–orbit interaction described by the Hamiltonian $H_{\mathrm{SO}}(\mathbf{k})$, where $\mathbf{k}$ is a wave vector. $H_{\mathrm{SO}}(\mathbf{k})$ is equivalent to a Zeeman term with the effective magnetic field dependent on $\mathbf{k}$. In the presence of scattering, the wave vector changes and, hence, the effective magnetic field also changes. Therefore, in the case of frequent scattering, the electrons move in a chaotically changing magnetic field. The spin dynamics in such a system has diffusion character, which leads to the loss of any specific spin orientation. This is called the D'yakonov–Perel' spin relaxation mechanism [4], which is the main spin relaxation mechanism in many III–V bulk semiconductors and heterostructures.

For a 2*D* system with any $H_{\mathrm{SO}}(\mathbf{k})$ (where $\mathbf{k}$ lies in the plane of the heterostructure), one can show, similarly to [3] (see also [4–6]), that the spin dynamics of electrons in the presence of elastic scattering is described by the following equations:

$$\dot{S}_i(t) = -\frac{1}{2\hbar^2}\sum_{n=-\infty}^{\infty}\frac{\int\limits_0^\infty d\varepsilon(F_+ - F_-)\tau_n A_n^{ji}}{\int\limits_0^\infty d\varepsilon(F_+ - F_-)}S_j(t), \qquad (1)$$

$$A_n^{ji} = \mathrm{Tr}\{[H_{-n}, [H_n, \sigma_j]]\sigma_i\}.$$

It should be noted that this is true only for times longer than the momentum relaxation time but shorter than the spin relaxation times. In Eq. (1), S_i are the spin density components ($i = x, y, z$); the integration is performed over energy $\varepsilon = \hbar^2k^2/2m$, where m is the electron effective mass; $F_\pm(\varepsilon)$ are distribution functions of electrons with the spin projection equal to ±1/2; σ_i are the Pauli matrices; H_n are the harmonics of the spin–orbit Hamiltonian:

$$H_n = \oint\frac{d\varphi_{\mathbf{k}}}{2\pi}H_{\mathrm{SO}}(\mathbf{k})\exp(-in\varphi_{\mathbf{k}}), \qquad (2)$$

---

[1] This paper was submitted by the authors in English.

1063-7826/02/3601-0091$22.00 © 2002 MAIK "Nauka/Interperiodica"

where $\varphi_{\mathbf{k}}$ is the angular coordinate of **k**; and the scattering times are given by

$$\frac{1}{\tau_n} = \oint d\theta W(\varepsilon, 0)(1 - \cos n\theta), \qquad (3)$$

where $W(\varepsilon, \theta)$ is the probability of elastic scattering by an angle θ for an electron with energy ε.

Equation (1) is valid for $2D$ electrons with any spin–orbit interaction $H_{\mathrm{SO}}(\mathbf{k})$. We now consider an asymmetrical zinc-blende heterostructure. There are two contributions to $H_{\mathrm{SO}}(\mathbf{k})$. The first, the so-called bulk inversion asymmetry (BIA) term, is due to the lack of inversion symmetry in the bulk material of which the heterostructure is made. To calculate this term, one must average the corresponding bulk expression over the size-quantized motion [6]. We investigate a heterostructure with the growth direction [001] coinciding with the z-axis and assume that only the first electron subband is populated. The BIA term has the form

$$H_{\mathrm{BIA}}(\mathbf{k}) = \gamma[\sigma_x k_x(k_y^2 - \langle k_z^2\rangle) + \sigma_y k_y(\langle k_z^2\rangle - k_x^2)], \qquad (4)$$

where we chose the x- and y-directions to be aligned with the principal axes in the heterostructure plane. Here, $\langle k_z^2\rangle$ is the squared operator $(-i\partial/\partial z)$ averaged over the ground state, and γ is the bulk spin–orbit interaction constant. It is seen that H_{BIA} contains terms both linear and cubic in **k**.

In asymmetrical heterostructures, there is an additional contribution to the spin–orbit Hamiltonian, which is absent in the bulk. It is caused by structure inversion asymmetry (SIA) and can be written as [7–9]

$$H_{\mathrm{SIA}}(\mathbf{k}) = \alpha(\sigma_x k_y - \sigma_y k_x), \qquad (5)$$

where α is proportional to the electric field E, acting on an electron:

$$\alpha = \alpha_0 eE. \qquad (6)$$

Here, e is the elementary charge and α_0 is a second spin–orbit constant determined by both bulk spin–orbit interaction parameters and properties of heterointerfaces. It should be stressed that, in asymmetrical heterostructures, E is caused mainly by the difference of the wave function and by band parameters at the interfaces, rather than by the average electric field [10].

H_{SIA} also contains terms linear in k. From Eq. (1), it follows that the harmonics with the same n are coupled in the spin dynamics equations. This leads to interference (linear in wave vector BIA- and SIA-terms) in spin relaxation [3].

For $H_{\mathrm{SO}} = H_{\mathrm{BIA}} + H_{\mathrm{SIA}}$, the system has C_{2v} symmetry; therefore, Eqs. (1) can be rewritten as follows:

$$\dot{S}_z = -\frac{S_z}{\tau_z}, \quad \dot{S}_x \pm \dot{S}_y = -\frac{S_x \pm S_y}{\tau_\pm}. \qquad (7)$$

The times τ_z, τ_+, and τ_- are the relaxation times of the spin parallel to the axes [001], [110], and $[1\bar{1}0]$, respectively.

If both spin subsystems come to equilibrium before the onset of spin relaxation, then

$$F_\pm(\varepsilon) = F_0(\mu_\pm - \varepsilon), \qquad (8)$$

where F_0 is the Fermi-Dirac distribution function and $\mu_\pm$ are chemical potentials of the electron spin subsystems. If the spin splitting is small, i.e.,

$$|\mu_+ - \mu_-| \ll |\mu_+|, \quad |\mu_-|,$$

then the expressions for the spin relaxation rates $1/\tau_i$ ($i = z, +, -$) have the form

$$\frac{1}{\tau_i} = \frac{\int_0^\infty d\varepsilon(\partial F_0/\partial\varepsilon)\Gamma_i(k)}{\int_0^\infty d\varepsilon(\partial F_0/\partial\varepsilon)}, \qquad (9)$$

where

$$\Gamma_z(k) = \frac{4\tau_1}{\hbar^2}\left[(\gamma^2\langle k_z^2\rangle^2 + \alpha^2)k^2 - \frac{1}{2}\gamma^2\langle k_z^2\rangle k^4 + \frac{1+\tau_3/\tau_1}{16}\gamma^2 k^6\right],$$

$$\Gamma_+(k) = \frac{2\tau_1}{\hbar^2}\left[(\alpha - \gamma\langle k_z^2\rangle)^2 k^2 - \frac{1}{2}\gamma\langle\alpha - \gamma\langle k_z^2\rangle\rangle k^4 + \frac{1+\tau_3/\tau_1}{16}\gamma^2 k^6\right], \qquad (10)$$

$$\Gamma_-(k) = \frac{2\tau_1}{\hbar^2}\left[(\alpha + \gamma\langle k_z^2\rangle)^2 k^2 - \frac{1}{2}\gamma\langle\alpha + \gamma\langle k_z^2\rangle\rangle k^4 + \frac{1+\tau_3/\tau_1}{16}\gamma^2 k^6\right].$$

Equations (9), (10) are valid for any electron energy distribution. If the electron gas is degenerate, then the spin relaxation times are given by

$$\frac{1}{\tau_i} = \Gamma_i(k_{\mathrm{F}}), \qquad (11)$$

where k_{F} is the Fermi wave vector determined by the total $2D$ electron concentration N:

$$k_{\mathrm{F}} = \sqrt{2\pi N}. \qquad (12)$$

In this case, the scattering time τ_1 in Eqs. (10) coincides with the transport relaxation time, τ_{tr}, which can be determined from the electron mobility.

For nondegenerate electrons, the spin relaxation times are determined, in particular, by the energy dependences of the scattering times τ_1 and τ_3. If $\tau_1, \tau_3 \propto \varepsilon^{\nu}$, then $\tau_3/\tau_1 = \text{const}$ and

$$\begin{aligned}\frac{1}{\tau_z} = \frac{4\tau_{\text{tr}}}{\hbar^2}\Bigg[&(\gamma^2\langle k_z^2\rangle^2 + \alpha^2)\frac{2mk_{\text{B}}T}{\hbar^2}\\ &-\frac{\nu+2}{2}\gamma^2\langle k_z^2\rangle\left(\frac{2mk_{\text{B}}T}{\hbar^2}\right)^2\\ &+(\nu+2)(\nu+3)\frac{1+\tau_3/\tau_1}{16}\gamma^2\left(\frac{2mk_{\text{B}}T}{\hbar^2}\right)^3\Bigg],\\ \frac{1}{\tau_\pm} = \frac{2\tau_{\text{tr}}}{\hbar^2}\Bigg[&(\pm\alpha - \gamma\langle k_z^2\rangle^2)\frac{2mk_{\text{B}}T}{\hbar^2}\\ &+\frac{\nu+2}{2}\gamma(\pm\alpha-\gamma\langle k_z^2\rangle)\left(\frac{2mk_{\text{B}}T}{\hbar^2}\right)^2\\ &+(\nu+2)(\nu+3)\frac{1+\tau_3/\tau_1}{16}\gamma^2\left(\frac{2mk_{\text{B}}T}{\hbar^2}\right)^3\Bigg].\end{aligned} \tag{13}$$

Here, T is the electron temperature and k_{B} is the Boltzmann constant. In the particular case of short-range scattering, $\nu = 0$, and $\tau_1 = \tau_3$ are equal to τ_{tr}, which is independent of temperature.

Spin relaxation times are very sensitive to the relationship between two spin–orbit interaction strengths, $\gamma\langle k_z^2\rangle$ and α. From Eqs. (11), (13), it follows that, at low concentration or temperature, $1/\tau_z$, $1/\tau_-$, and $1/\tau_+$ are determined by the sum of squared $\gamma\langle k_z^2\rangle$ and α, by their squared sum, and squared difference, respectively. This may lead to a considerable difference between the three times, i.e., to a total spin relaxation anisotropy if $\gamma\langle k_z^2\rangle$ and α are close in magnitude.

In real III–V systems, the relations between H_{BIA} and H_{SIA} may be different. H_{BIA} or H_{SIA}A may be dominant [11, 12], or they may be comparable [13].

The value of $\langle k_z^2\rangle$ depends on the shape of the heteropotential and will be calculated for the given asymmetrical heterostructures below. The constant γ is known for GaAs from optical orientation experiments [5]. Correct theoretical expressions for γ and α_0 have been derived in terms of the three-band $\mathbf{k}\cdot\mathbf{p}$ model [13, 14]. The heterointerfaces give a contribution to α_0 in addition to that from the bulk [15]. At large wave vectors, α_0 starts to depend on k [16, 17]. Here, we assume concentrations and temperatures to be sufficiently low, allowing us to ignore this effect.

The spin relaxation rates for two types of asymmetrical structures, a heterojunction and a triangular QW, are calculated below. The scattering is assumed to be short-range ($\nu = 0$, $\tau_3 = \tau_1 = \tau_{\text{tr}}$). All parameters are chosen to correspond to the GaAs/AlAs heterostructure: $\gamma = 27$ eV Å^3, and $m = 0.067m_0$, where m_0 is the free electron mass and $\alpha_0 = 5.33$ Å^2. The time τ_{tr} is 0.1 ps and assumed to be independent of the electron concentration.

3. SPIN RELAXATION IN A HETEROJUNCTION

In a heterojunction, the extent of the spin–orbit interaction is governed by the 2D carrier concentration N; $\langle k_z^2\rangle$ can be estimated as follows [18]:

$$\langle k_z^2\rangle = \frac{1}{4}\left(\frac{16.5\pi Ne^2m}{\kappa\hbar^2}\right)^{2/3}, \tag{14}$$

where κ is the dielectric constant. The mean electric field acting on an electron can be taken as equal to half the maximum field in the junction:

$$E = \frac{2\pi Ne}{\kappa}. \tag{15}$$

Figure 1 shows the concentration dependence of the reciprocal spin relaxation times for degenerate electrons in a GaAs/AlAs heterojunction ($\kappa = 12.55$). The inset shows the spin–orbit interaction strengths, $\gamma\langle k_z^2\rangle$ and α, and the absolute value of their difference, as functions of electron concentration.

One can see a spin relaxation anisotropy for all three directions over a wide range of concentrations. $1/\tau_+$ is less than $1/\tau_-$ at small N and greater than $1/\tau_-$ at large concentrations. This is due to the fact that the first term in (10) is larger for $1/\tau_-$, and the second, for $1/\tau_+$. Therefore, at a certain concentration, the times τ_+ and τ_- must be equal. From Eqs. (10) and (11) it follows that this takes place when

$$k_{\text{F}}^2 = 4\langle k_z^2\rangle, \tag{16}$$

which is fulfilled at $N = 1.1 \times 10^{13}$ cm^{-2}, as illustrated in Fig. 1. At larger concentrations, the spin relaxation is again totally anisotropic.

Despite the fact that $\gamma\langle k_z^2\rangle$ and α are close in magnitude over a wide range of concentrations (see the inset of Fig. 1), all three spin relaxation rates depend monotonically on N. This happens because, as the concentration increases, k_{F} increases as well, and the terms in H_{SO}, which are cubic in the wave vector, become important. The growth of these terms with N dominates the change in $(\alpha - \gamma\langle k_z^2\rangle)^2$ in (10); hence, the concentration dependence of $1/\tau_+$ is monotonic.

The situation changes in the case of a Boltzmann gas. For non-degenerate electrons, the mean wave vector and the concentration are independent. For temperatures up to 300 K, the characteristic $k^2 \propto 2mk_{\text{B}}T/\hbar^2$ is much less than $\langle k_z^2\rangle$, and the spin relaxation rates are determined by the first terms in (13). As a result, all three spin relaxation times are different up to 300 K at

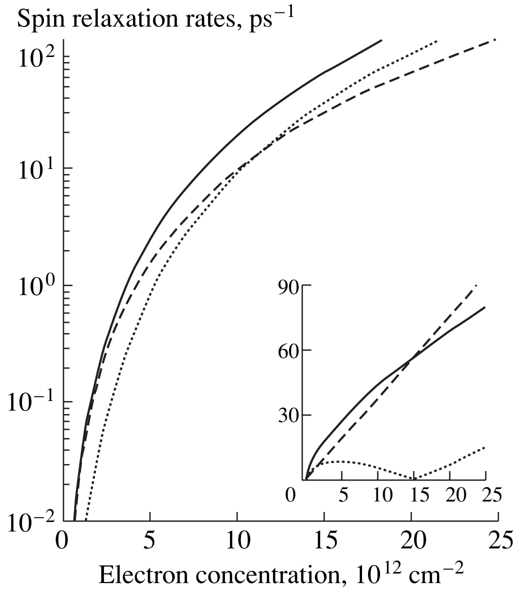

Fig. 1. Concentration dependences of the reciprocal spin relaxation times, $1/\tau_z$ (solid line), $1/\tau_-$ (dashed line), and $1/\tau_+$ (dotted line), for a GaAs/AlAs heterostructure at zero temperature. The parameters are given in the text. The inset shows the spin–orbit interaction strengths, $\gamma\langle k_z^2\rangle$ (solid line), α (dashed), and $|\gamma\langle k_z^2\rangle - \alpha|$ (dotted), in eV Å, as functions of the electron concentration $N/(10^{21}\text{ cm}^{-2})$.

a given concentration. The results of relevant calculations are presented in Fig. 2.

The times τ_+ and τ_- are equal to each other only at a certain temperature. According to (13), the corresponding condition is

$$T = \frac{\hbar^2\langle k_z^2\rangle}{mk_B(1+\nu/2)}. \tag{17}$$

With the GaAs parameters and $\nu = 0$ in (14), it can be seen that (17) is satisfied at $T \approx 100$ K for $N = 10^{11}$ cm^{-2} and at $T \approx 290$ K for $N = 5 \times 10^{11}$ cm^{-2}, in agreement with Fig. 2.

At a fixed temperature, the spin relaxation rates are governed by the electron concentration. According to Eqs. (13), the dependences of $1/\tau_i$ on N are similar to the curves in the inset of Fig. 1. In particular, from Eqs. (13) it follows that $1/\tau_z$ and $1/\tau_-$ must be close in magnitude and both greatly exceed $1/\tau_+$. In addition, $1/\tau_+$ depends on concentration nonmonotonically. This is confirmed completely by the results presented in Fig. 3. One can see that $1/\tau_+ \ll 1/\tau_z \approx 1/\tau_-$, and the rate $1/\tau_+$ has a minimum when plotted as a function of concentration. This minimum is at $N = 1.4 \times 10^{13}$ cm^{-2} when the terms in H_{SO} linear in the wave vector cancel out. The corresponding condition is

$$\gamma\langle k_z^2\rangle = \alpha. \tag{18}$$

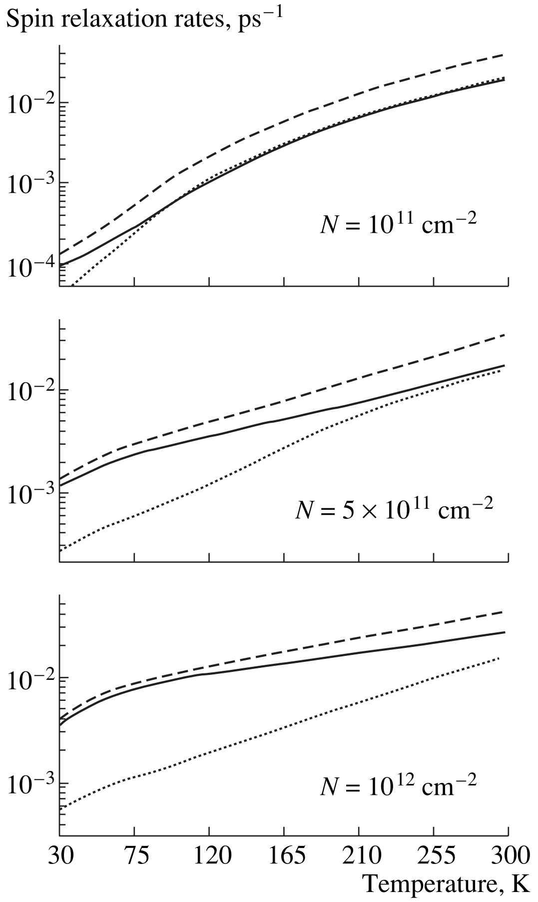

Fig. 2. Temperature dependences of spin relaxation rates, $1/\tau_-$ (solid line), $1/\tau_z$ (dashed line), and $1/\tau_+$ (dotted line), for a GaAs/AlAs heterostructure at different electron concentrations.

At this concentration, the spin relaxation time τ_+ is very large but remains finite owing to the terms cubic in k. Therefore, the difference in the spin relaxation times is more pronounced at a low temperature. At high T, the cubic (in the wave vector) terms become significant in H_{SO}, and the minimum in $1/\tau_+$ disappears. However, $1/\tau_+$ is still much less than $1/\tau_-$; i.e., huge spin relaxation anisotropy occurs in the plane of the heterojunction even at room temperature.

4. SPIN RELAXATION IN A TRIANGULAR QUANTUM WELL

In this section, we investigate spin relaxation in the following asymmetrical system. We consider a structure with an infinitely high barrier at $z < 0$ and constant electric field E at $z > 0$.

In the framework of this model,

$$\langle k_z^2\rangle = a\left(\frac{2meE}{\hbar^2}\right)^{2/3}, \tag{19}$$

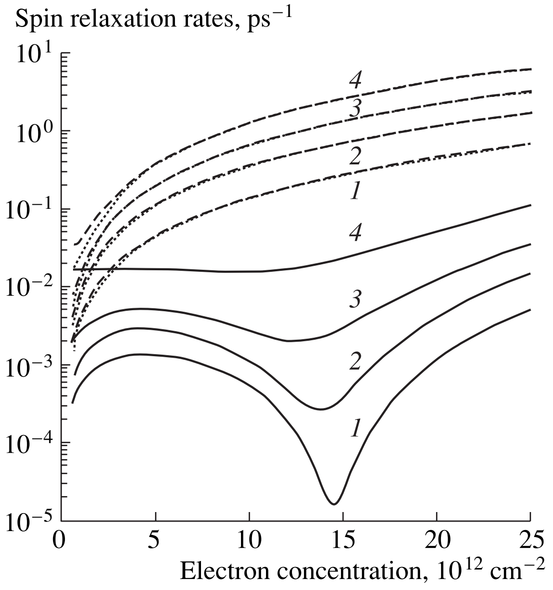

Fig. 3. Concentration dependences of the reciprocal spin relaxation times, $1/\tau_+$ (solid line), $1/\tau_z$ (dashed line), and $1/\tau_-$ (dotted line), for Boltzmann electron gas in GaAs/AlAs heterostructure at temperatures T = (*1*) 30, (*2*) 77, (*3*) 150, and (*4*) 300 K.

where

$$a = \frac{\int_0^\infty dx[\mathrm{Ai}'(x-\beta)]^2}{\int_0^\infty dx[\mathrm{Ai}(x-\beta)]^2} \approx 0.78. \tag{20}$$

Here, $(-\beta)$ is the first root of the Airy function:

$$\mathrm{Ai}(-\beta) = 0, \quad \beta \approx 2.338.$$

The value of α is determined by the difference of both the wavefunction and band parameters at the interfaces [10]. This may lead to a more complicated dependence of α on E than in (6). However, if E is not too high, we have the linear law, and, therefore, we use Eq. (6) in our calculations.

In Fig. 4, the spin relaxation rates are plotted for the triangular GaAs QW at different electric fields. It can be seen that total spin relaxation anisotropy occurs for both degenerate and Boltzmann gases in wide ranges of concentrations and temperatures. The times τ_+ and τ_- coincide only at a specific concentration or tempera-

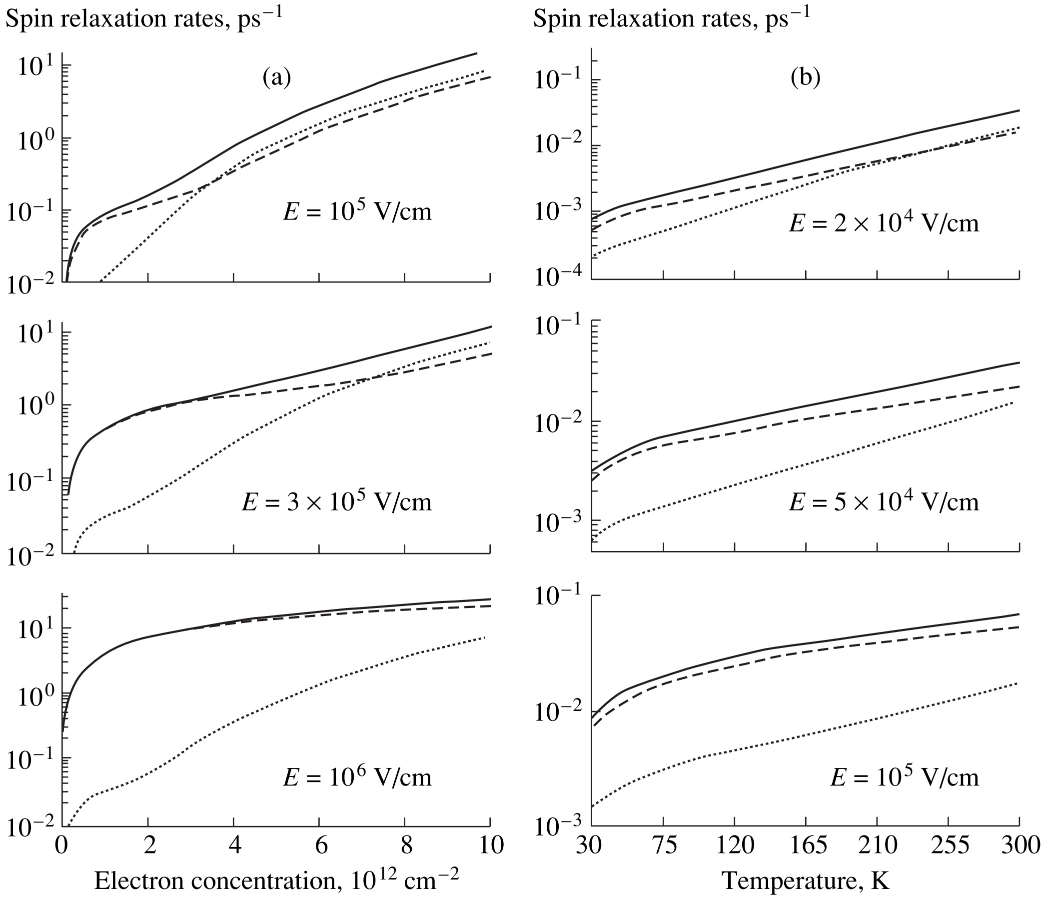

Fig. 4. Spin relaxation rates, $1/\tau_z$ (solid line), $1/\tau_-$ (dashed line), and $1/\tau_+$ (dotted line), in a triangular GaAs QW at different electric fields; (a) corresponds to a degenerate electron gas, and (b) is for the Boltzmann gas.

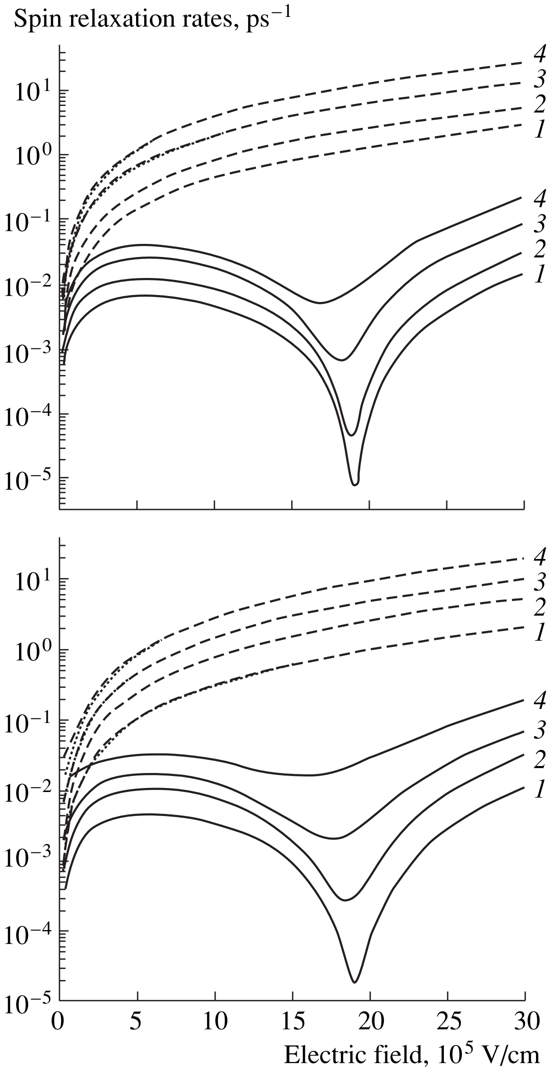

Fig. 5. Spin relaxation rates, $1/\tau_+$ (solid line), $1/\tau_z$ (dashed line), and $1/\tau_-$ (dotted line), in a triangular GaAs QW as functions of the electric field; (a) corresponds to degenerate electrons with concentrations N = (*1*) 10^{11}, (*2*) 3×10^{11}, (*3*) 5×10^{11}, and (*4*) 10^{12} cm^{-2}; (b) corresponds to the Boltzmann gas at temperatures T, = (*1*) 30, (*2*) 77, (*3*) 150, and (*4*) 300 K.

ture. For degenerate electrons, according to Eq. (16), the corresponding curves intersect at $N \approx 3.4 \times 10^{12}$ cm^{-2} for $E = 10^5$ V/cm and at $N \approx 7 \times 10^{12}$ cm^{-2} for $E = 3 \times 10^5$ V/cm, in agreement with Fig. 4a. For a Boltzmann gas, the intersection of τ_+ and τ_- occurs according to (17), at $T \approx 150$ K for $E = 10^4$ V/cm and at $T \approx 240$ K for $E = 2 \times 10^4$ V/cm. This is also confirmed by Fig. 4b.

The behavior of the reciprocal spin relaxation times in the electric field is illustrated in Fig. 5 for both degenerate and Boltzmann electron gases. The dependences of $\gamma\langle k_z^2 \rangle$ and α on the electric field are similar to those in the inset of Fig. 1: their values are close in magnitude, so the difference between them is very small. This leads to a minimum in the dependence of $1/\tau_+$ on E. The cancellation condition (18) is fulfilled at $E \approx 1.9 \times 10^6$ V/cm. The electric field of this strength can be created in heterostructures containing a gate, allowing for the experimental observation of the nonmonotonic spin relaxation rate dependence shown in Fig. 5.

5. CONCLUSION

It has been shown [19–21] that the inclusion of both the BIA and SIA terms (4) and (5) into H_{SO} leads to conduction band spin-splitting anisotropy in **k**-space in III–V semiconductor heterojunctions. However, the spin relaxation analysis performed in [20] ignored this effect.

The authors of [22] showed that the BIA and SIA terms interfere in weak localization but are additive in spin relaxation. In this paper, we demonstrate that the terms in H_{SO} that are linear in the wave vector also cancel out in spin relaxation.

In a recent experiment [23], the spin relaxation anisotropy was observed for uncommonly used (110) GaAs QWs. In this experiment, the spin relaxation in the growth direction was suppressed because of the "built-in" anisotropy of the sample, resulting from the presence of heterointerfaces. In the present paper, we predict spin relaxation suppression in the plane of a heterostructure. Moreover, all three spin relaxation times are different in our case, and this effect takes place in ordinary (001) heterostructures.

To observe the predicted spin relaxation anisotropy, one can perform time-resolved measurements similar to those in [23]. In steady-state experiments, spin relaxation can be investigated by means of the Hanle effect. To obtain the spin relaxation times, one has to take into account the fact that, in asymmetrical heterostructures, the Landé g-factor not only has diagonal in-plane components (g_{xx}) but also off-diagonal ones (g_{xy}) [24]. The degree of photoluminescence polarization in a magnetic field $\mathbf{B} \perp z$ is described by the following expression:

$$P(\mathbf{B}) = \frac{P(0)}{1 + [\mu_{\mathrm{B}}(g_{xx} \pm g_{xy})B/\hbar^2]^2 \tau_z \tau_{\mp}}, \qquad (21)$$

where the upper and lower signs correspond to the experimental geometry $\mathbf{B} \parallel [110]$ and $\mathbf{B} \parallel [1\bar{1}0]$, respectively ($\mu_{\mathrm{B}}$ is the Bohr magneton).

We show that the terms linear in the wave vector in the spin–orbit Hamiltonian interfere, which leads to a huge anisotropy of the spin relaxation times. At a high concentration or temperature, this effect starts to disappear, owing to predominance of the terms cubic in k in H_{SO} which are present only in H_{BIA}. However, the higher-order terms in H_{SIA} are not forbidden by symmetry either. These terms can also interfere with these in

H_{BIA} and cause additional nonmonotonic special features in the dependences of the spin relaxation times on the structure parameters.

In conclusion, we have calculated the spin relaxation times for an III–V heterojunction and a triangular QW. The observance of spin relaxation anisotropy in all three directions is predicted in a wide range of structure parameters and temperatures.

ACKNOWLEDGMENTS

We thank J. Vincent for his critical reading of the manuscript. This study was supported by the Russian Foundation for Basic Research (project nos. 00-02-17011, 00-02-16894, and 01-02-17528) and the Russian State Programme “Physics of Solid-State Nanostructures”.

REFERENCES

1. J. Nitta, T. Akazaki, H. Takayanagi, and T. Enoki, Phys. Rev. Lett. **78**, 1335 (1997).
2. B. E. Kane, Nature **393**, 133 (1998).
3. N. S. Averkiev and L. E. Golub, Phys. Rev. B **60**, 15582 (1999).
4. M. I. D’yakonov and V. I. Perel’, Fiz. Tverd. Tela (Leningrad) **13**, 3581 (1971) [Sov. Phys. Solid State **13**, 3023 (1972)].
5. G. E. Pikus and A. N. Titkov, in *Optical Orientation*, Ed. by F. Meier and B. P. Zakharchenya (North-Holland, Amsterdam, 1984; Nauka, Leningrad, 1989).
6. M. I. D’yakonov and V. Yu. Kachorovskiĭ, Fiz. Tekh. Poluprovodn. (Leningrad) **20**, 178 (1986) [Sov. Phys. Semicond. **20**, 110 (1986)].
7. F. J. Ohkawa and Y. Uemura, J. Phys. Soc. Jpn. **37**, 1325 (1974).
8. F. T. Vas’ko, Pis’ma Zh. Éksp. Teor. Fiz. **30**, 574 (1979) [JETP Lett. **30**, 541 (1979)].
9. Yu. L. Bychkov and E. I. Rashba, Pis’ma Zh. Éksp. Teor. Fiz. **39**, 66 (1984) [JETP Lett. **39**, 78 (1984)].
10. P. Pfeffer, Phys. Rev. B **59**, 15902 (1999).
11. B. Jusserand, D. Richards, H. Peric, and B. Etienne, Phys. Rev. Lett. **69**, 848 (1992).
12. D. Stein, K. von Klitzing, and G. Weimann, Phys. Rev. Lett. **51**, 130 (1983).
13. W. Knap, C. Skierbiszewski, A. Zduniak, *et al.*, Phys. Rev. B **53**, 3912 (1996).
14. L. G. Gerchikov and A. V. Subashiev, Fiz. Tekh. Poluprovodn. (St. Petersburg) **26**, 131 (1992) [Sov. Phys. Semicond. **26**, 73 (1992)].
15. E. A. de Andrada e Silva, G. C. La Rocca, and F. Bassani, Phys. Rev. B **55**, 16293 (1997).
16. R. Winkler and U. Rössler, Phys. Rev. B **48**, 8918 (1993).
17. L. Wissinger, U. Rössler, R. Winkler, *et al.*, Phys. Rev. B **58**, 15375 (1998).
18. T. Ando, A. B. Fowler, and F. Stern, Rev. Mod. Phys. **54**, 437 (1982).
19. G. Lommer, F. Malcher, and U. Rössler, Phys. Rev. Lett. **60**, 728 (1988).
20. E. A. de Andrada e Silva, Phys. Rev. B **46**, 1921 (1992).
21. B. Jusserand, D. Richards, G. Allan, *et al.*, Phys. Rev. B **51**, 4707 (1995).
22. F. G. Pikus and G. E. Pikus, Phys. Rev. B **51**, 16928 (1995).
23. Y. Ohno, R. Terauchi, T. Adachi, *et al.*, Phys. Rev. Lett. **83**, 4196 (1999).
24. V. K. Kalevich and V. L. Korenev, Pis’ma Zh. Éksp. Teor. Fiz. **57**, 557 (1993) [JETP Lett. **57**, 571 (1993)].

Semiconductors, Vol. 36, No. 1, 2002, pp. 98–101. Translated from Fizika i Tekhnika Poluprovodnikov, Vol. 36, No. 1, 2002, pp. 104–108.
Original Russian Text Copyright © 2002 by Gavrilov, Belogorokhov, Belogorokhova.

A Mechanism of Oxygen-Induced Passivation of Porous Silicon in the HF : HCl : C_2H_5OH Solutions

S. A. Gavrilov*, A. I. Belogorokhov, and L. I. Belogorokhova*****

* *Moscow State Institute of Electronic Engineering (Technical University),*
Zelenograd, Moscow oblast, 103498 Russia
e-mail: pcfme@dpts.miee.ru
** *State Research Institute for the Rare-Metals Industry, Moscow, 109017 Russia*
*** *Faculty of Physics, Moscow State University, Vorob'evy gory, Moscow, 119899 Russia*

Submitted February 5, 2001; accepted for publication May 11, 2001

Abstract—The problem of stabilizing the properties of porous silicon films was studied. A thermodynamical analysis of electrochemical processes occurring in the course of anodic Si dissolution is performed. A new description of electrode reaction of silicon interaction with hydrofluoric acid is suggested. It is shown that hydrogen-induced passivation of the Si surface governs the equilibrium dissolution potential of the silicon electrode. Thermodynamic calculations indicate that it is possible to substitute the chemically and thermally unstable surface groups (of the SiH_x type) for more stable silicon–oxygen compounds directly in the course of formation of porous Si in electrolytes with the addition of strong hydrohalic acids. The results obtained made it possible to explain thermodynamically the stabilizing effect of an HCl additive in electrolytes used for formation of porous Si on its chemical and physical properties. © *2002 MAIK "Nauka/Interperiodica".*

INTRODUCTION

The discovery of the visible luminescence of porous silicon (*por*-Si) [1] has stimulated numerous studies aimed at exploring the possibility of the development of various devices based on *por*-Si (see [2, 3]). In this context, it became urgently necessary to ascertain the laws governing the variations in the photoluminescent properties of *por*-Si and in the physicochemical state of the *por*-Si surface as a result of exposure to the environment. At the same time, the problem of ensuring the stability of the *por*-Si properties has arisen. It is well known that the hydrogen-induced passivation of the surface of silicon nanocrystallites is thermally and chemically unstable [4, 5]. As a result of uncontrolled variations in the chemical composition of the porous layer, unpredictable changes in the optical properties of the material occur. This makes it difficult to obtain adequate and reproducible data on the *por*-Si structure in its relation to luminescent and optical properties.

In order to stabilize the physical and optical characteristics of *por*-Si, physicists and technologists most often use either rapid thermal oxidation [6] or deposition of coatings with special properties [2, 3]. Recently, attention has been drawn to the methods for enhancing the stability of the crystallite surface by modifying the composition of the electrolyte in which the *por*-Si layer is formed. It is well known that the stable oxygen-induced passivation of *por*-Si is ensured by adding H_2O_2 to a conventional solution of HF in a water–ethanol mixture [7]. However, no data have been reported [7] on the luminescent properties of the *por*-Si layers obtained, which makes it difficult to advance the inferences about the applicability of this method to the technology of fabricating light-emitting structures. Previously, we have found that the stability and the photoluminescence intensity of *por*-Si formed in solutions based on whether the HF and HCl mixtures are enhanced [8]. The mechanism of the effect of HCl on the properties of the formed *por*-Si layers has been discussed in a number of publications [9–11]. Reactions of Si with electrolyte containing HCl have been recently analyzed in detail [11]. It is assumed [11] that a decrease in the concentration of the nonradiative-recombination centers is related to the HCl-activated formation of silicon–oxygen compounds.

In this paper, we suggest a description of the oxygen-induced passivation of silicon nanocrystals in HF solutions that contain a certain amount of HCl; this description is based on the consideration of the conditions for electrochemical equilibrium in aqueous solutions of hydrofluoric acid. The suggested approach made it possible to refine the mechanism of the anodic dissolution of Si and to substantiate the possibility of producing stable silicon–oxygen complexes at the surface of crystallites that compose the *por*-Si layer when it is formed in hydrofluoric acid.

EXPERIMENTAL

We used KDB-12 (*p*-Si:B, $\rho = 12\ \Omega$ cm) wafers with both surfaces polished and with (100) orientation as the starting material. Porous Si was formed under galvanostatic conditions for 300 s, with the anode-current density being equal to 10 mA/cm^2. In the experiments, we used solutions with various volume fractions of HF, HCl, and C_2H_5OH. The samples thus treated were then kept in an atmosphere of D_2O vapors for 10 min. The absorption spectra in the infrared (IR) range of wavelengths (300–5000 cm^{-1}) were recorded using an IFS-113v Fourier-transform IR spectrometer (Bruker, Germany). The samples were transferred to the vacuum chamber of the spectrometer within 2 min immediately after their preparation.

RESULTS AND DISCUSSION

In Fig. 1, we show the transmission spectra of IR emission from the samples treated in the solutions with different volume fractions of HF and HCl. It is found that an absorption band, peaked at 1075 cm^{-1}, emerges in the spectrum of the sample treated in a solution that contains HCl and has a low volume fraction of HF. This band is related to the absorption of light at the vibrations of the Si–O bonds that are incorporated in the Si–O–Si bridge bonds. The position and shape of the absorption peak are found to be similar to those observed in SiO_2 that is formed as a result of the high-temperature oxidation of silicon in dry oxygen [12]. In Fig. 2, we show the transmission spectra of the samples exposed to the D_2O vapors. By comparing the above spectra, we can see that the samples prepared in an electrolyte without the addition of HCl react actively with D_2O. This is supported by the fact that, in the vicinity of 1532 cm^{-1}, a band appears that is related to the stretching vibrations of the SiD_x [13, 14] bonds (for reference, the corresponding SiH_x vibration yields the IR band, peaked at about 2166 cm^{-1}, in between the bands related to SiH_3 and SiH_2).

We should note that the samples passivated by oxygen in the course of preparation with respect to the heavy water vapors are inert. It is well known that the water vapor is the major oxidizing agent, which enters into the composition of the surrounding atmosphere, for the Si surface coated with the SiH_x groups. At room temperature, the native oxide is formed according to the mechanism of dissociative adsorption [15]. As a result, it is mainly the near-surface located Si–OH(D) and Si–H(D) groups that are formed. Taking into account the appreciable isotopic shift of the vibration frequencies of Si–D bonds in reference to those of Si–H bonds, the study of the interaction of *por*-Si with heavy water may serve as an informative method for assessing the chemical stability of the porous layer. Consequently, the obtained results may indicate that a chemically stable structure is formed as a result of treatment in diluted HF solutions. In addition, according to our previous results, this chemical stability is retained even at elevated temperatures, which makes it possible to record the photoluminescence spectra at high levels of laser-radiation excitation [8].

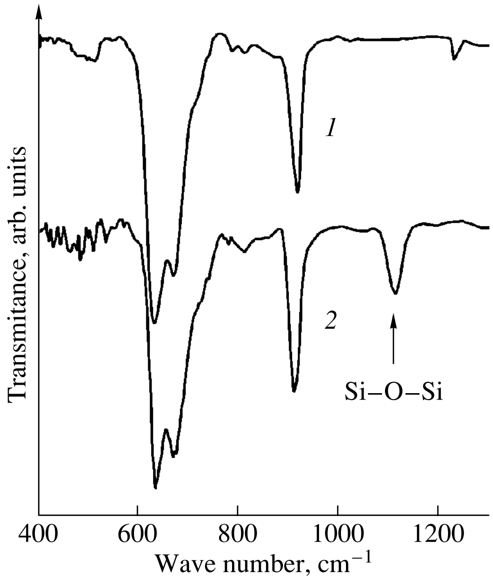

Fig. 1. The Fourier transmission spectra of the as-prepared porous Si samples formed in solutions with different volume fractions of components: (*1*) HF : C_2H_5OH = 1 : 5 and (*2*) HF : C_2H_5OH : HCl = 1 : 5 : 1.

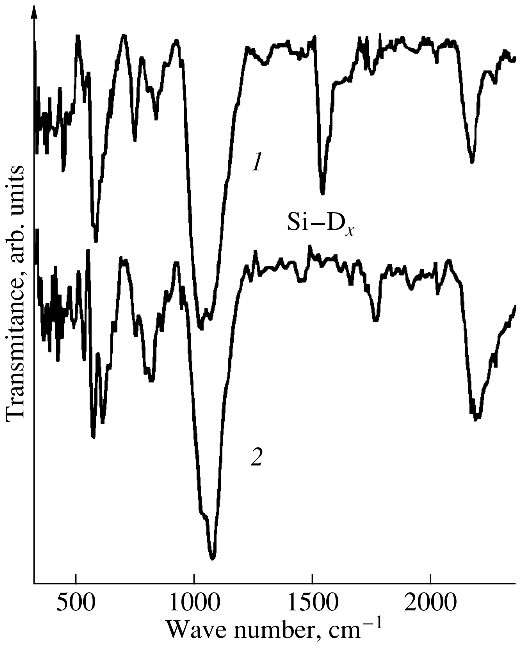

Fig. 2. The transmission Fourier spectra of the samples of porous Si formed in solutions with different volume fractions of components (curve *1* corresponds to HF : C_2H_5OH = 1 : 5 and curve *2* corresponds to HF : C_2H_5OH : HCl = 1 : 5 : 1); prior to measuring the spectra, the samples were exposed to D_2O vapors.

Previously, we also observed an enhanced (close to ideal) hydrophobicity of the surface of *por*-Si formed as a result of treatment in the HCl-containing solutions [10]. This may be indirectly indicative of the absence of

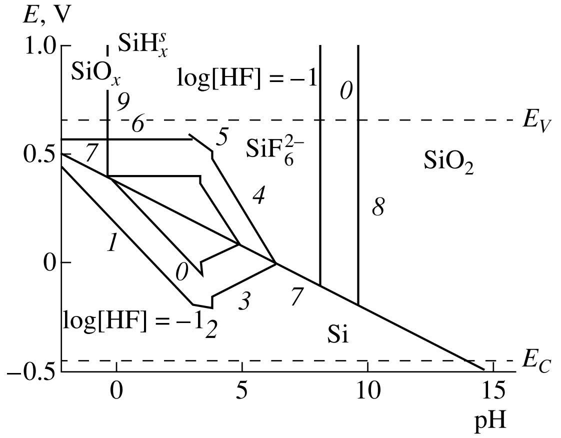

Fig. 3. The calculated diagram of electrochemical equilibrium in a system consisting of Si and an aqueous solution of HF. The curves numbered 0 within the panel represent the equilibrium lines calculated for log[HF] = 0. Designations of other lines are expounded in the text.

dangling surface bonds and charged chemisorbed dipoles, which represent the nonradiative-recombination centers; this inference accounts for an increase in the intensity of photoluminescence of *por*-Si prepared in an unconventional electrolyte [8].

The Fourier spectroscopy data mentioned above made it possible to ascertain the determining role of oxygen-induced passivation of the surface of silicon nanocrystallites in enhancing the stability and intensity of photoluminescence. However, it is generally believed that silicon–oxygen compounds are thermodynamically unstable in aqueous solutions of HF. This contradiction ceases to exist as a result of detailed analysis and refinement of the conditions for electrochemical equilibrium in a system that consists of Si and an HF aqueous solution.

It is typically assumed [16] that formation of porous Si is described by the following electrode reaction:

$$\mathrm{Si} + 6\mathrm{HF} \longrightarrow \mathrm{SiF}_6^{2-} + \mathrm{H}_2 + 4\mathrm{H}^+ + 2e^-. \qquad (1)$$

The potential of reaction (1) is defined by the equation written as

$$\begin{aligned} E &= -2.241 - 0.1182pH - 0.1773\log[\mathrm{HF}] \\ &\quad + 0.0295\log\{[\mathrm{SiF}_6^{2-}]p_{\mathrm{H}_2}\}. \end{aligned} \qquad (1a)$$

Henceforth, the potential E is expressed in V; concentrations, in mol/l; and $p_{\mathrm{H}_2} = p'_{\mathrm{H}_2}/p^0_{\mathrm{H}_2}$, where p'_{H_2} is the pressure of gaseous hydrogen in the system and $p^0_{\mathrm{H}_2}$ = 1.01325×10^5 Pa. The theoretically predicted value of the equilibrium potential for reaction (1) is inconsistent with experimental data. First, the spontaneous disposition of silicon of both types of conductivity in HF solutions should be observed for such a low value of the potential. This follows from the energy position of the edges of the allowed-state bands located at 0.45 and 0.65 eV (in reference to the hydrogen electrode) for the conduction-band bottom (E_C) and the valence-band top (E_V), respectively. In addition, hydrogen-induced passivation, which is always prevalent at the silicon surface in contact with aqueous solutions of HF, does not introduce local states in the silicon band gap [17]. Therefore, the band edges are pinned at the Si/HF interface; the energy barrier of such a junction would inevitably be tunneling-thin in reference to the potential of reaction (1).

The second experimental result, which contradicts reaction (1), consists in the fact that, according to a number of publications, the potential of the anodic decomposition of silicon is in the range of 0.1–0.3 V (in reference to the standard hydrogen electrode) [17–19].

In order to ascertain the exact mechanism of the anodic dissolution of silicon in hydrofluoric acid, we have to consider the actual crystal surface in more detail. It is well known that, in an HF aqueous solution, hydrogen-induced passivation is most favorable thermodynamically [20]; i.e., the equilibrium potential of the silicon electrode in aqueous HF solutions is governed by the hydrogenated-surface potential. Therefore, the anodic reaction of silicon dissolution can be represented as

$$\mathrm{Si{-}SiH}_2^s + 6\mathrm{HF} = \mathrm{SiH}_2^s + \mathrm{SiF}_6^{2-} + \mathrm{H}_2 + 4\mathrm{H}^+ + 2e^-, \qquad (2)$$

$$\begin{aligned} E &= 0.187 - 0.1182pH - 0.1773\log[\mathrm{HF}] \\ &\quad + 0.0295\log\{[\mathrm{SiF}_6^{2-}]p_{\mathrm{H}_2}\}. \end{aligned} \qquad (2a)$$

The potential of reaction (2) was calculated taking into account the silicon sublimation energy, which is equal to 112 kcal/mol [21]. Consideration of the hydrogen-induced passivation of the surface made it possible to calculate the potential of the silicon anodic-oxide formation and to determine the potential corresponding to the transition from the *por*-Si formation to the polishing etching. These two processes can be described, respectively, by the following reactions:

$$\mathrm{SiH}_2^s + 2\mathrm{H_2O} = \mathrm{SiO}_2 + 4\mathrm{H}^+ + \mathrm{H}_2 + 4e^-, \qquad (3)$$

$$E = 0.379 - 0.0591pH + 0.0148\log p_{\mathrm{H}_2}, \qquad (3a)$$

$$\mathrm{SiF}_6^{2-} + \mathrm{H}_2 + 2\mathrm{H_2O} = \mathrm{SiO}_2 + 6\mathrm{HF} + 2e^-, \qquad (4)$$

$$\begin{aligned} E &= 0.56 + 0.1173\log[\mathrm{HF}] \\ &\quad - 0.0295\log\{[\mathrm{SiF}_6^{2-}]p_{\mathrm{H}_2}\}. \end{aligned} \qquad (4a)$$

The adequacy of this description of reactions occurring during the anodic dissolution of silicon in aqueous HF solutions is supported by *in situ* studies of the Fourier spectra. Thus, it has been ascertained [18] that the Si–O–Si bonds appear at the silicon surface at a potential of 0.7 V (in reference to the hydrogen electrode) during the anodic dissolution of Si in HF. The hydrogen-induced passivation alone is characteristic of the surface at lower potentials.

The calculated potentials for the reactions made it possible to plot a potential–pH diagram that defines the stability domains for the dissolved and condensed substances in a system consisting of Si and an aqueous HF solution (Fig. 3). Lines *1*, *2*, and *3* in the diagram represent the dependence of the potential for reaction (2) on pH and account for the domains of prevalence of dissociated forms of the hydrofluoric acid, such as HF, HF_2^-, and F^-. Similarly, lines *4*, *5*, and *6* define the conditions for the transition to electrochemical polishing of silicon as a result of the predominant formation of SiO_2 [reaction (4)]. Line *7* demonstrates the potential of the possible SiO_2 formation according to reaction (3). Line *8* puts a leftmost bound on the domain of chemical stability of the formed anodic SiO_2. In Fig. 3, the straight dotted lines indicate the positions of the band edges for the allowed silicon states E_C and E_V in reference to the electrochemical-potential scale.

According to the diagram, the reaction of formation of silicon–oxygen compounds (mainly, SiO_2) at the Si surface is most favorable for moderate HF concentrations and small values of pH. In Fig. 3, the stability domain for oxygen compounds at the silicon surface is bounded from the right by line *9*. Since hydrofluoric acid is a medium-strength acid, small pH values can be ensured by adding a strong acid (e.g., HCl) to the electrolyte. Consequently, the suggested description of the electrochemical processes substantiates the thermodynamic possibility of forming an oxide phase at the silicon surface treated in the diluted HF acid solutions and makes it possible to explain the enhancement in the stability and intensity of the photoluminescence of *por*-Si obtained [8] as a result of Si treatment in the HF : HCl : C_2H_5OH solutions. Unfortunately, within the scope of this study, we failed to determine the exact crystallographic structure of the oxide phase that is stable during treatment in HF. This problem is of interest in its own right and requires additional study.

CONCLUSION

The experimental results reported here made it possible to demonstrate the determining role of the surface chemical composition of silicon nanocrystals in ensuring the stability of physical and chemical properties of porous Si (*por*-Si). The thermodynamic analysis of electrochemical processes occurring in the course of the anodic dissolution of Si made it possible to suggest a new description for the electrode reaction of interaction between Si and HF. It is shown that the hydrogen-induced passivation of the Si surface governs the equilibrium dissolution potential of the silicon electrode. The thermodynamic calculations showed that it is possible to replace the chemically and thermally unstable SiH_x groups with more stable silicon–oxygen compounds directly in the course of the *por*-Si formation in the electrolytes with the addition of strong hydrohalic acids. The results obtained made it possible to interpret thermodynamically the stabilizing effect of the HCl additive to the electrolytes used for formation of *por*-Si on the chemical and physical properties of *por*-Si.

ACKNOWLEDGMENTS

This study was supported by the INTAS.

REFERENCES

1. L. T. Canham, Appl. Phys. Lett. **57**, 1046 (1990).
2. L. V. Belyakov, D. N. Goryachev, and O. M. Sreseli, Fiz. Tekh. Poluprovodn. (St. Petersburg) **34**, 1386 (2000) [Semiconductors **34**, 1334 (2000)].
3. S. Lazarouk, S. Katsouba, A. Tomlinson, *et al.*, Mater. Sci. Eng. B **69–70**, 114 (2000).
4. E. A. Shelonin, M. V. Naĭdenkova, A. M. Khort, *et al.*, Fiz. Tekh. Poluprovodn. (St. Petersburg) **32**, 494 (1998) [Semiconductors **32**, 443 (1998)].
5. T. Arigane, K. Yoshida, T. Wadayama, and A. Hatta, Surf. Sci. **427–428**, 304 (1999).
6. A. M. Orlov and A. V. Sindyaev, Zh. Tekh. Fiz. **69** (6), 135 (1999) [Tech. Phys. **44**, 729 (1999)].
7. Z. Yamani, W. H. Thompson, L. AbuHassan, and M. H. Nayfen, Appl. Phys. Lett. **70**, 3404 (1997).
8. A. I. Belogorokhov, R. Enderlein, A. Tabata, *et al.*, Phys. Rev. B **56**, 10276 (1997).
9. S. Zangooie, R. Jansson, and H. Arwin, Appl. Surf. Sci. **136**, 123 (1998).
10. S. A. Gavrilov, T. N. Zavaritskaya, V. A. Karavanskiĭ, *et al.*, Élektrokhimiya **33**, 1064 (1997).
11. J. L. Gole, J. A. De Vincentis, L. Seals, *et al.*, Phys. Rev. B **61**, 5615 (2000).
12. R. C. Newman, *Infra-red Studies of Crystal Defects* (Taylor and Francis, London, 1978).
13. S. Watanabe, Appl. Surf. Sci. **162–163**, 146 (2000).
14. T. Matsumoto, A. I. Belogorokhov, L. I. Belogorokhova, *et al.*, Nanotechnology **11**, 340 (2000).
15. J.-H. Cho, K. S. Kim, S.-H. Lee, and M.-H. Kang, Phys. Rev. B **61**, 4503 (2000).
16. D. R. Turner, J. Electrochem. Soc. **105**, 402 (1958).
17. S. Ottow, G. S. Popkirov, and H. Foll, J. Electroanal. Chem. **445**, 29 (1998).
18. C. DaFonseca, F. Ozanam, and J.-N. Chazalviel, Surf. Sci. **365**, 1 (1996).
19. M. Bailes, S. Bohm, L. M. Peter, *et al.*, Electrochim. Acta **43**, 1757 (1998).
20. G. F. Cerofolini and L. Meda, Appl. Surf. Sci. **89**, 351 (1995).
21. U. D. Veryatin, V. P. Mashirev, N. G. Ryabtsev, V. I. Tarasov, B. D. Rogozkin, and I. V. Korobov, *Thermodynamic Properties of Inorganic Compounds: A Handbook* (Atomizdat, Moscow, 1965).

Translated by A. Spitsyn